NASA CONTRACTOR REPORT

NASA CR-66661

NASA CR-66661

FINAL REPORT

STUDY OF DIRECT VERSUS ORBITAL ENTRY FOR MARS MISSIONS

Volume III - Appendix A - Launch Vehicle Performance and Flight Mechanics

Prepared by

MARTIN MARIETTA CORPORATION
DENVER, COLORADO

for

Langley Research Center

NATIONAL AERONATUICS AND SPACE ADMINISTRATION • WASHINGTON, D.C. • AUGUST 1968

NASA CR-66661

FINAL REPORT

STUDY OF DIRECT VERSUS ORBITAL ENTRY FOR MARS MISSIONS

VOLUME III: APPENDIX A - LAUNCH VEHICLE PERFORMANCE AND FLIGHT MECHANICS

By Hugh N. Zeiner and Donald W. Marquet

Prepared under Contract No. NAS1-7976 by
MARTIN MARIETTA CORPORATION
Denver, Colorado

for

NATIONAL AERONAUTICS AND SPACE ADMINISTRATION

FOREWORD

This Final Report for the "Study of Direct Versus Orbital Entry for Mars Missions" (NASA Contract NAS1-7976) is provided in accordance with Part III A.4 of the contract schedule as amended. The report is in six volumes as follows:

NASA CR-66659 - Volume I	-	Summary;
NASA CR-66660 - Volume II	-	Parametric Studies, Final Analyses, and Conceptual Designs;
NASA CR-66661 - Volume III	-	Appendix A - Launch Vehicle Performance and Flight Mechanics;
NASA CR-66662 - Volume IV	-	Appendix B - Entry and Terminal Phase Performance Analysis;
NASA CR-66663 - Volume V	-	Appendix C - Entry Configuration Analysis;
NASA CR-66664 - Volume VI	-	Appendix D - Subsystem Studies and Parametric Data.

APPENDIX A

CONTENTS

APPENDIX A

APPENDIX A

APPENDIX A

APPENDIX A

APPENDIX A

APPENDIX A

APPENDIX A

LAUNCH VEHICLE PERFORMANCE AND FLIGHT MECHANICS

APPENDIX A

1. LAUNCH VEHICLE CAPABILITY

The performance capability of various Titan III family launch vehicles to Mars was presented in reference A1. These results dealt primarily with maximizing useful payload in Mars orbit. Subsequent analyses (refs. A2 and A3) presented updated performance for the 1973 Type I and 1975 Type I and II opportunities. The analyses of references A1 thru A3 made use of several simplifying assumptions. An optimum spacecraft was assumed; the propellant quantity was assumed to be variable according to midcourse correction and Mars orbit insertion requirements for each launch date. In practice, a fixed capability spacecraft will be used with propellant available for the maximum requirement over the 30-day launch period. Other simplifications included launch vehicle velocity loss for a single launch azimuth and payload-dependent items, such as the shroud and adapter, assumed constant for all launch vehicles. The results herein represent a more comprehensive analysis with an attempt at eliminating the simplifying assumptions discussed above. Four launch vehicles are considered -- Titan IIIC, Titan IIIF/Stretched Transtage, Titan IIIC/Centaur, and Titan IIIF/Centaur. Mars mission opportunities of 1973, 1975, and 1977 with both Type I and Type II transfer trajectories are considered.

Mission Requirements

Earth escape energy (C_3) requirements for the six opportunity/transfer type combinations are shown in figures A1 thru A6. These are presented as energy contours for a range of launch date-encounter date combinations. Overlays of Mars approach energy (V_{HE}) and declination of the departure asymptote (DLA) are supplied in an envelope inside the rear cover of this report. Loci of minimum C_3 and V_{HE} are indicated.

The relationship between C_3 and velocity required for Mars transfer injection (V_{Inj}) is given by

$$V_{Inj} = \left(C_3 + 2\frac{\mu}{r}\right)^{\frac{1}{2}}$$

where

μ = GM

G = universal gravitational constant

M = planet mass

r = radius at injection.

The velocity required for Mars orbit insertion $\left(\Delta V_{OI}\right)$ is expressed as a function of V_{HE} by

$$\Delta V_{OI} = \left(V_{HE}^2 + 2\ \mu/r_P\right)^{\frac{1}{2}} - \left(\sqrt{1+\epsilon}\right)\left(\sqrt{\mu/r_P}\right) + \Delta V_{LOSS}$$

where

ϵ = Mars orbit eccentricity

r_P = radius vector to Mars orbit periapsis.

The relationship between DLA and launch azimuth (LAZ) is discussed below under launch vehicle characteristics.

The energy contours in figures A1 thru A6 are presented as an illustration. In actual practice, a digital program has been developed that computes C_3, V_{HE}, and DLA as functions of launch and encounter dates for a given opportunity and transfer type. The computation is simply described as a point-to-point conic using planet mean orbital elements. The required values of C_3 and V_{HE} are related to velocity requirements by the above expressions. The velocity requirements are then applied to the launch vehicles described below.

For this study, the Mars orbit periapsis altitude is 1000 km. Two Mars orbit eccentricities are used, 0.6144 and 0.785, corresponding to apoapsis altitudes 15 000 and 33 070 km, respectively. A velocity of 75 mps is used to account for Mars orbit insertion losses and orbit trim. In addition, a midcourse correction velocity of 75 mps is assumed. These values are both conservative.

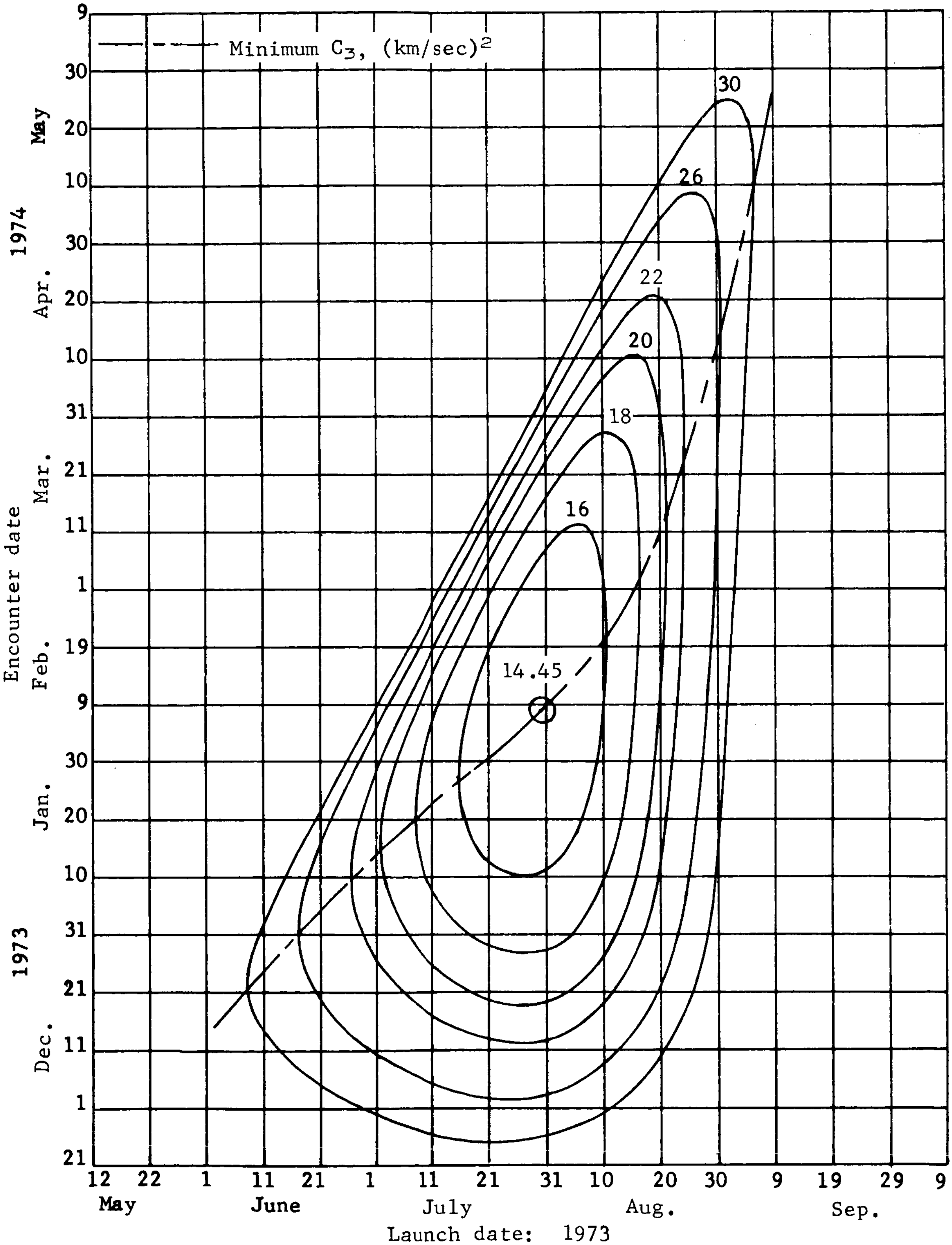

Figure A1.- Earth Departure Energy, Mars 1973, Type I

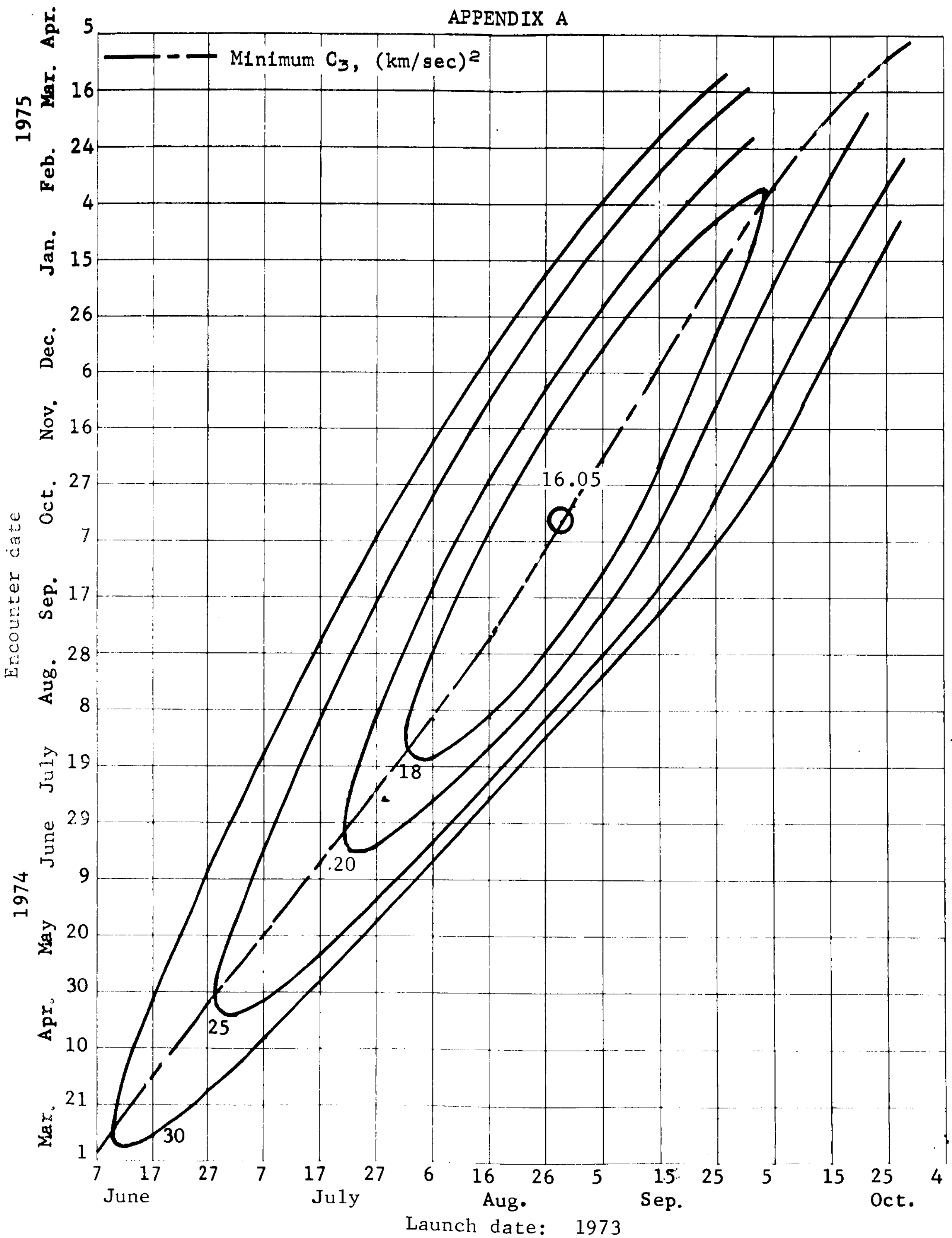

Figure A2.- Earth Departure Energy, Mars 1973, Type II

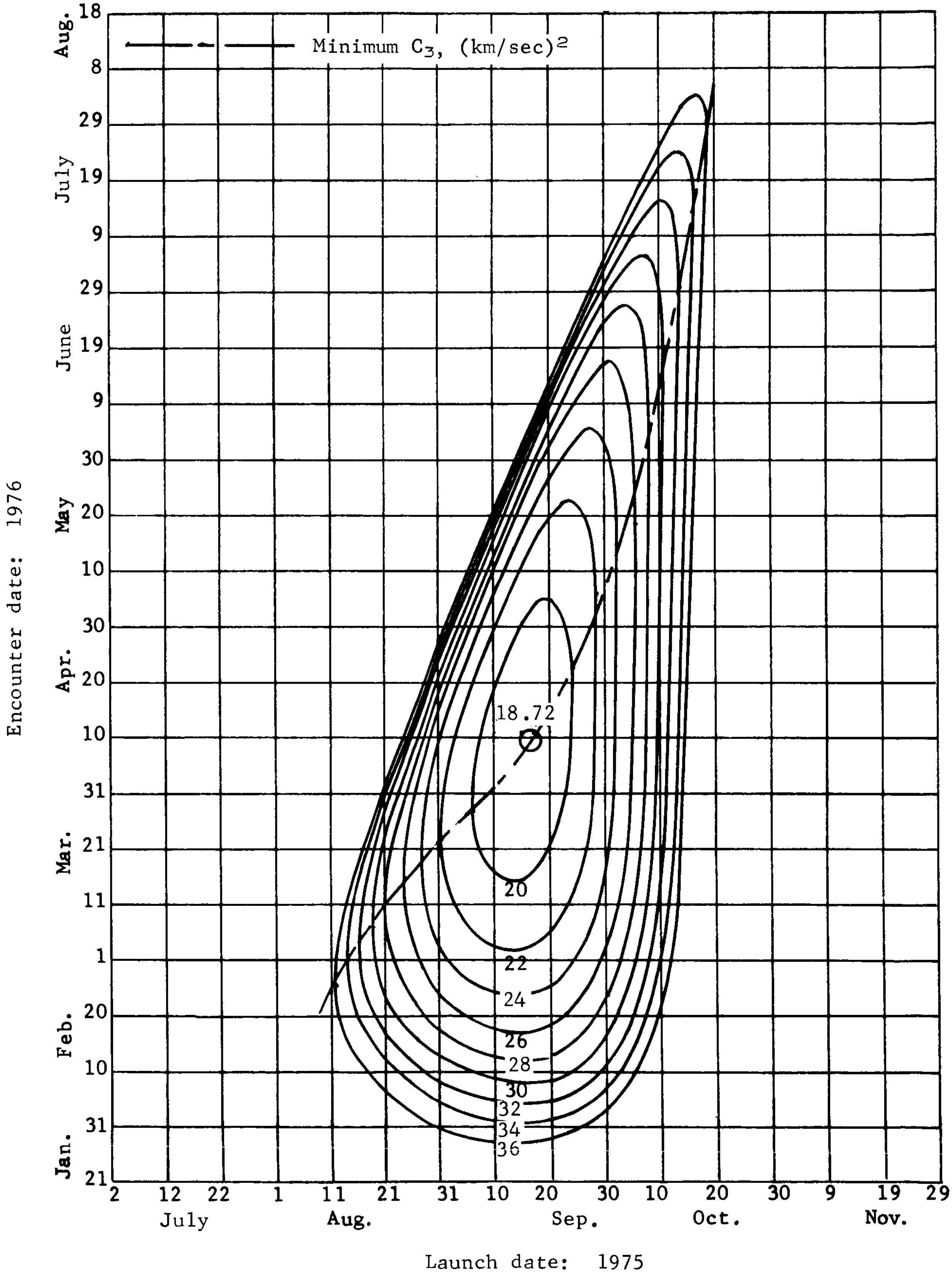

Figure A3.- Earth Departure Energy, Mars 1975, Type I

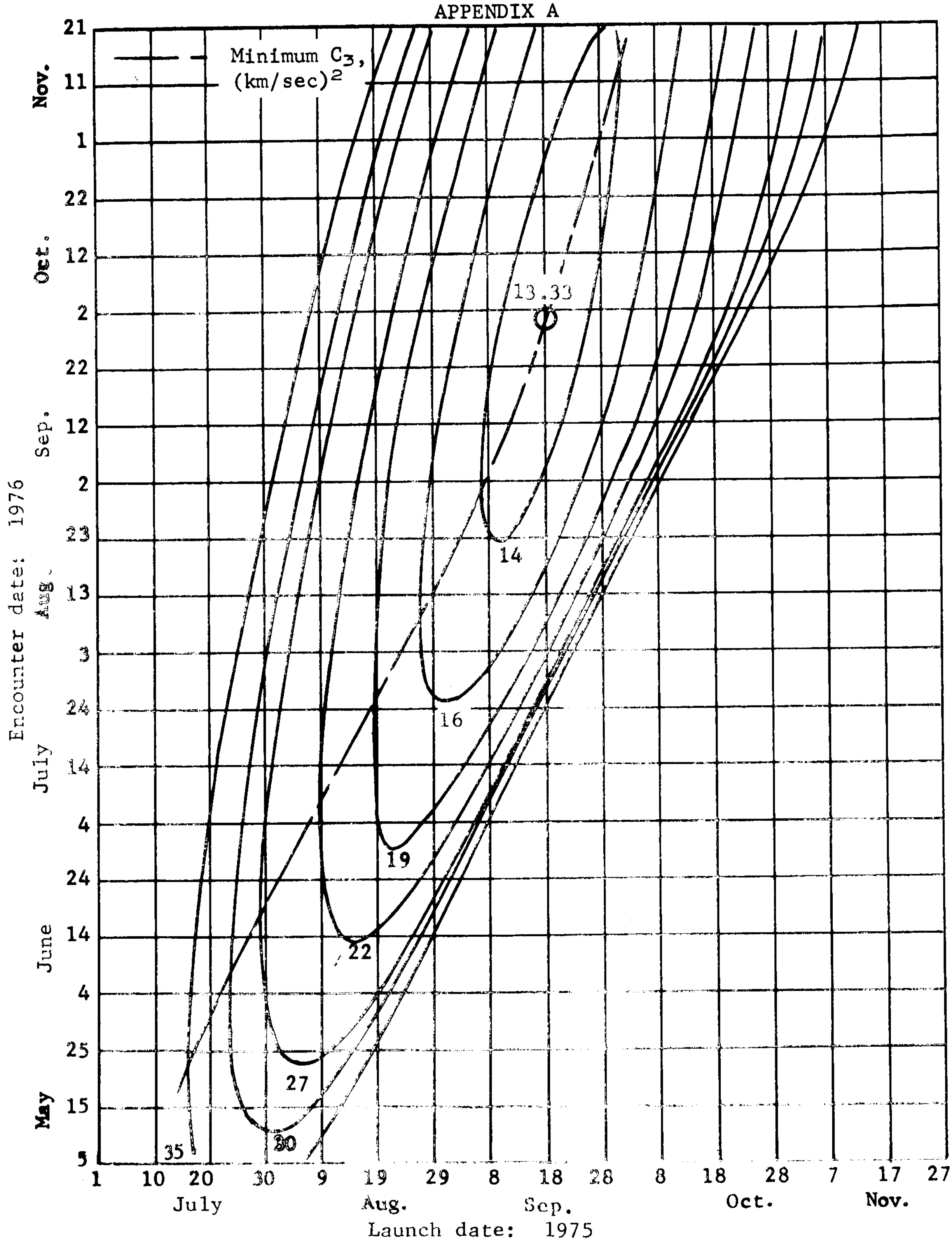

Figure A4.- Earth Departure Energy, Mars 1975, Type II

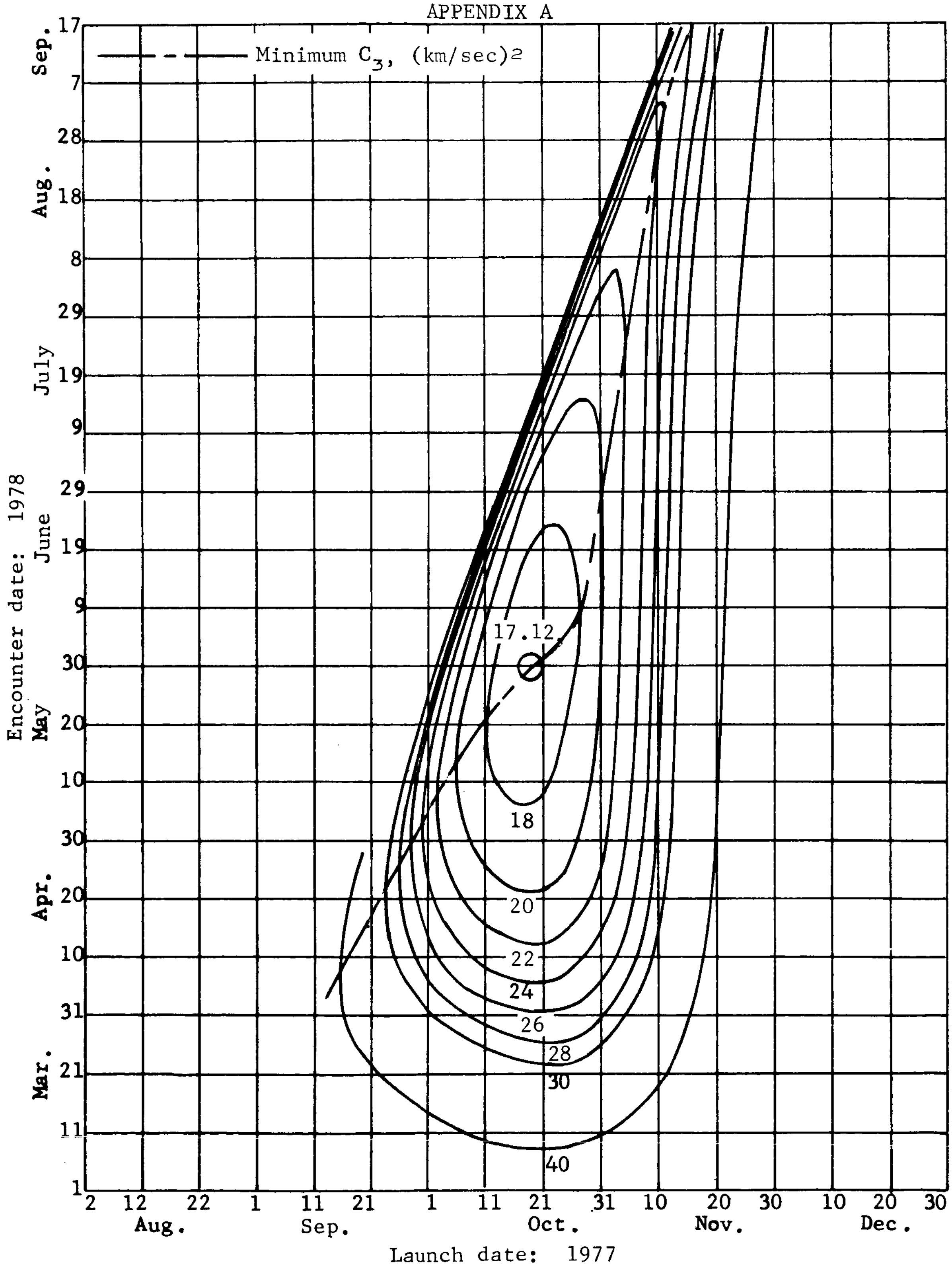

Figure A5.- Earth Departure Energy, Mars 1977, Type I

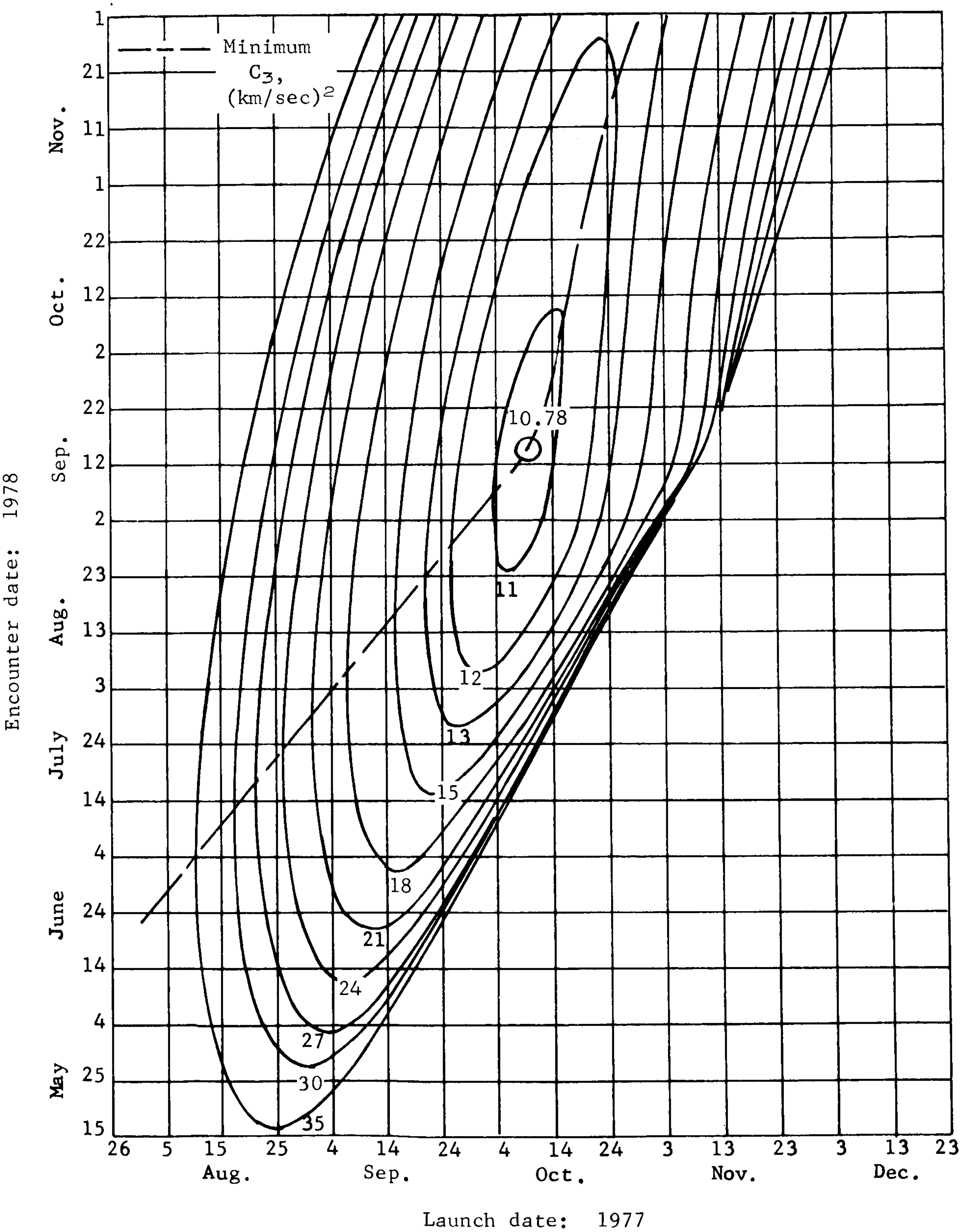

Figure A6.- Earth Departure Energy, Mars 1977, Type II

APPENDIX A

Launch Vehicle Description

The Titan IIIC vehicle consists of the basic Titan III liquid propellant core with two 5-segment solid propellant strap-on motors. The Transtage provides upper stage capability and is included in the Titan IIIC designation. The performance data quoted herein are for a follow-on class vehicle. This is essentially Article 19 with changes expected to be incorporated before the mission time period considered in this analysis. In general, the performance data represent 15:1 expansion ratio Stage I engines and ullage blowdown pressurization system. Also included is a battery change that improves Transtage burnout weight by approximately 100 lb. The Titan IIIC/Centaur is a Titan IIIC with the Transtage replaced by Centaur. The Titan IIIF is a growth version of the Titan IIIC with increased Stage I propellant capacity and 7-segment solid rocket motor strap-ons. The upper stages used in combination with the Titan IIIF for this study are the Stretched Transtage and the Centaur. The Stretched Transtage provides increased propellant capability over the standard version. It is used with the Titan IIIF (rather than using the standard Transtage) to allow a circular Earth park orbit. With a lighter upper stage, an elliptical park orbit would be achieved with the attendant problems discussed in reference A2. A more detailed description of the launch vehicles including the upper stages may be found in reference A5.

Basic launch vehicle performance capability in terms of payload versus velocity is shown in figure A7. The Titan IIIC data shown represent the latest update as discussed above. Data for the other vehicles were taken directly from reference A5. At a typical inject velocity of 38 500 fps, payloads range from 3150 to 12 500 lb.

It is evident, in the light of the ground rules indicated in figure A7 that adjustments must be made to the data for the velocity losses and additional structural weights accompanying an actual mission application. For launches from ETR, DLA defines the required launch azimuth as shown in figure A8. For values of $|DLA| \leq 36°$, a constant launch azimuth of 115° is used in this analysis. This is the southernmost launch azimuth allowed by range safety considerations. A rather arbitrary northernmost launch azimuth is assumed to be 45°, with a corresponding declination of $\pm 50°$. The launch azimuth-declination combinations used provide a minimum 2-hr daily launch window, shown in figure A9. Note that the left-hand scale of figure A9 is used to define daily launch window only; it is not an indication of time of day. The data for both figures A8 and A9 also appear in reference A4.

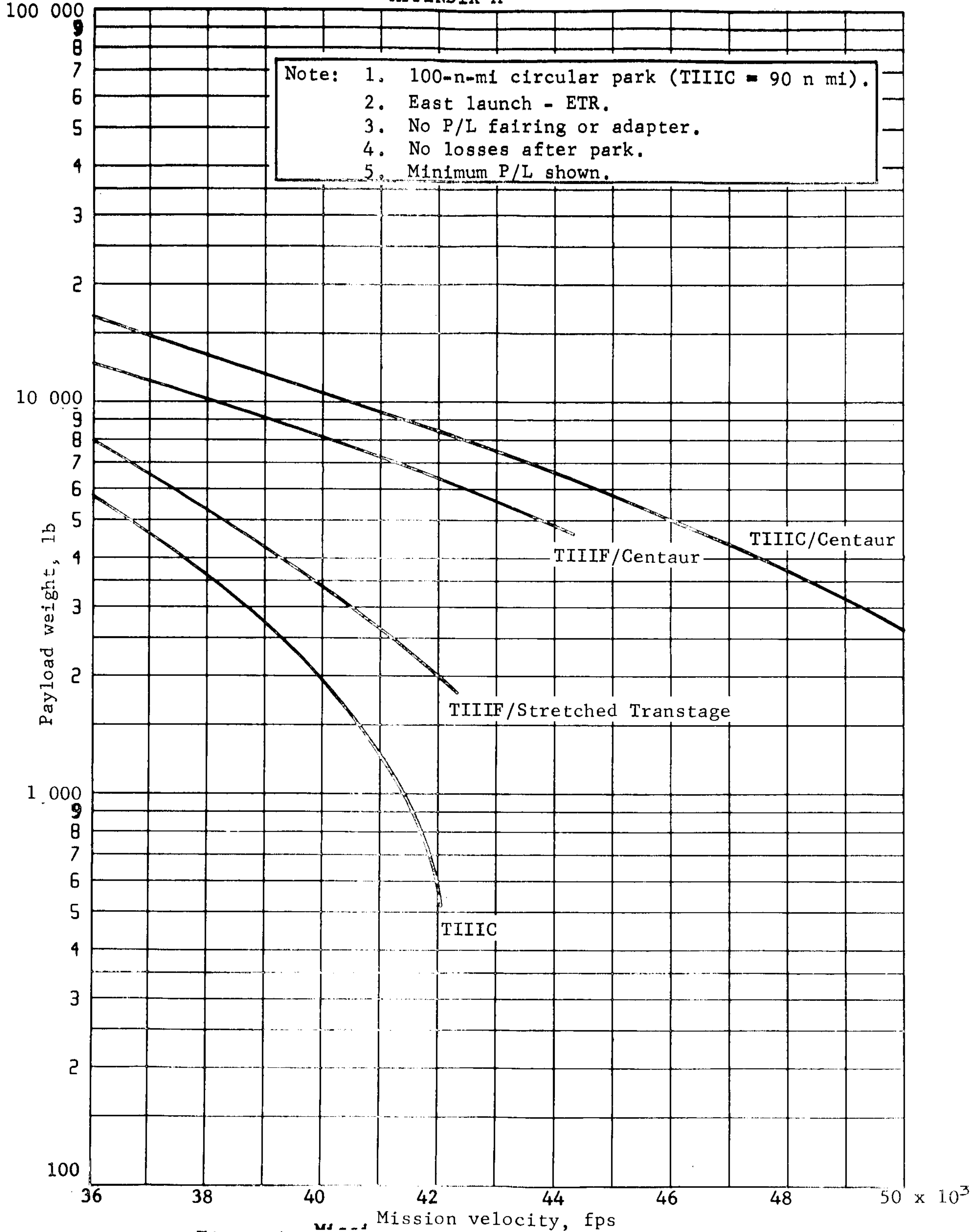

Figure A7.- Titan III Family, Payload Versus Velocity

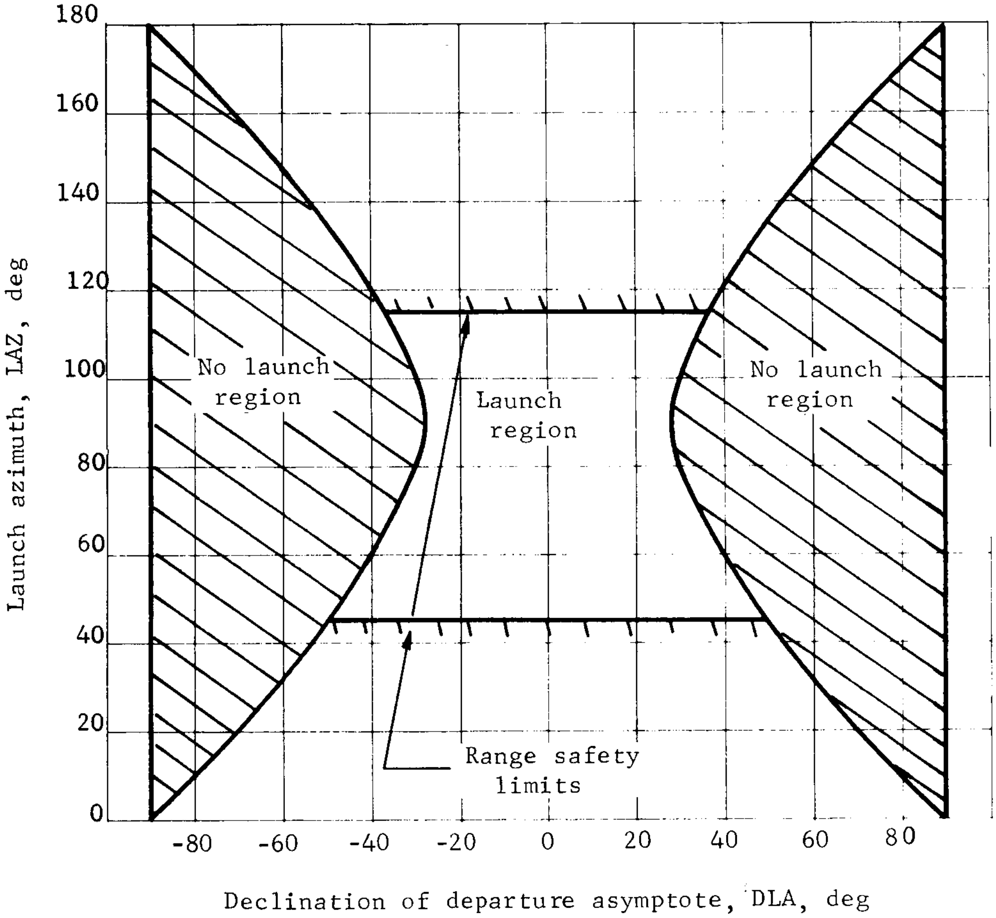

Figure A8.- Limiting Launch Azimuth Versus Declination of Departure Asymptote for ETR

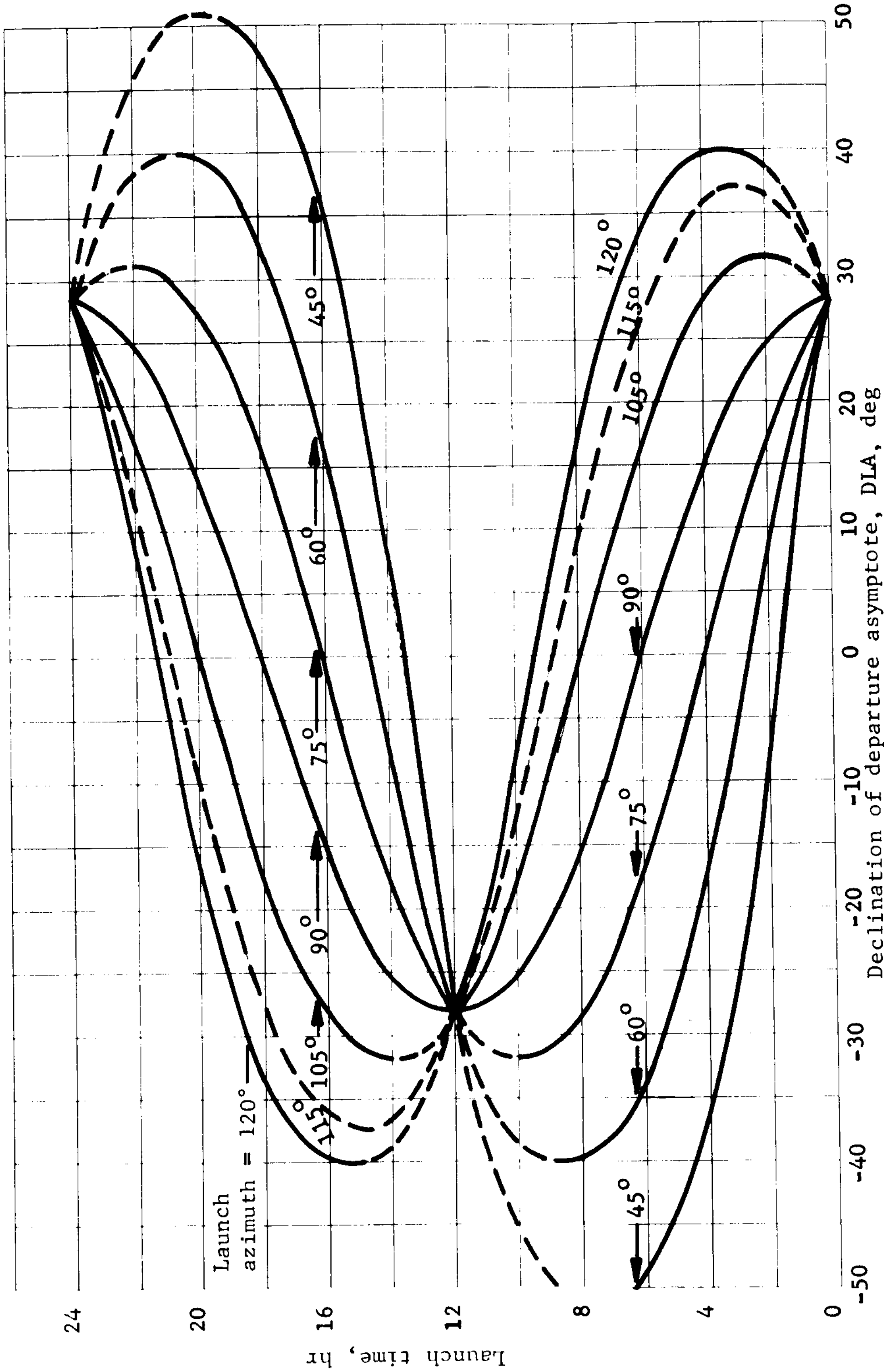

Figure A9.- Launch Time Versus Declination of Departure Asymptote for ETR

APPENDIX A

Where $36° < |DLA| \leq 50°$, the basic launch vehicle data are corrected by the Δ velocity shown in figure A10. The correction of figure A10 accounts for the difference between a due-east launch from ETR and launch at the azimuth corresponding to the value of DLA required by a launch date/arrival date combination. Where $|DLA| > 50°$ for optimum payload studies, the arrival date (for a given launch date) is adjusted to $DLA = 50°$, and the velocity correction of figure A10 at $DLA = 50°$ is applied. For more general payload studies, (i.e., payload at a given launch date/arrival date combination) the actual value of DLA is used, and the velocity correction of figure A10 (extrapolated where required) is used. In addition to the launch azimuth loss, a superorbital (leaving park orbit) velocity loss of 50 fps is assumed. This is a gravity loss and is estimated on the basis of a digital simulation.

An actual mission involves a payload; this implies a shroud or fairing to protect the payload from the boost environment and an adapter to attach the payload to the launch vehicle. The fairing is jettisoned early in Stage I flight where the dynamic pressure environment is nearly zero. However, some fairing hardware remains with the launch vehicle; the fairing correction must therefore be evaluated in two parts -- jettisoned and fixed. Fairing and adapter weights used for this study are given in Table A1. Also shown in the table are fairing diameters and barrel lengths. The fairings are described in more detail in the main body of the report. The effect of fairing weight on payload capability is described below.

TABLE A1.- STRUCTURAL WEIGHT CORRECTIONS TO BASIC LAUNCH VEHICLE PERFORMANCE

Launch vehicle	Weight correction, lb			Fairing dimension, in.	
	Jettisoned fairing	Fixed fairing	Adapter	Outside diameter	Barrel length
TIIIC	1480	70	250	[a]120	144
TIIIF/Stretched Transtage	3570	200	340	200	220
TIIIC/Centaur[b]	5560	250	500	200	220
TIIIF/Centaur[b]	6270	280	590	200	280

[a]Inside diameter.

[b]Centaur shrouded by the fairing.

APPENDIX A

The adapter and fixed fairing weights are subtracted directly from the payload shown in figure A7. However, the jettisoned fairing weight must be adjusted to account for the fact that it is not present during the later portion of the boost trajectory. The payload adjustment, $\Delta W_{P/L}$, to figure A7 is obtained from

$$\Delta W_{P/L} = \Delta W_{F_J} \frac{\partial W_{P/L}}{\partial W_{F_J}}$$

where ΔW_{F_J} is the jettisoned fairing weight. Values of $\partial W_{P/L}/\partial W_{F_J}$ are taken from figure A11 and are on the order of 6 to 8% at the inject velocities of interest (≈ 38 000 to 39 000 fps).

The resulting corrected launch vehicle capability is shown in figure A12 as a function of C_3 (Earth escape energy). It is seen that the payload at 38 500 fps ($C_3 = 16.3$ km^2/sec^2) has dropped to 2470 and 10 640 lb as a result of the applied corrections. This includes expenditure of midcourse propellant quantities of 65 and 275 lb, respectively. Using the Titan IIIC vehicle and the 1973 Type I mission as an example, the payload capability is computed as follows:

First launch date	7/13/73
C_3, km/sec^2	16.3
Inject velocity, fps	38 500
Uncorrected payload, lb*	3150

Payload corrections are as tabulated.

Item	ΔV, fps	ΔW, lb	ΔP/L, lb
115° launch azimuth	170	----	147
Inject gravity loss	50	----	43
Fixed fairing	----	70	70
Jettisoned fairing	----	1480	105
Adapter (launch vehicle/spacecraft)	----	250	250
Midcourse propellant	----	65	65
Total			680

*East launch, ETR, 90-n mi circular Earth park orbit, no payload fairing or adapter, no losses after park orbit.

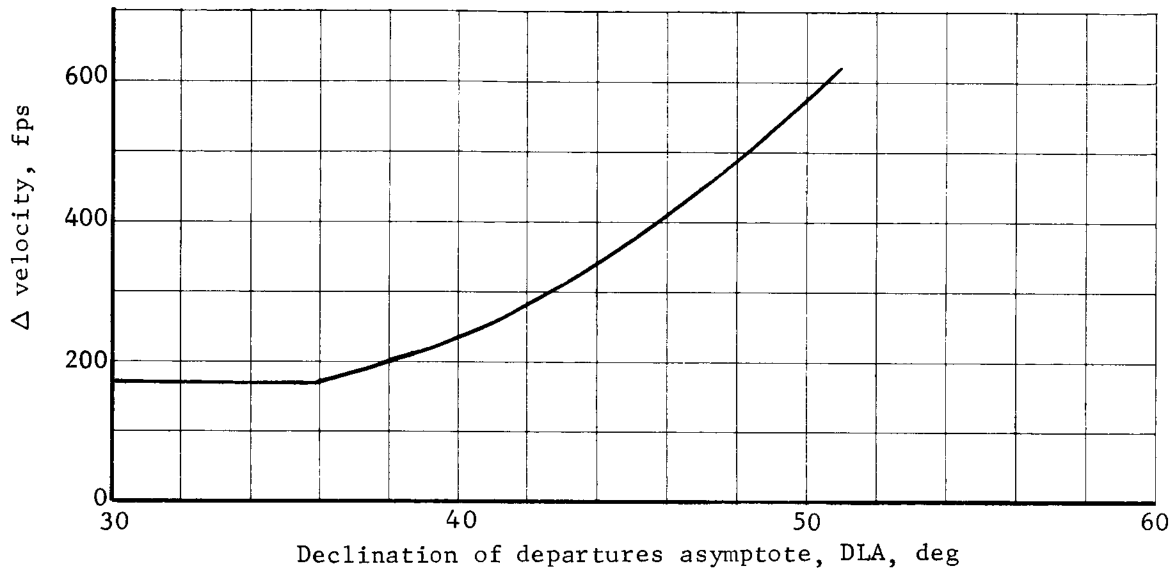

Figure A10.- Velocity Loss due to Declination

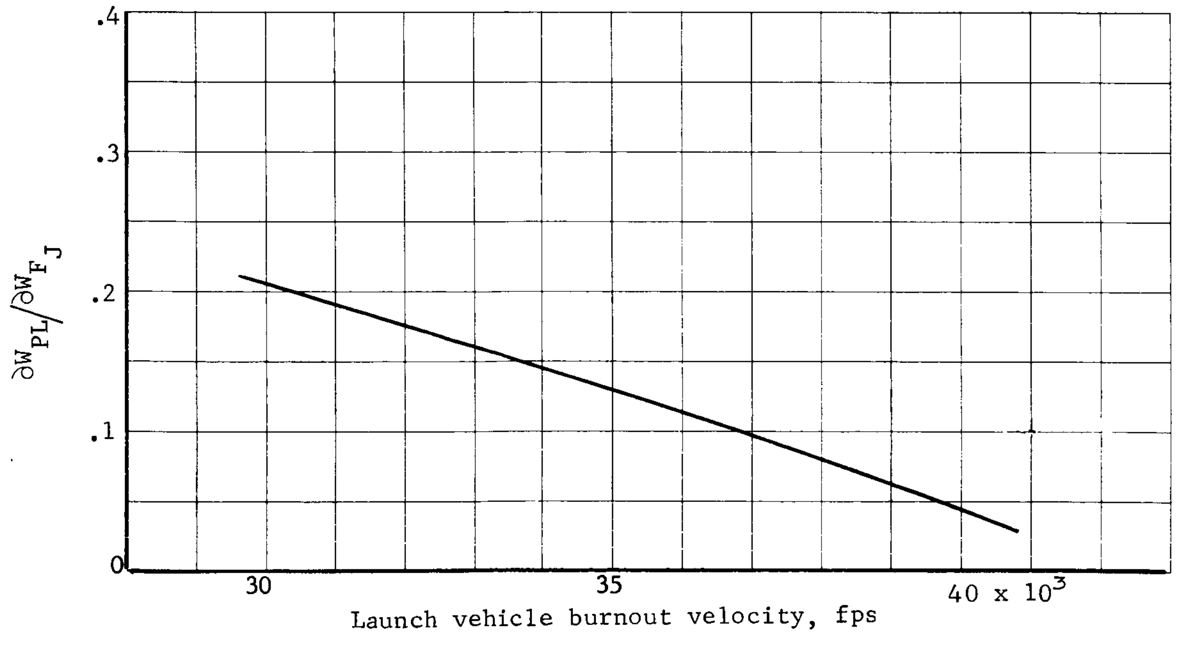

Figure A11.- Payload Weight Fraction of Jettisoned Fairing

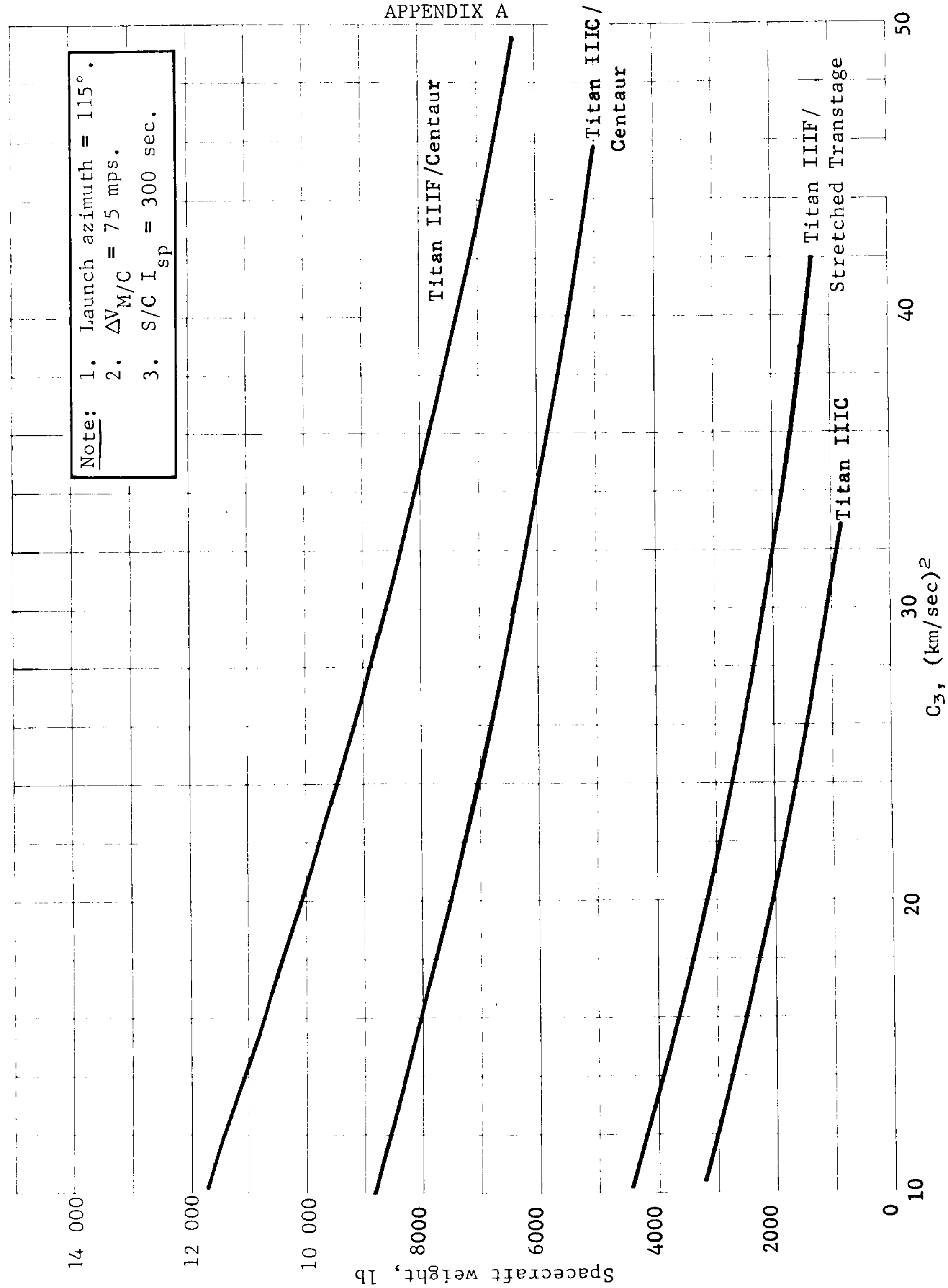

Figure A12.- Launch Vehicle Capability after Midcourse Correction

Therefore, allowable spacecraft weight after midcourse correction is 3150 - 680 or 2470 lb.

The spacecraft,* supplies the midcourse correction and Mars orbit insertion impulses. A spacecraft propulsion system specific impulse (I_{sp}) of 300 to 309 sec is used depending on application. For this study, entry capsule system weight is the variable to be correlated with design studies. Fixed maximum and minimum useful in-orbit orbiter weight values of 890 and 620 lb, respectively, are used. Useful in-orbit orbiter weight, for performance purposes, is spacecraft burnout weight less propulsion system inert weight less capsule system weight. Note that the capsule adapter and sterilization canister are considered a part of the total capsule system weight. Spacecraft propulsion inerts differ somewhat according to the application (i.e., midcourse correction only or midcourse + Mars orbit insertion). These will be shown with the applicable performance data.

In general, capsule system weight is spacecraft weight less the orbiter useful weight, orbiter propellant, and orbiter propulsion inert weight. For any maneuver involving a velocity change (ΔV), the propellant weight (W_P) required is

$$W_P = W_O - W_F$$

$$= W_O\left(1 - W_F/W_O\right)$$

$$= W_O\left(1 - e^{-\Delta V/C_J}\right)$$

where

W_O = weight before maneuver

W_F = weight after maneuver

$C_J = g_{\oplus} I_{sp}$

$g_{\oplus}$ = Earth g (32.2 ft/sec^2).

*Precise nomenclature is spacecraft (capsule system included) or orbiter (capsule system ejected).

APPENDIX A

For a given propulsion system, inert weight (W_{PI}) is related to propellant weight and propellant mass fraction (λ) by

$$W_{PI} = W_P(1/\lambda - 1)$$

Spacecraft Capability

Contours of spacecraft weight are shown in figures A13 thru A36 for the four launch vehicles and six mission opportunity/ transfer type combinations. Values after midcourse correction are shown; midcourse correction ΔV of 75 mps and a spacecraft specific impulse of 300 sec are used. The weights shown are injected payload less midcourse propellant required. These are essentially contours of constant C_3 expressed in terms of the weights shown. Slight differences in shape from the C_3 contours shown earlier are the result of launch azimuth velocity loss effects. As discussed earlier, where $|DLA| \leq 36°$, a 170-fps constant velocity loss due to launch azimuth is used. Where declination is greater than 36°, velocity loss is increased (see fig. A10). Thus, for $|DLA| > 36°$, the arrival date for a given launch date must be shifted slightly toward lower C_3 to give the desired payload value. These contours are presented as an illustration. They may be used for rapid evaluation of the launch period and arrival date combinations.

Also shown in figures A13 thru A36 are direct entry capsule system weights (total) for maximum and minimum weight flyby spacecraft. Useful flyby spacecraft weight values used are 890 lb (maximum) and 620 lb (minimum). For the direct entry capsule system with flyby spacecraft, we have

$$W_{C/S} = W_{S/C} - W_{F/B} - W_{PI}$$

where

$W_{C/S}$ = capsule system weight

$W_{S/C}$ = spacecraft weight (after midcourse correction)

$W_{F/B}$ = flyby vehicle useful weight

W_{PI} = spacecraft propulsion inert weight.

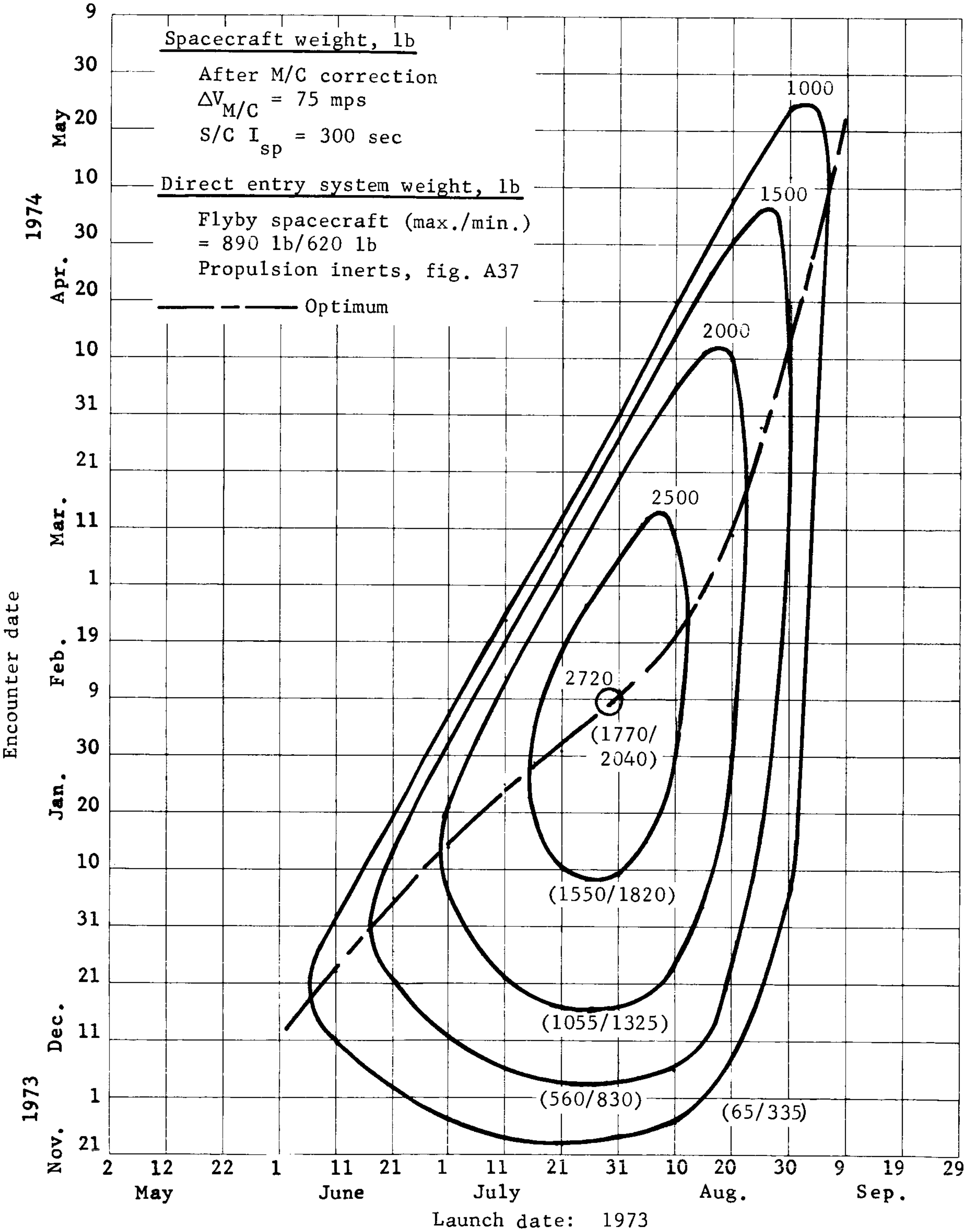

Figure A13.- Spacecraft Weight, Mars 1973, Type I, Titan IIIC

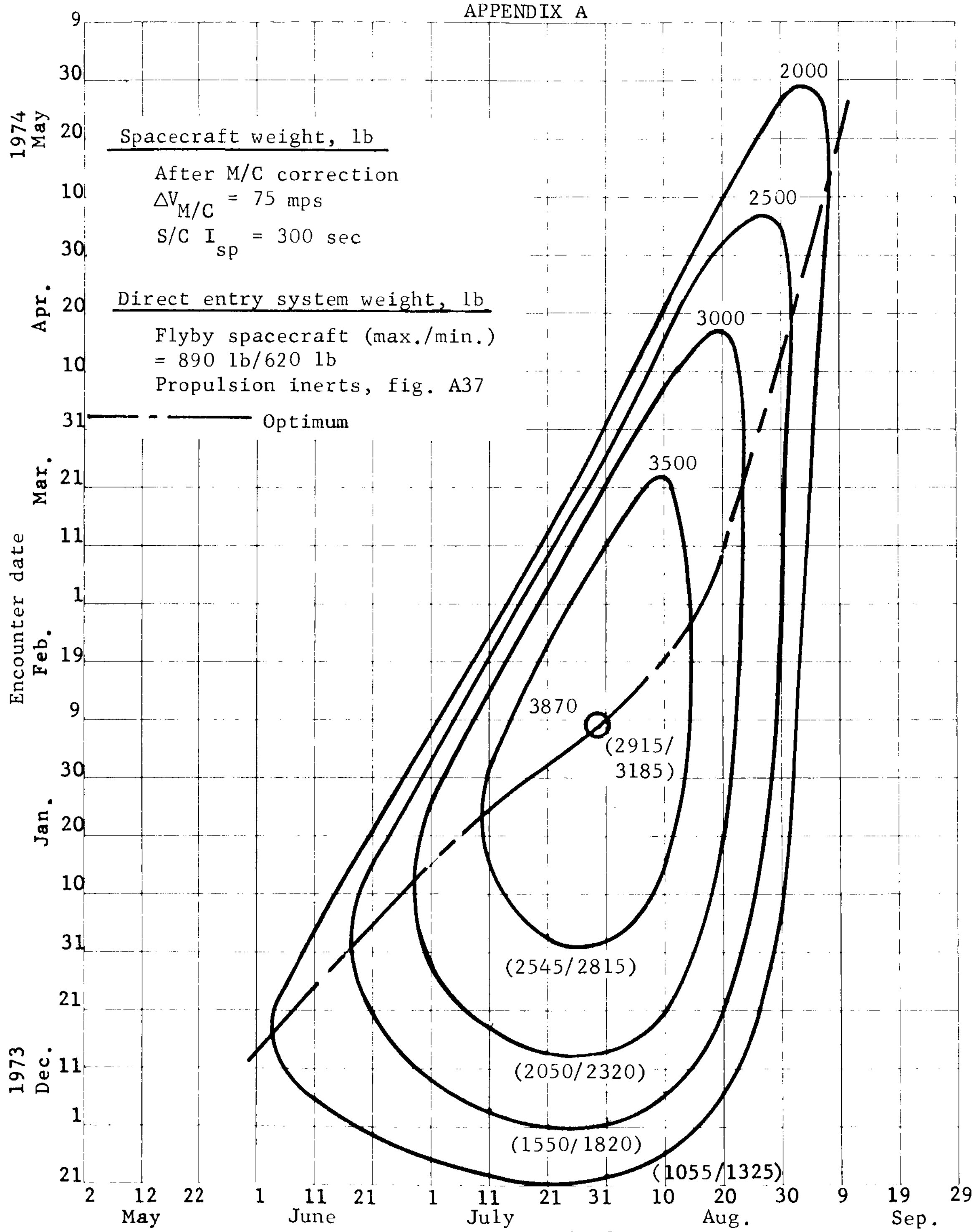

Figure A14.- Spacecraft Weight, Mars 1973, Type I, Titan IIIF/ Stretched Transtage

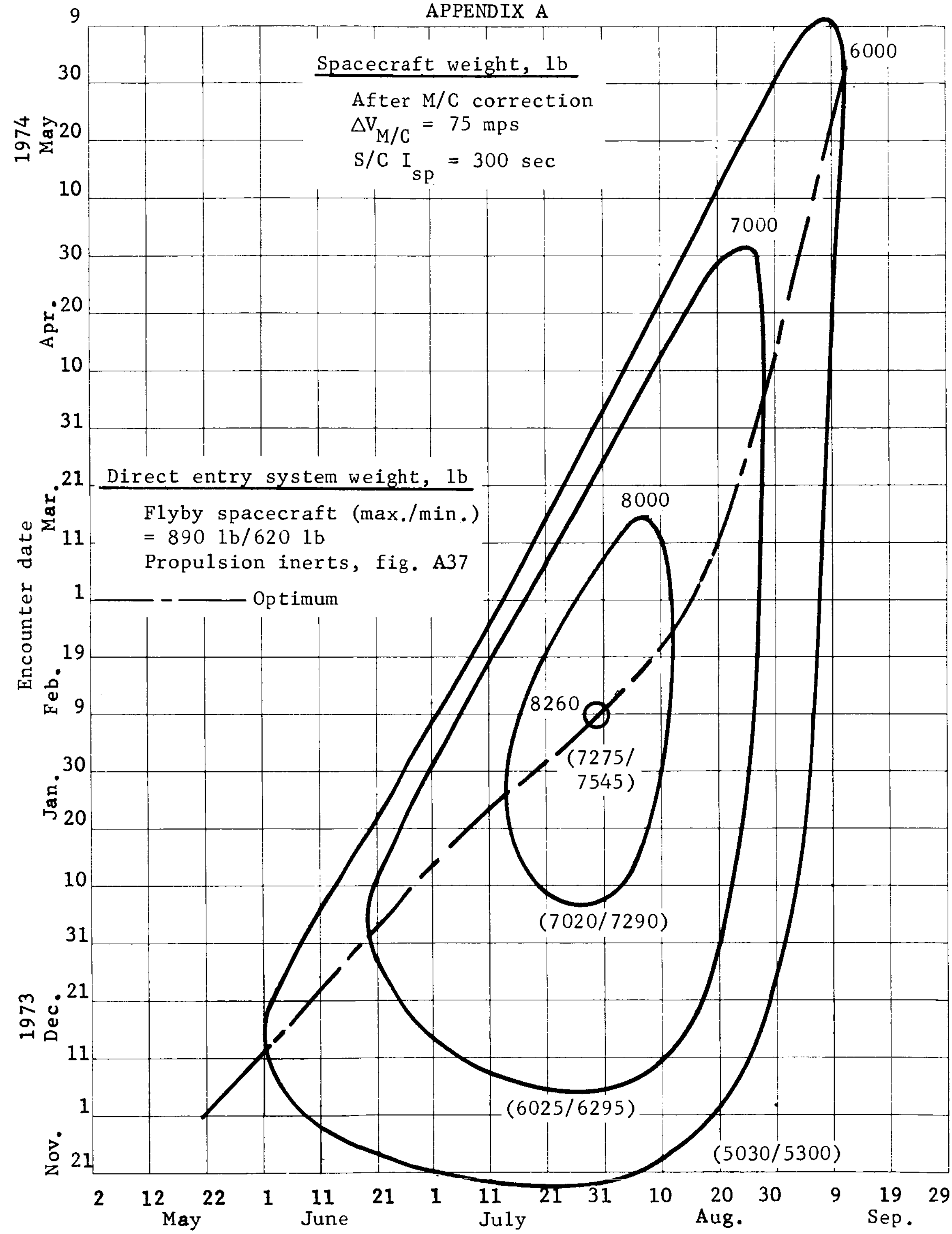

Figure A15.- Spacecraft Weight, Mars 1973, Type I, Titan IIIC/Centaur

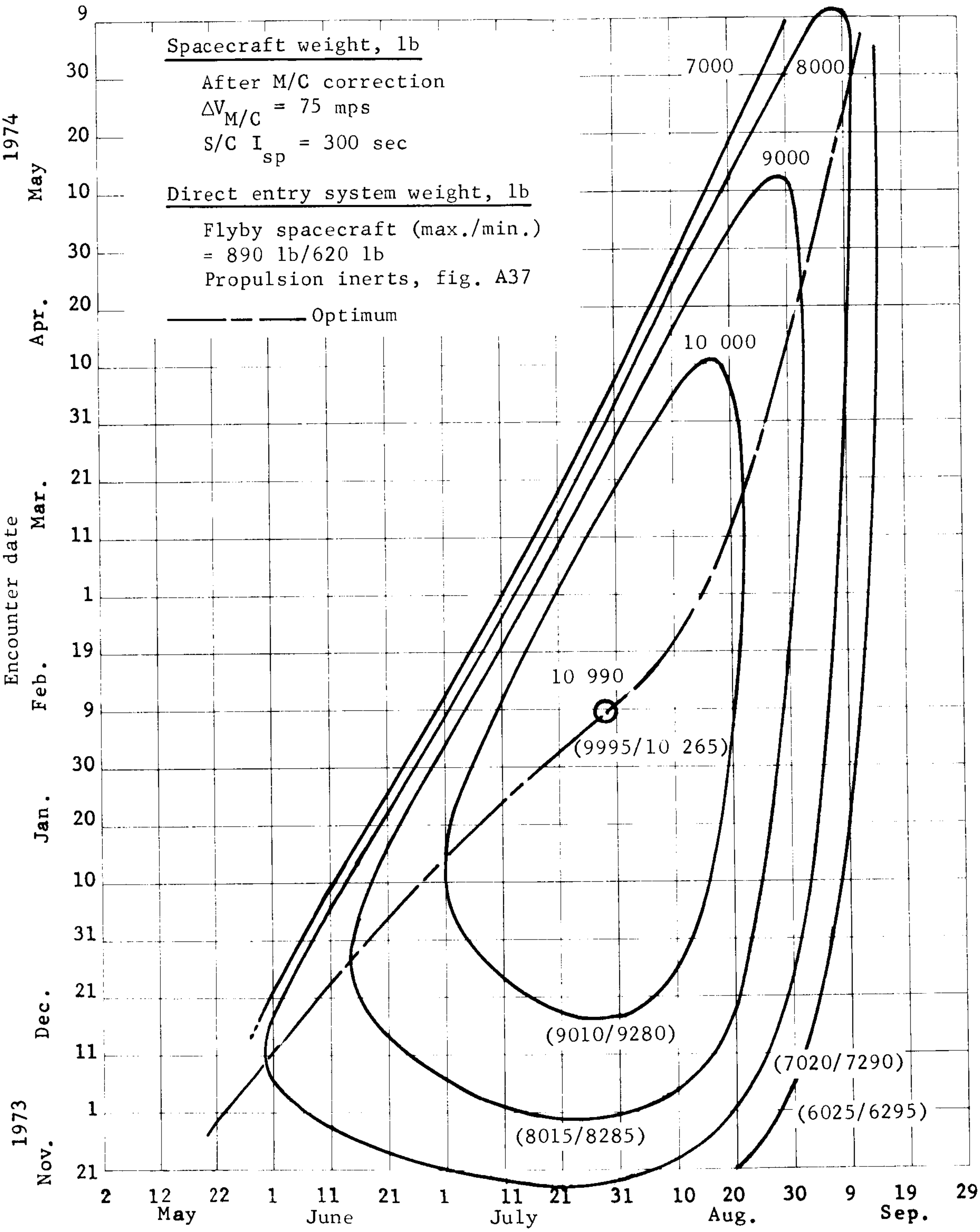

Figure A16.- Spacecraft Weight, Mars 1973, Type I, Titan IIIF/Centaur

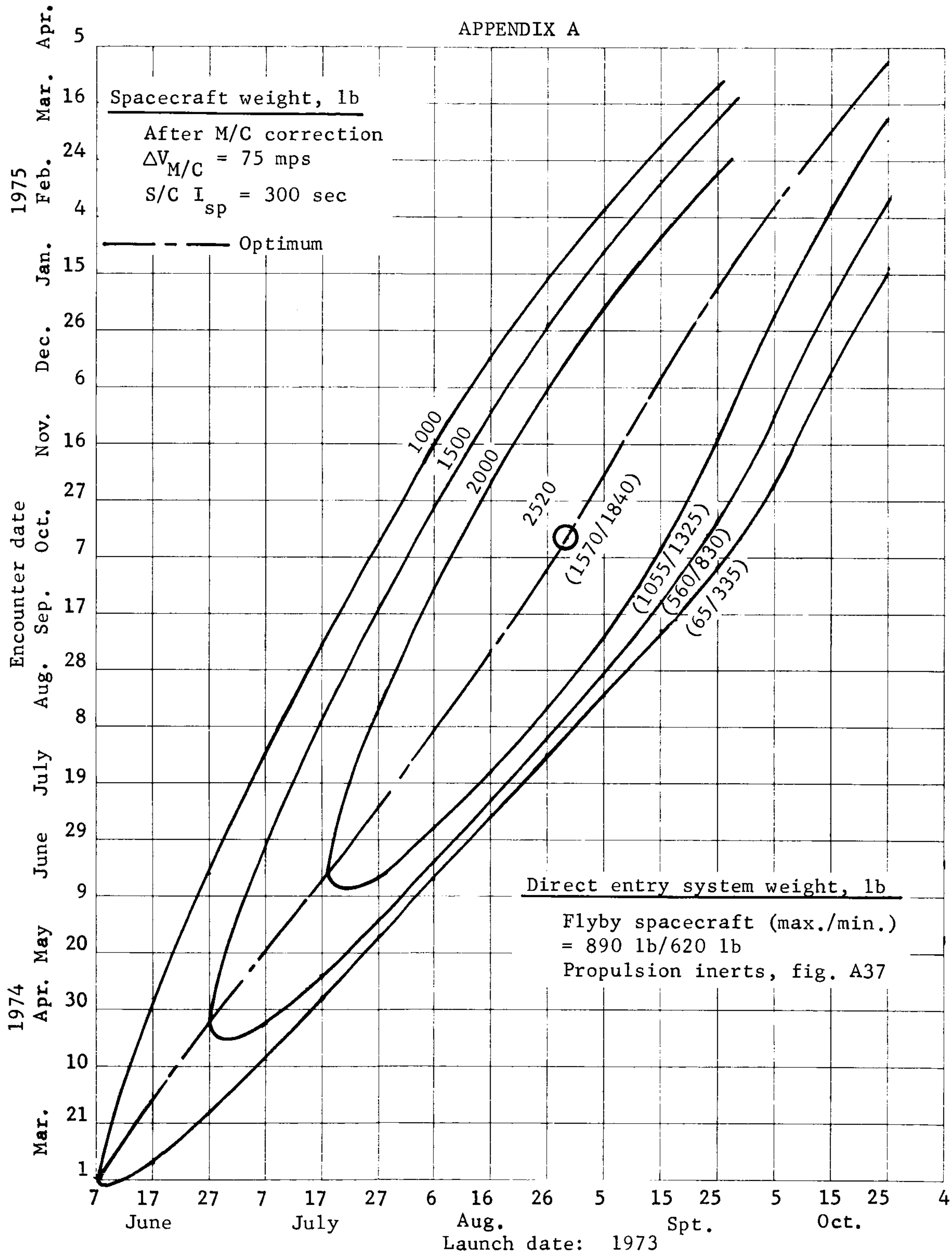

Figure A17.- Spacecraft Weight, Mars 1973, Type II, Titan IIIC

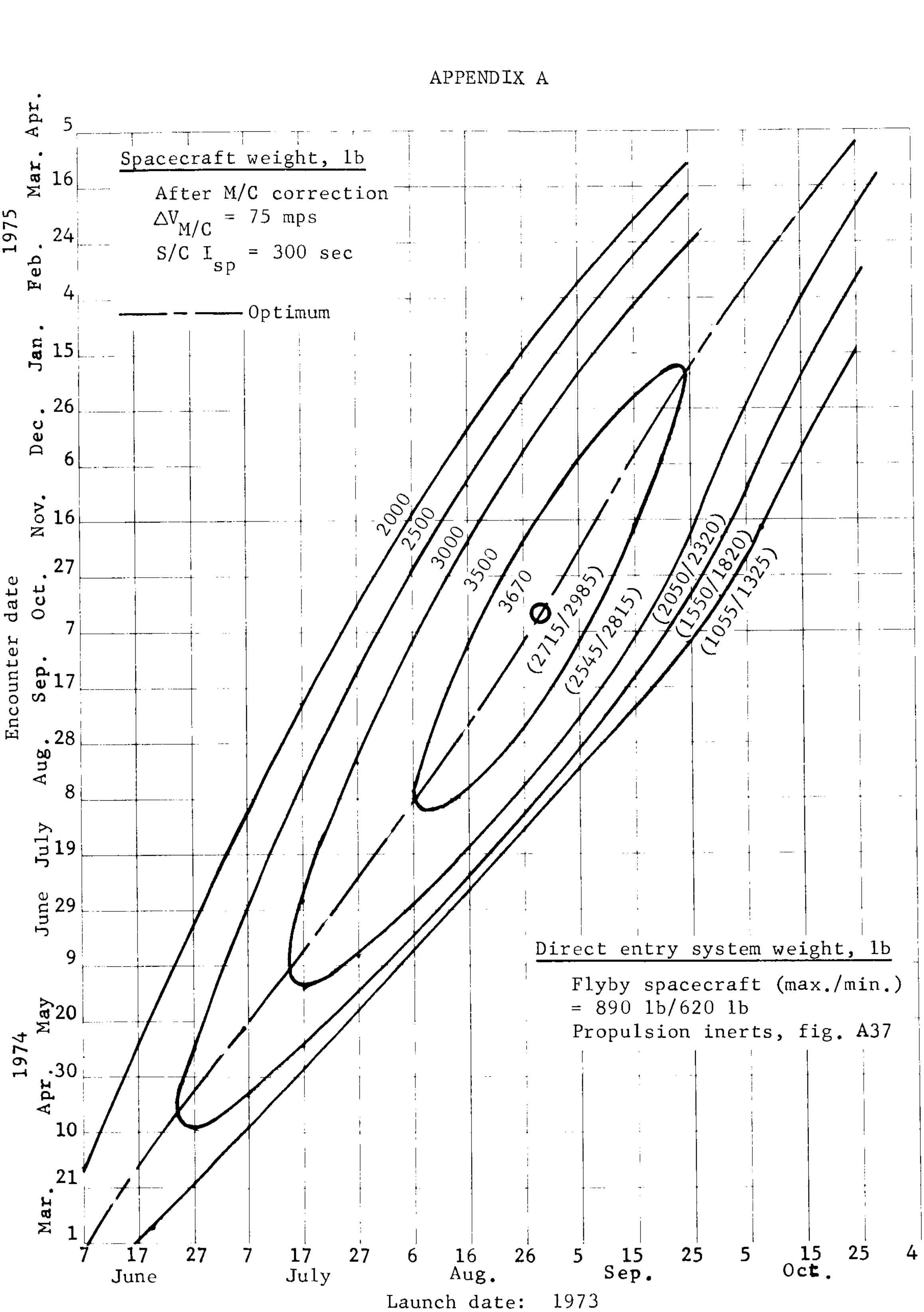

Figure A18.- Spacecraft Weight, Mars 1973, Type II, Titan IIIF/ Stretched Transtage

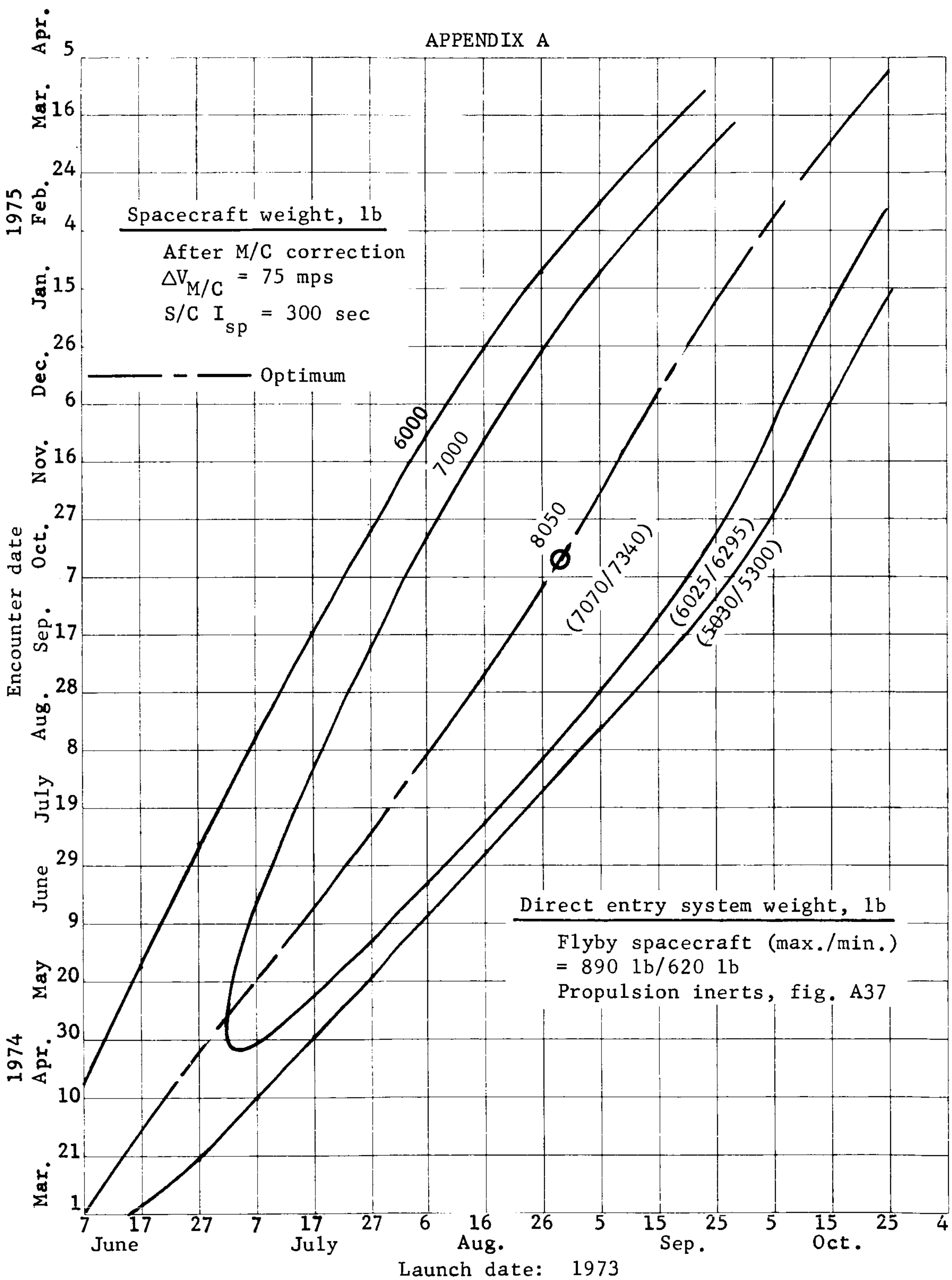

Figure A19.- Spacecraft Weight, Mars 1973, Type II Titan IIIC/Centaur

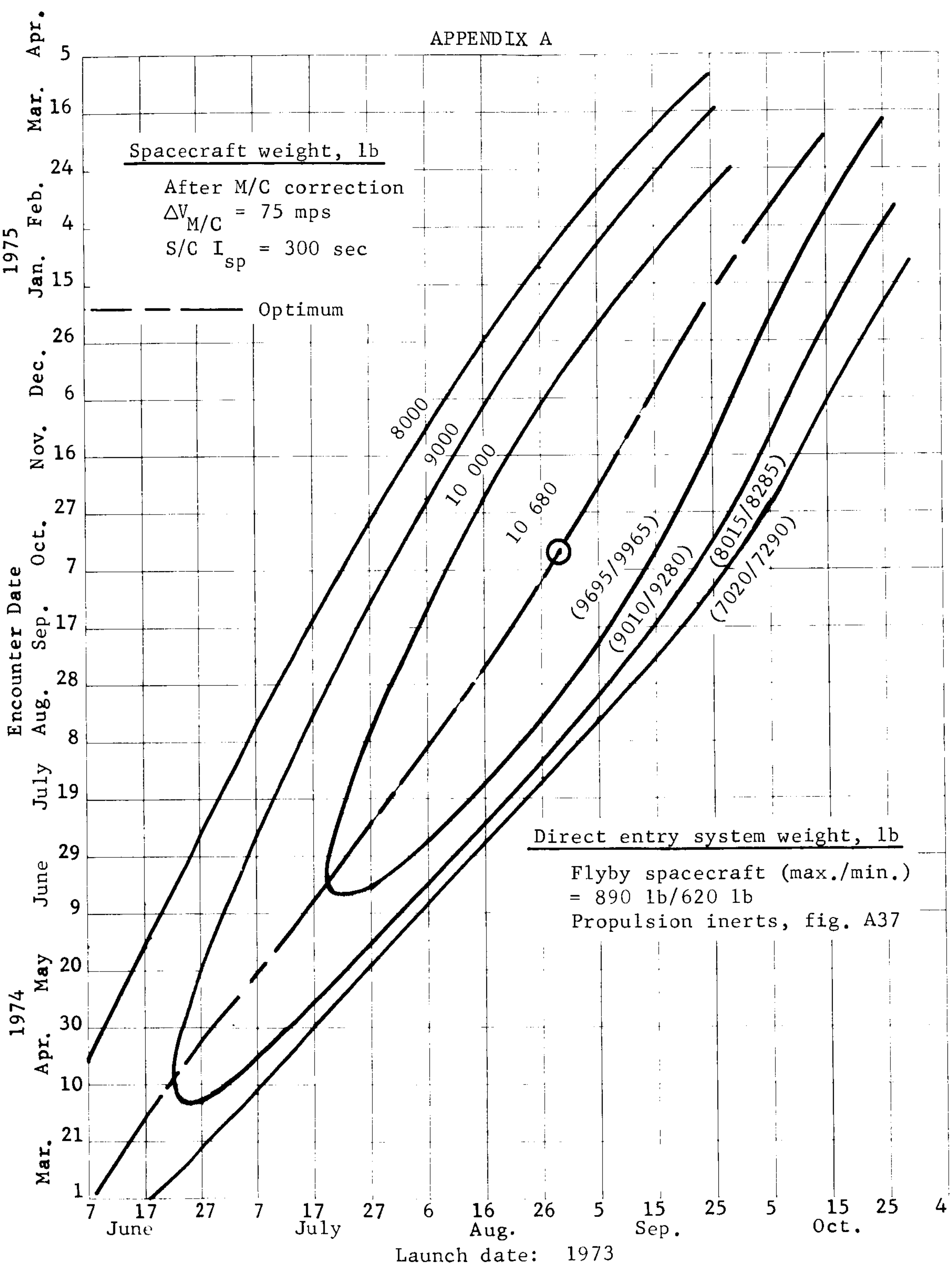

Figure A20.- Spacecraft Weight, Mars 1973, Type II, Titan IIIF/Centaur

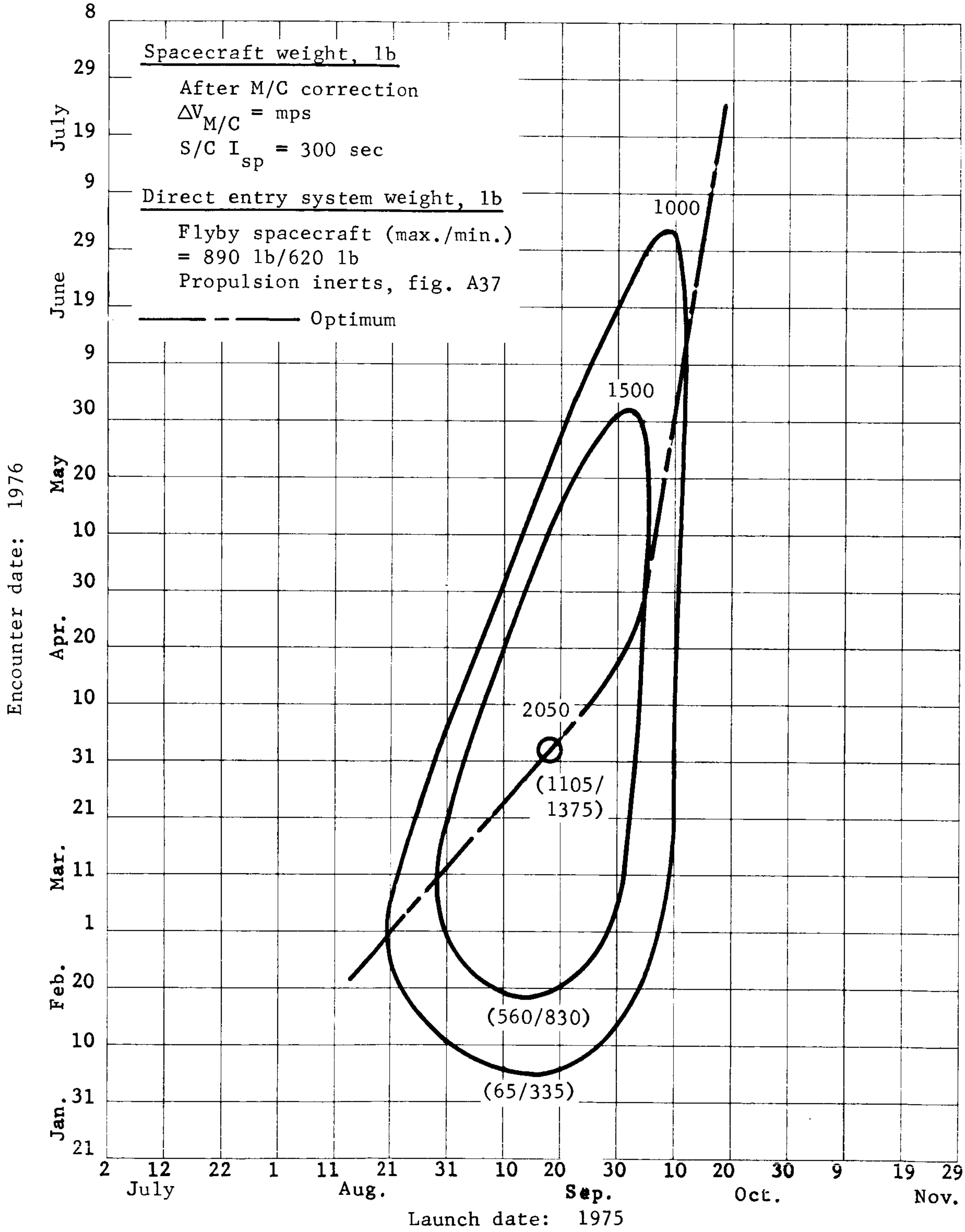

Figure A21.- Spacecraft Weight, Mars 1975, Type I, Titan IIIC

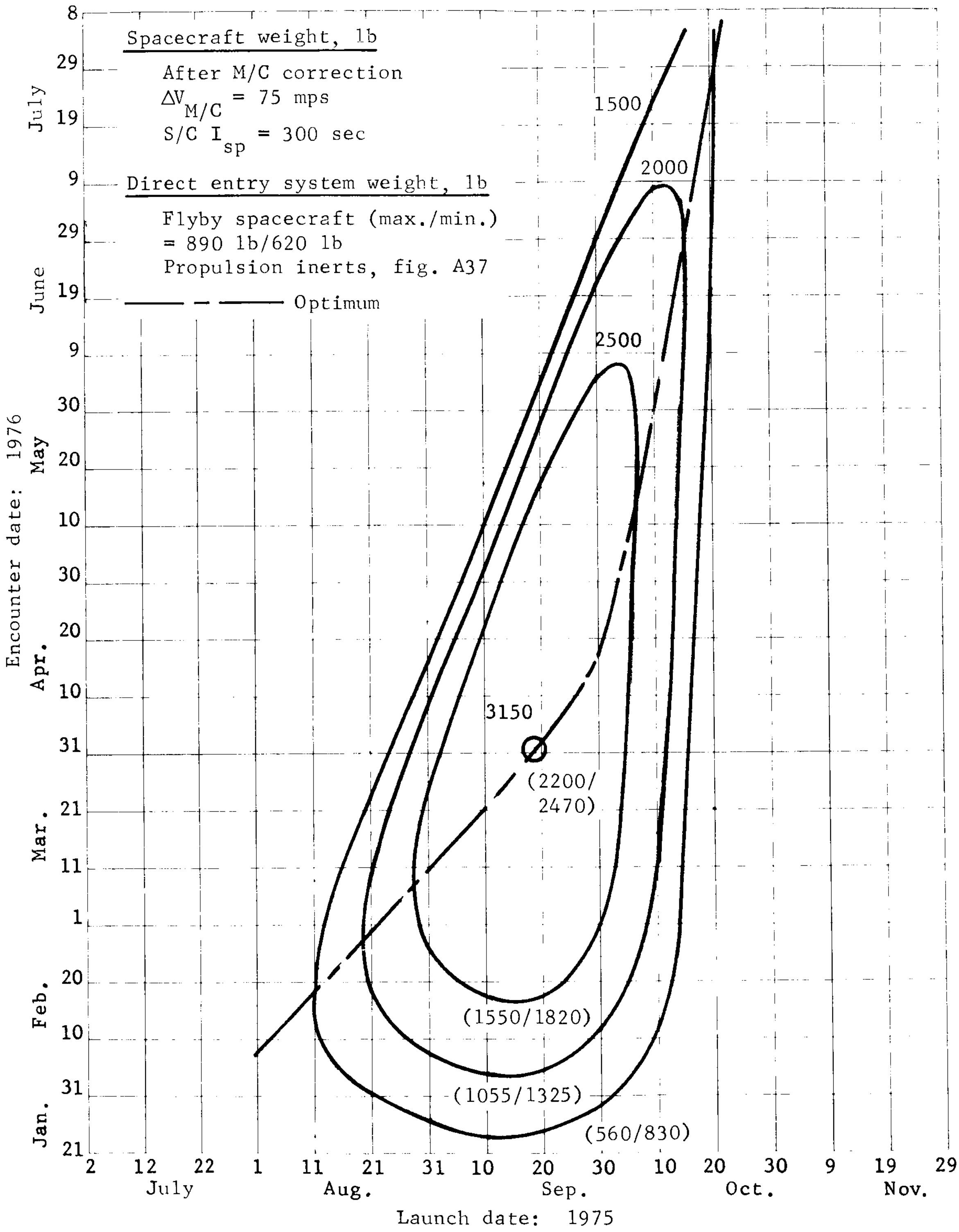

Figure A22.- Spacecraft Weight, Mars 1975, Type I, Titan IIIF/Transtage

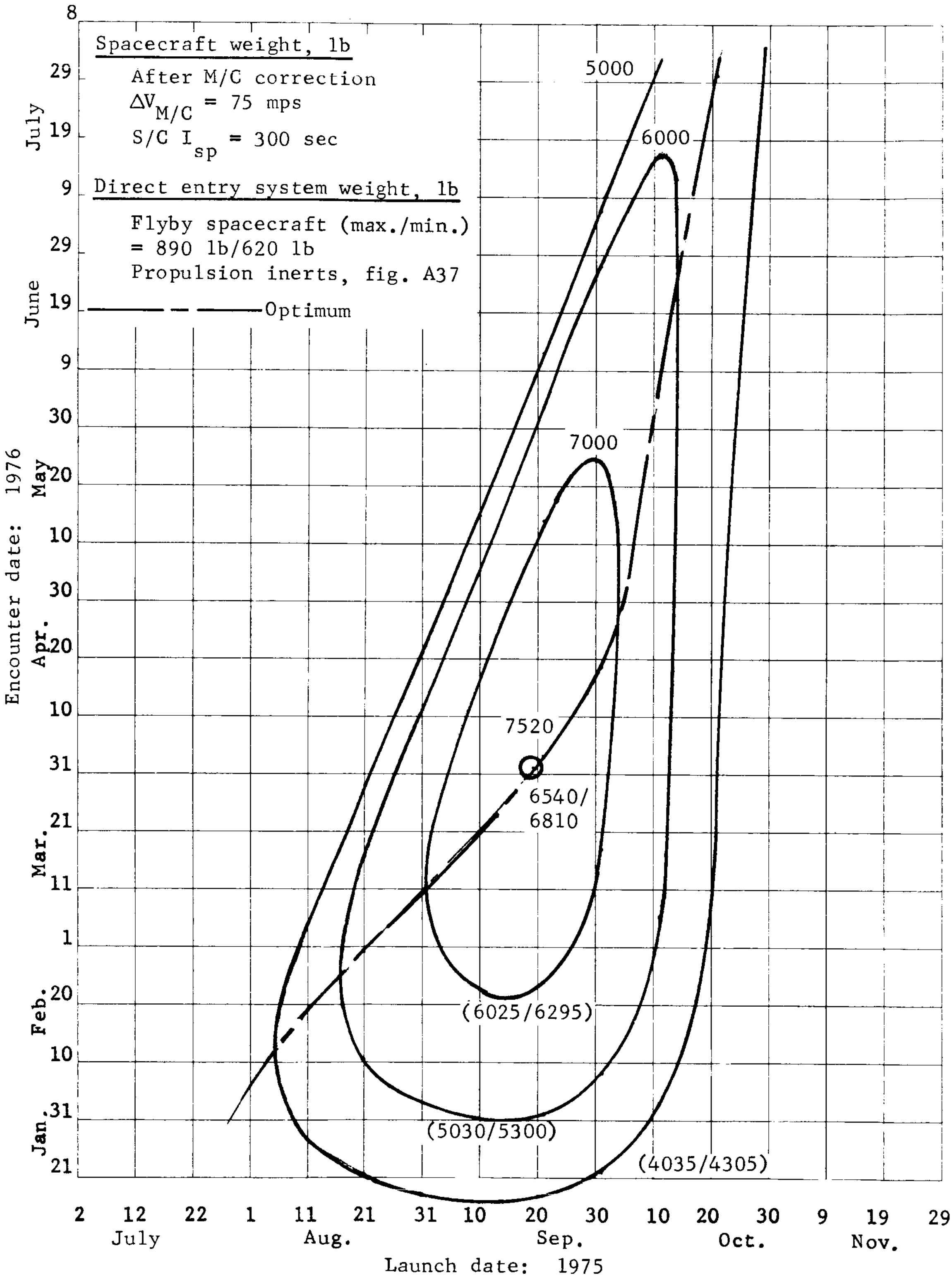

Figure A23.- Spacecraft Weight, Mars 1975, Type I, Titan IIIC/Centaur

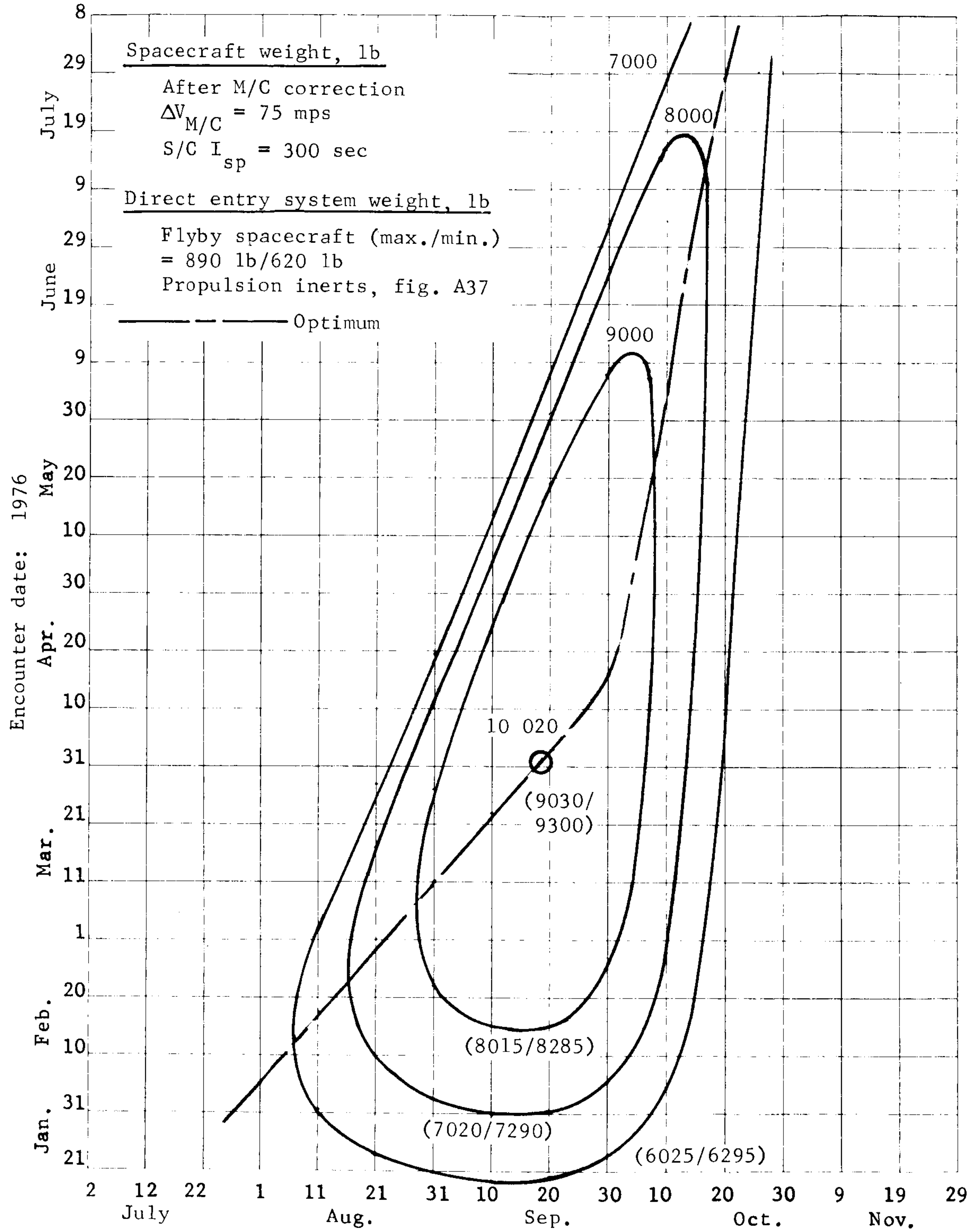

Figure A24.- Spacecraft Weight, Mars 1975, Type I, Titan IIIF/Centaur

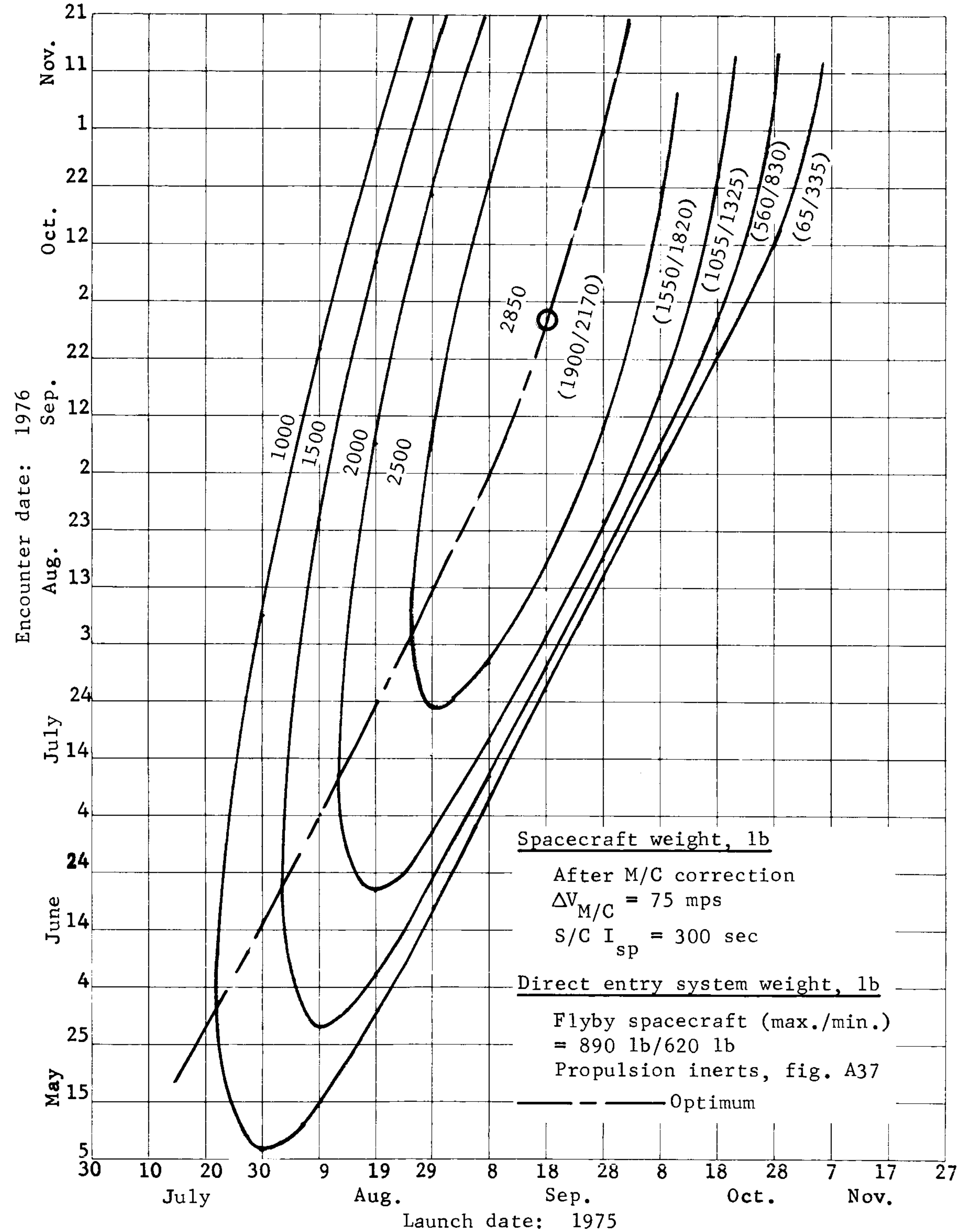

Figure A25.- Spacecraft Weight, Mars 1975, Type II, Titan IIIC

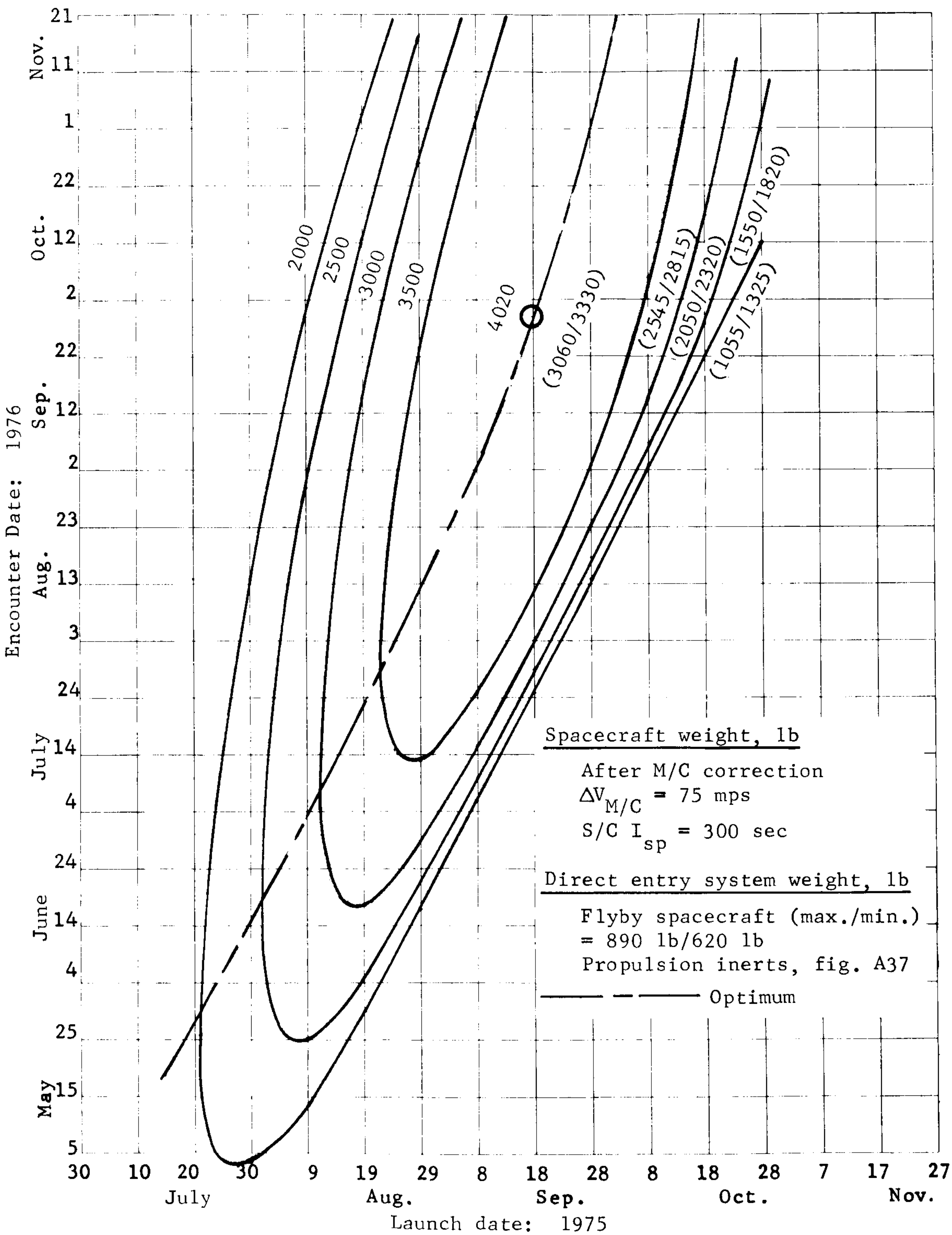

Figure A26.- Spacecraft Weight, Mars 1975, Type II, Titan IIIF/Stretched Transtage

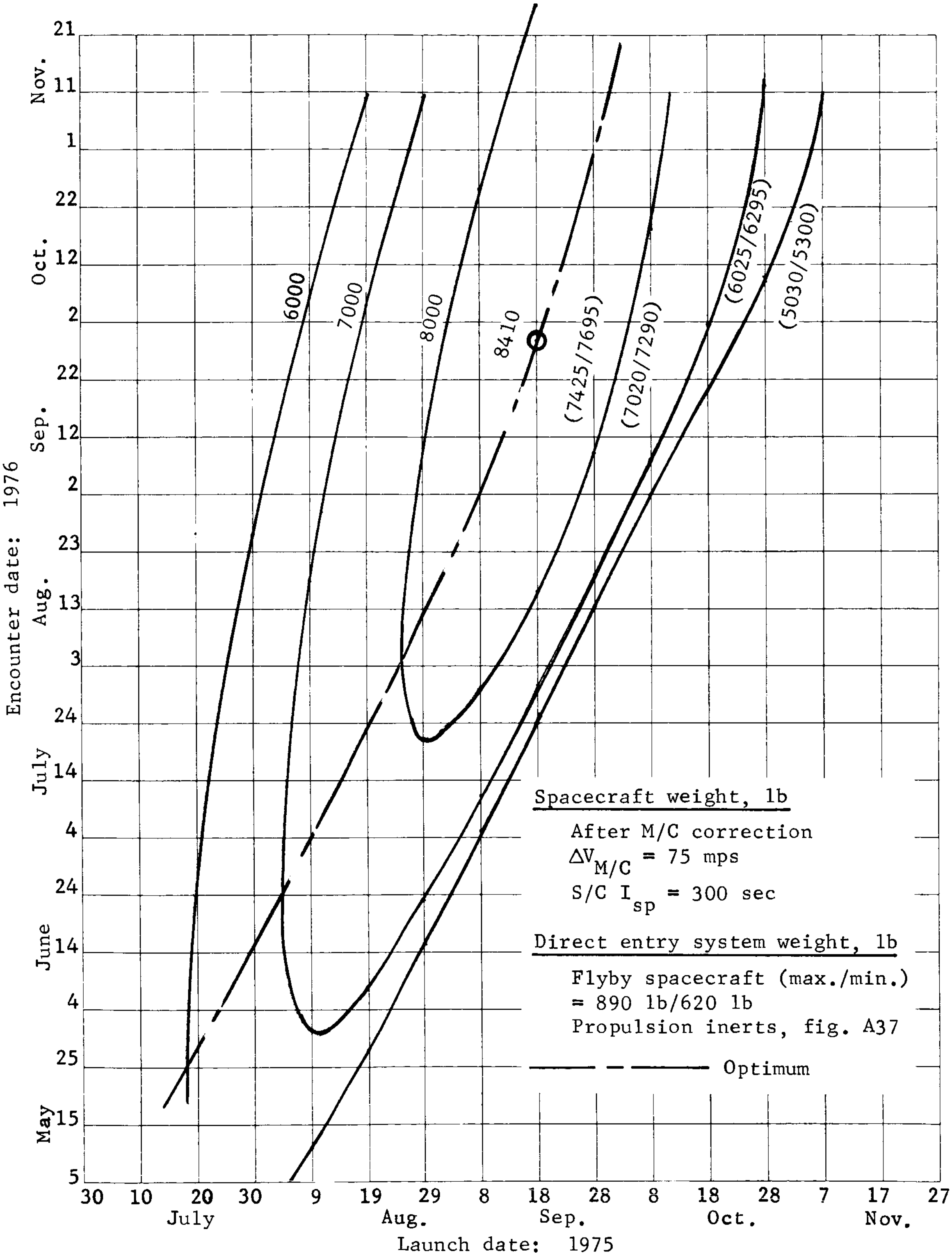

Figure A27.- Spacecraft Weight, Mars 1975, Type II, Titan IIIC/Centaur

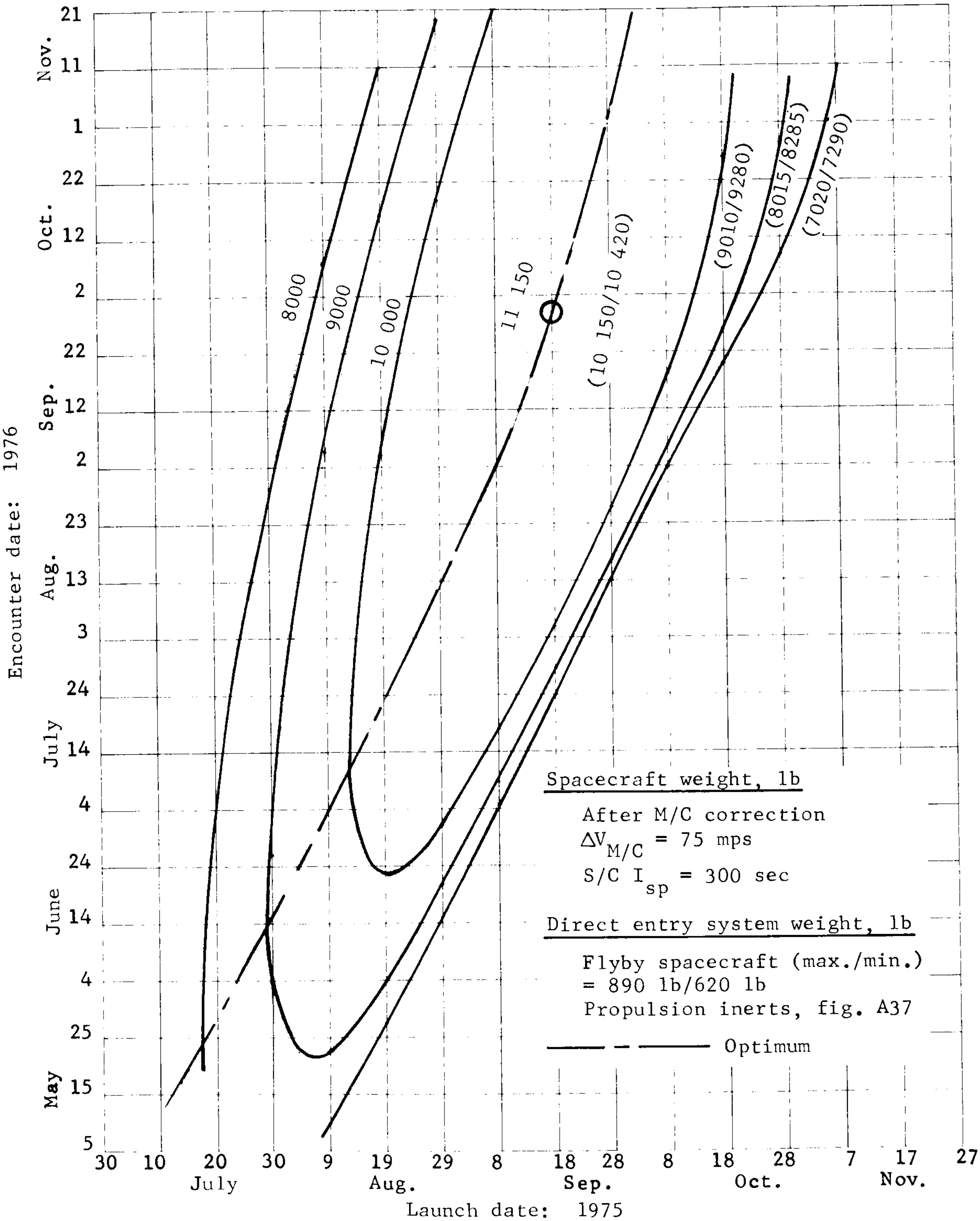

Figure A28.- Spacecraft Weight, Mars 1975, Type II, Titan IIIF/Centaur

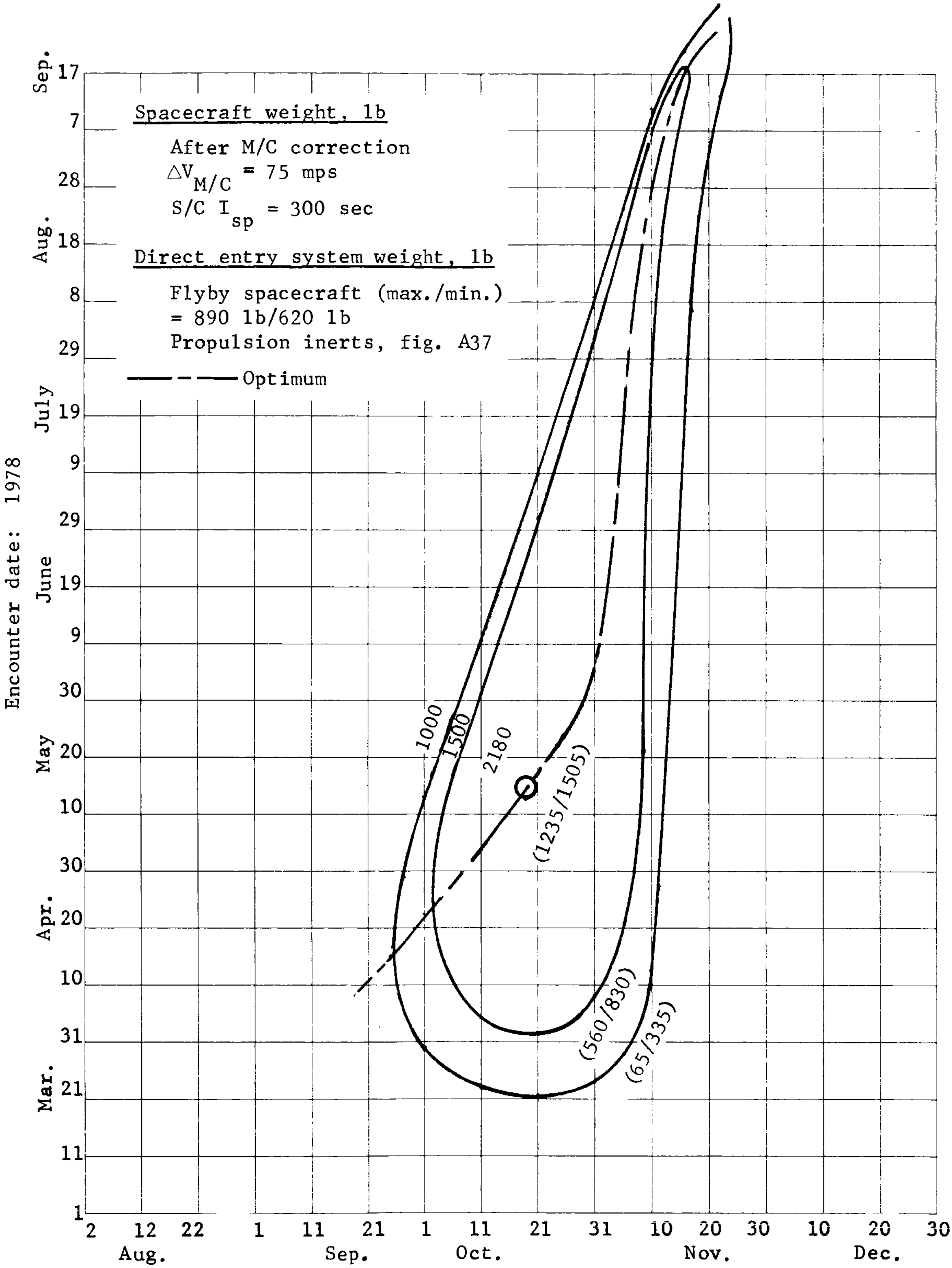

Figure A29.- Spacecraft Weight, Mars 1977, Type I, Titan IIIC

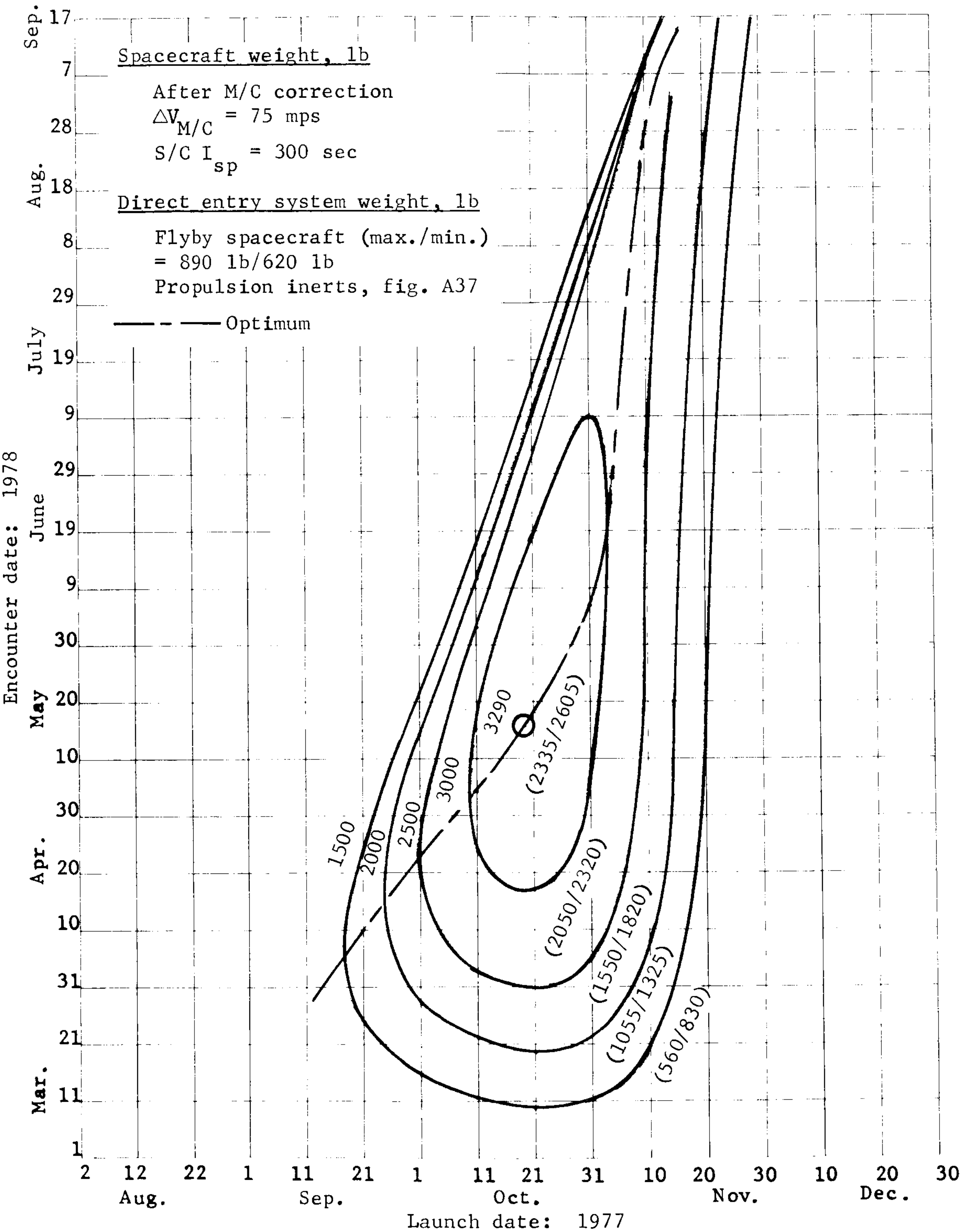

Figure A30.- Spacecraft Weight, Mars 1977, Type I, Titan IIIF/Stretched Transtage

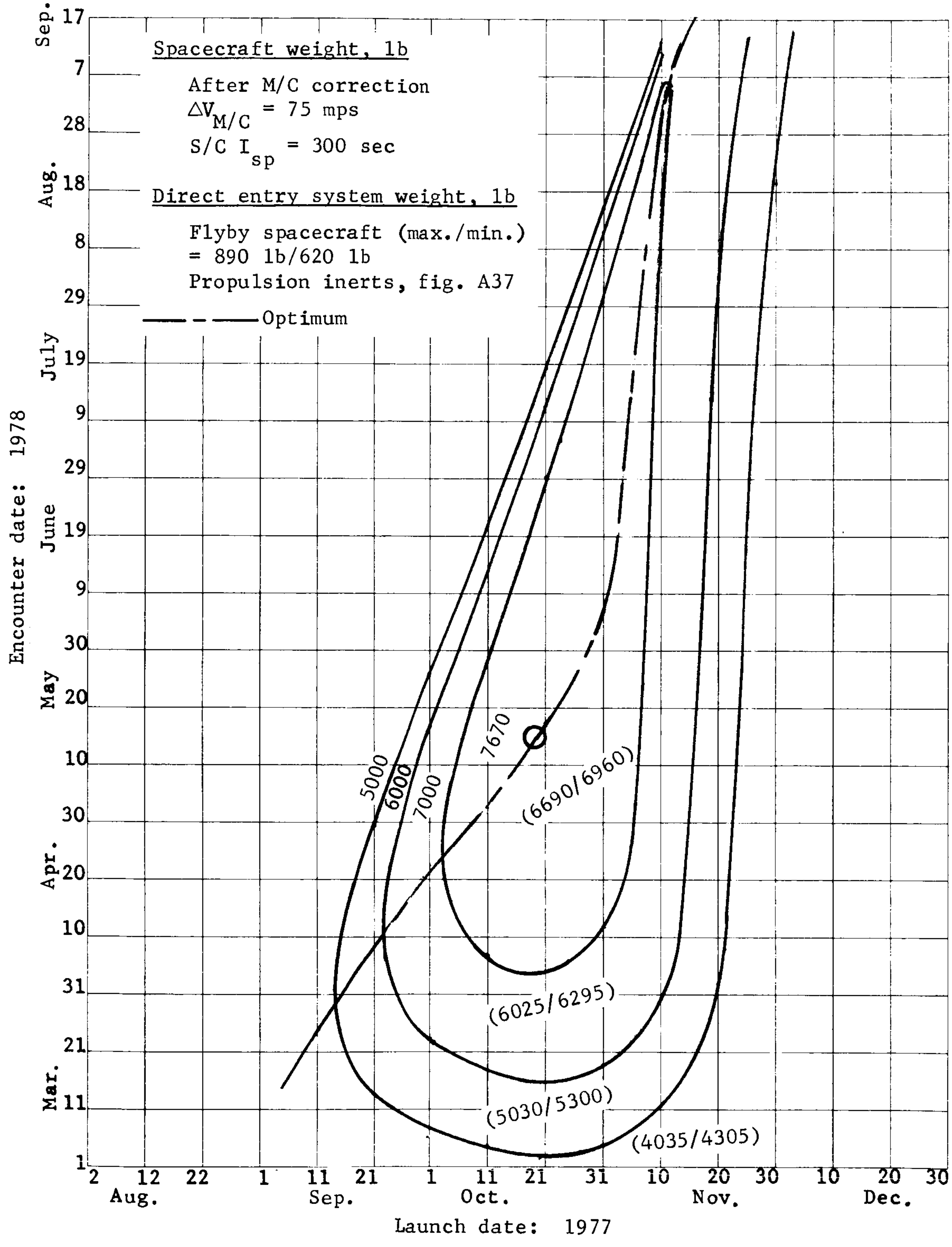

Figure A31.- Spacecraft Weight, Mars 1977, Type I, Titan IIIC/Centaur

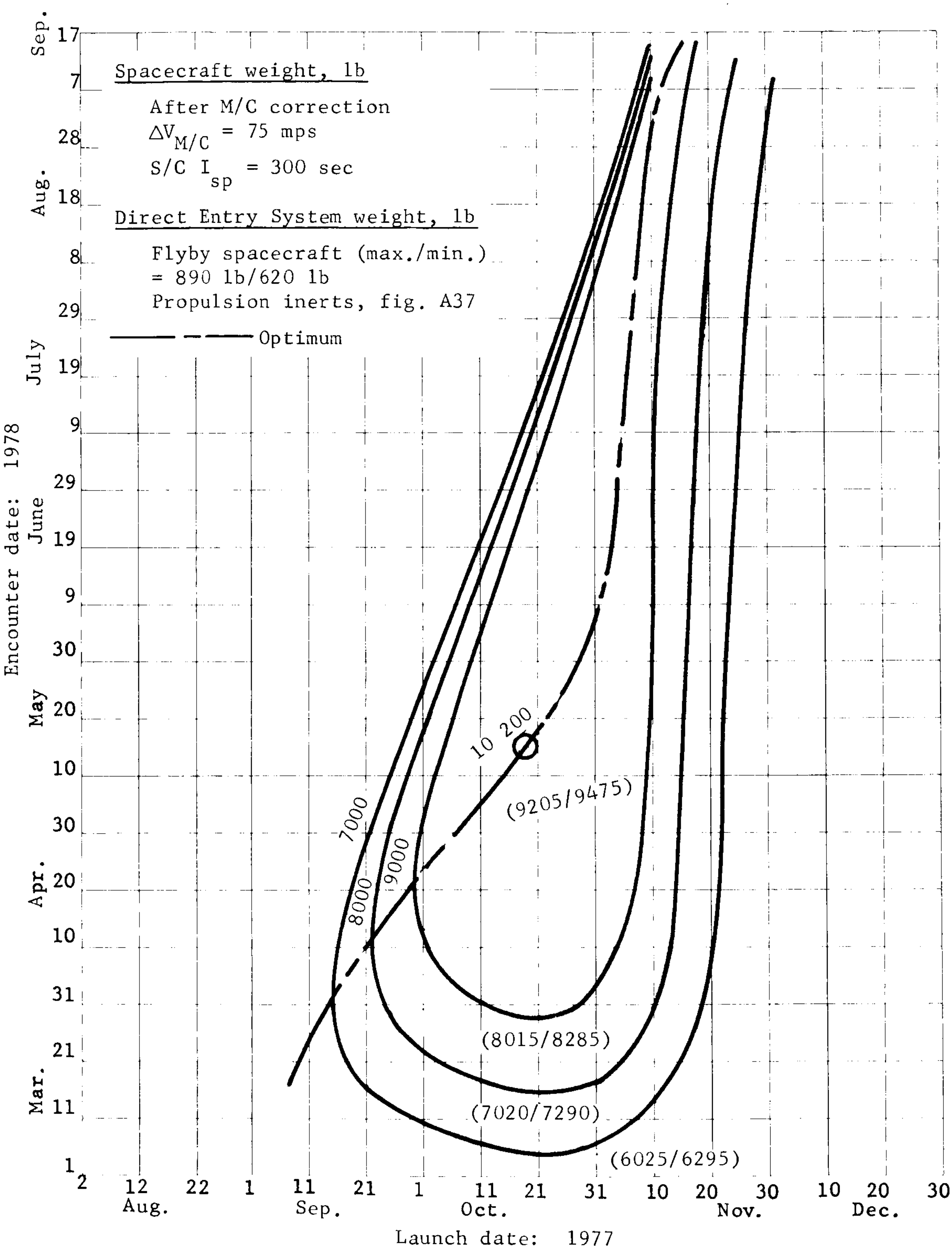

Figure A32.- Spacecraft Weight, Mars 1977, Type I, Titan IIIF/ Centaur

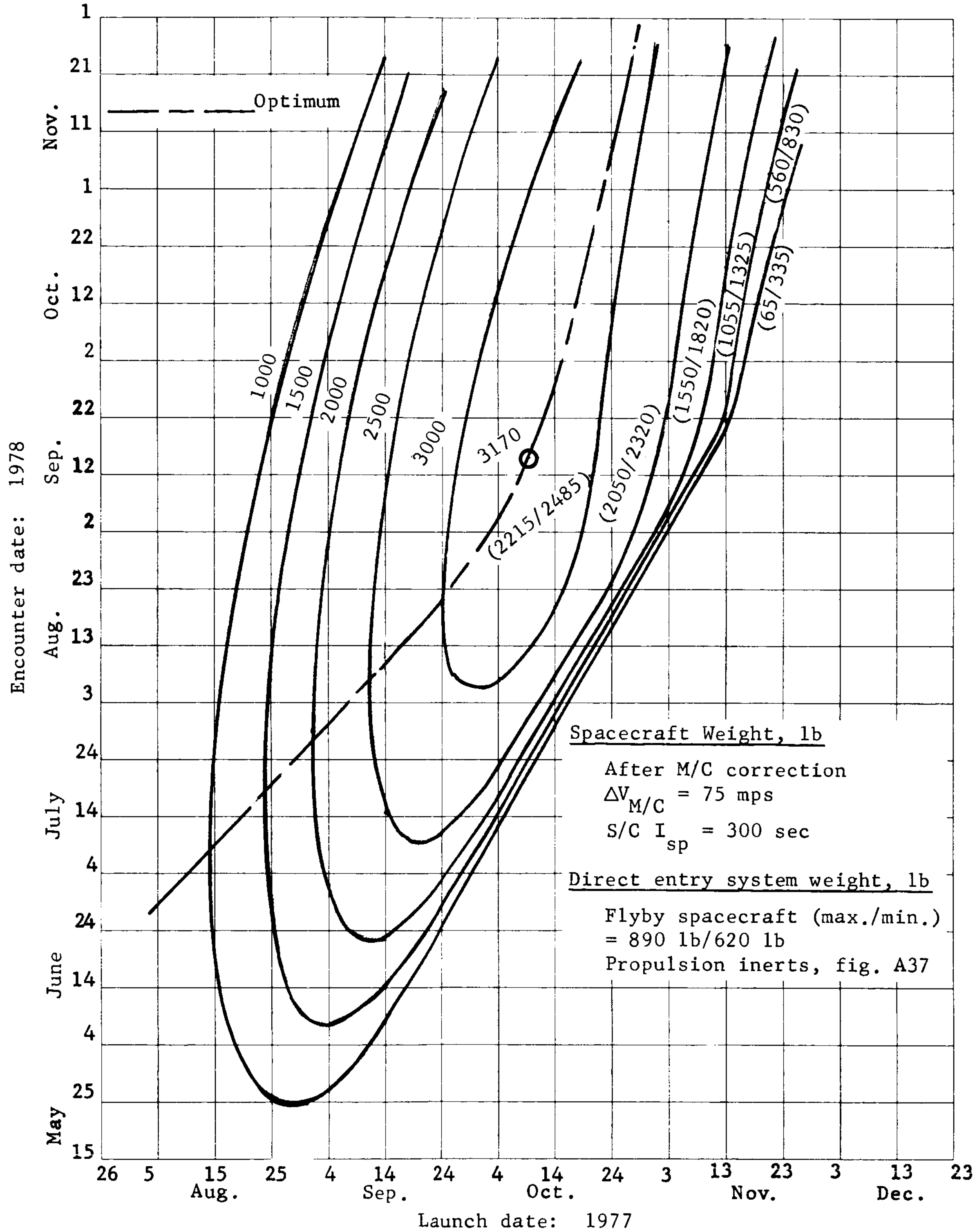

Figure A33.- Spacecraft Weight, Mars 1977, Type II, Titan IIIC

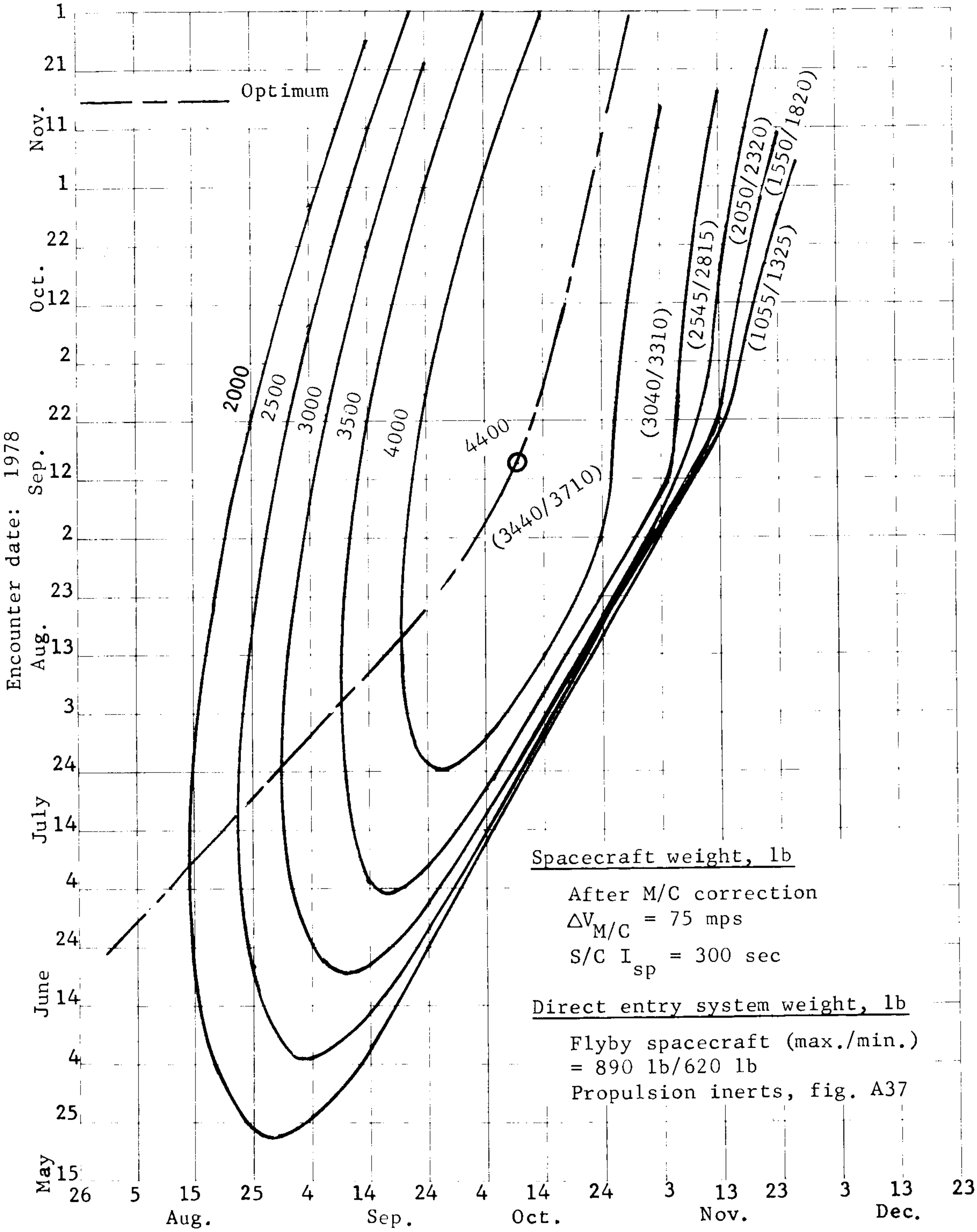

Figure A34.- Spacecraft Weight, Mars 1977, Type II, Titan IIIF/ Stretched Transtage

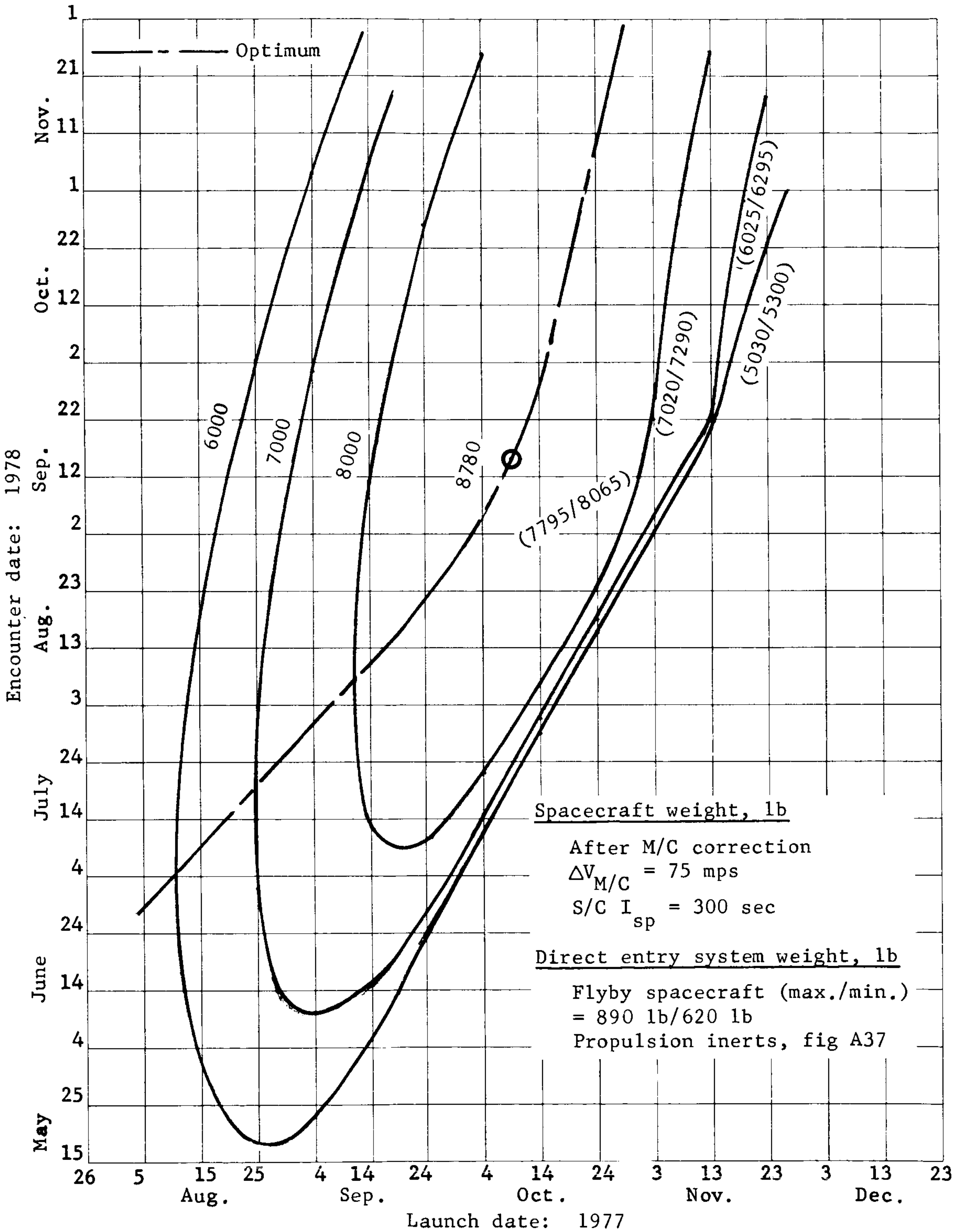

Figure A35.- Spacecraft Weight, Mars 1977, Type II, Titan IIIC/Centaur

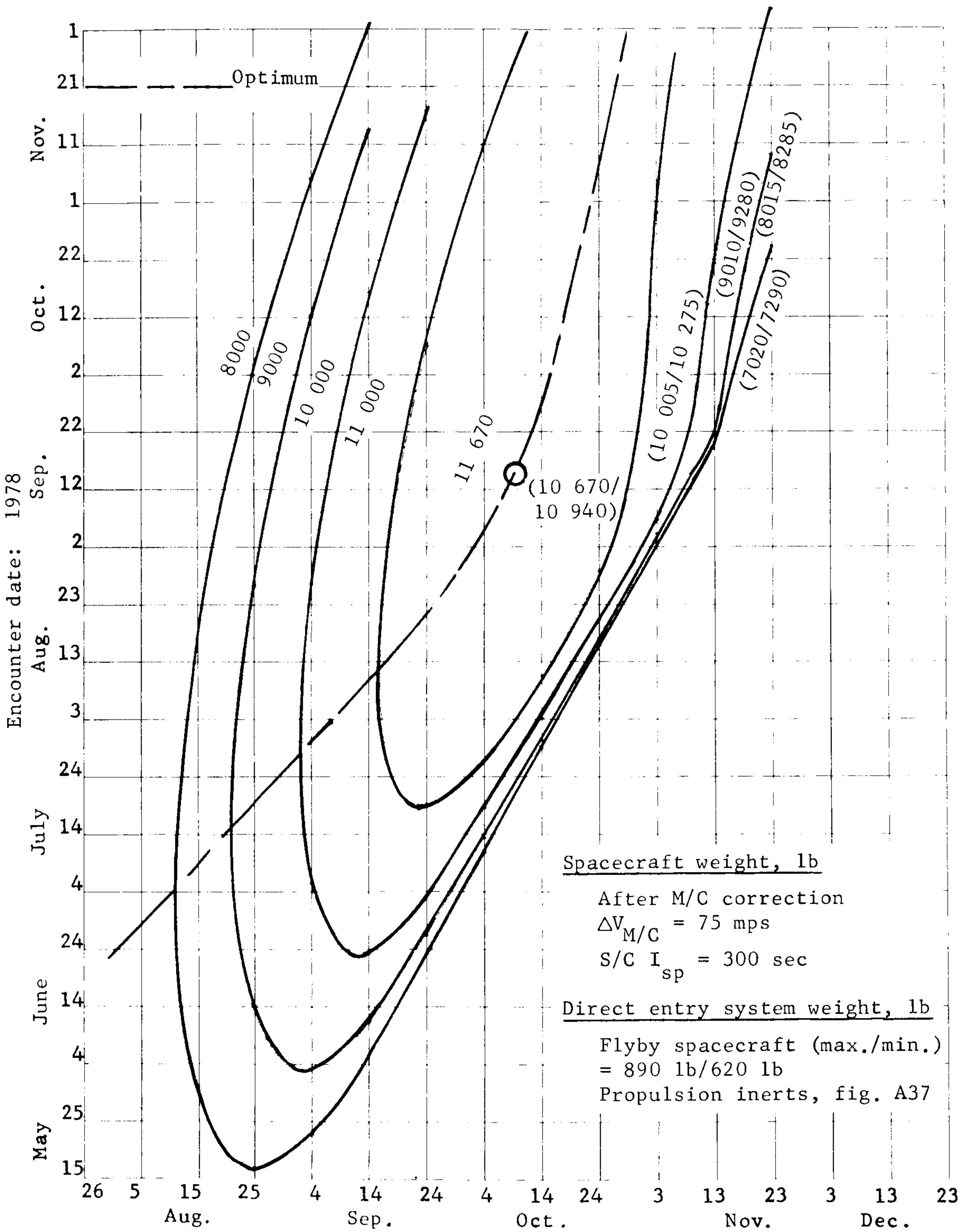

Figure A36.- Spacecraft Weight, Mars 1977, Type II, Titan IIIF/Centaur

$W_{S/C}$ already has the propellant for midcourse correction removed. For this case, where ΔV midcourse is constant, W_{PI} is expressed as a function of $W_{S/C}$. Letting $W_{S/C} = W_F$ in the previous expressions,

$$W_{PI} = W_{S/C}\left(e^{-\Delta V/C_J} - 1\right)(1/\lambda - 1)$$

The result is shown in figure A37.

As an example, in figure A38 an optimum spacecraft weight of 2470 lb is shown corresponding to a launch period beginning on 7/13/73. Capsule system weight is computed as follows:

$W_{S/C} = 2470$ lb;

$W_{F/B} = 890/620$ lb;

$W_{PI} = 60$ lb (from figure A37);

$$\left.\begin{aligned} W_{C/S} &= 2470 - 890 - 60 = 1520 \text{ lb;} \\ W_{C/S} &= 2470 - 620 - 60 = 1790 \text{ lb.} \end{aligned}\right\} \text{ shown in table A2}$$

The capsule system weights include spacecraft adapter and sterilization canister.

The optimum spacecraft weights over a 30-day launch period are summarized in figures A38 thru A43. The effect of declination as discussed above is shown by the Titan IIIC curve in figure A42. The dotted line to the right of 11/15/77 is based on $|DLA| \leq 36°$. Between 11/10/77 and 11/15/77 the declination increases to approximately 45° with the corresponding reduction in payload shown. Optimum weights range from 2470 to 11 400 lb for the higher performance transfers. The first day of the launch period and the total capsule system weights for flyby spacecraft corresponding to the data of figures A38 thru A43 are given in table A2. The capsule system weight range is 1500 to 11 000 lb, neglecting the lower performance transfer types (i.e., 1975-I and 1977-I).

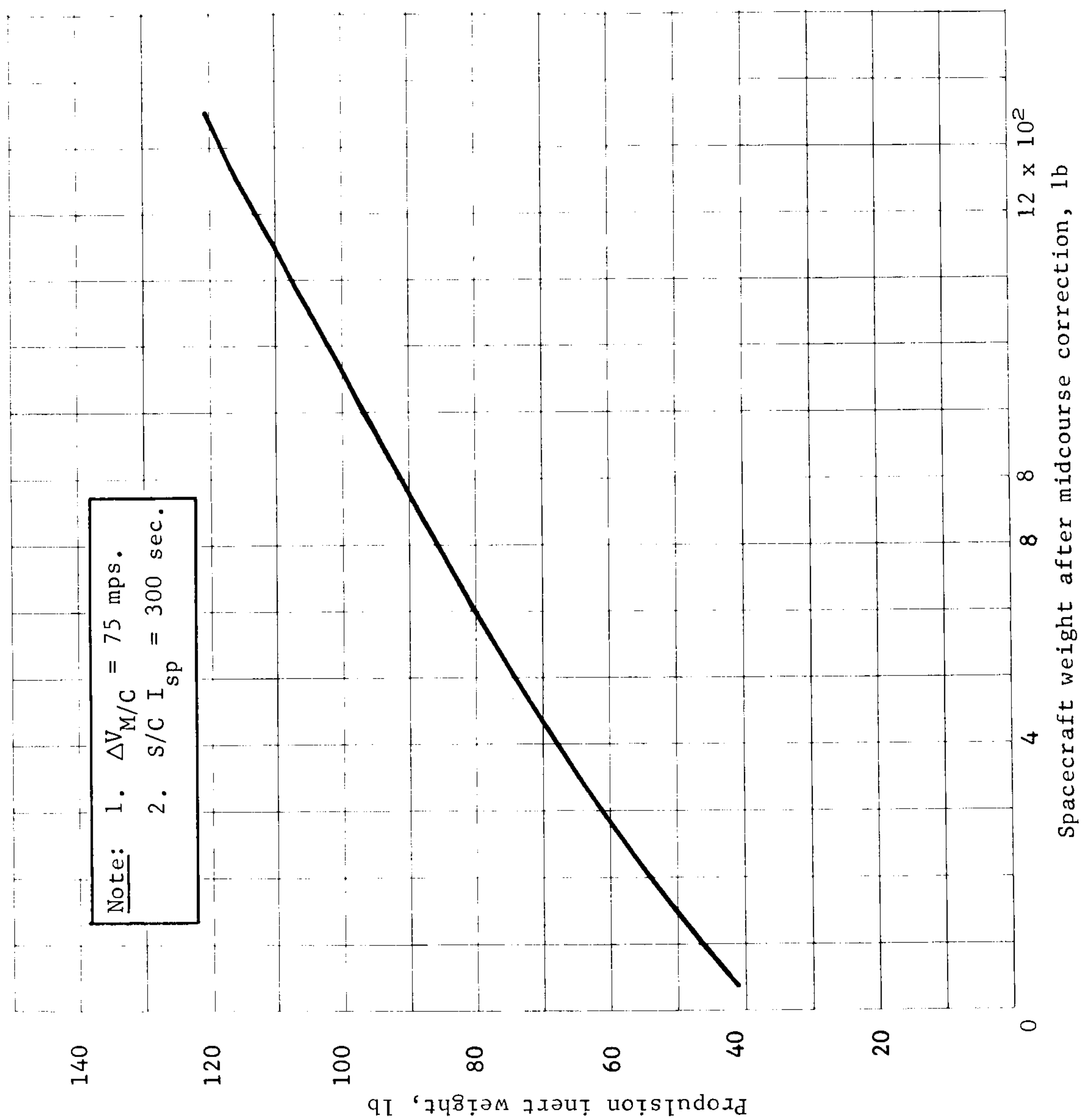

Figure A37.- Propulsion System Inert Weight for Flyby Spacecraft

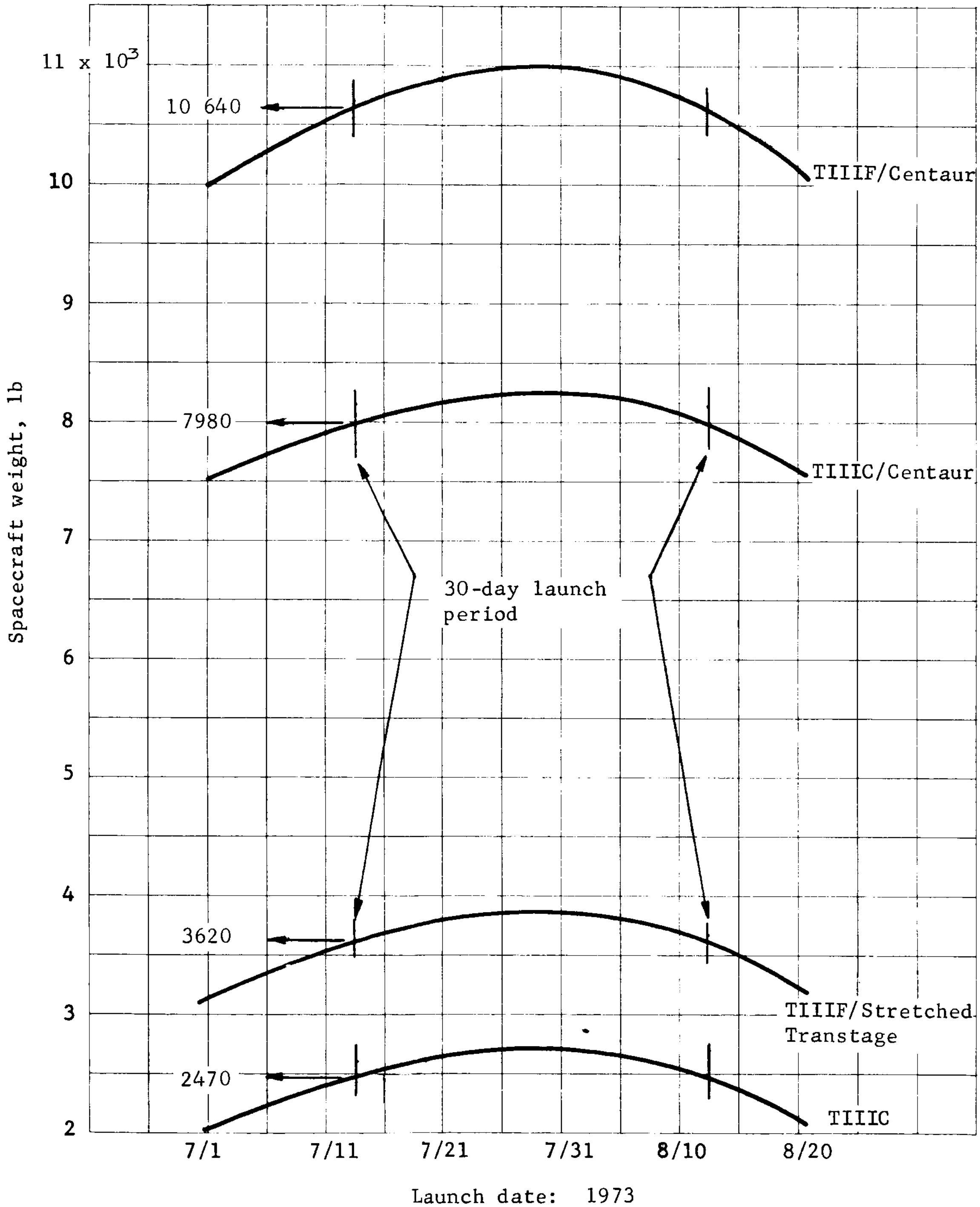

Figure A38.- Optimum Spacecraft Weight after Midcourse Correction, Mars 1973, Type I

APPENDIX A

TABLE A2.- OPTIMUM CAPSULE SYSTEM WEIGHT FOR FLYBY SPACECRAFT, 30-DAY LAUNCH PERIOD

Mission opportunity	Transfer type	First launch date	Capsule system weight, lb[a]			
			TIIIC	TIIIF/ Stretched Transtage	TIIIC/ Centaur	TIIIF/ Centaur
1973	I	7/13/73	1520/1790	2665/2935	7000/7270	9645/9915
	II	8/24/73	1505/1775	2645/2915	6990/7260	9615/9885
1975	I	[b]9/2/75	720/990	1800/2070	6095/6365	8480/8750
	II	[b]9/5/75	1790/2060	2945/3215	7305/7575	9995/10 265
1977	I	10/1/77	855/1125	1920/2190	6255/6525	8860/9130
	II	9/25/77	2070/2340	3260/3530	7615/7885	10 620/10 890

[a]890-lb spacecraft/620-lb spacecraft.

[b]9/1/75 for TIIIC/Centaur.

[c]9/4/75 for TIIIC/Centaur, TIIIF/Stretched Transtage.

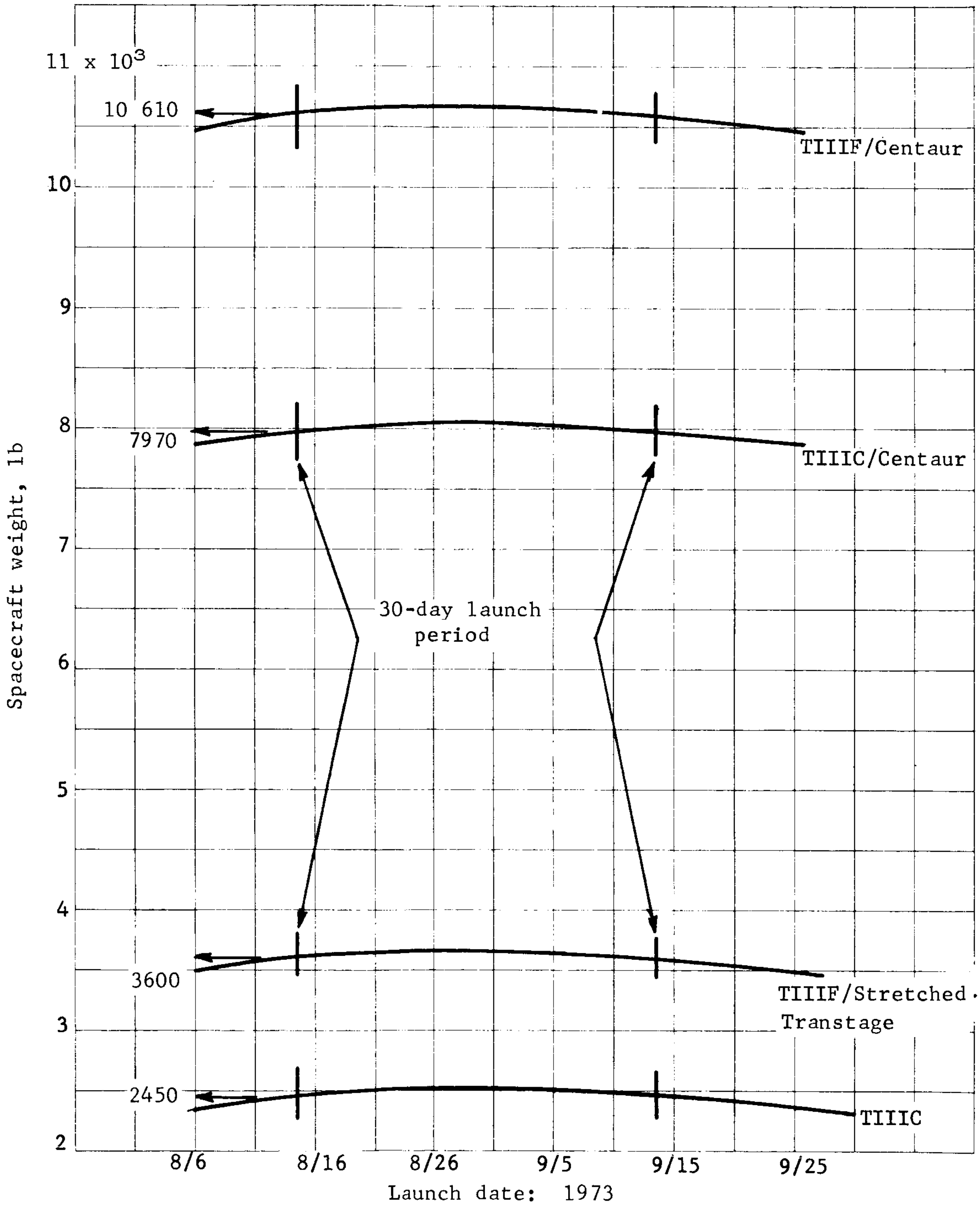

Figure A39.- Optimum Spacecraft Weight after Midcourse Correction, Mars 1973, Type II

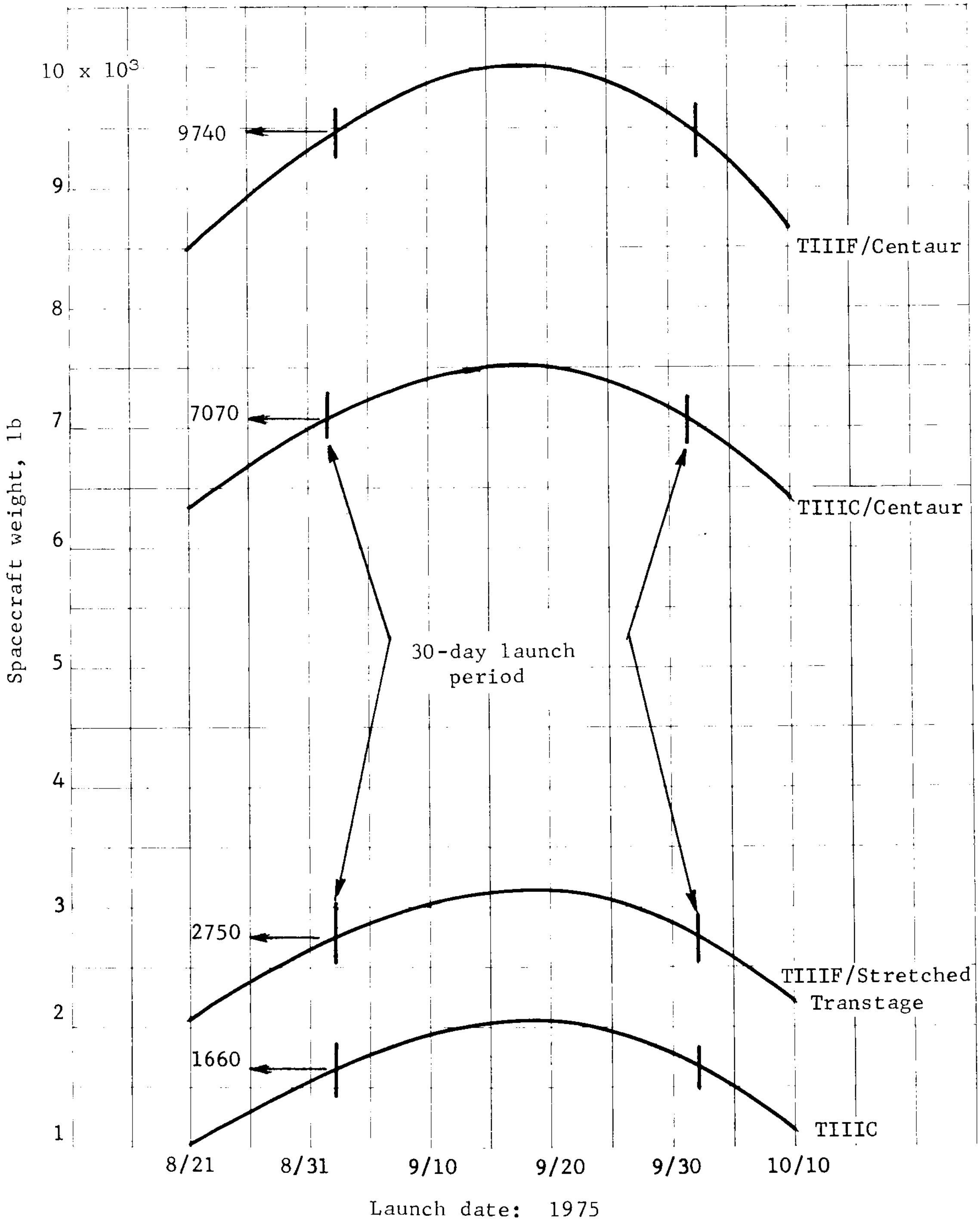

Figure A40.- Optimum Spacecraft Weight after Midcourse Correction, Mars 1975, Type I

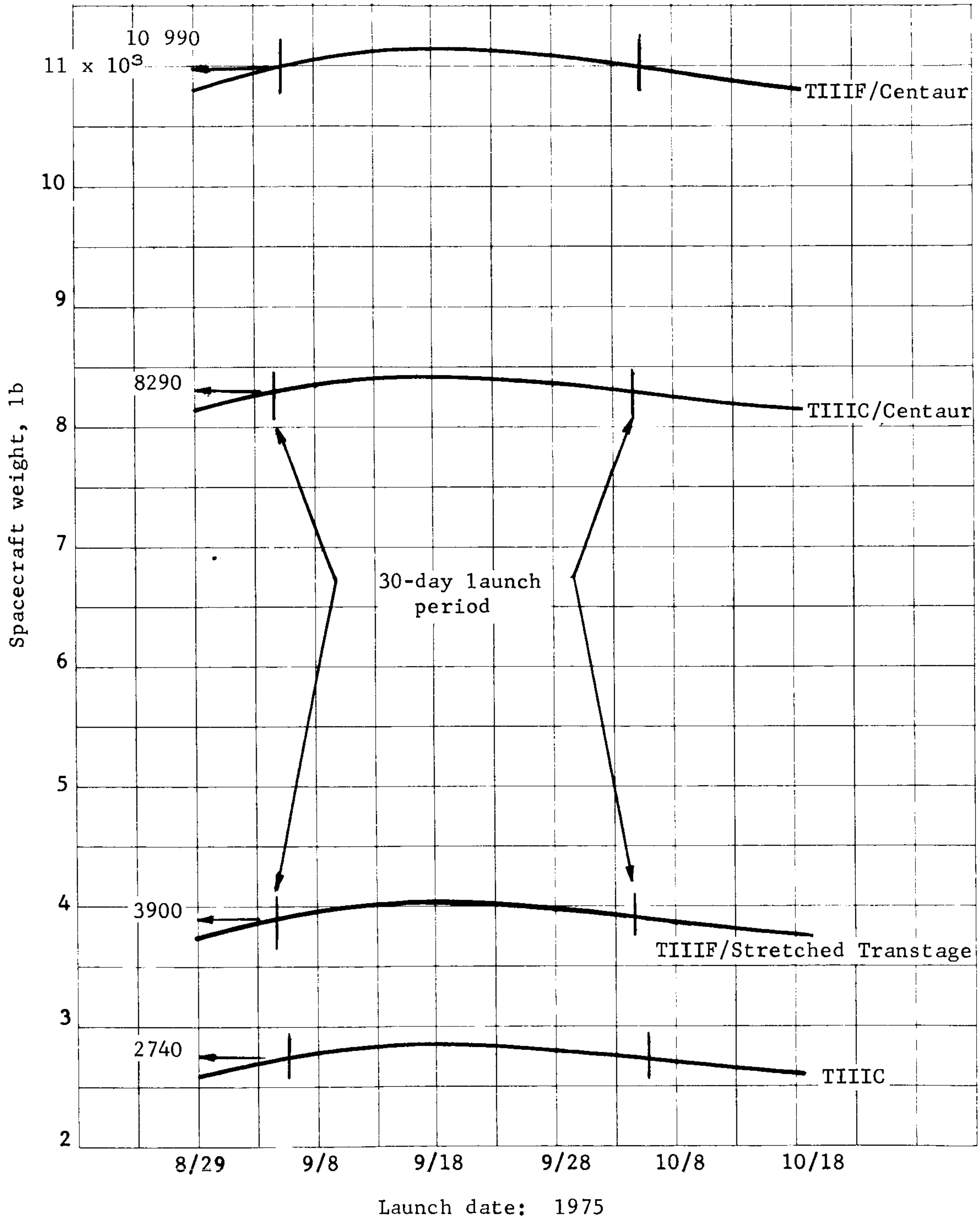

Figure A41.- Optimum Spacecraft Weight after Midcourse Correction, Mars 1975, Type II

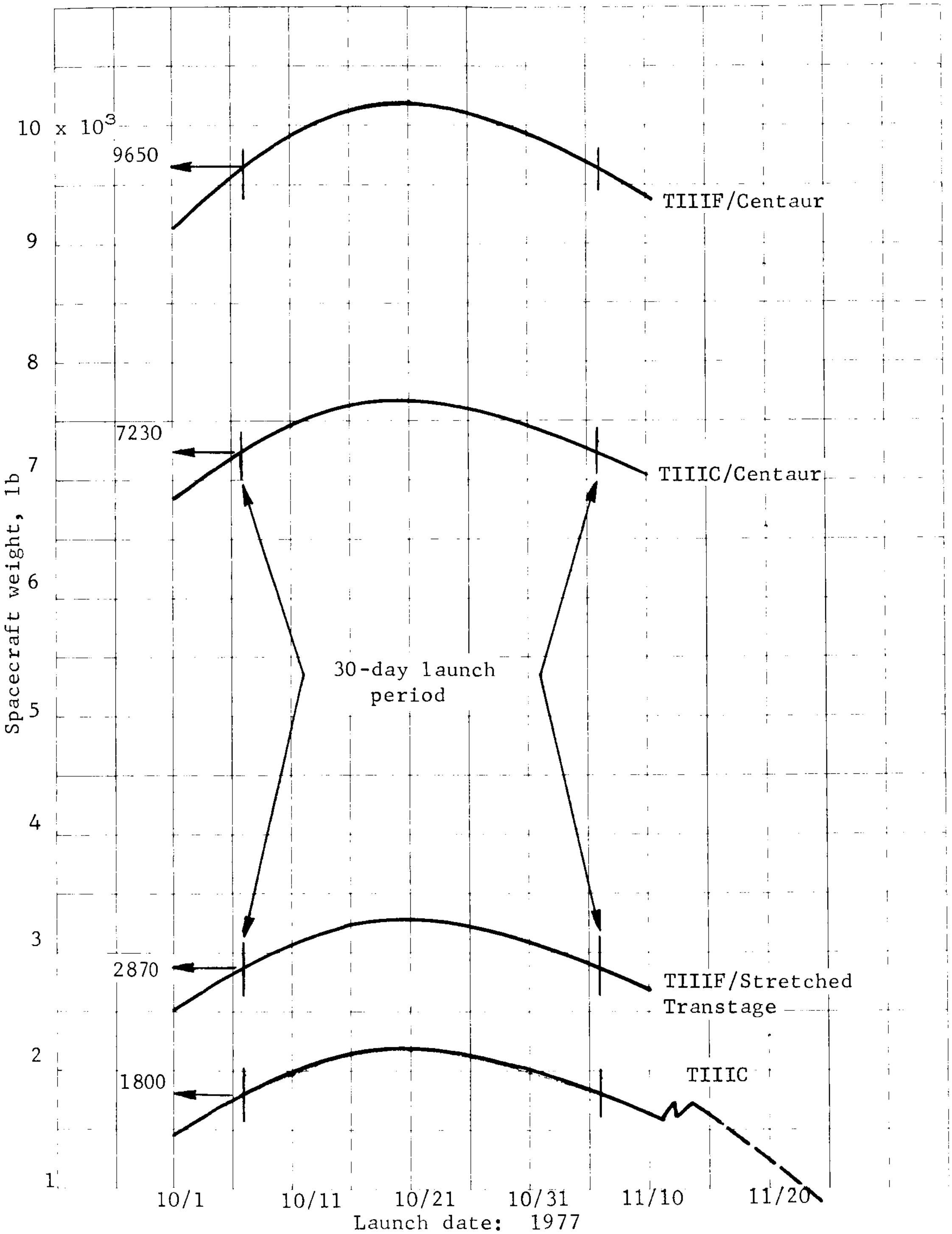

Figure A42.- Optimum Spacecraft Weight after Midcourse Correction, Mars 1977, Type I

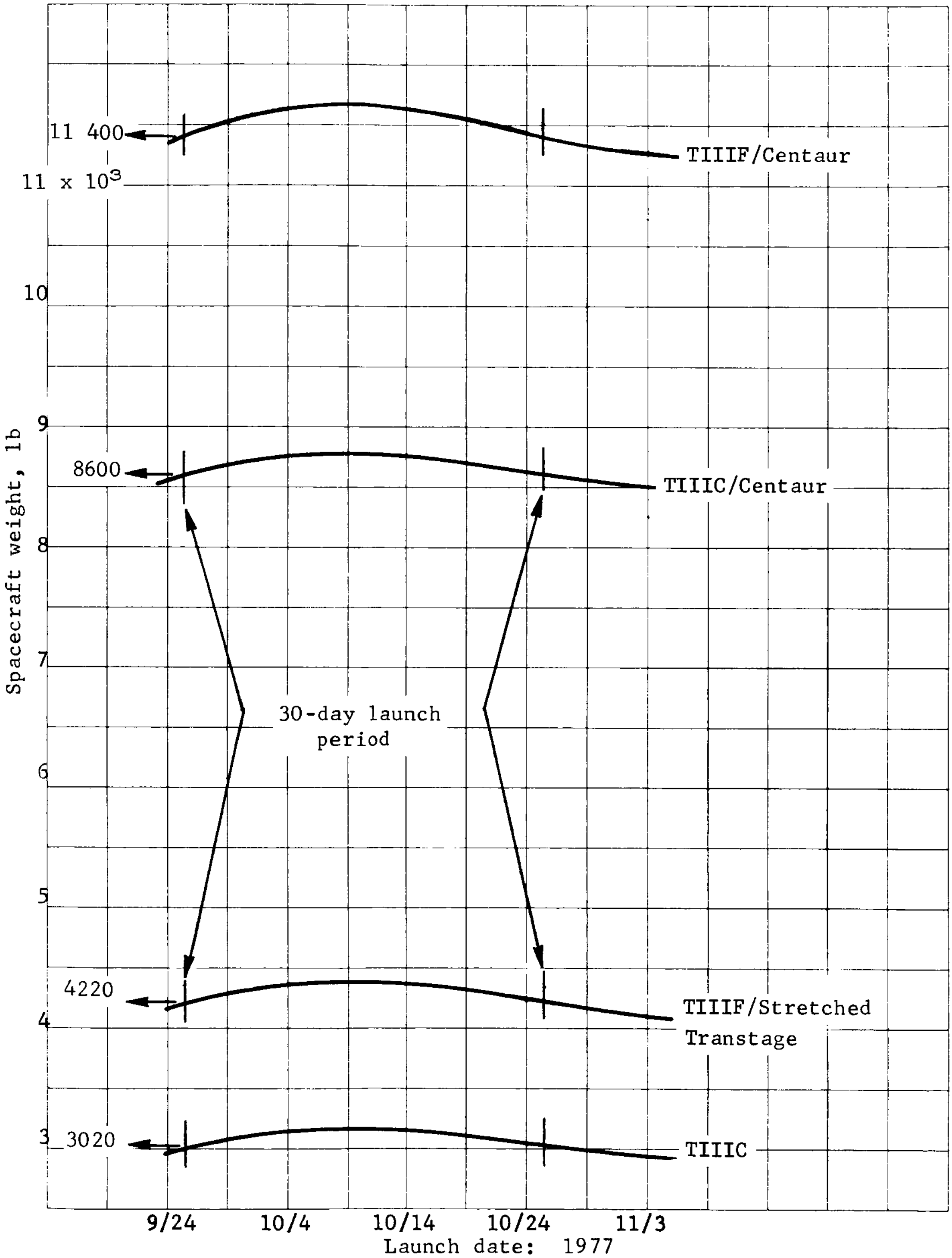

Figure A43.- Optimum Spacecraft Weight after Midcourse Correction, Mars 1977, Type II

APPENDIX A

In-Orbit Capability

For the entry-from-orbit case, the orbiter and capsule system are taken into orbit. The launch vehicle payload in Mars orbit is determined by spacecraft capability, orbit insertion requirements, and orbiter characteristics. The results lead directly to capsule system weight for the entry-from-orbit mode. The optimum spacecraft capability, discussed in the previous section, corresponds essentially to minimum C_3 required for each launch date. Optimum useful payload in Mars orbit requires a strong bias toward arrival dates giving the minimum V_{HE}. Two Mars orbits are considered, both having a periapsis altitude of 1000 km. Apoapsis altitudes are 15 000 and 33 070 km (synchronous) leading to eccentricities of 0.614 and 0.785, respectively. Spacecraft specific impulse is 309 sec, and propellant mass fraction is shown in figure A44.

Figures A45 thru A56 show optimum useful in-orbit weight for the four launch vehicles, six mission/type combinations, and two orbit eccentricities. Useful in-orbit weight for a 30-day launch period is indicated. The useful in-orbit weight $(W_{P/L})$ is defined as total weight in orbit, less propulsion system inert weight. Thus

$$W_{P/L} = W_{C/S} + W_{OR} = W_{S/C} - W_P - W_{PI}$$

where

W_{OR} = useful in-orbit orbiter weight

W_P = propellant required for orbit insertion.

W_{PI} must be based on the total spacecraft propellant (i.e., midcourse correction + orbit insertion). This is determined using λ from figure A44. As shown earlier

$$W_{PI} = W_P(1/\lambda - 1)$$

where

W_P = total spacecraft propellant required (midcourse correction and orbit insertion)

λ = propellant mass fraction.

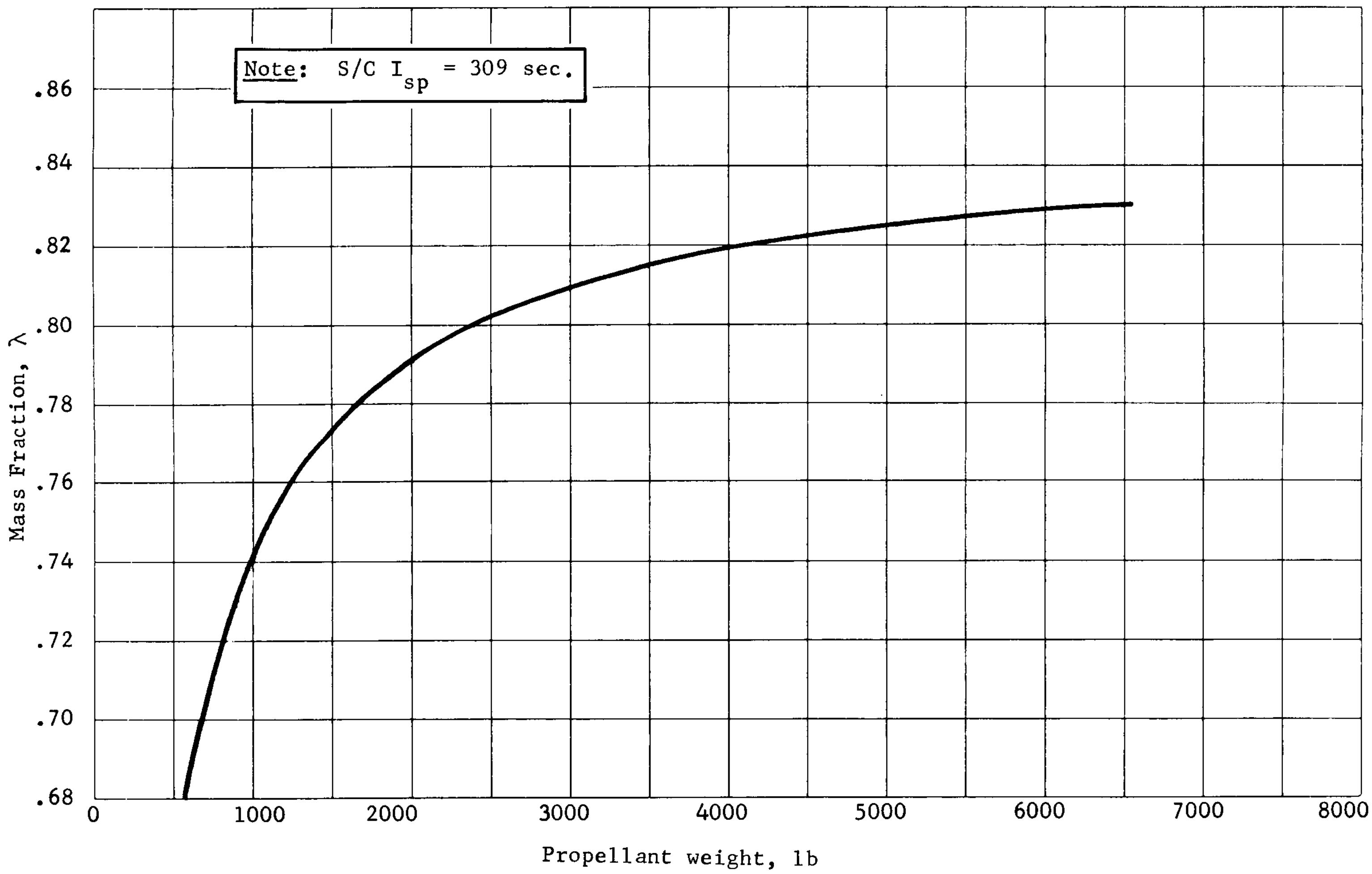

Figure A44.- Propulsion System Mass Fraction for Orbiter

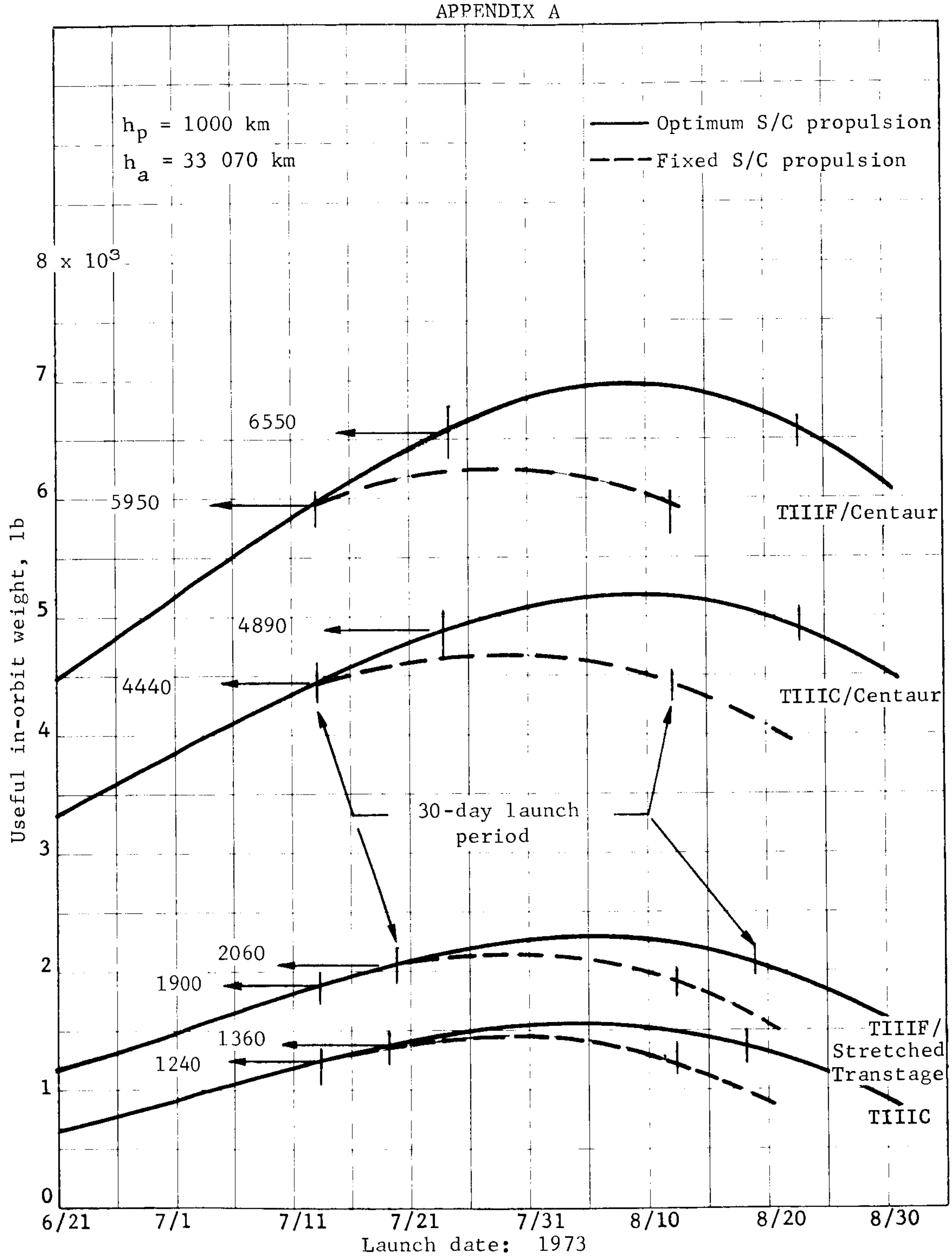

Figure A45.- Optimum Payload in Orbit, Mars 1973, Type I

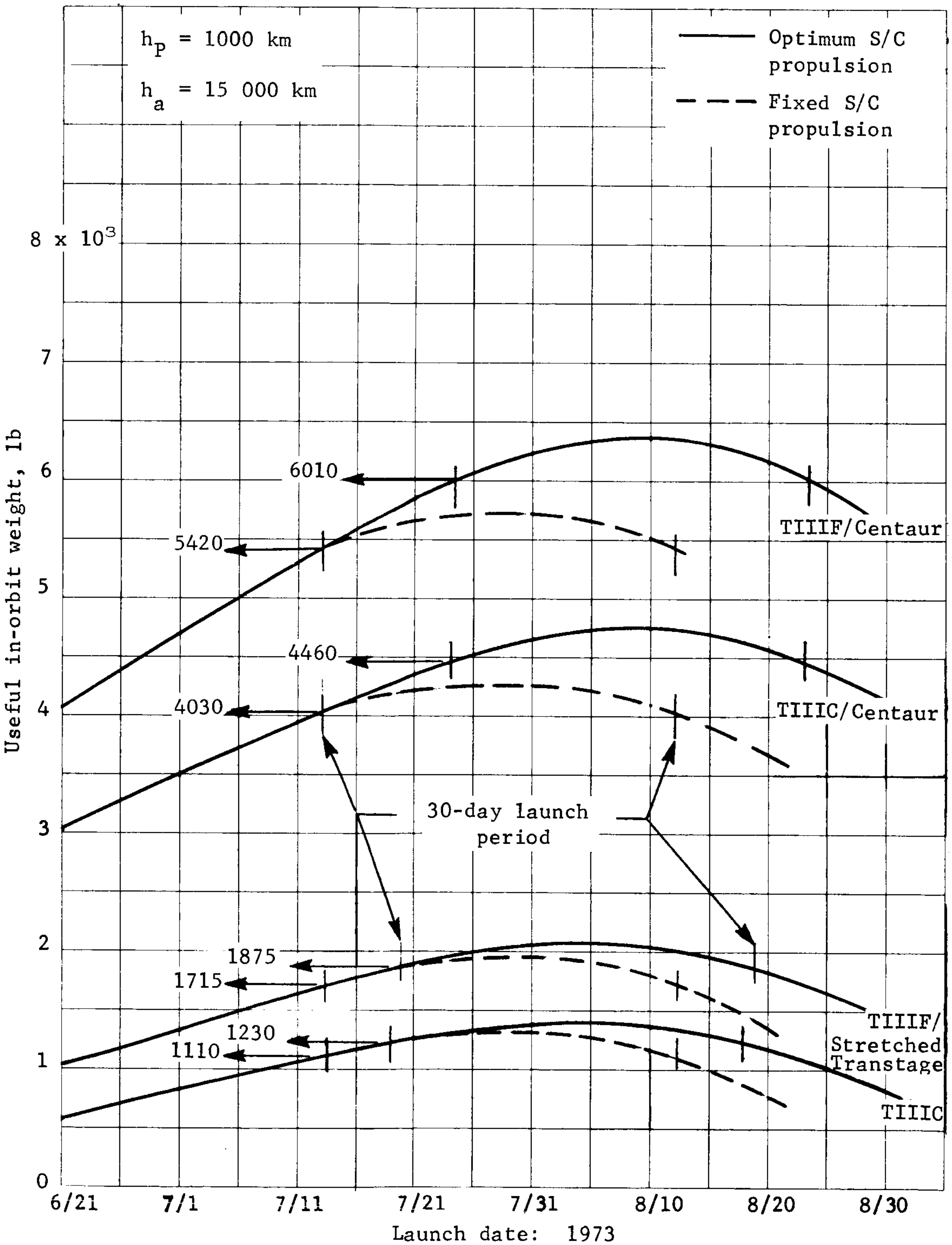

Figure A46.- Optimum Payload in Orbit, Mars 1973, Type I

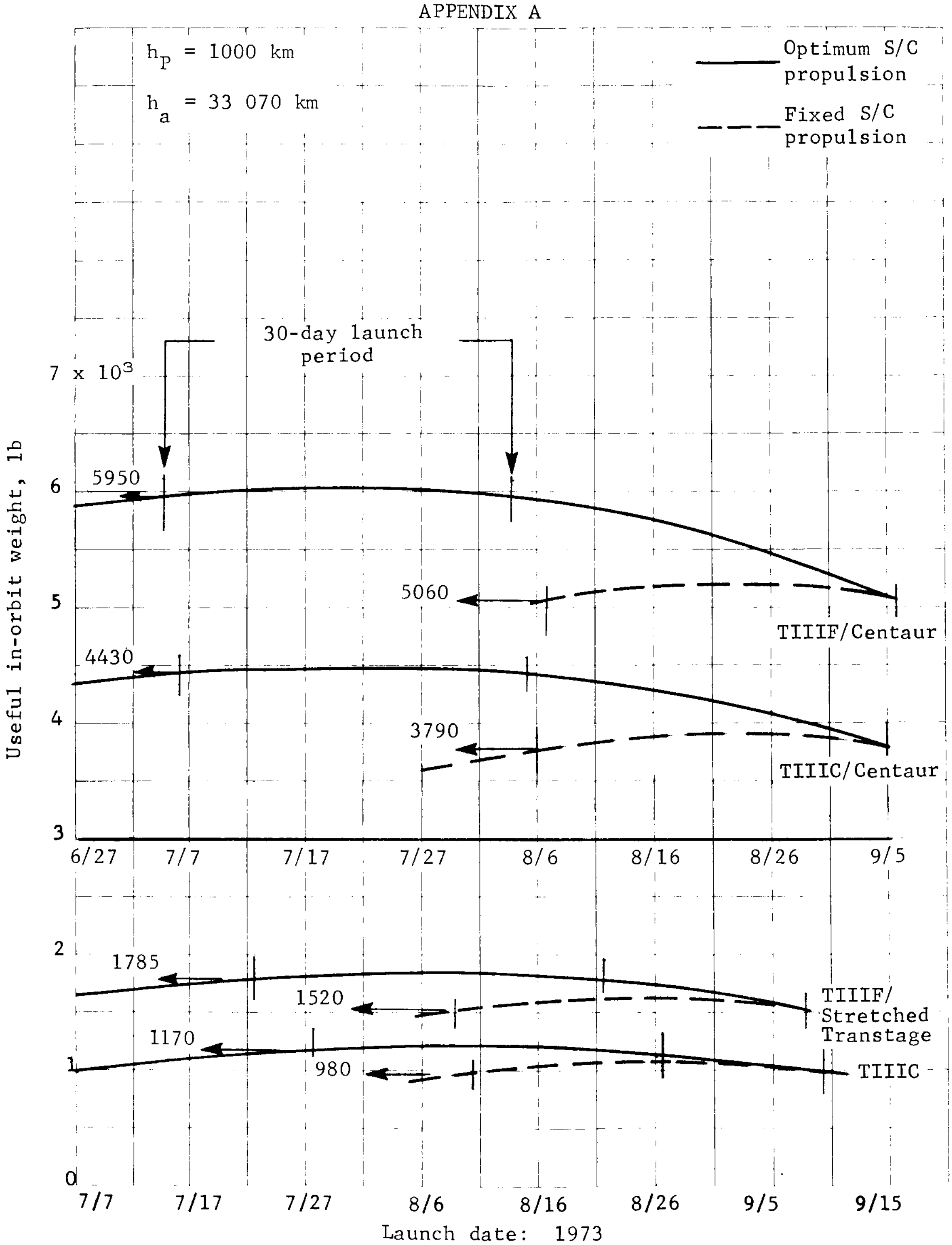

Figure A47.- Optimum Payload in Orbit, Mars 1973, Type II

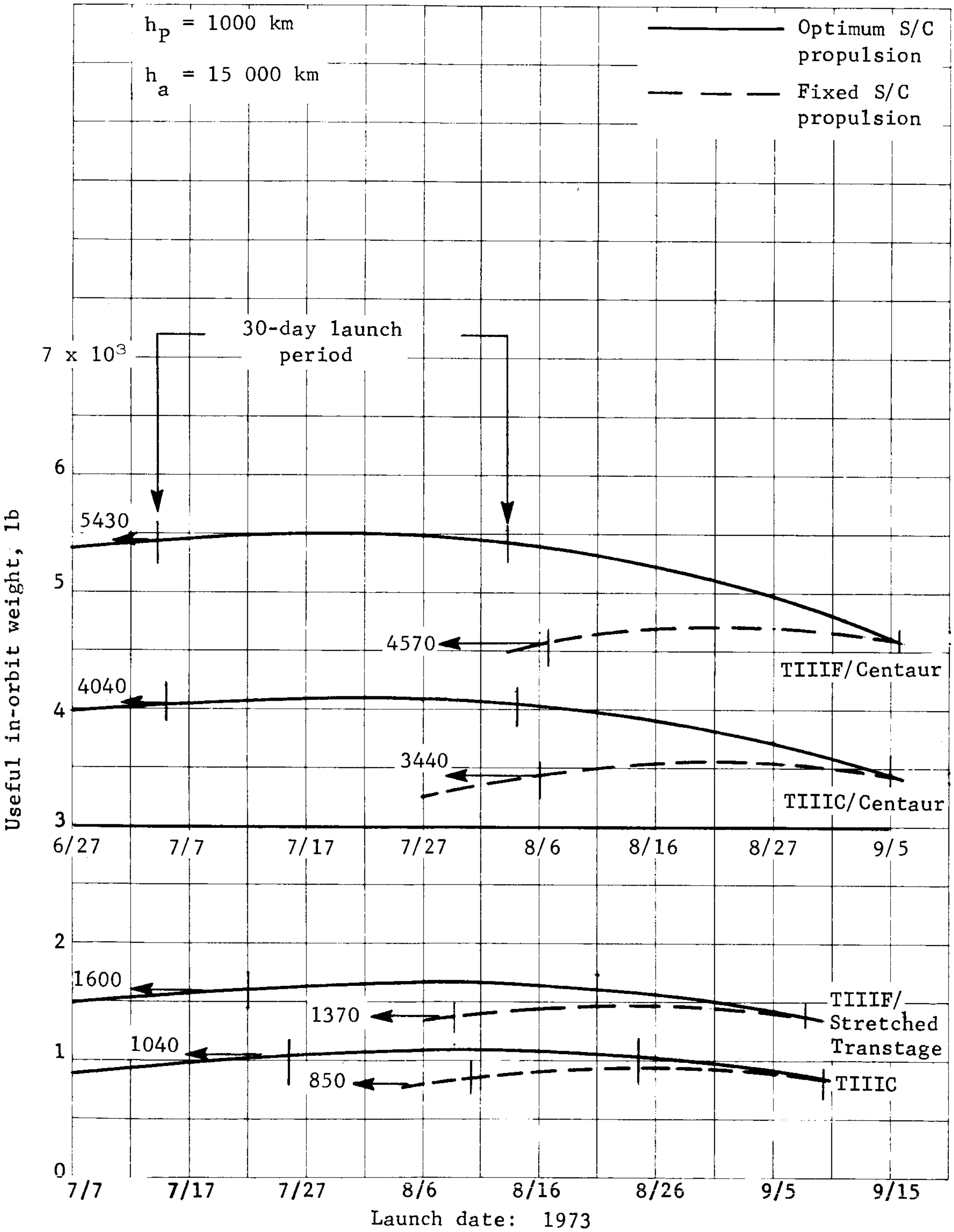

Figure A48.- Optimum Payload in Orbit, Mars 1973, Type II

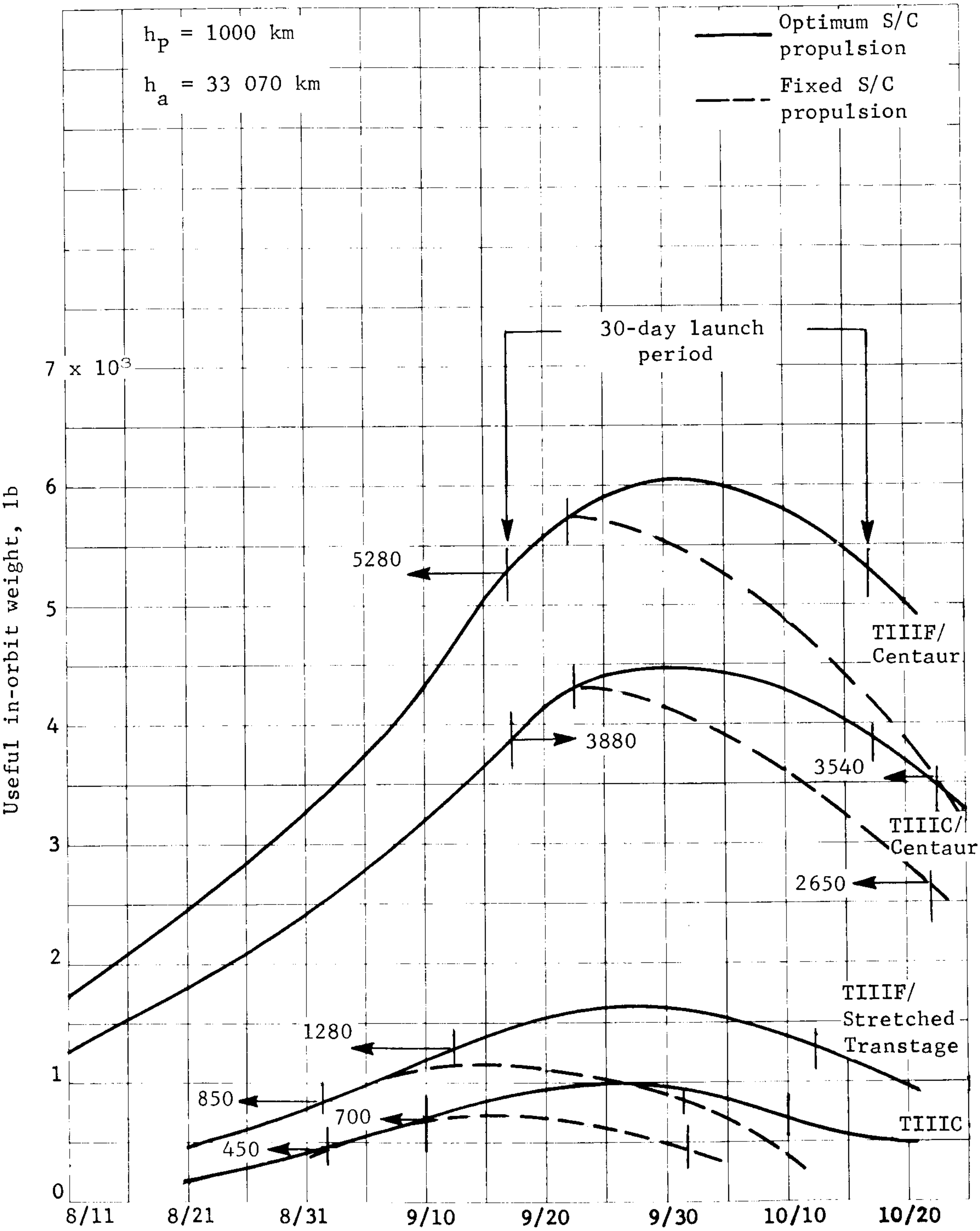

Figure A49.- Optimum Payload in Orbit, Mars 1975, Type I

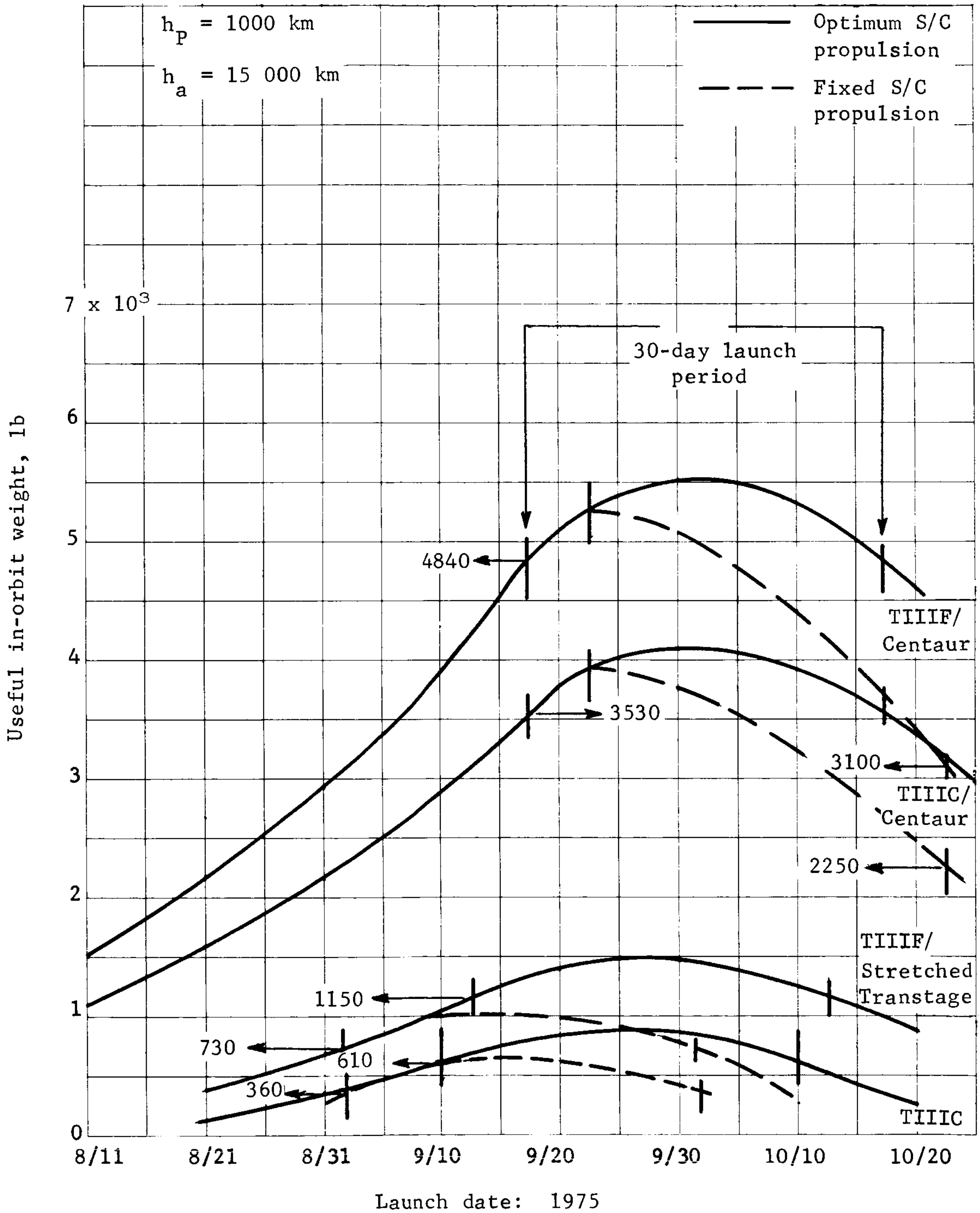

Figure A50.- Optimum Payload In Orbit, Mars 1975, Type I

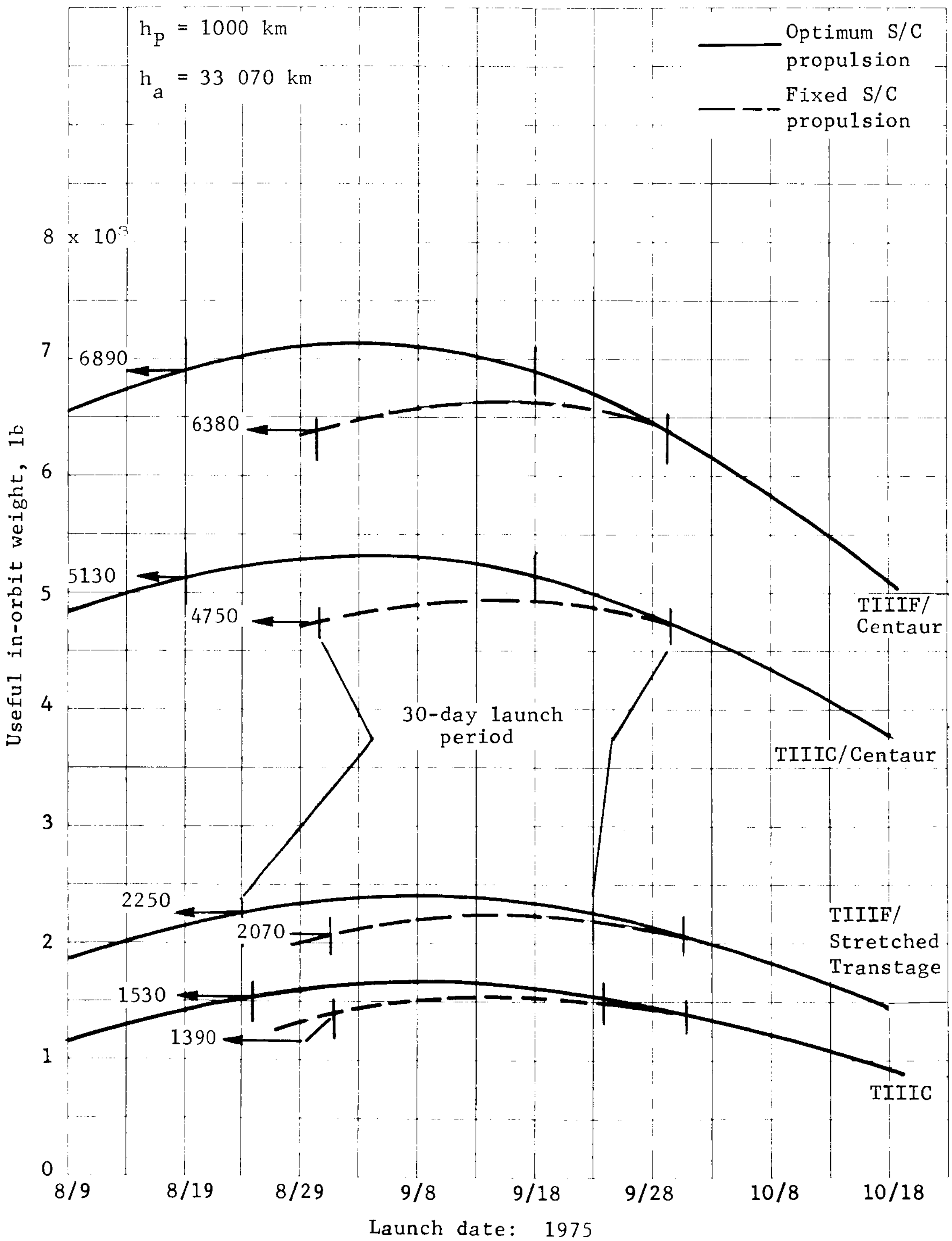

Figure A51.- Optimum Payload in Orbit, Mars 1975, Type II

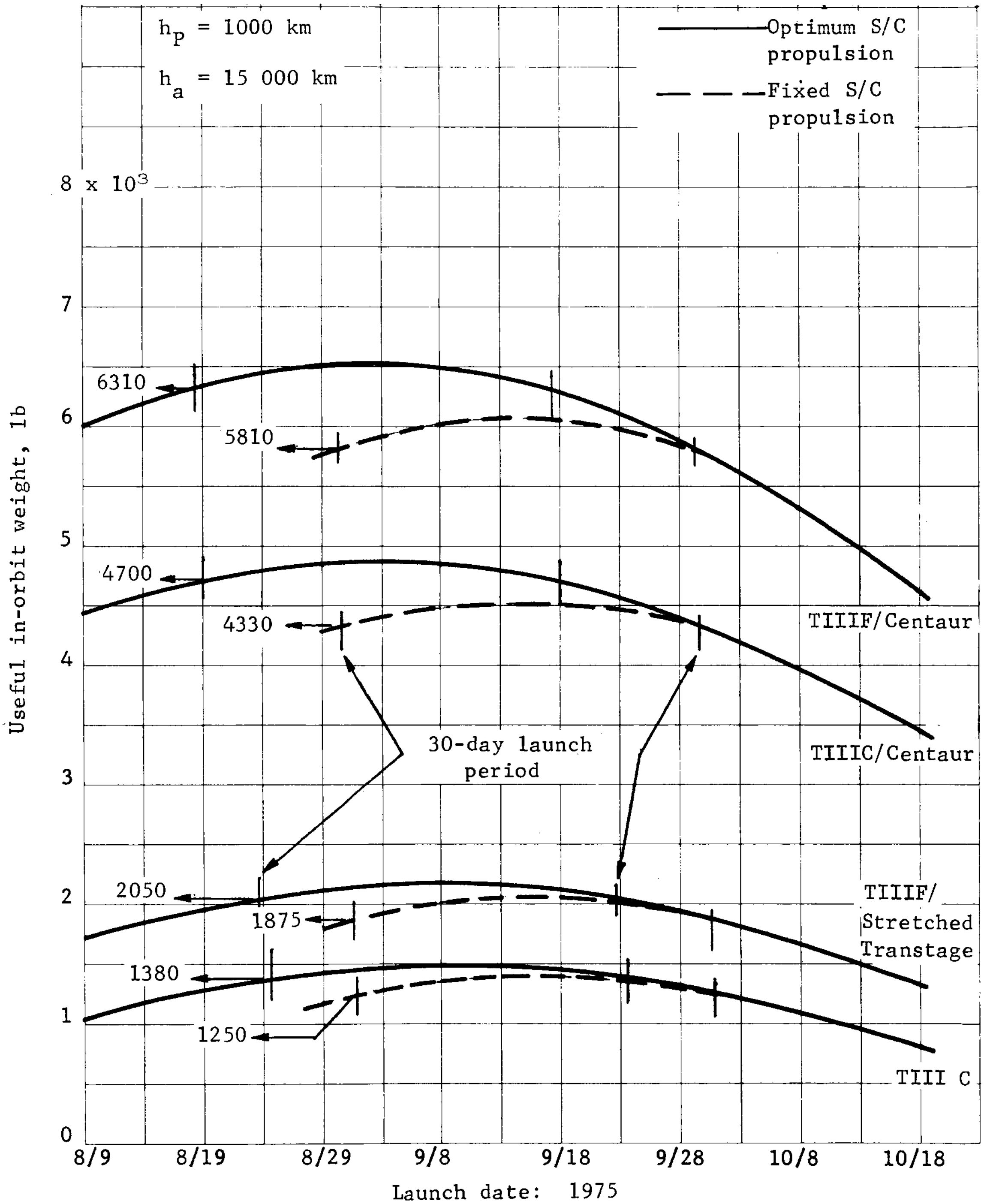

Figure A52.- Optimum Payload in Orbit, Mars 1975, Type II

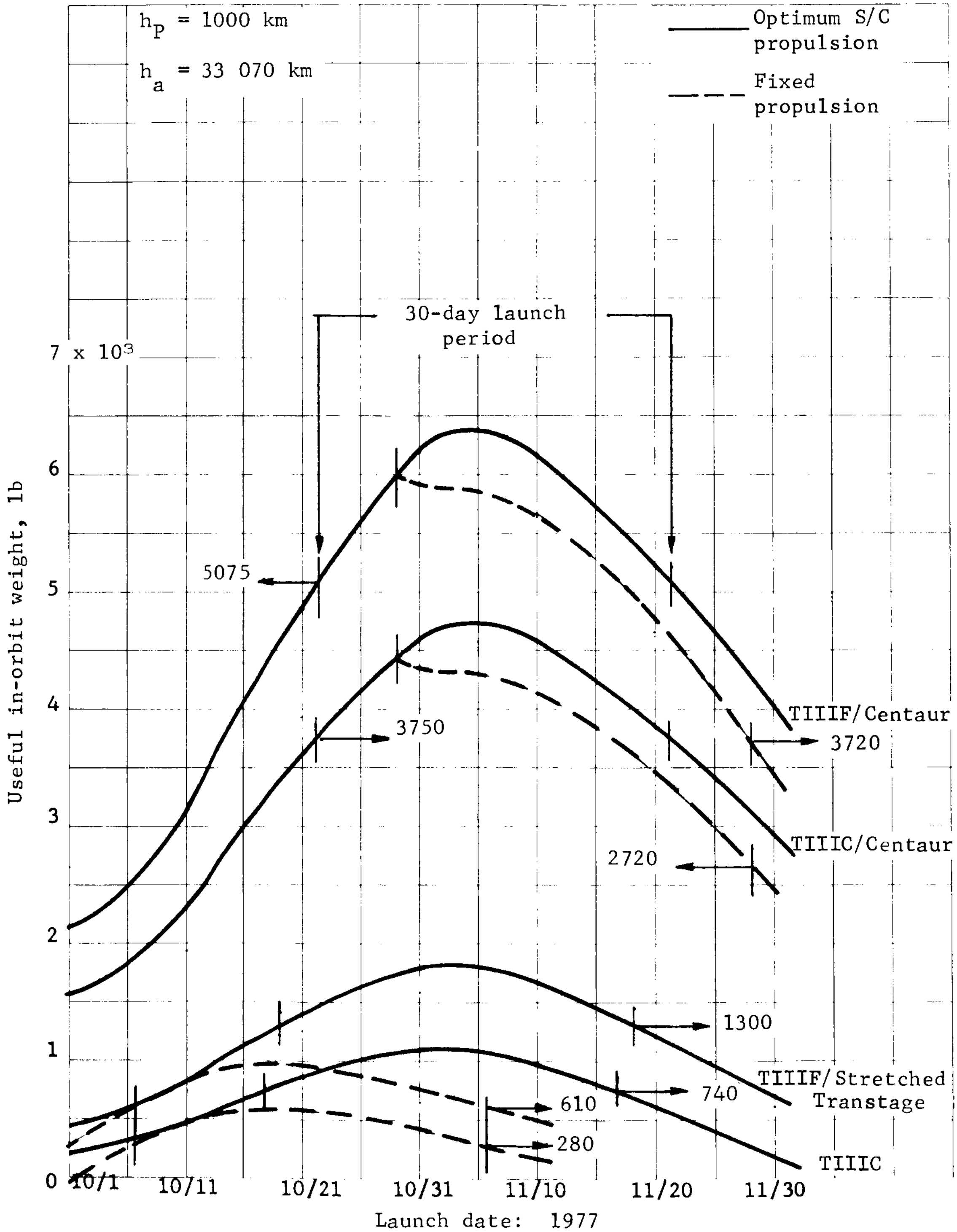

Figure A53.- Optimum Payload in Orbit, Mars 1977, Type I

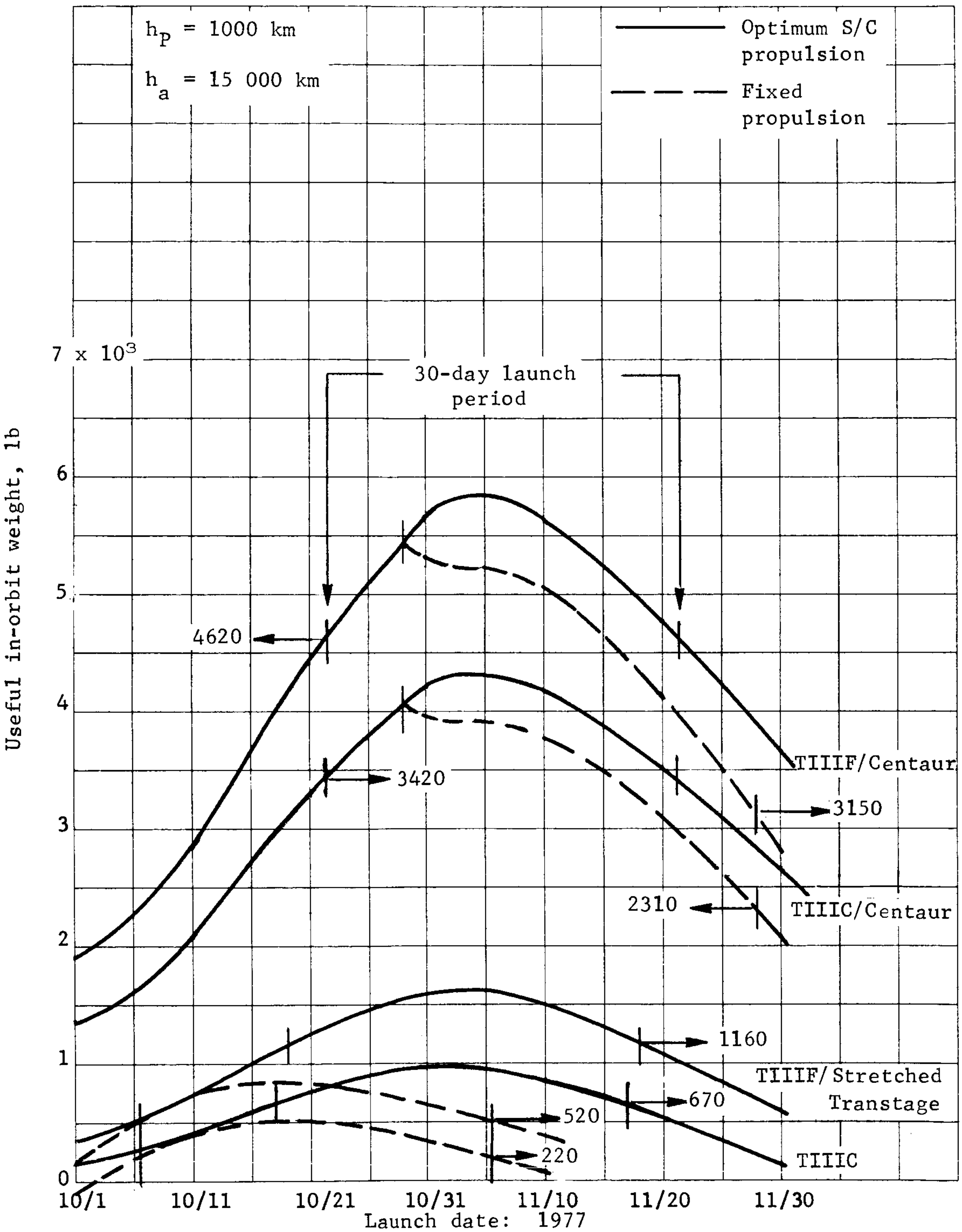

Figure A54.- Optimum Payload in Orbit, Mars 1977, Type I

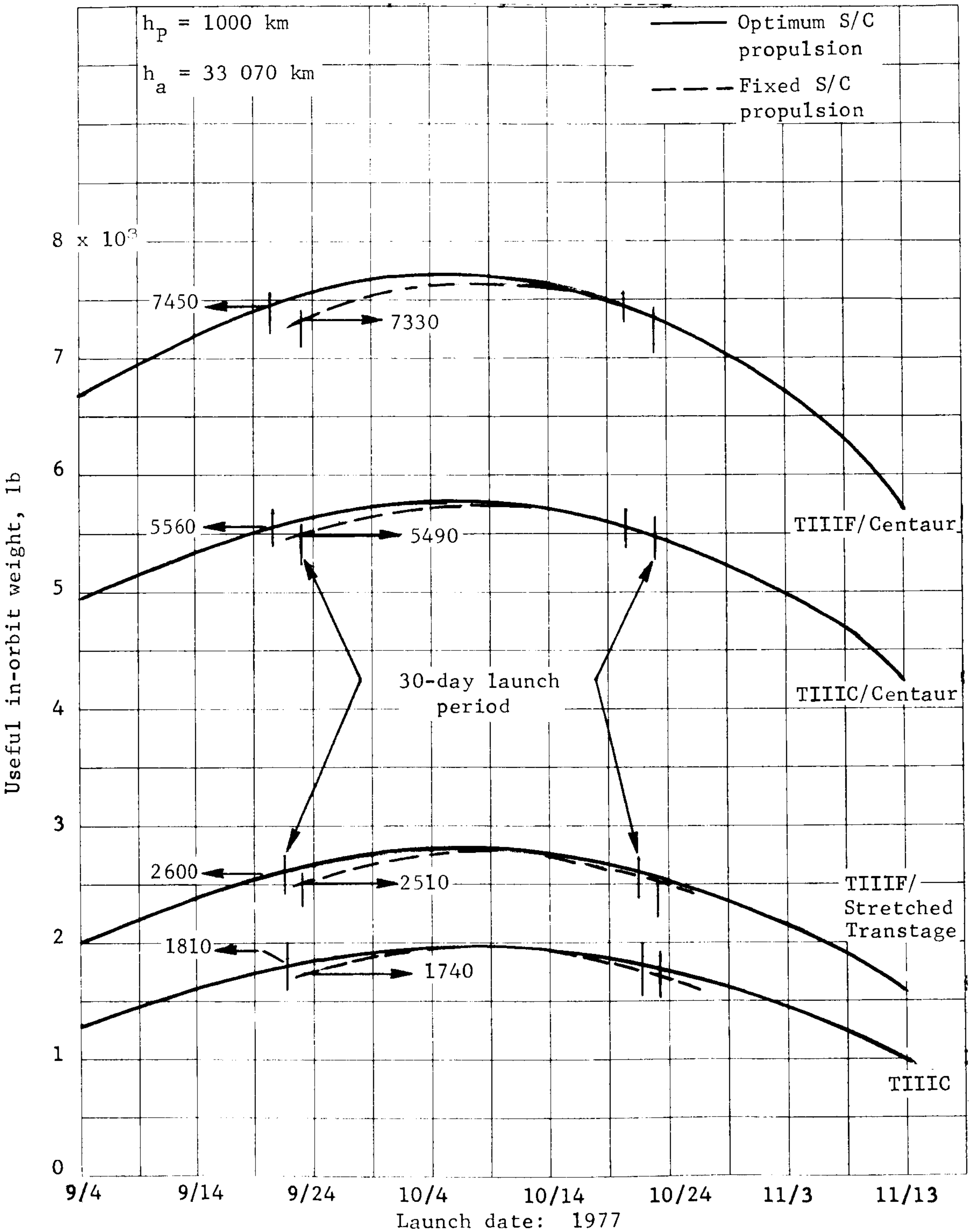

Figure A55.- Optimum Payload in Orbit, Mars 1977, Type II

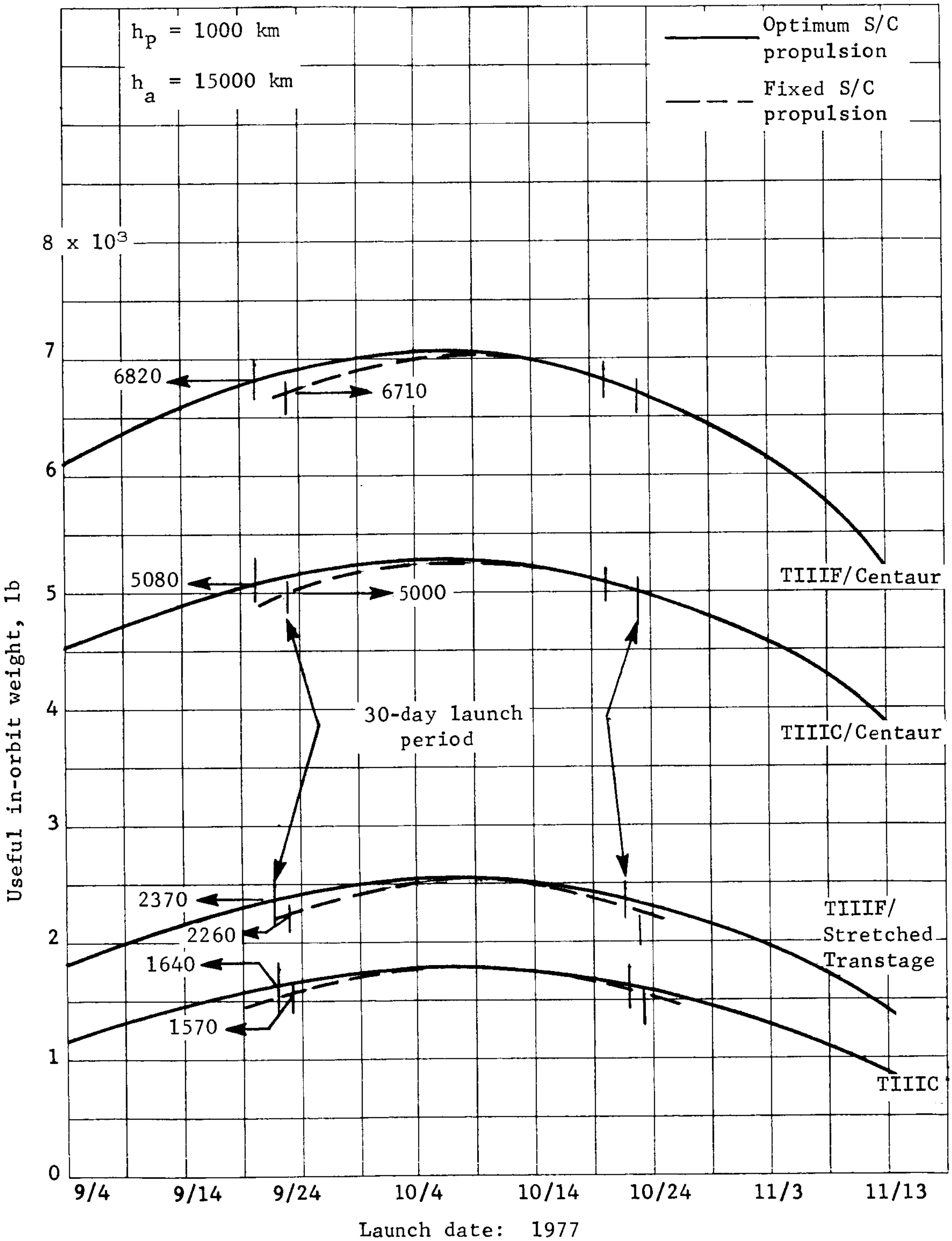

Figure A56.- Optimum Payload in Orbit, Mars 1977, Type II

APPENDIX A

Using a launch date of 7/19/73, the Titan IIIC spacecraft weight for maximum payload in orbit is 2547 lb. This is within a few pounds of the optimum spacecraft weight for that date as shown in figure A38. This value (2547 lb) reflects a midcourse propellant of 65 lb already removed. The V_{HE} for this case is 2.98 km/sec, leading to an orbit insertion requirement (ΔV_{OI}) of 1.23 km/sec or 4030 fps including losses (75 mps). The propellant weight is

$$W_P = W_0\left(1 - e^{-\Delta V \ C_J}\right)$$

where

$$W_0 = W_{S/C} = 2547 \text{ lb}$$

$$\Delta V = 4030 \text{ fps}$$

$$C_J = 309\ (32.174) = 9942 \text{ fps.}$$

Substituting,

$$W_P = 2547\left(1 - e^{-4030/9942}\right) = 858 \text{ lb.}$$

The total propellant = 858 + 65 = 923 lb.

From figure A44, $\lambda = 0.737$ (using a digital curve fit). The inert spacecraft weight is

$$W_{PI} = 923(1/0.737 - 1) = 329 \text{ lb}$$

Therefore, the value shown in figure A45 for a 7/19/73 launch date is

$$W_{P/L} = 2547 - 858 - 329 = 1360 \text{ lb.}$$

To arrive at the capsule system weights shown in table A3

$$W_{C/S} = W_{S/C} - W_{OR} - W_P - W_{PI} = W_{P/L} - W_{OR}.$$

APPENDIX A

TABLE A3.- OPTIMUM CAPSULE SYSTEM WEIGHT FOR ENTRY FROM ORBIT, OPTIMUM SPACECRAFT, 30-DAY LAUNCH PERIOD

Mission opportunity	Transfer type	Orbit eccentricity	Capsule system weight, lb[a]			
			TIIIC	TIIIF/ Stretched Transtage	TIIIC/ Centaur	TIIIF/ Centaur
1973	I	0.785	470/740	1170/1440	4000/4270	5660/5930
		0.614	340/610	985/1255	3570/3840	5120/5390
	II	0.785	280/550	895/1165	3540/3810	5060/5330
		0.614	150/420	710/980	3150/3420	4540/4810
1975	I	0.785	----/80	3390/660	2990/3260	4390/4660
		0.614	----/----	260/530	2640/2910	3950/4220
	II	0.785	640/910	1360/1630	4240/4510	6000/6270
		0.614	490/760	1160/1430	3810/4080	5420/5690
1977	I	0.785	----/120	410/680	2860/3130	4185/4455
		0.614	----/50	270/540	2530/2800	3730/4000
	II	0.785	920/1190	1710/1980	4670/4940	6560/6830
		0.614	750/1020	1480/1750	4190/4460	5930/6200

[a]890-lb orbiter/620-lb orbiter.

APPENDIX A

Substituting, using the useful spacecraft weights given earlier,

$$W_{C/S} = 1360 - 890 = 470 \text{ lb}$$

or

$$W_{C/S} = 1360 - 620 = 740 \text{ lb}.$$

The solid lines in figures A45 thru A56 indicate payload using an optimum spacecraft.* That is, the propellant weight and insert system weight are allowed to vary according to actual requirements for each launch date. A real-world spacecraft, however, would be designed with a fixed size tankage for a given launch opportunity. Further, the propellant loaded would be the maximum required over the launch period. Adjustment of propellant load as a function of launch date probably would not be attempted due to launch facility implications. Therefore, a fixed spacecraft payload is shown by a set of dashed curves in figures A45 thru A56. The fixed spacecraft payloads are generated by first determining the maximum propellant required for an arbitrary 30-day launch period. Payloads for launch dates over the 30-day period are then determined (based on the maximum propellant requirement) and a minimum payload established. This procedure is followed for several different 30-day periods and a launch period corresponding to the highest minimum payload is established. A preliminary study indicates that the optimum 30-day period for fixed spacecraft is the one that equalizes the payload at the end of the period. An exception is for the larger launch vehicles and the 1975 Type I and 1977 Type I opportunities. For those cases, the high declinations force an arrival date adjustment away from optimum to meet launch azimuth constraints, $|DLA| = 50°$; an improvement in minimum fixed spacecraft payload is found using a 30-day period where the payloads are not equal at the ends of the period. It is felt that a slight improvement over the results shown could be made by adjusting arrival date in the direction of lower C_3 until the total propellant loaded is used for all launch dates. This "fine tuning" is beyond the scope of the parametric study, however. The fixed orbiter payloads in orbit range from 1110 to 7450 lb over the total range of opportunities, orbits, and launch vehicles. Again, this generalization reflects the higher performance transfers for each opportunity.

---

*In this case, the terms orbiter and spacecraft are interchangeable when speaking of propulsion system characteristics.

APPENDIX A

Values of total capsule system weight corresponding to the 30-day payloads of figures A45 thru A56 are given in tables A3 and A4 for optimum and fixed spacecraft, respectively. These values are determined by subtracting the useful in-orbit orbiter weights of 890 lb (maximum) and 620 lb (minimum) from the values in the figures. Note that in this case, propulsion system inert weights have already been subtracted to give the total useful payload in orbit. Capsule system weights (fixed spacecraft) range from 220 to 6710 lb for the entry-from-orbit mode.

TABLE A4.- OPTIMUM CAPSULE SYSTEM WEIGHT FOR ENTRY FROM ORBIT, FIXED SPACECRAFT, 30-DAY LAUNCH PERIOD

Mission opportunity	Transfer type	Orbit eccentricity	Capsule system weight, lb[a]			
			TIIIC	TIIIF/ Stretched Transtage	TIIIC/ Centaur	TIIIF/ Centaur
1973	I	0.785	350/620	1010/1280	3550/3820	5060/5330
		0.614	220/490	825/1095	3140/3410	4530/4800
	II	0.785	90/360	630/900	2900/3170	4170/4440
		0.614	----/230	480/750	2550/2820	3680/3950
1975	I	0.785	----/----	----/230	1760/2030	2650/2920
		0.614	----/----	----/110	1360/1630	3210/2480
	II	0.785	500/770	1180/1450	3860/4130	5490/5760
		0.614	360/630	985/1255	3440/3710	4920/5190
1977	I	0.785	----/----	----/----	1830/2100	2830/3100
		0.614	----/----	----/----	1420/1690	2260/2530
	II	0.785	850/1120	1620/1890	4600/4870	6440/6710
		0.614	680/950	1370/1640	4110/4380	5820/6090

[a]890-lb orbiter/620-lb orbiter.

APPENDIX A

Orbit Positioning

For the entry-from-orbit mode, targeting analyses have established a requirement for orbit positioning. The periapsis shifts required are: 12 to 30° for the 15 000-km orbit and 7 to 25° for the 33 070-km orbit. These values correspond to 1973 Type I launch dates of 7/13 to 8/12. Velocity increments are 30 to 150 mps for both orbits as shown in figure A57(a). The effect upon payload in orbit is presented in figures A58 and A59 for the 1973 Type I mission. The resulting capsule system weights are shown in table A5. A capsule system weight reduction of 10 to 60 lb is indicated, compared to the no-positioning data. Shown in figure A57(b) is the orbit insertion ΔV with and without the orbit positioning increment. The effect of the increment is to reduce the total ΔV required between the end points of the launch period. When speaking of fixed orbiter propulsion, the propulsion system is sized for the maximum requirement. Therefore, the inclusion of the positioning ΔV tends to reduce the payload loss resulting from fixing the orbiter propulsion. For example, in figure A45 (no shift), fixed orbiter propulsion reduces the payload in orbit from 1360 to 1240 lb, or 120 lb. Figure A58 (with shift) shows a reduction due to fixing the orbiter of 70 lb, from 1300 to 1230 lb. Note also that for a fixed orbiter the effect of the periapsis shift itself results in a Titan IIIC payload reduction of only 10 lb.

TABLE A5.- OPTIMUM CAPSULE SYSTEM WEIGHT FOR ENTRY FROM ORBIT, ORBIT POSITIONING, 30-DAY LAUNCH PERIOD, 1973 TYPE I

Orbit eccentricity	Capsule system weight, lb[a]			
	TIIIC	TIIIF/ Stretched Transtage	TIIIC/ Centaur	TIIIF/ Centaur
(a) Optimum Spacecraft Propulsion				
0.785	410/680	1050/1320	3710/3980	5300/5570
0.614	260/530	900/1170	3310/3580	4785/5055
(b) Fixed Spacecraft Propulsion				
0.785	340/610	980/1250	3500/3770	5000/5270
0.614	220/490	790/1060	3080/3350	4460/4730

[a]890-lb orbiter/620-lb orbiter.

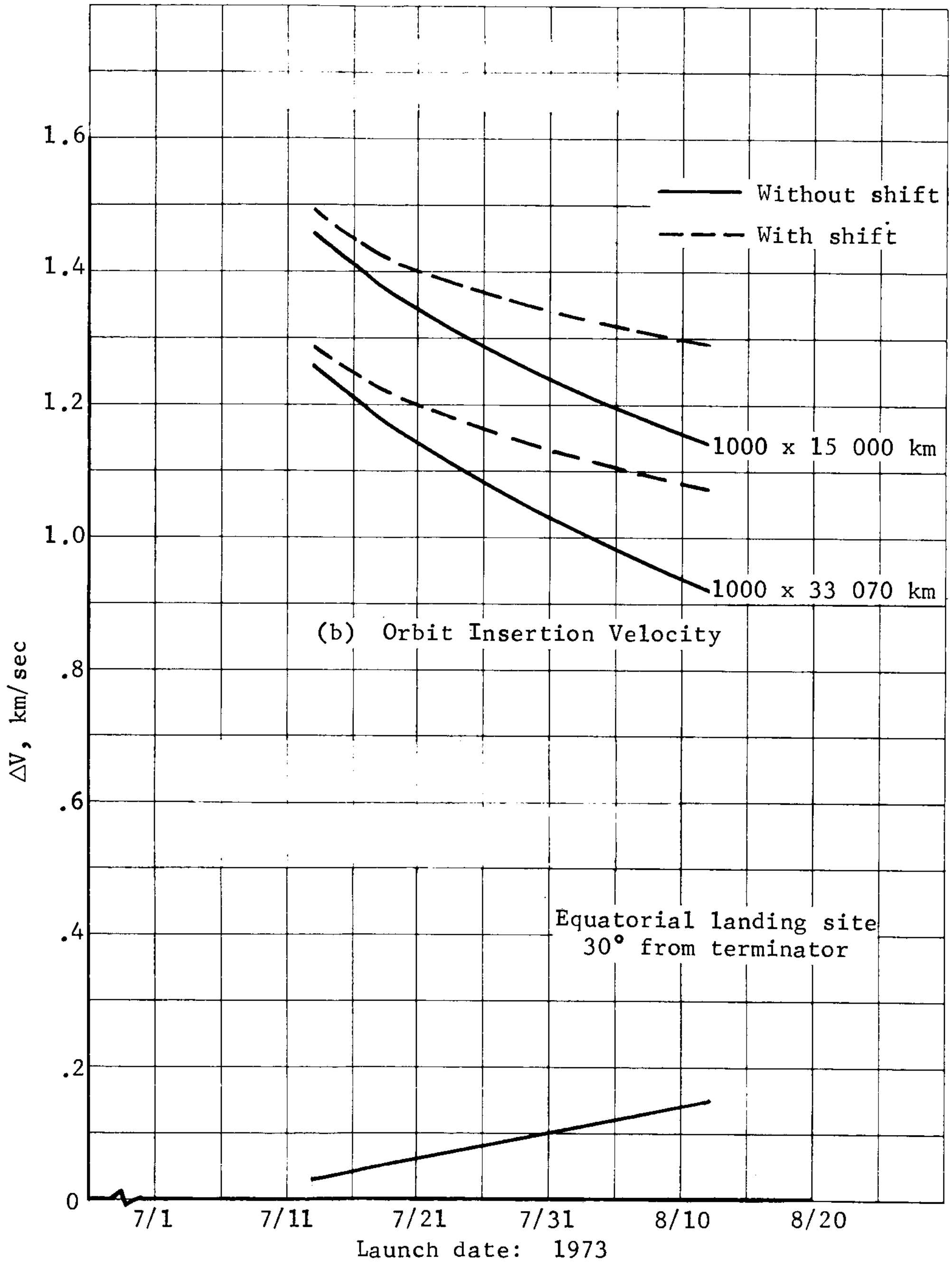

(a) Velocity Increment Required for Periapsis Shift

Figure A57.- Orbit Insertion Velocity and Velocity Increment Required for Periapsis Shift, Mars 1973, Type I

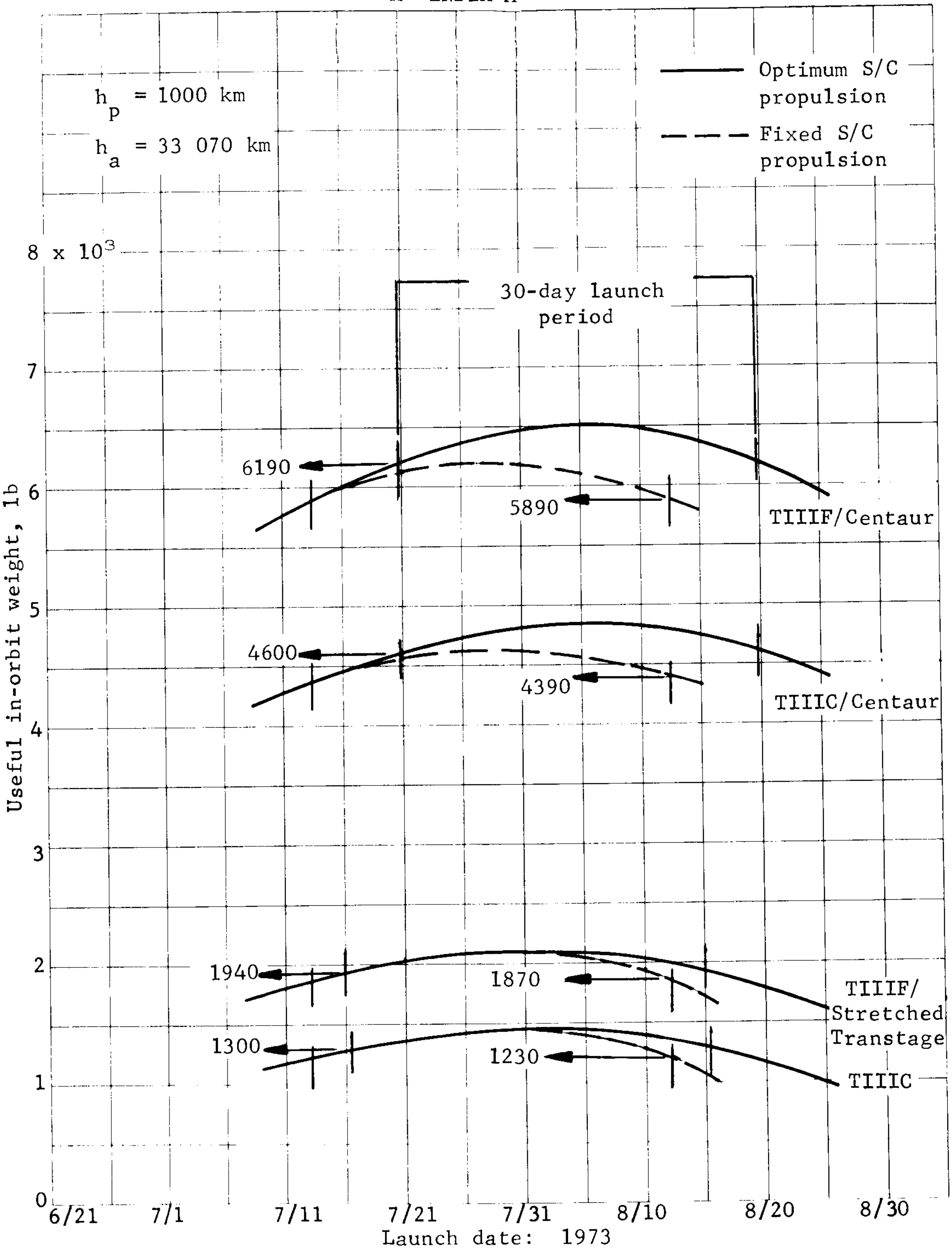

Figure A58.- Optimum Payload in Orbit, Orbit Positioning, Periapsis Shift = 7 to 25°, Mars 1973, Type I

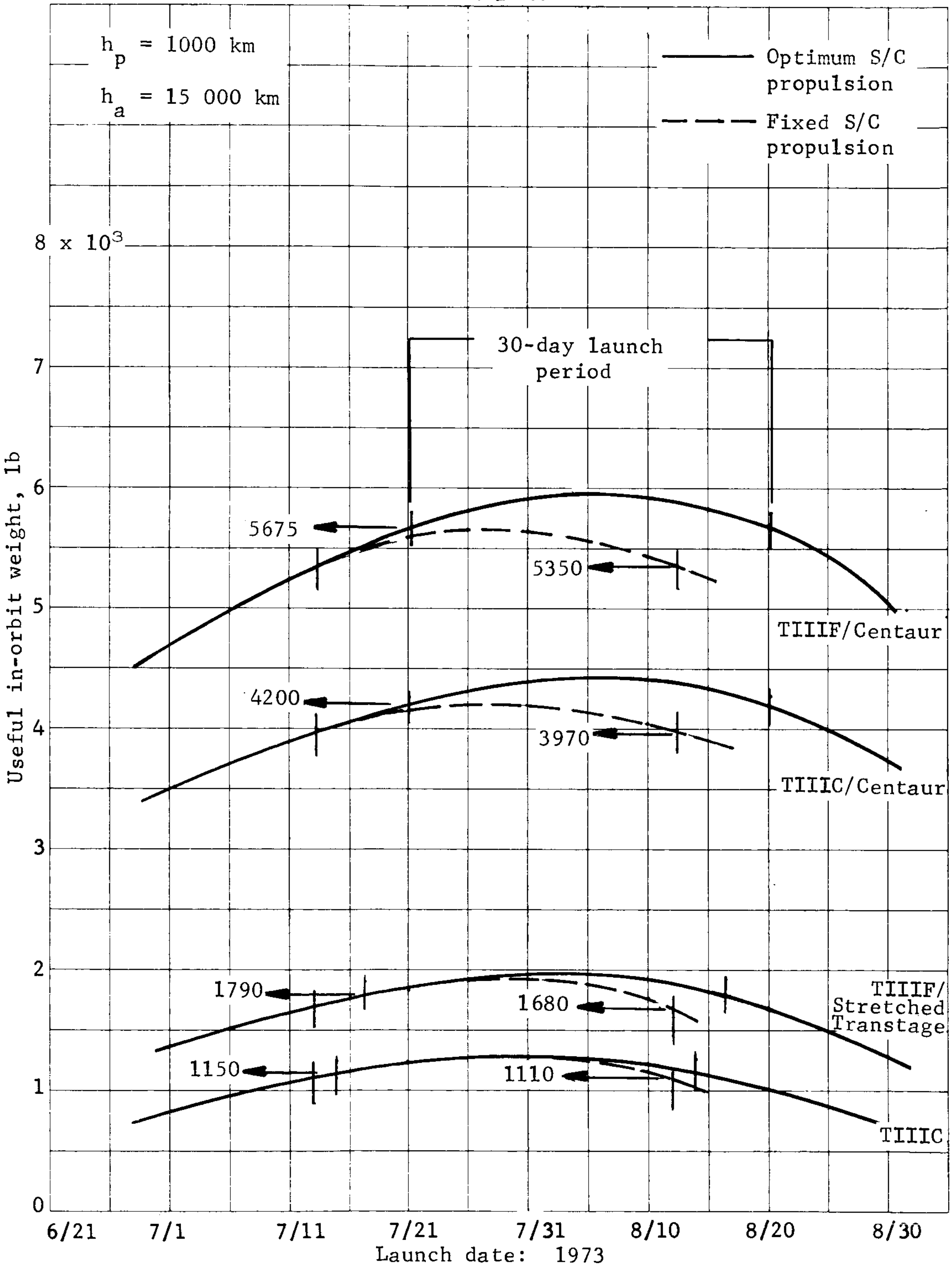

Figure A59.- Optimum Payload in Orbit, Orbit Positioning Periapsis Shift = 12 to 30°, Mars 1973, Type I

APPENDIX A

Direct Entry Capability

Figures A60 thru A71 present optimum direct entry capsule system weight for the four launch vehicles, six mission opportunity/transfer types, and two orbit eccentricity combinations. The capsule system is ejected after midcourse correction and enters the Martian atmosphere from the heliocentric trajectory. The remaining orbiter is then taken into Mars orbit. Orbiter propulsion and Mars orbit characteristics are described in the previous subsection. Declination/launch azimuth constraints are also as discussed previously. Two useful in-orbit orbiter weights, 890 lb (maximum) and 620 lb (minimum) are used. Data are shown for optimum orbiter propulsion; values of capsule system weight for a 30-day launch period are indicated. The arrival dates for the optimum direct entry capsule system weights are somewhat different than for the orbital entry system. Whereas the optimum orbital arrival dates were biased heavily toward minimum V_{HE}, the direct entry dates are biased somewhat back toward minimum C_3. This is because the total orbital vehicle is now much lighter than before, reducing the dependence on V_{HE}. Maximum capsule weight is a stronger function of maximum spacecraft weight increasing the dependence on C_3. The results from the figures are summarized in table A6.

Capsule system weight for the direct entry case with an orbiter is determined using the same approach as for the orbital case. In actual computation, however, an iteration is required to obtain the required useful in-orbit orbiter weight (890 or 620 lb) after capsule system separation.

For a launch date of 7/16/73, the data in figure A60 and table A6 (from a digital iteration) indicate a direct entry capsule system weight of 710 lb with an 890-lb orbiter. The corresponding spacecraft weight for that date is 2530 lb, again within a few pounds of the optimum (fig. A38). The total orbiter weight before orbit insertion is then

$$W_{OR_{Tot}} = 2530 - 710 = 1820 \text{ lb.}$$

The ΔV_{OI} is 4230 fps; following the procedure outlined above for the orbit case, the orbit insertion propellant is 622 lb. Adding $W_{P_{M/C}}$ of 63 lb gives a total spacecraft/orbiter propellant of 685 lb. From figure A44, $\lambda = 0.69$ (digital curve fit) and $W_{PI} = 308$ lb. Thus, useful orbiter weight in orbit is

$$W_{OR} = 1820 - 622 - 308 = 890$$

which is the required minimum useful in-orbit orbiter weight.

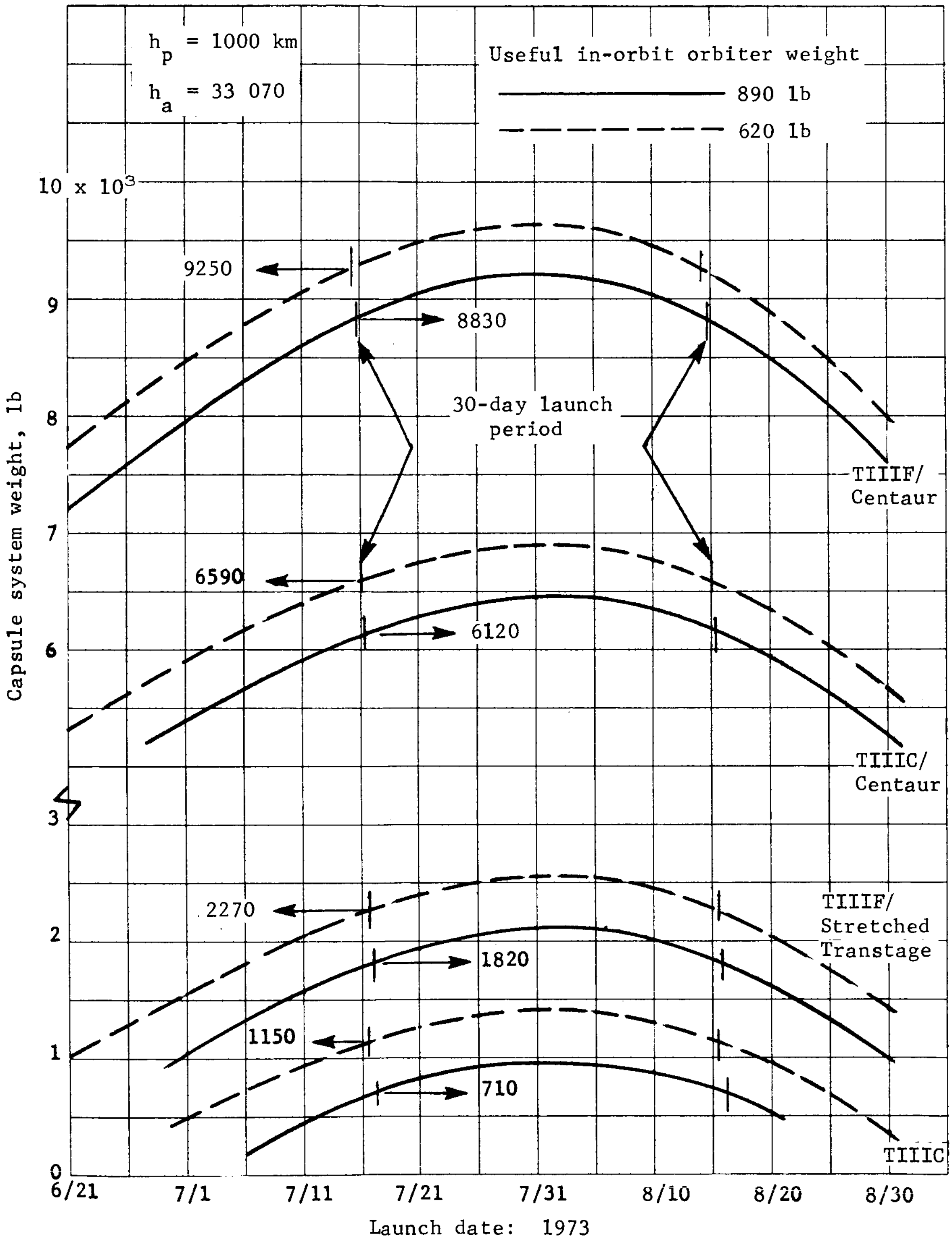

Figure A60.- Optimum Direct Entry System Weight, Optimum Orbiter Propulsion, Mars 1973, Type I

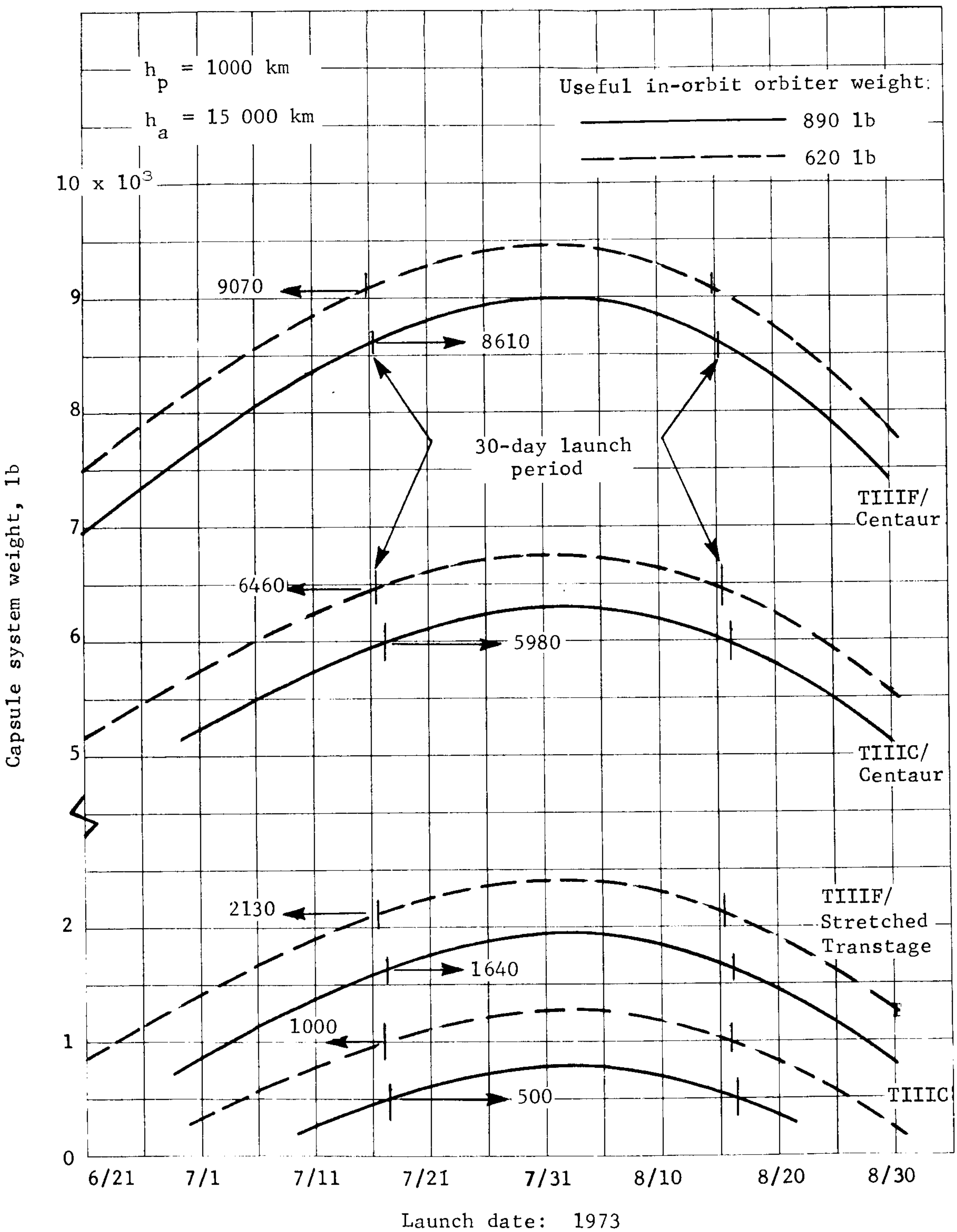

Figure A61.- Optimum Direct Entry System Weight, Optimum Orbiter Propulsion, Mars 1973, Type I

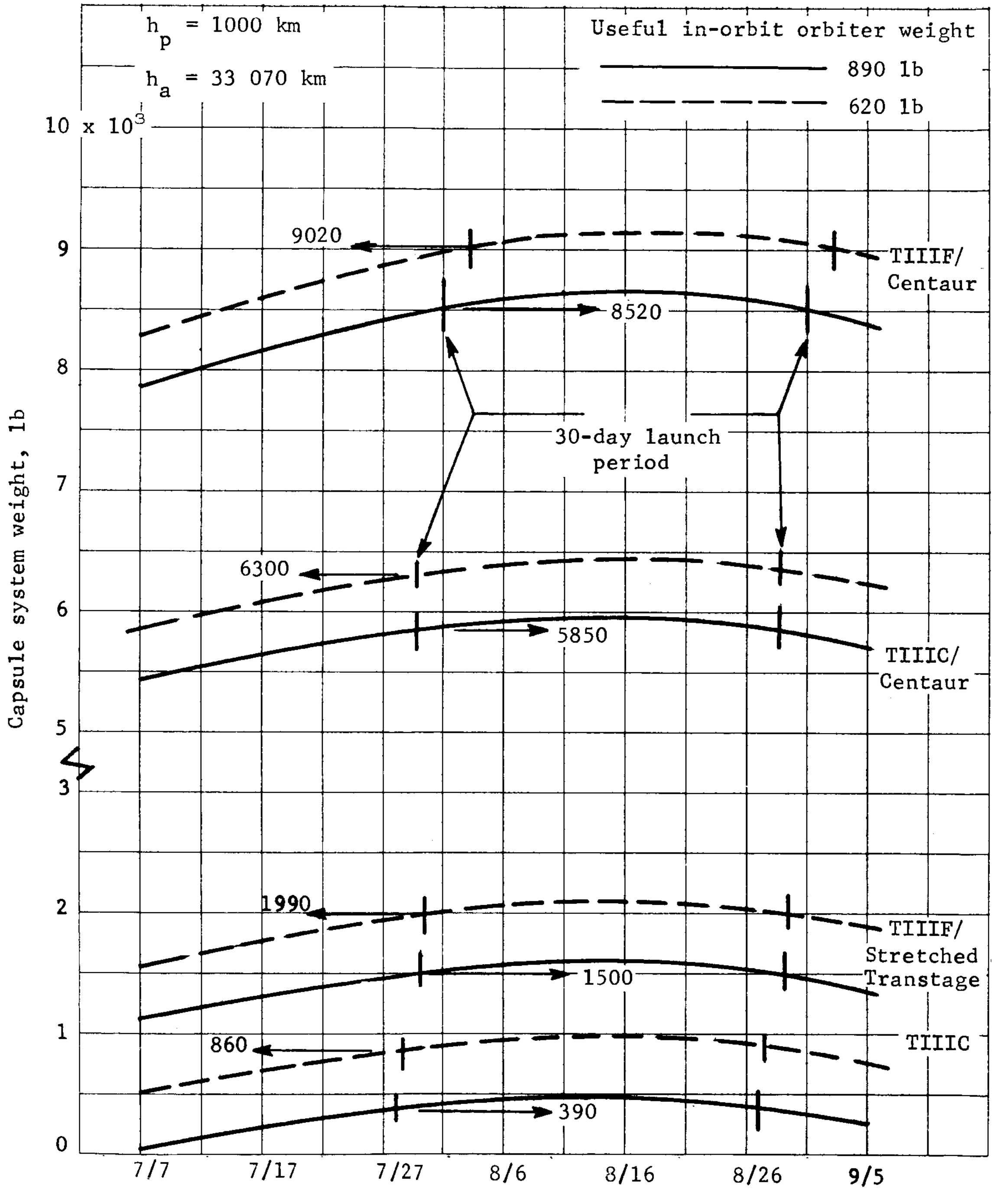

Figure A62.- Optimum Direct Entry System Weight, Optimum Orbiter Propulsion, Mars 1973, Type II

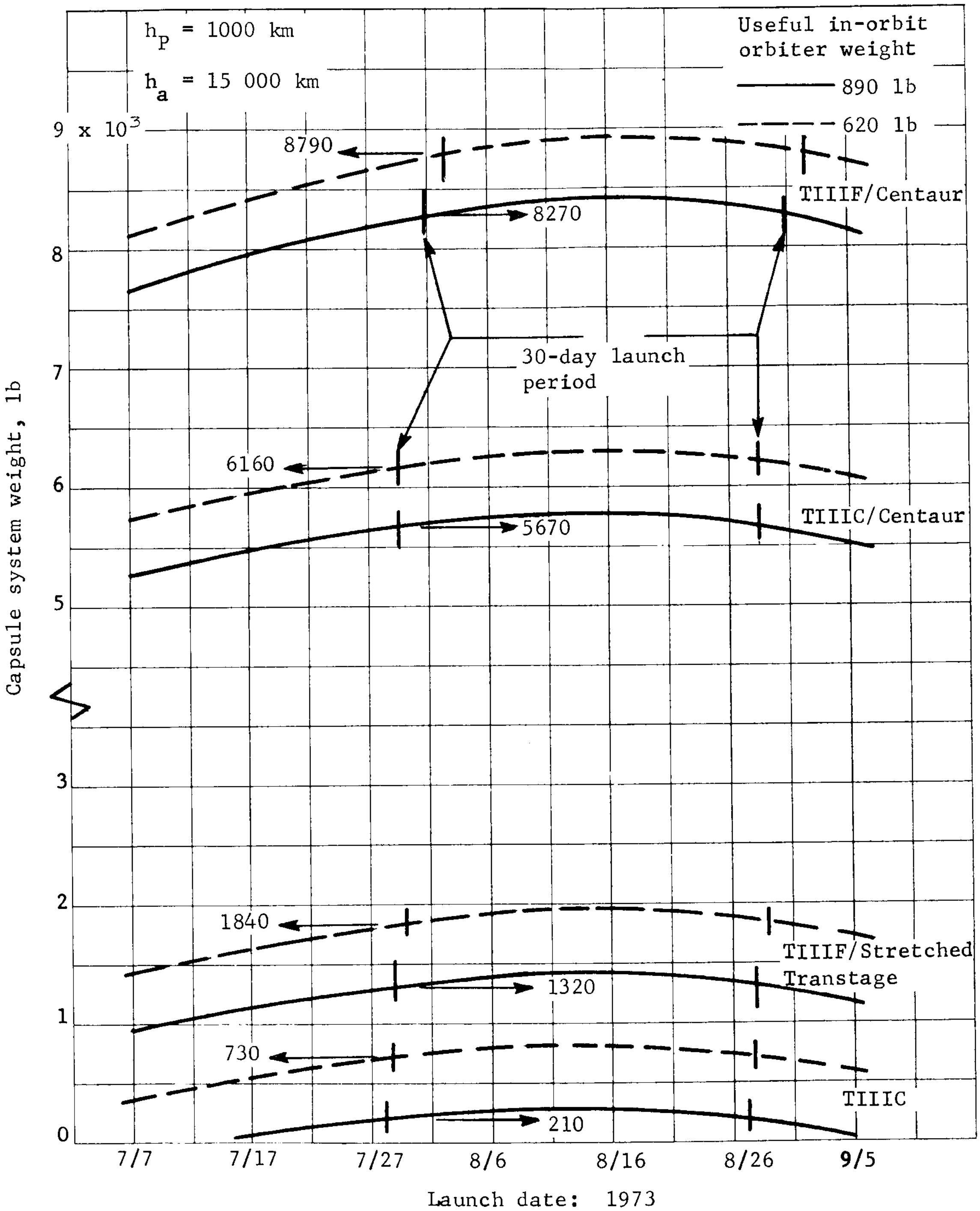

Figure A63.- Optimum Direct Entry System Weight, Optimum Orbiter Propulsion, Mars 1973, Type II

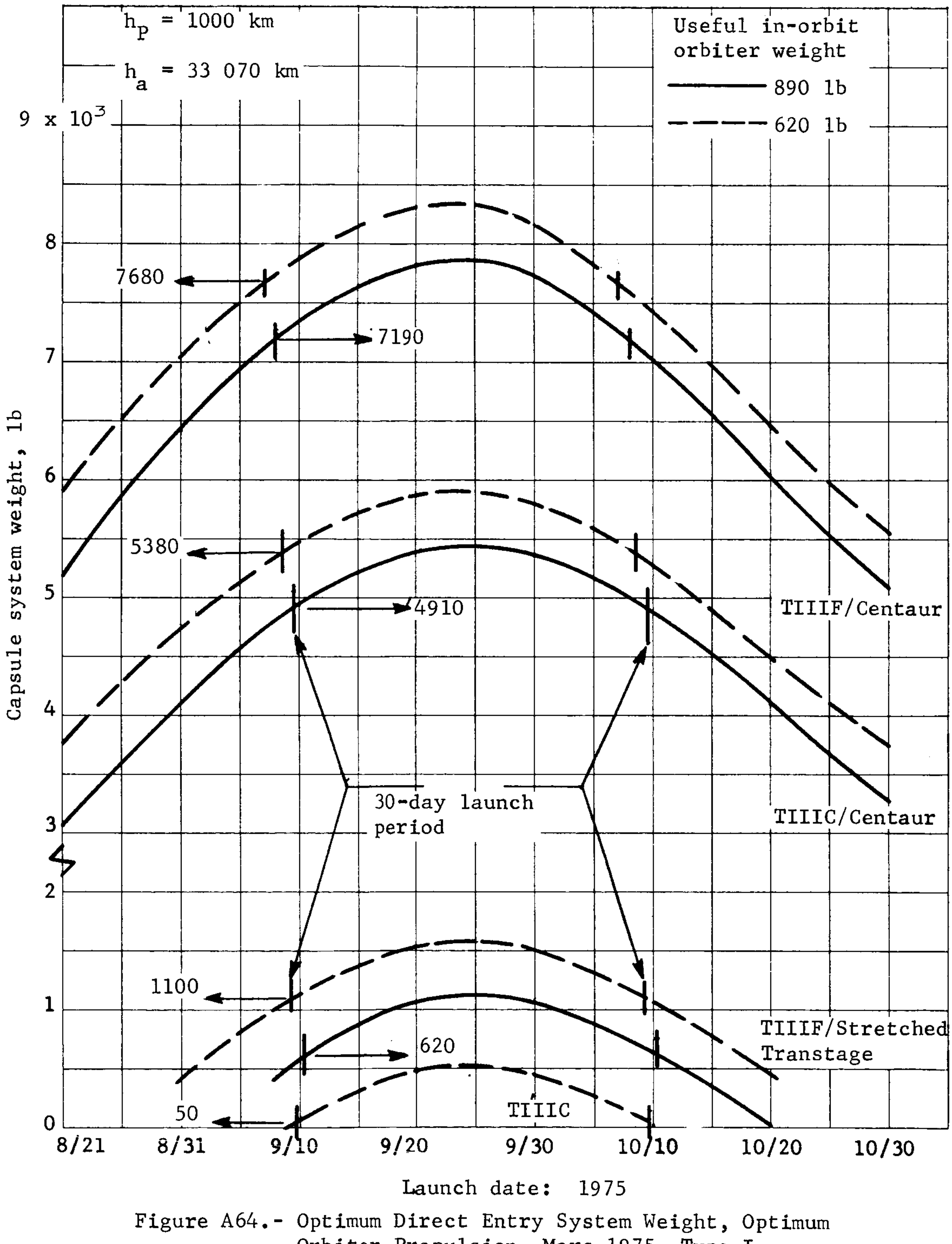

Figure A64.- Optimum Direct Entry System Weight, Optimum Orbiter Propulsion, Mars 1975, Type I

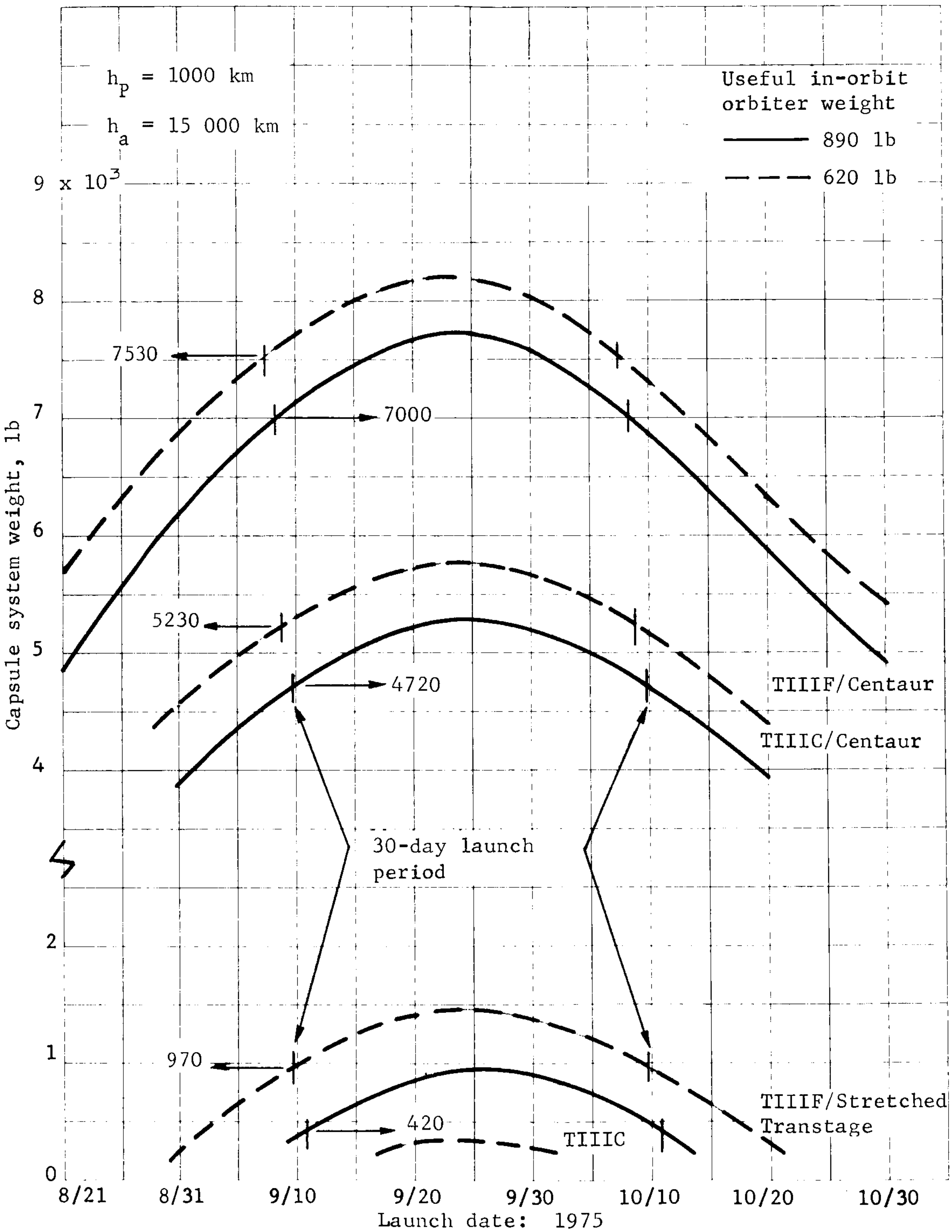

Figure A65.- Optimum Direct Entry System Weight, Optimum Orbiter Propulsion, Mars 1975, Type I

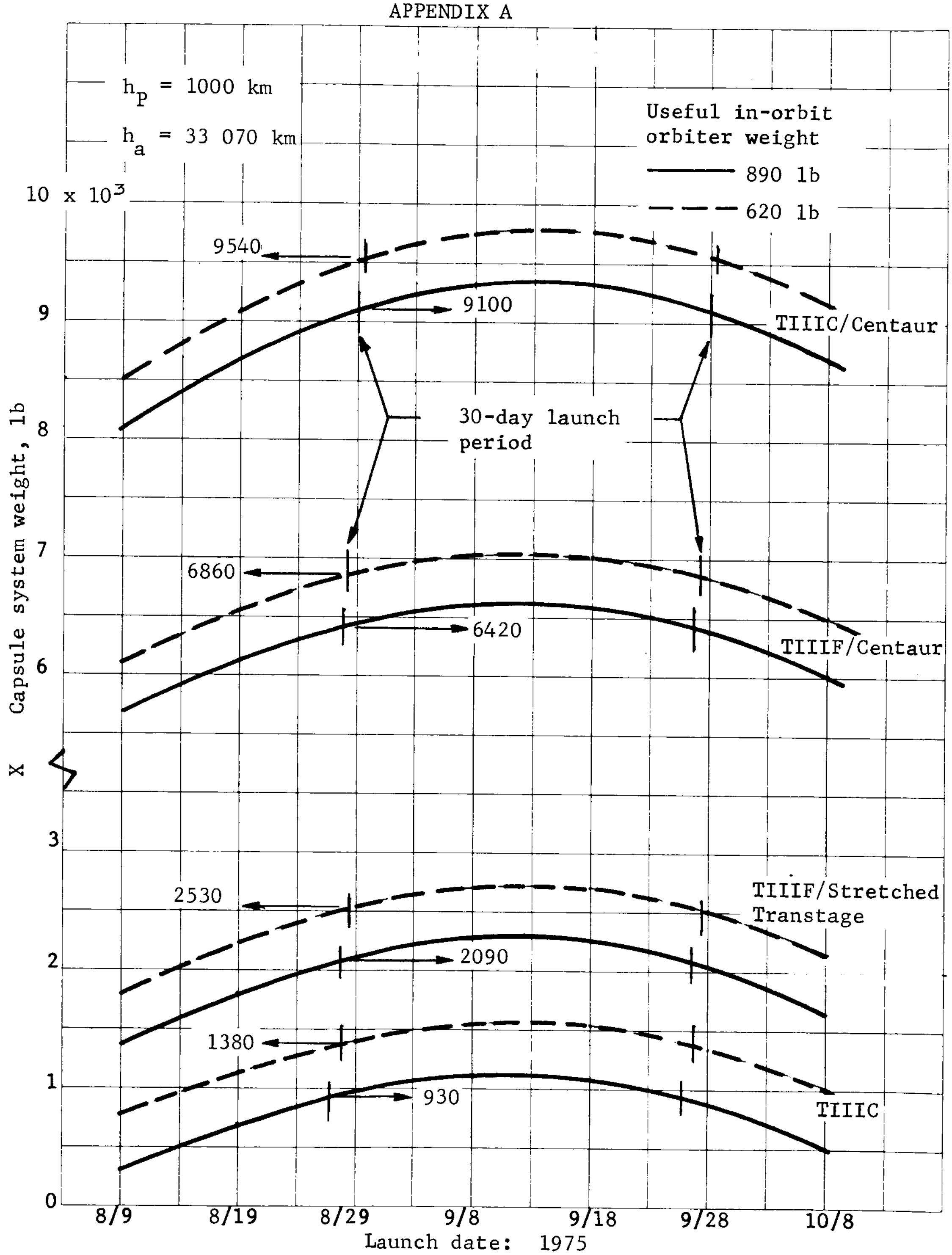

Figure A66.- Optimum Direct Entry System Weight, Optimum Orbiter Propulsion, Mars 1975, Type II

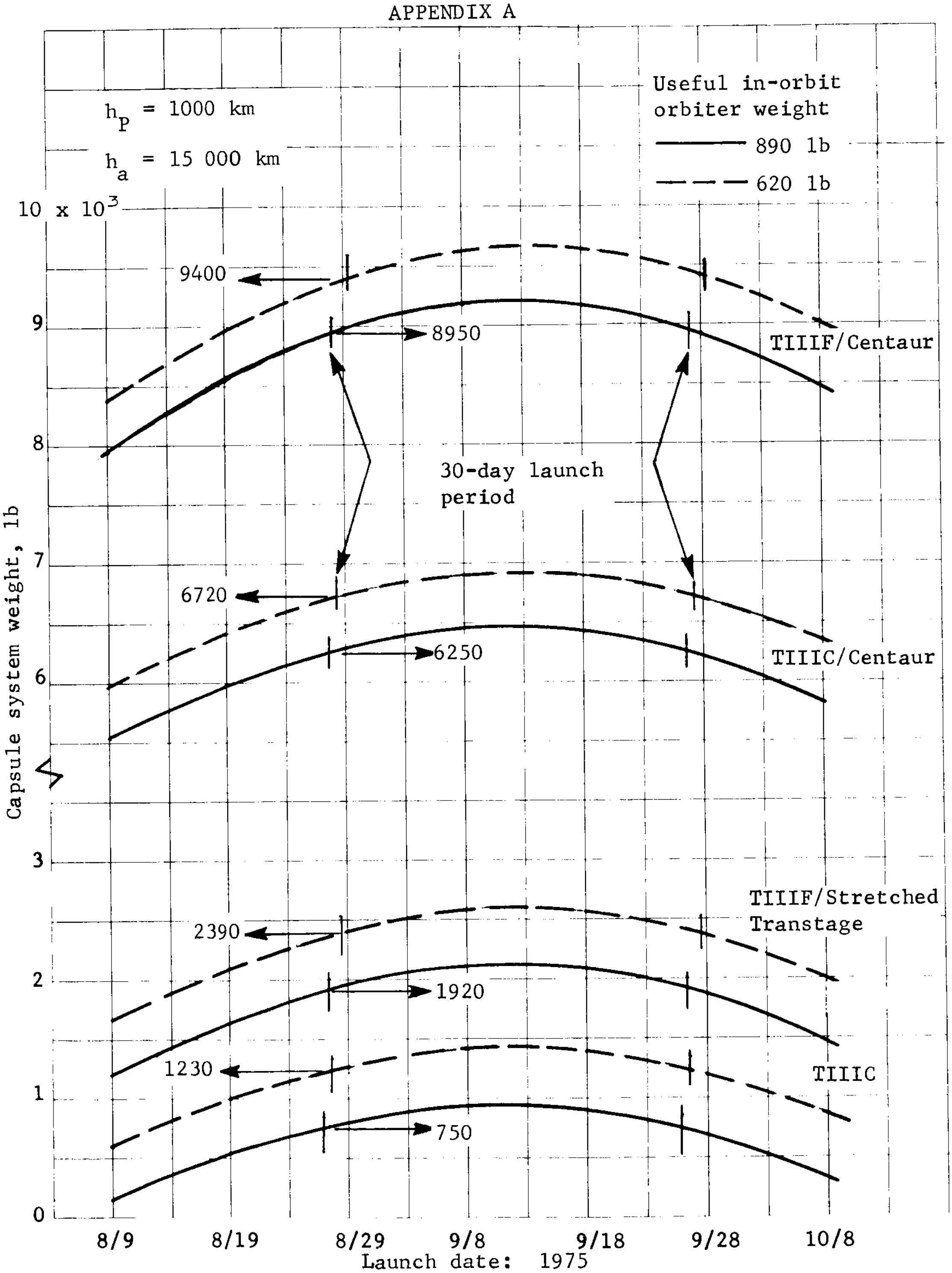

Figure A67.- Optimum Direct Entry System Weight, Optimum Orbiter Propulsion, Mars 1975, Type II

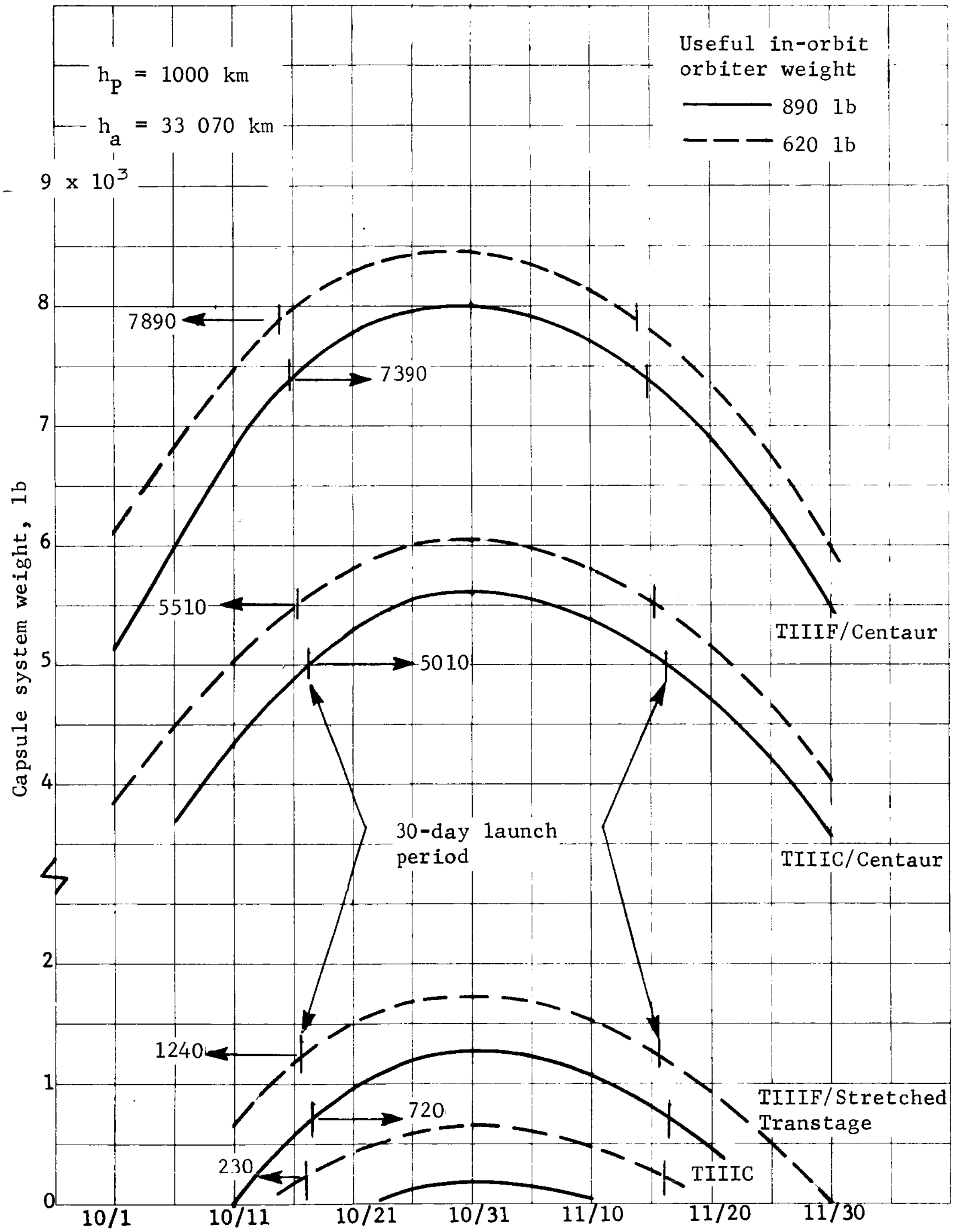

Figure A68.- Optimum Direct Entry System Weight, Optimum Orbiter Propulsion, Mars 1977, Type I

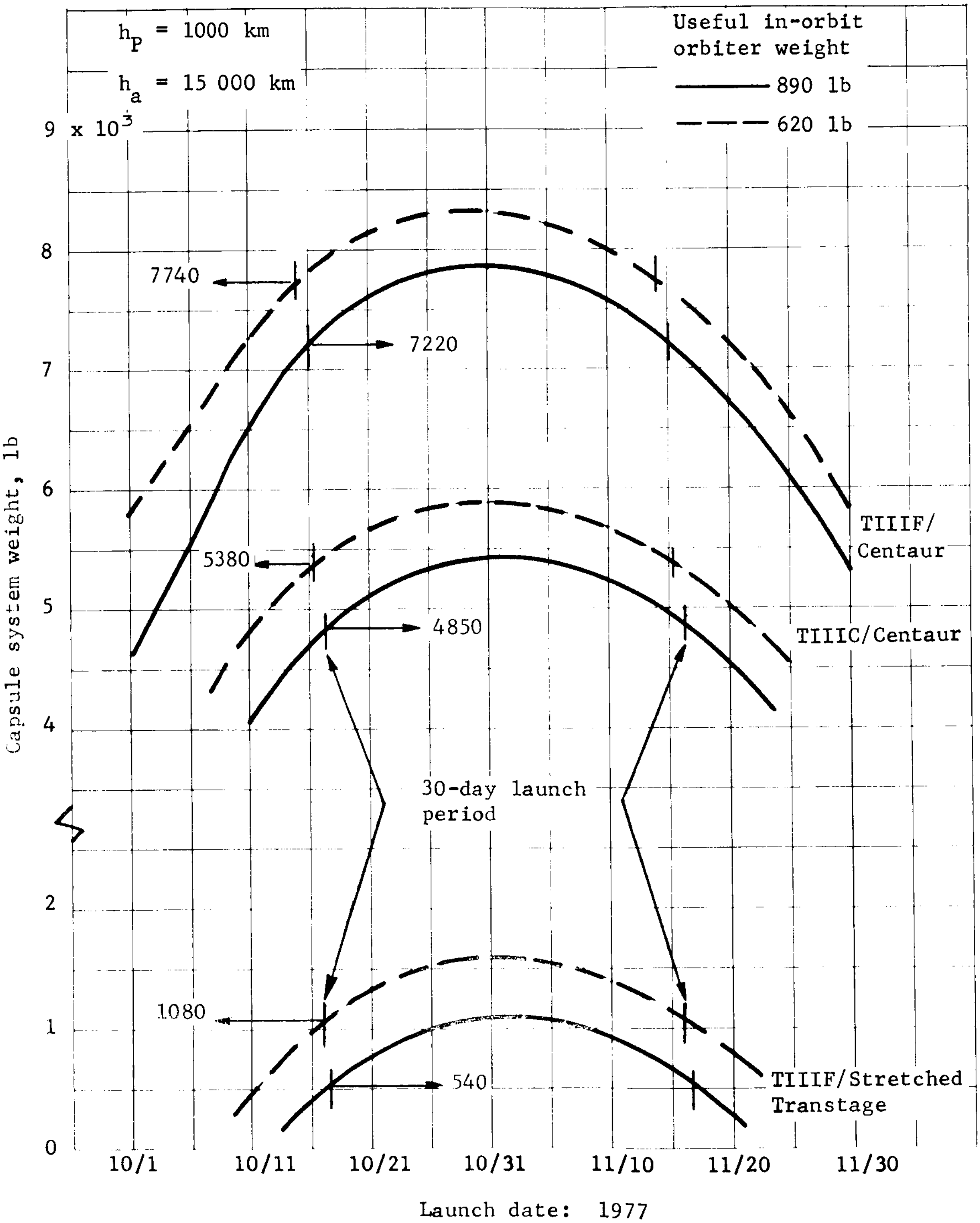

Figure A69.- Optimum Direct Entry System Weight, Optimum Orbiter Propulsion, Mars 1977, Type I

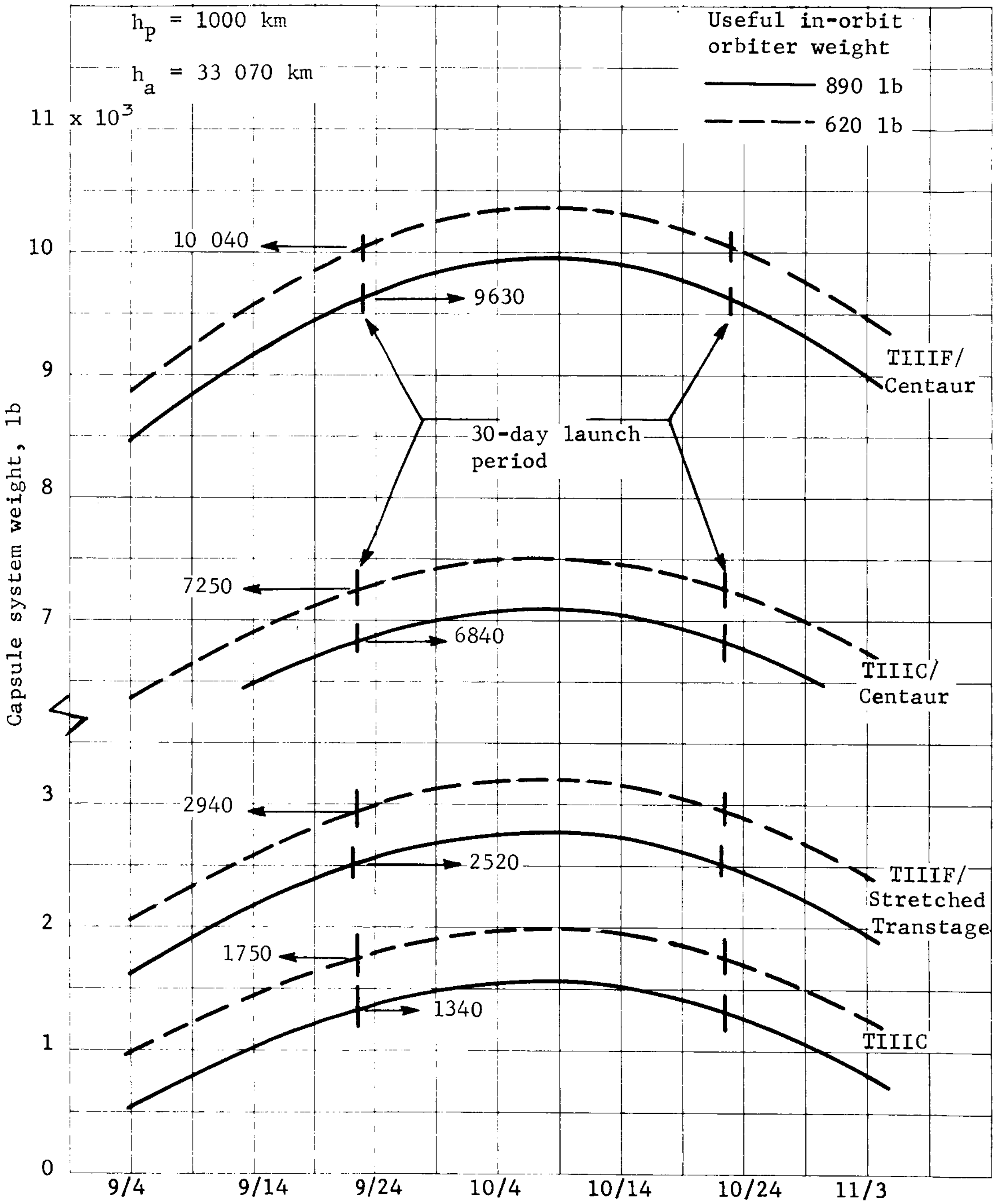

Launch date: 1977

Figure A70.- Optimum Direct Entry System Weight, Optimum Orbiter Propulsion, Mars 1977, Type II

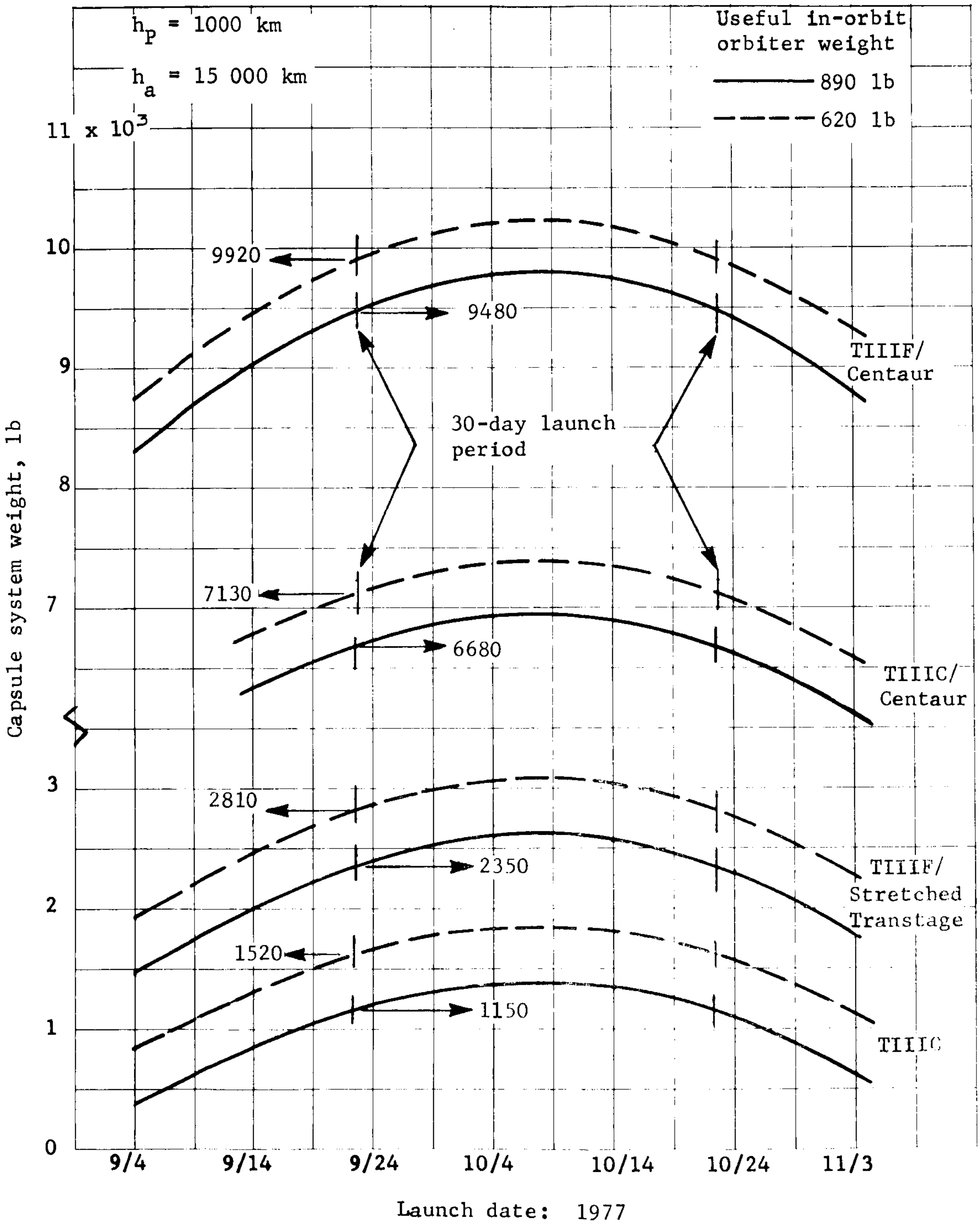

Figure A71.- Optimum Direct Entry System Weight, Optimum Orbiter Propulsion, Mars 1977, Type II

TABLE A6.- OPTIMUM DIRECT ENTRY CAPSULE SYSTEM WEIGHT, OPTIMUM ORBITER PROPULSION, 30-DAY LAUNCH PERIOD

Mission opportunity	Transfer type	Orbit eccentricity	Capsule system weight, lb[a]			
			TIIIC	TIIIF/ Stretched Transtage	TIIIC/ Centaur	TIIIF/ Centaur
1973	I	0.785	710/1150	1820/2270	6120/6590	8830/9250
		0.614	500/1000	1640/2130	5980/6460	8610/9070
	II	0.785	390/860	1500/1990	5850/6300	8520/9020
		0.614	210/730	1320/1840	5670/6160	8270/8790
1975	I	0.785	----/50	620/1100	4910/5380	7190/7680
		0.614	----/----	420/970	4720/5230	7000/7530
	II	0.785	930/1380	2090/2530	6420/6860	9100/9540
		0.614	750/1230	1920/2390	6250/6720	8950/9400
1977	I	0.785	----/230	720/1240	5010/5510	7390/7890
		0.614	----/----	540/1080	4850/5380	7220/7740
	II	0.758	1340/1750	2520/2940	6840/7250	9630/10 040
		0.614	1150/1520	2350/2810	6680/7130	9480/9920

[a]890-lb orbiter/620-lb orbiter.

The difference in capsule system weights shown in table A6 for maximum and minimum orbiters is on the order of 400 lb. This is greater than the difference of 270 lb between the maximum and minimum orbiter useful weights. The additional improvement is due to the different propulsion system weights (propellant and inert) required for inserting the two different sized orbiters into orbit.

As in the previous subsection, we are faced with a real-world spacecraft/orbiter in which the propellant quantity and propulsion system are sized for the maximum requirement for a given opportunity. Tables A7 and A8 summarize the direct entry results for the fixed orbiter. These data were obtained by finding the minimum capsule system weight for several 30-day periods. The weights shown in table A7 correspond to the highest minimum for the opportunity. The first date of the corresponding 30-day launch period is shown in table A8. Capsule system weights for the fixed orbiter range from 270 to 10 000 lb.

TABLE A7.- OPTIMUM DIRECT ENTRY CAPSULE SYSTEM WEIGHT, FIXED ORBITER PROPULSION, 30-DAY LAUNCH PERIOD

Mission opportunity	Transfer type	Orbit eccentricity	Capsule system weight, lb[a]			
			TIIIC	TIIIF/ Stretched Transtage	TIIIC/ Centaur	TIIIF/ Centaur
1973	I	0.785	450/940	1570/2060	5920/6390	8590/9060
		0.614	270/790	1390/1910	5740/6250	8340/8840
	II	0.785	125/660	1235/1765	5590/6110	8235/8775
		0.614	----/500	1050/1610	5410/5960	7985/8535
1975	I	0.785	----/----	----/450	4210/4770	6490/7080
		0.614	----/----	----/270	3880/4570	6250/6920
	II	0.785	750/1210	1870/2340	6220/6670	8870/9310
		0.614	560/1070	1690/2190	6040/6525	8690/9190
1977	I	0.785	----/----	80/630	4360/4920	6630/7180
		0.614	----/----	----/470	4170/4750	6420/7030
	II	0.785	1280/1700	2570/2910	6790/7220	9580/10 000
		0.614	1100/1575	2300/2770	6640/7090	9420/9910

[a] 890-lb orbiter/620-lb orbiter.

TABLE A8.- FIRST LAUNCH DATE, DIRECT ENTRY CAPSULE SYSTEM, FIXED ORBITER PROPULSION, 30-DAY LAUNCH PERIOD

Mission opportunity	Transfer type	Orbit eccentricity	First launch date			
			TIIIC	TIIIF/ Stretched Transtage	TIIIC/ Centaur	TIIIF/ Centaur
1973	I	0.785	7/12/73	7/11/73	7/11/73	7/10/73
		0.614	7/12/73	7/11/73	7/11/73	7/10/73
	II	0.785	8/6/73	8/6/73	8/6/73	8/6/73
		0.614	8/6/73	8/6/73	8/6/73	8/6/73
1975	I	0.785	----	9/2/75	9/2/75	9/3/75
		0.614	----	9/3/75	9/2/75	9/2/75
	II	0.785	8/30/75	8/30/75	8/30/75	8/30/75
		0.614	8/30/75	8/30/75	8/30/75	8/31/75
1977	I	0.785	----	10/20/77	10/19/77	10/18/77
		0.614	----	10/20/77	10/19/77	10/18/77
	II	0.785	9/25/77	9/25/77	9/25/77	9/25/77
		0.614	9/25/77	9/25/77	9/25/77	9/25/77

APPENDIX A

Conversion of Capsule System Weight to Entry Weight

The capsule system weight includes the entry system plus the spacecraft adapter, sterilization canister, the capsule propulsion system, and the terminal guidance system, where applicable. To relate capsule system weight to entry weight, these component weights must be identified. The entry weight (W_E) is related to capsule system weight $(W_{C/S})$ by

$$W_E = W_{C/S} - W_A - W_C - W_{EL} - W_{PS} - W_S - W_{TG}$$

where

W_A is capsule to orbiter adapter weight

W_C is sterilization canister weight

W_{EL} is adapter electrical system weight

W_{PS} is total deorbit propulsion system weight

W_S is propulsion module structural weight

W_{TG} is capsule terminal guidance system weight (where applicable).

In general, W_A, W_C, W_{EL}, W_{TG} are reference aeroshell diameter $(D_{A/S})$ dependent; W_{PS}, W_S are functions of the velocity increment (deflection or deorbit for direct and orbital modes, respectively) and propulsion system characteristics. The weights are determined below according to this grouping; the presentation, however, is made on the basis of the system mode under consideration. The system modes are as follows:

1) Direct entry, no terminal guidance,

   Deflection ΔV = 17.5 mps, 175 mps

   Monopropellant propulsion system;

2) Orbital entry (no terminal guidance)

   Deorbit ΔV = 150 mps, 300 mps

   Monopropellant and solid propulsion systems.

APPENDIX A

The velocity increments are determined by the targeting analysis, discussed in Section 2 of this appendix. The results are presented in figures A72 thru A74 for the above system modes and various aeroshell diameters. Design data using refined velocity increments are shown in figure A75. Diameter-dependent weights are as follows:

1) Adapter,

$W_A = 18, \; D_{A/S} \leq 15$ ft

$W_A = 18 + 12\,(D_{A/S} - 15), \; D_{A/S} > 15$ ft;

2) Sterilization canister,

$W_C = 2.43\,(D_{A/S})^{1.76}, \; D_{A/S} \leq 15$ ft

$W_C = 5.22\,(D_{A/S})^{1.51}, \; D_{A/S} > 15$ ft;

3) Adapter electrical,

$W_{EL} = 24$ lb (constant);

4) Terminal guidance,

$W_{TG} = 36 + 1.1\,D_{A/S}$.

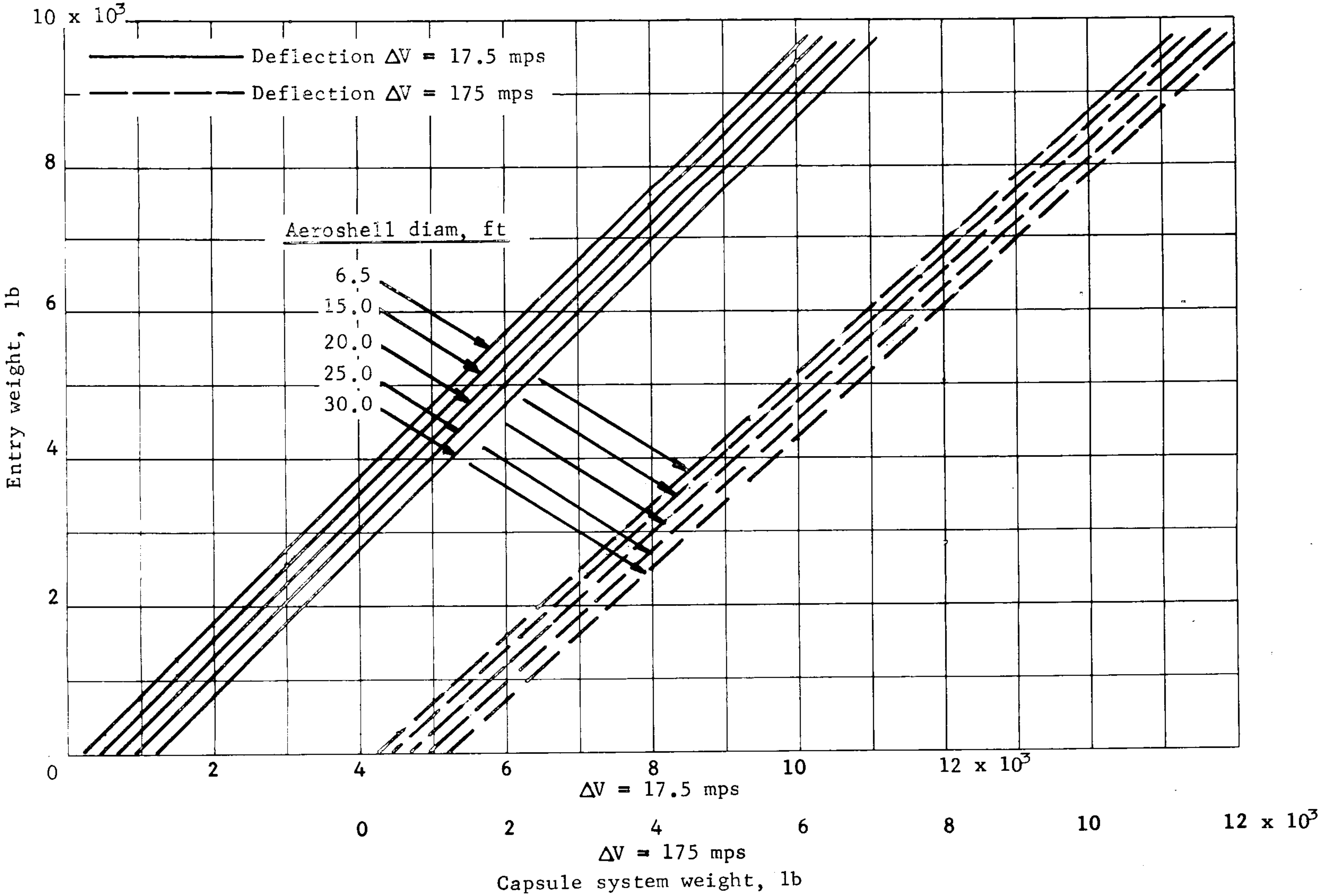

Figure A72.- Entry Weight Versus Capsule System Weight, Direct Mode, No Terminal Guidance, Monopropellant Propulsion System

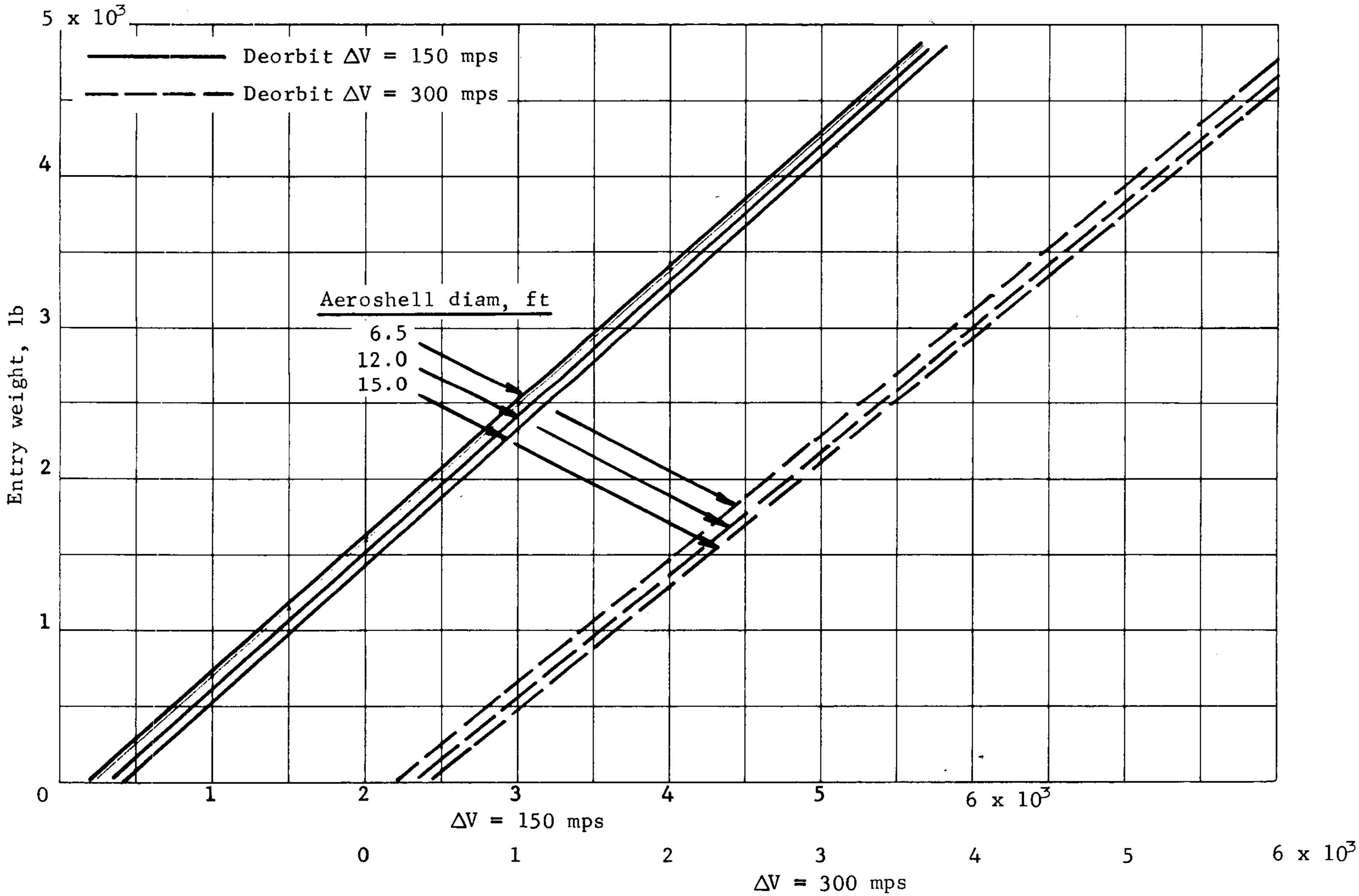

Figure A73.- Entry Weight Versus Capsule System Weight, Orbit Mode, No Terminal Guidance, Monopropellant Propulsion System

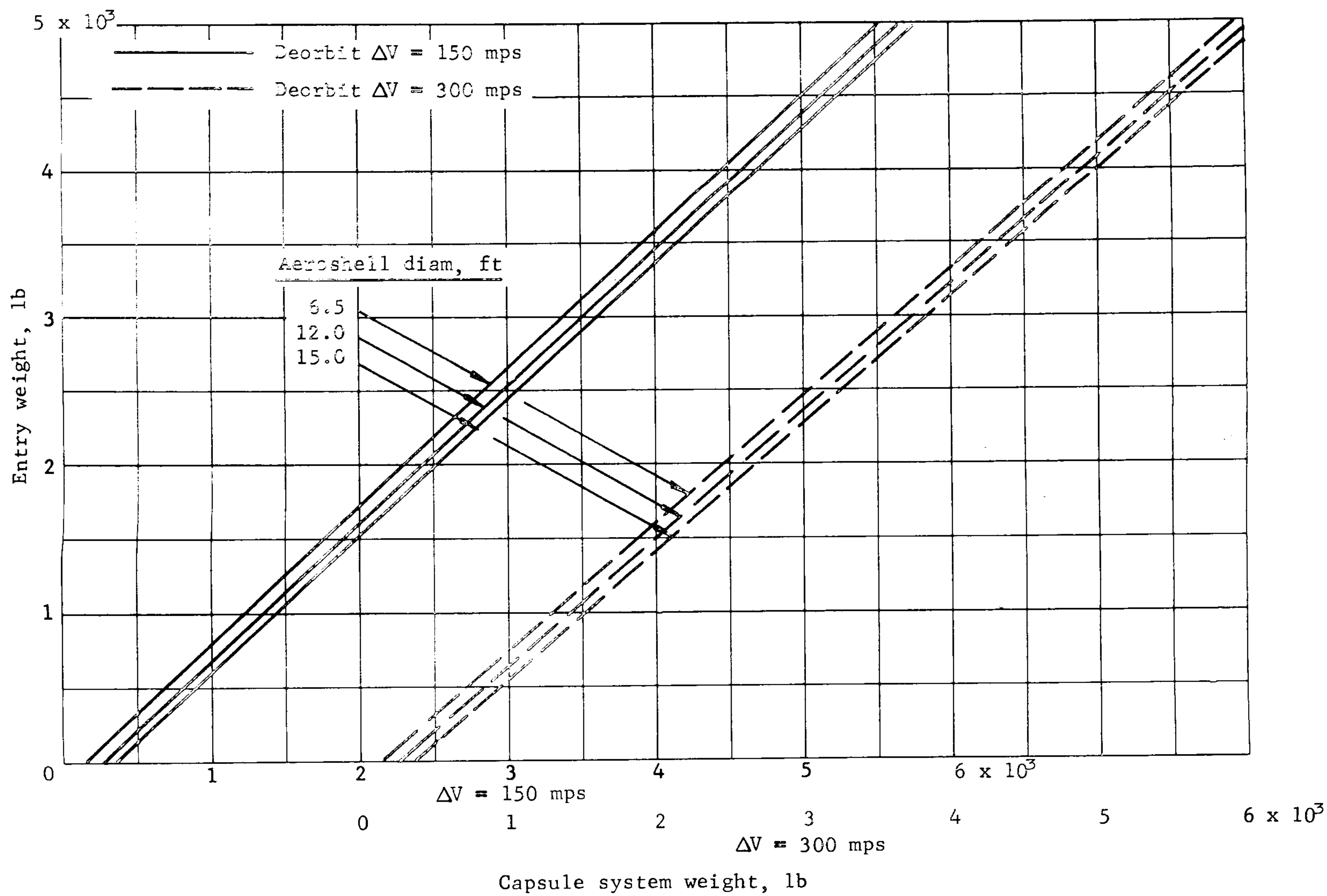

Figure A74.- Entry Weight Versus Capsule System Weight, Orbit Mode, No Terminal Guidance, Solid Propulsion System

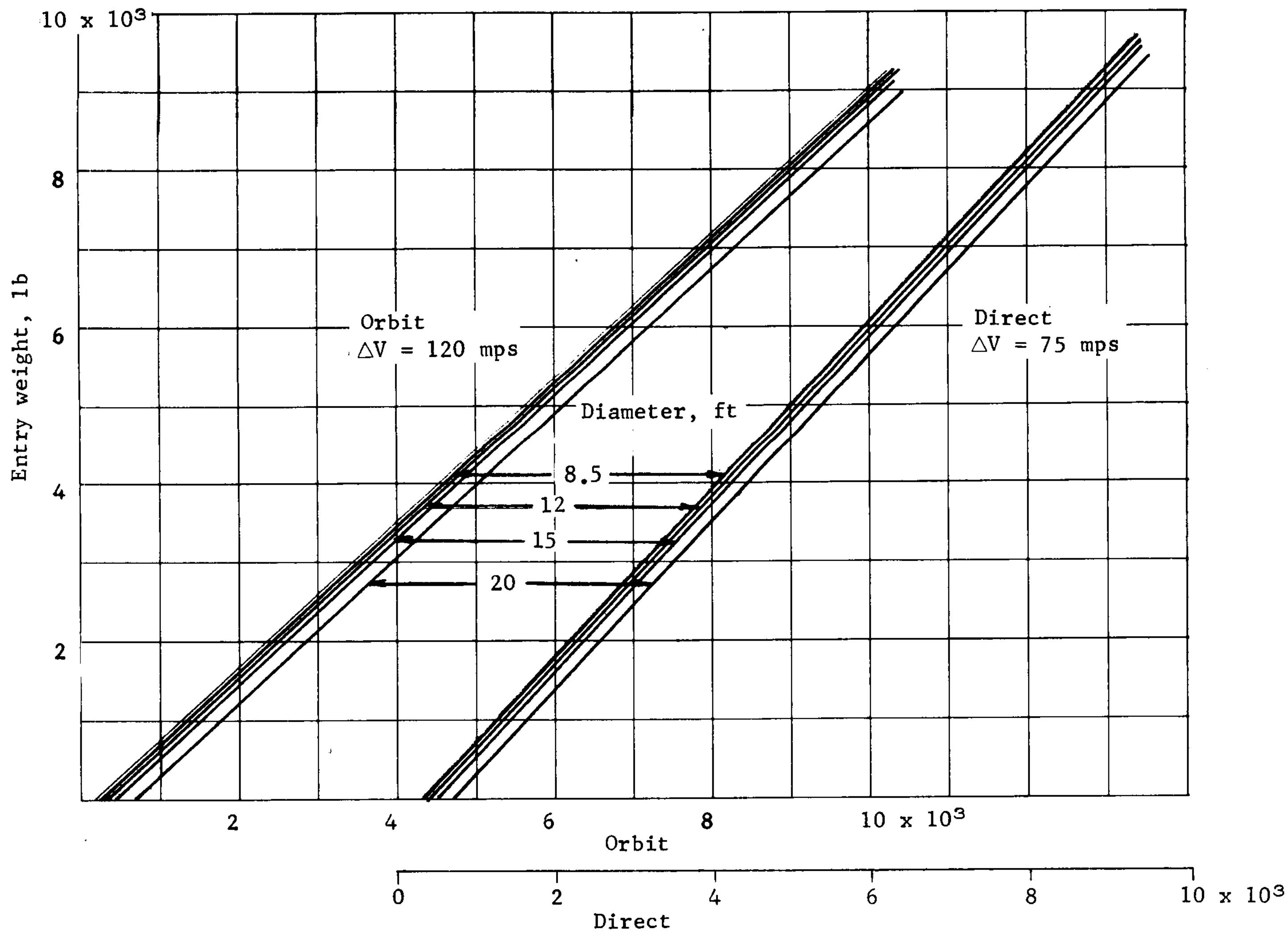

Figure A75.- Entry Weight Versus Capsule System Weight, Point Design Cases, Monopropellant Propulsion System

APPENDIX A

Velocity-dependent weights are:

1) Propulsion system,

$$W_{PS} = f \text{ (total impulse) as defined in figure A76 for the propulsion systems shown above}$$

$$\text{Total impulse} = W_P \left(I_{sp}\right)$$

where

W_P = propellant weight

I_{sp} = specific impulse

$$W_P = W_O\left(1 - e^{-\Delta V/C_J}\right)$$

where

$W_O = W_{C/S} - W_A - W_C - W_{EL}$

ΔV = velocity increment required (deflection or deorbit)

$C_J = I_{sp} \times 32.174$ ft/sec^2;

2) Propulsion module structure,

$$W_S = 4 + 0.16 \left(W_O + W_{PS}\right)^{0.7}.$$

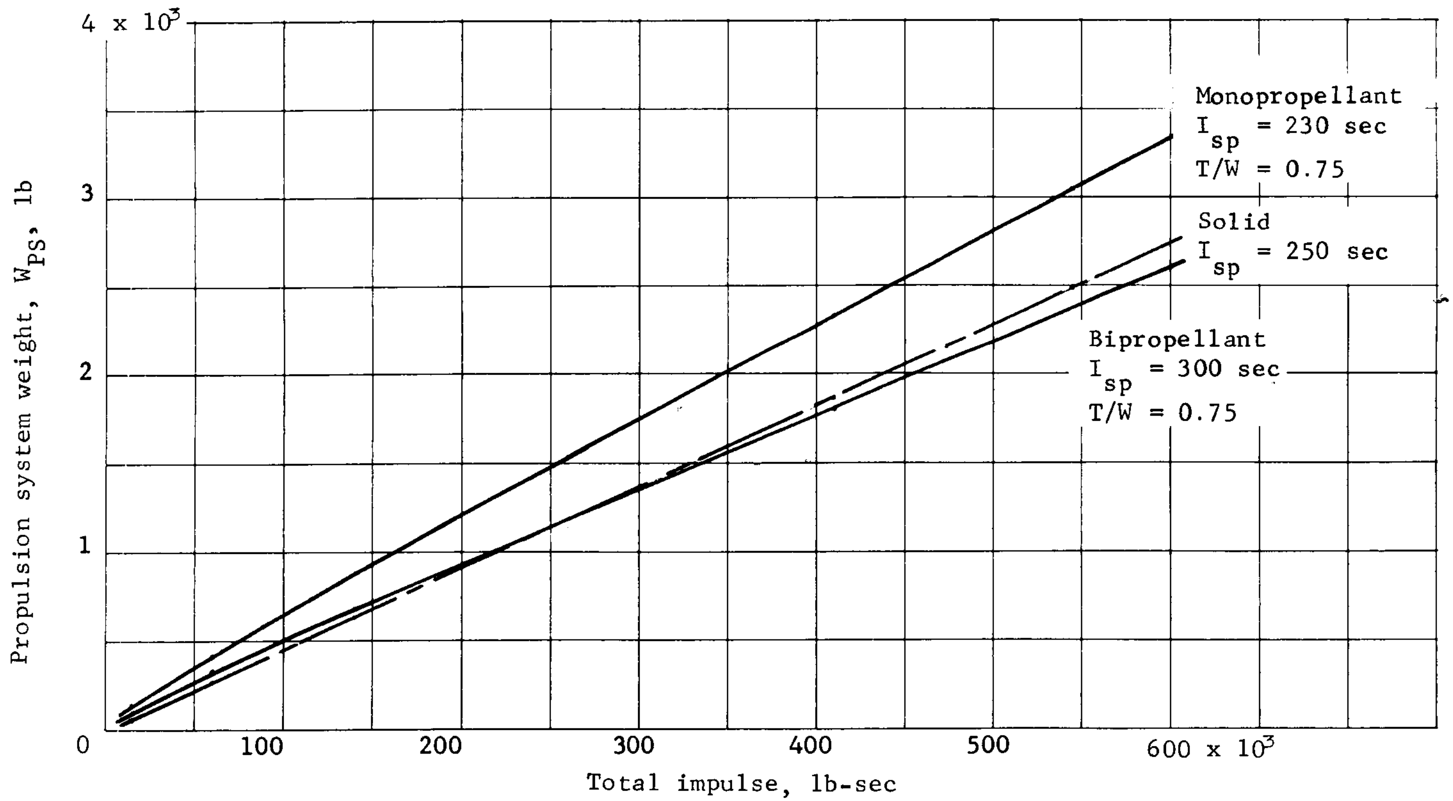

Figure A76.- Capsule System Propulsion Characteristics

APPENDIX A

This page intentionally left blank.

APPENDIX A

2. EJECTION/DEORBIT MANEUVER STRATEGY AND TARGETING

The ejection/deorbit maneuver strategy is independent of launch period selection. The analysis provides the possible locations of the landing site with respect to orbit periapsis for both the direct and orbit modes. The maneuver strategies consider tradeoffs between propulsive requirements, telecommunications requirements, and the entry dispersions due to navigation uncertainty and maneuver execution errors. The targeting analysis considers the means for obtaining longitude and latitude control of the landing site as well as its location with respect to the evening terminator. The output of the above analysis is a comparison of the range of possible landing sites on Mars for the direct and orbit modes during the 1973-I launch opportunity. The analysis is developed in the following order:

1) Ejection requirements, direct mode;
2) Relay communication link constraints, direct mode;
3) Deorbit requirements, orbit mode;
4) Relay communication link constraints, orbit mode;
5) Landing site flexibility, direct mode;
6) Landing site flexibility, orbit mode.

Ejection Requirements, Direct Mode

The impulse required for capsule ejection, ΔV_{EJ}, is dependent on the following parameters with the ranges studied shown: periapsis altitude $(h_p = 1000, 2000\ \text{km})$; capsule ejection distance $(50\,000 < R_{EJ} < 500\,000\ \text{km})$; hyperbolic excess velocity $(2.4 < V_{HE} < 3.6\ \text{km/sec})$; entry flight path angle $(-20° < \gamma_E < -38°)$; and ejection angle $(-10° < \tau_{EJ} < -90°)$.

The capsule coast time, time from ejection to entry, is shown as a function of R_{EJ} and V_{HE} in figure A77. The coast time is important in the consideration of power required for the ACS and varies from 3 to 55 hr over the R_{EJ} and V_{HE} range considered. The entry velocity is dependent on approach hyperbolic excess velocity, V_{HE}, and is shown in figure A78.

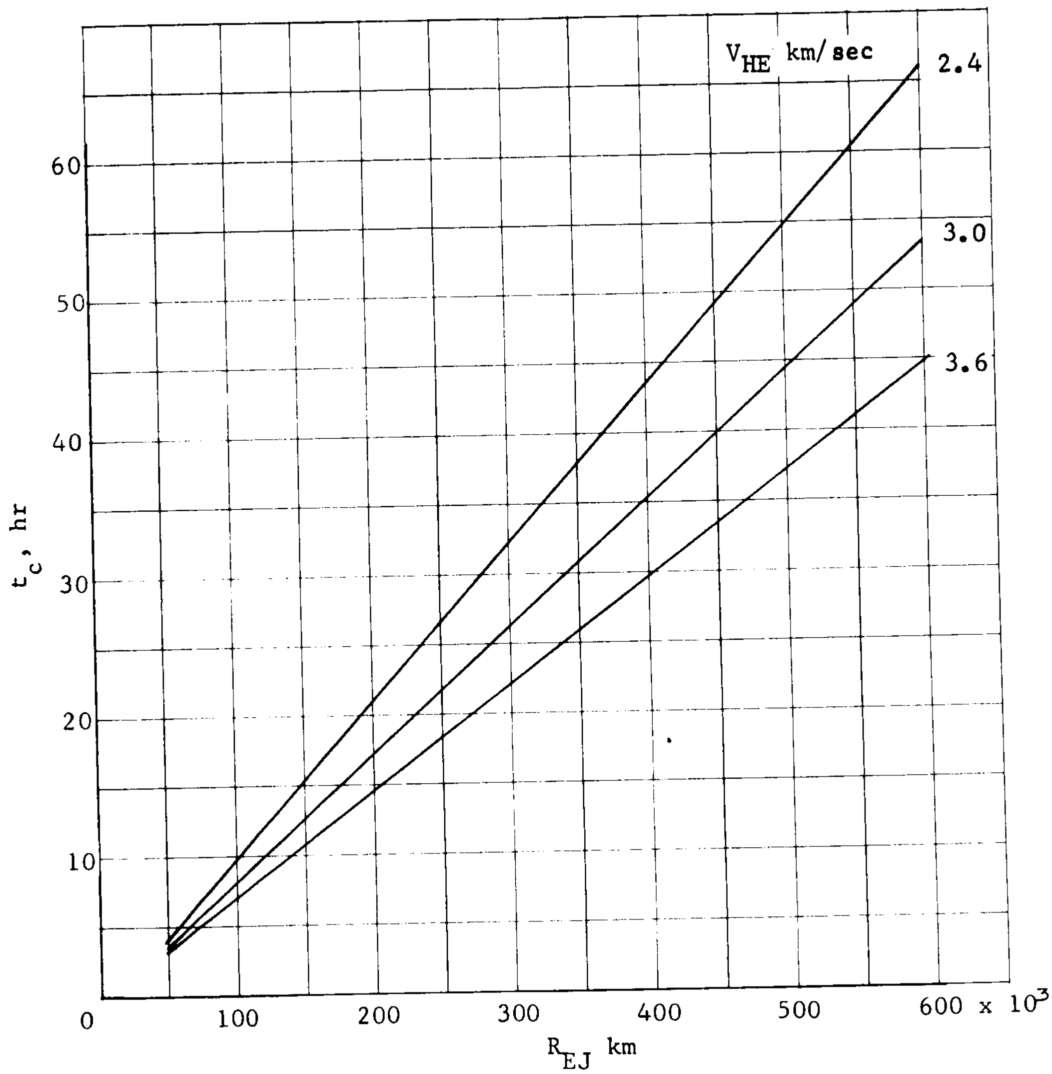

Figure A77.- Coast Time Dependence on Ejection Distance

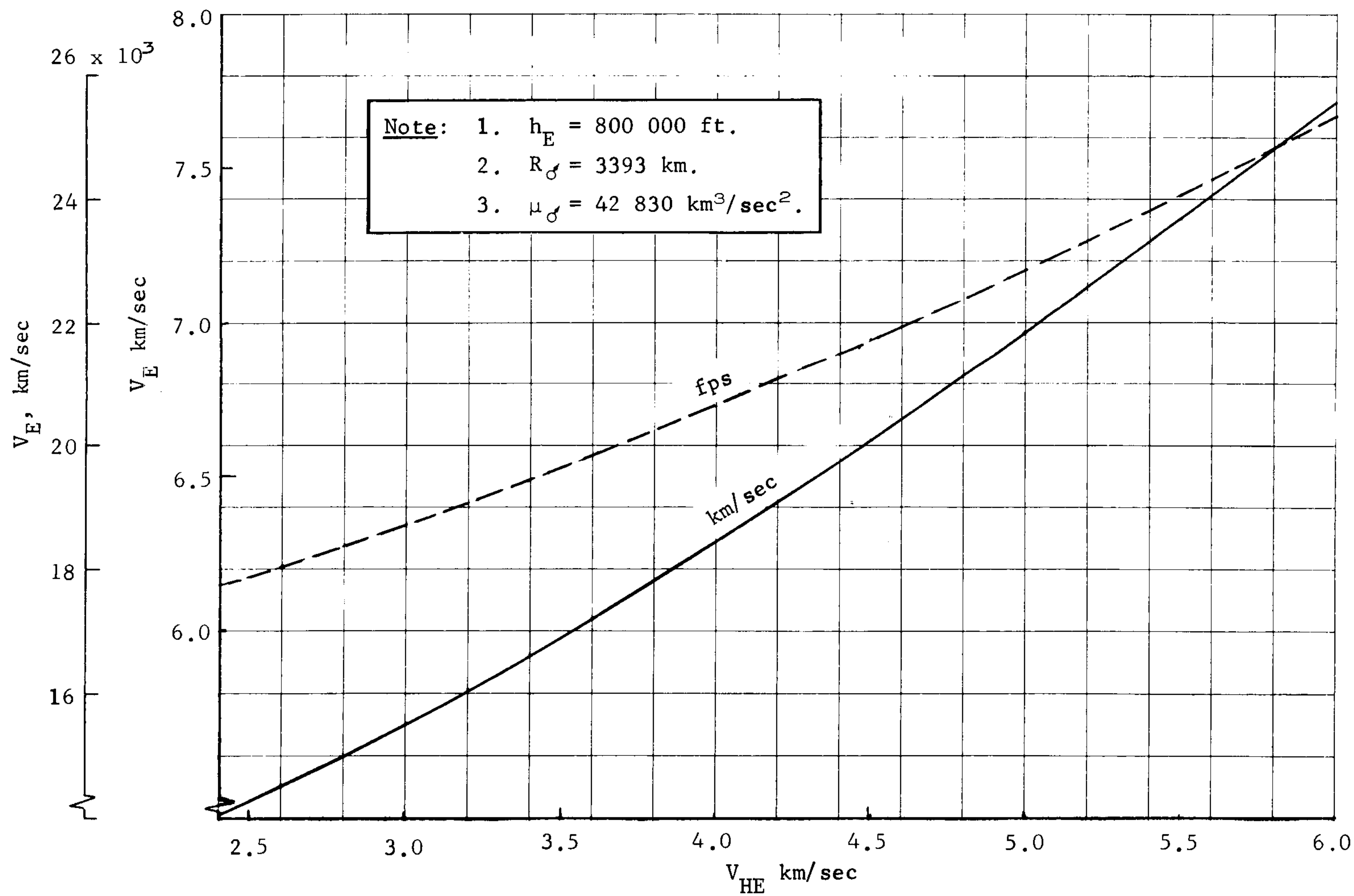

Figure A78.- Mars Entry Velocity versus V_{HE}

APPENDIX A

For the V_{HE} range considered, the entry velocity varies between 17 700 fps and 19 800 fps. The angle between the $\vec{V}_{HE}$ and periapsis, τ', is a function of V_{HE} and periapsis altitude, h_p, and is shown in figure A79. For an h_p of 1000 km, τ' varies between 52.5° and 63.6° over a V_{HE} range from 2.5 to 3.5 km/sec. The atmospheric entry point $(h_E = 800\ 000$ ft$)$ is located with respect to the approach trajectory periapsis by the angle β, as shown in figure A80. It is a function of γ_E and V_{HE} and is essentially invariant with the ejection maneuver. The variation in β over the range of V_{HE} and γ_E considered is 24.5 to 53°. A 1° change in γ_E changes β by about 1.4°. The β variation is illustrated for an h_p of 1000 km and an R_{EJ} of 50 000 km. It is a function of R_{EJ} and increases slightly, less than a few degrees, with larger capsule ejection distances. Higher h_p decreases β, but τ' is increased by nearly the same amount so that the entry location with respect to the $\vec{V}_{HE}$ is invariant with h_p. Appendix B shows the large sensitivity of landed equipment weight to γ_E and little flexibility in γ_E is available for targeting.

The ΔV_{EJ} is shown in figure A81 for an h_p of 1000 km, R_{EJ} of 50 000 km and a γ_E of -20°. The independent variable used throughout is orbiter lead angle, λ. This is the central angle measured at Mars between the capsule and orbiter at the time of entry. A negative λ corresponds to the orbiter lagging the capsule. The lead angle replaces the more conventional lead time since it is extremely useful in analyzing the relay link performance during entry as discussed below. It will be shown that λ should be kept roughly in the -5 to -20° range to satisfy communication constraints. To point out the variation of ΔV_{EJ} with V_{HE}, R_{EJ}, γ_E, and h_p, a λ of -17.5° will be used. The ΔV_{EJ} increases with increasing V_{HE} as shown in figure A81, while the τ_{EJ} decreases. The ejection angle is shown to be important in the error analysis of maneuver errors discussed later in section 3. For a V_{HE} of 3.0 km/sec the ΔV_{EJ} is 100 m/sec. The effect of larger R_{EJ} is shown in figures A82 thru A84.

The ΔV_{EJ} is seen to be nearly inversely proportional to R_{EJ}. The ΔV_{EJ} at 500 000 km has decreased to 9 m/sec. The ejection distance is also important in the analysis of possible entry corridors and is discussed later in this section. The effect of steeper γ_E is shown in figures A85 thru A92 where γ_E of -30° and -40° are shown. For an ejection distance of 50 000 km the ΔV_{EJ} is 160 m/sec for a γ_E of -30° and 270 m/sec for a γ_E of -40°. The ΔV_{EJ} increases with h_p and a full set of data is shown for 2000 km in figures A93 thru A104. For a R_{EJ} of 50 000 km and a γ_E of -20°, the ΔV_{EJ} is 170 m/sec as compared to 100 m/sec for an h_p of 1000 km.

At this point it should be emphasized that the choice of nominal γ_E for a given landed equipment weight is selected on the basis of design aeroshell diameter and the predicted entry dispersions, not any of the ejection requirements discussed in this section.

Although spin stabilization is not used in any of the point designs the angle of attack at entry, α_E, is shown for the above parameters in figures A105 thru A128. It can be seen that small λ, which requires large τ_{EJ}, result in large negative α_E. The selection of orbiter lead angle, λ, is discussed in the following section.

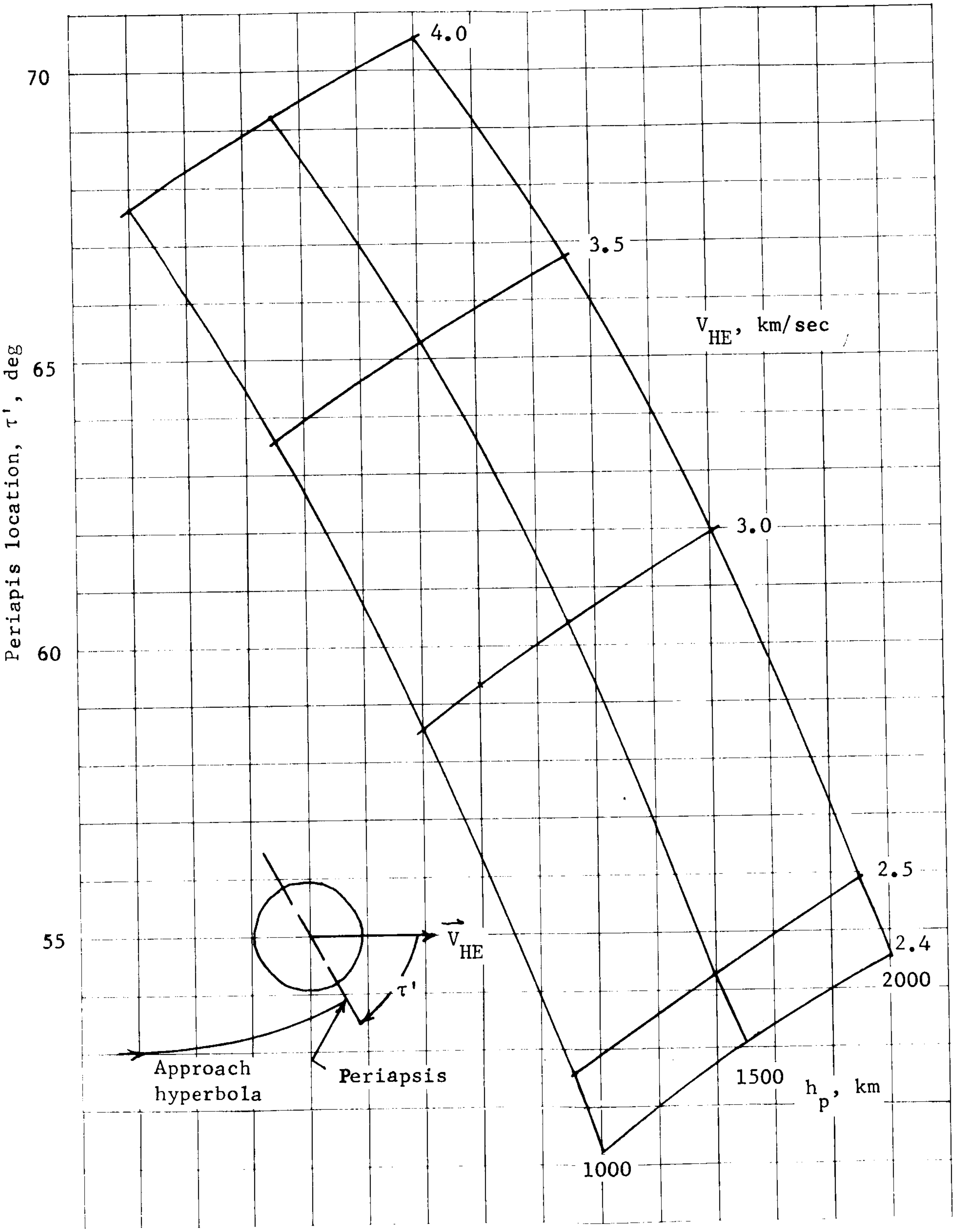

Figure A79.- Periapsis Location Sensitivity to $\vec{V}_{HE}$ and Periapsis Altitude

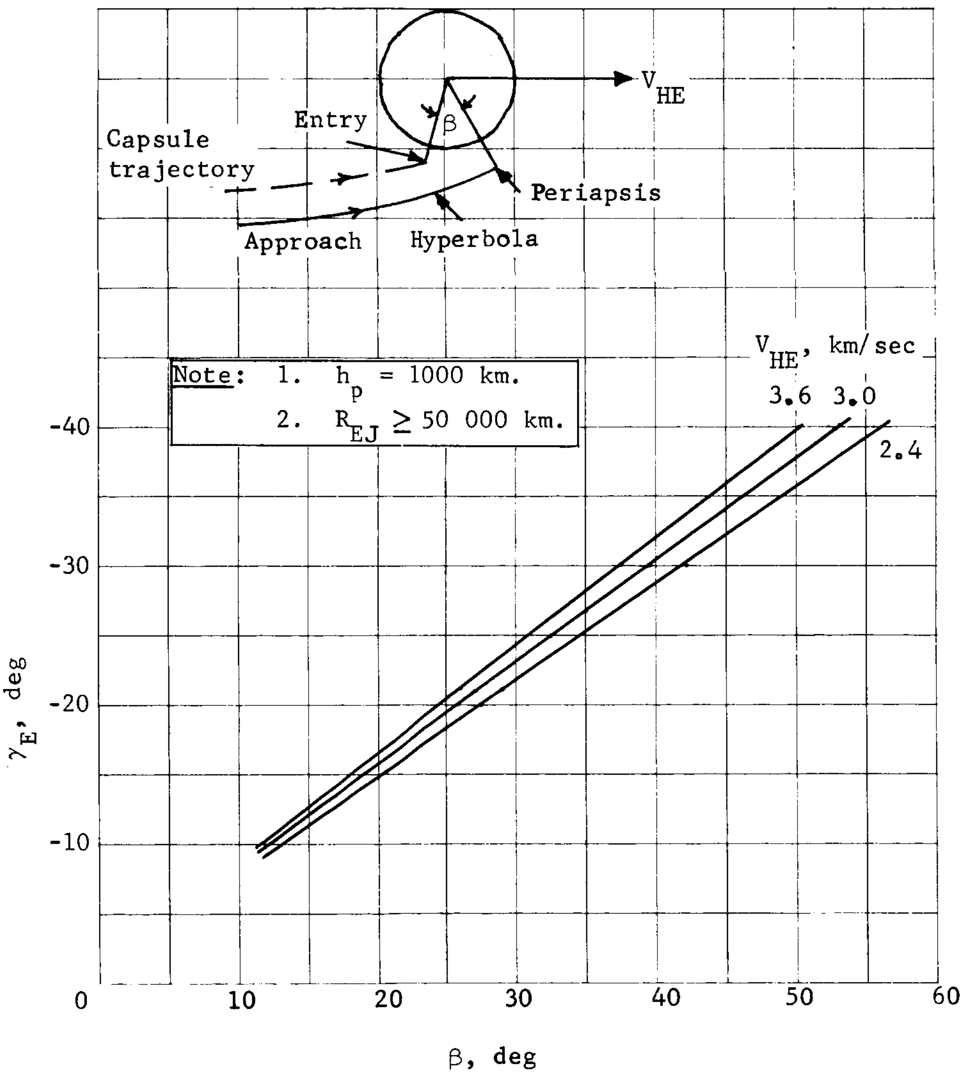

Figure A80.- Entry Location (Direct Mode)

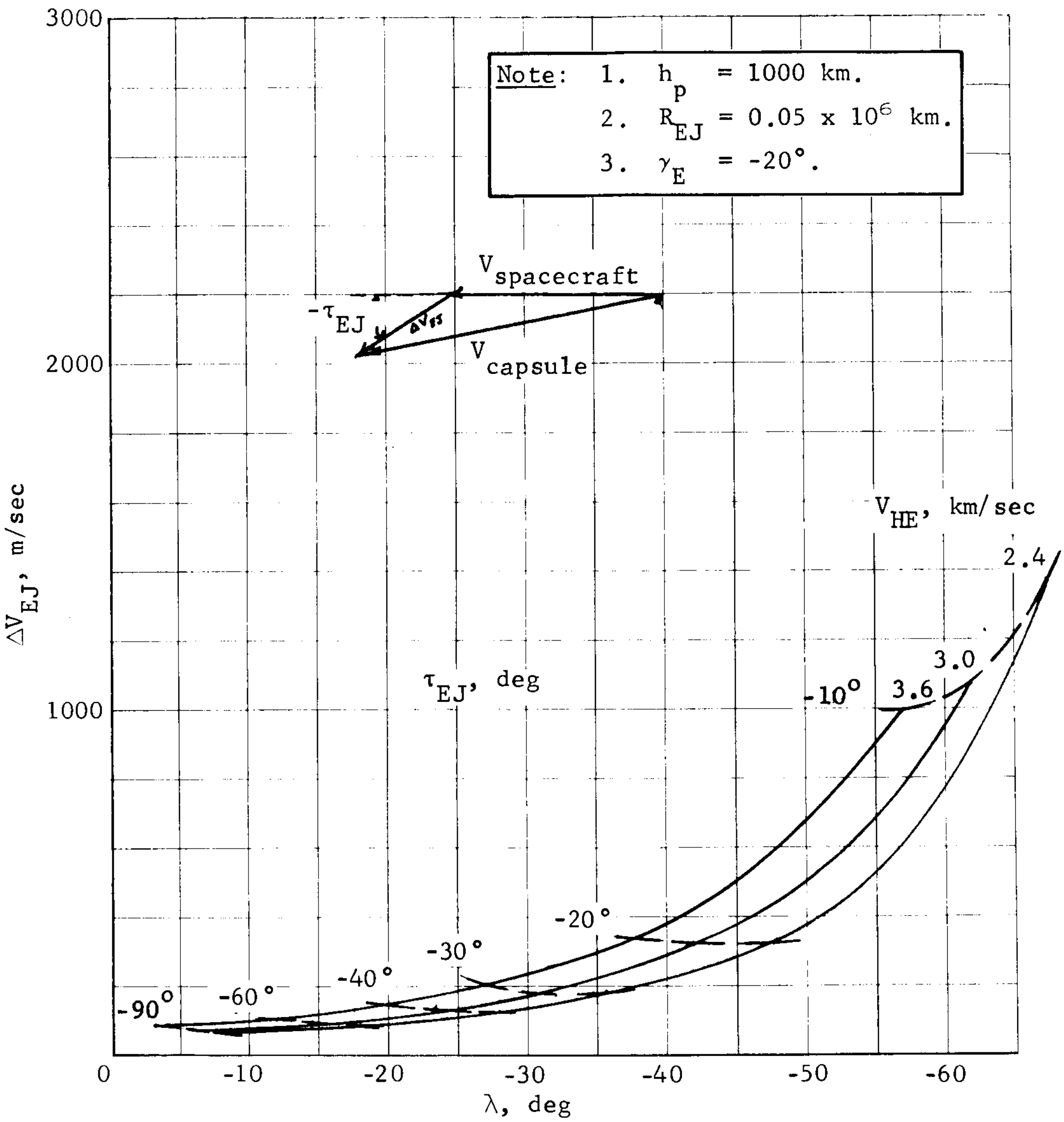

Figure A81.- Ejection ΔV Requirements

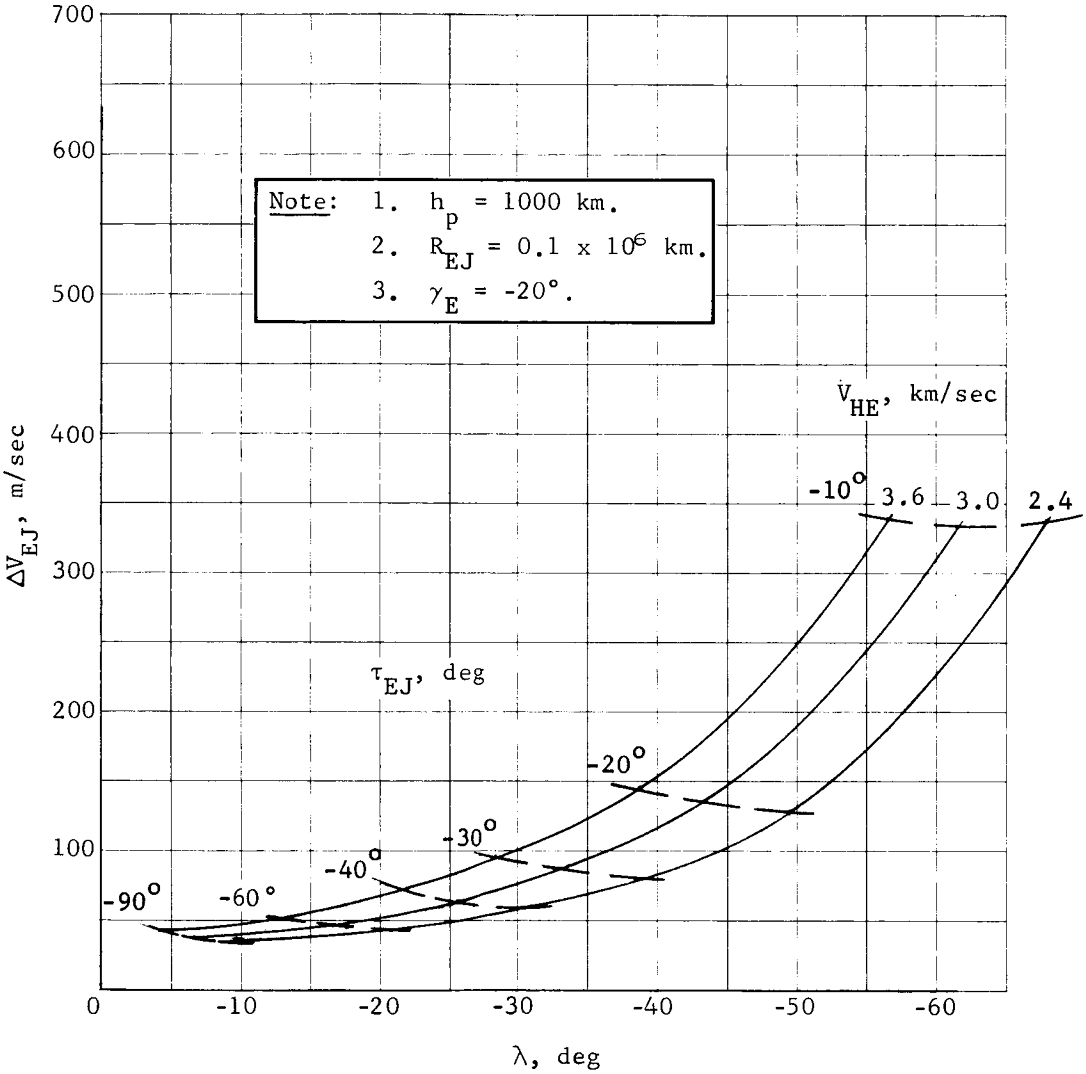

Figure A82.- Ejection ΔV Requirements

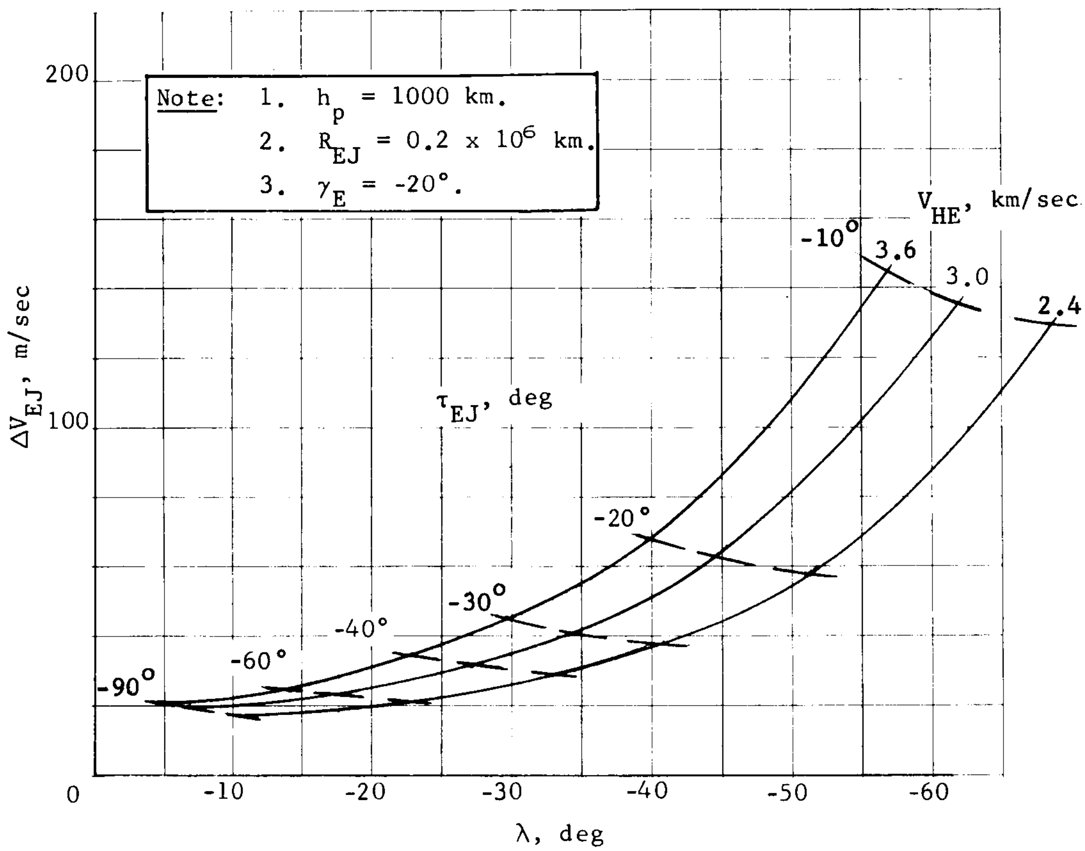

Figure A83.- Ejection ΔV Requirements

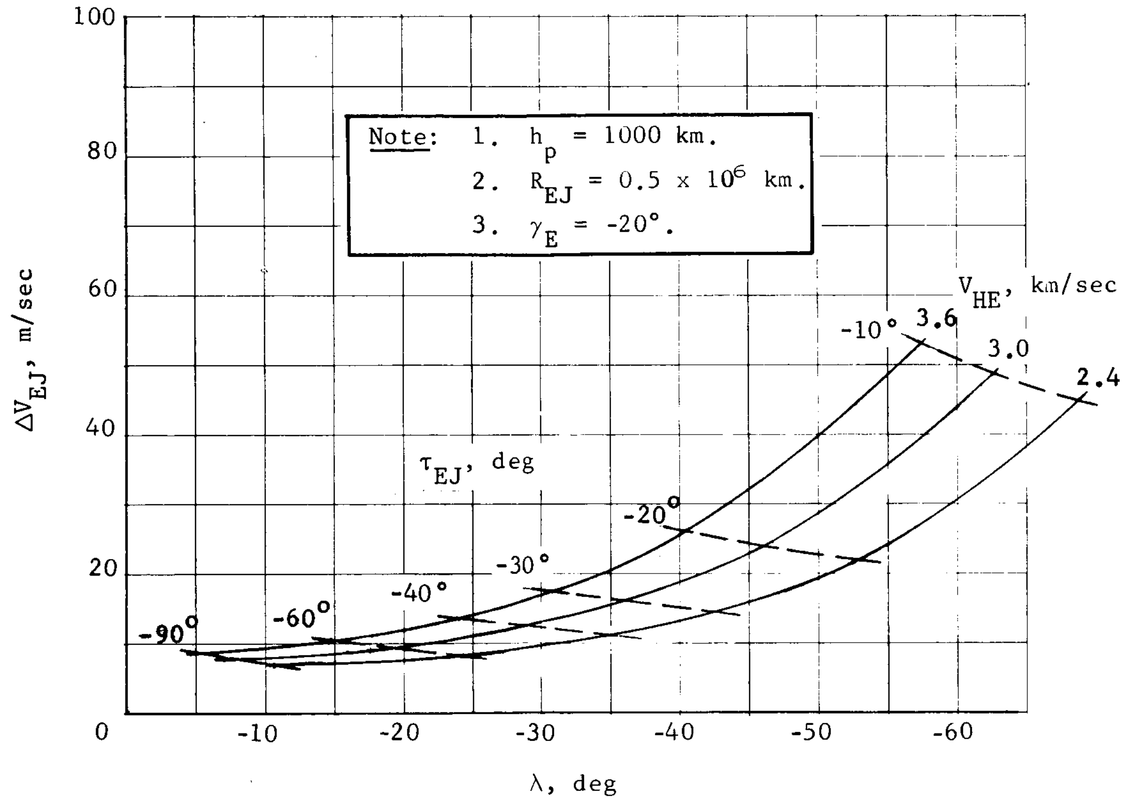

Figure A84.- Ejection ΔV Requirements

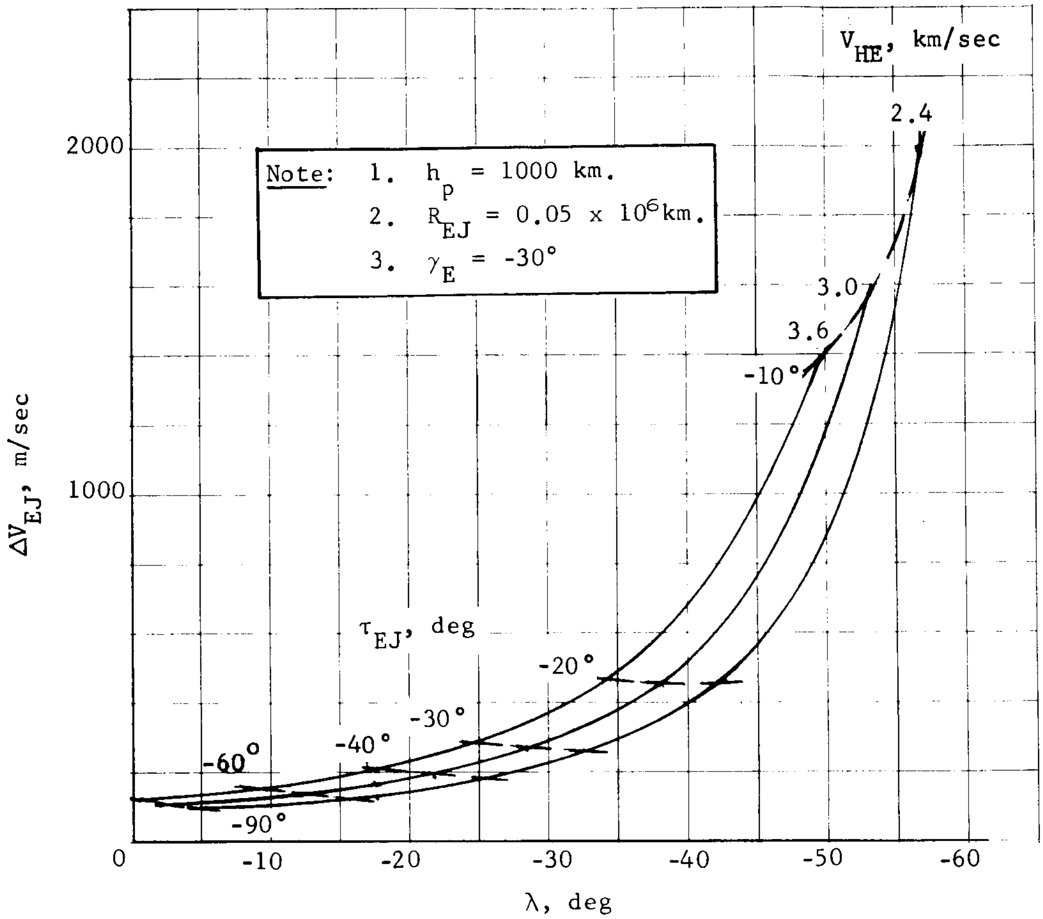

Figure A85.- Ejection ΔV Requirements

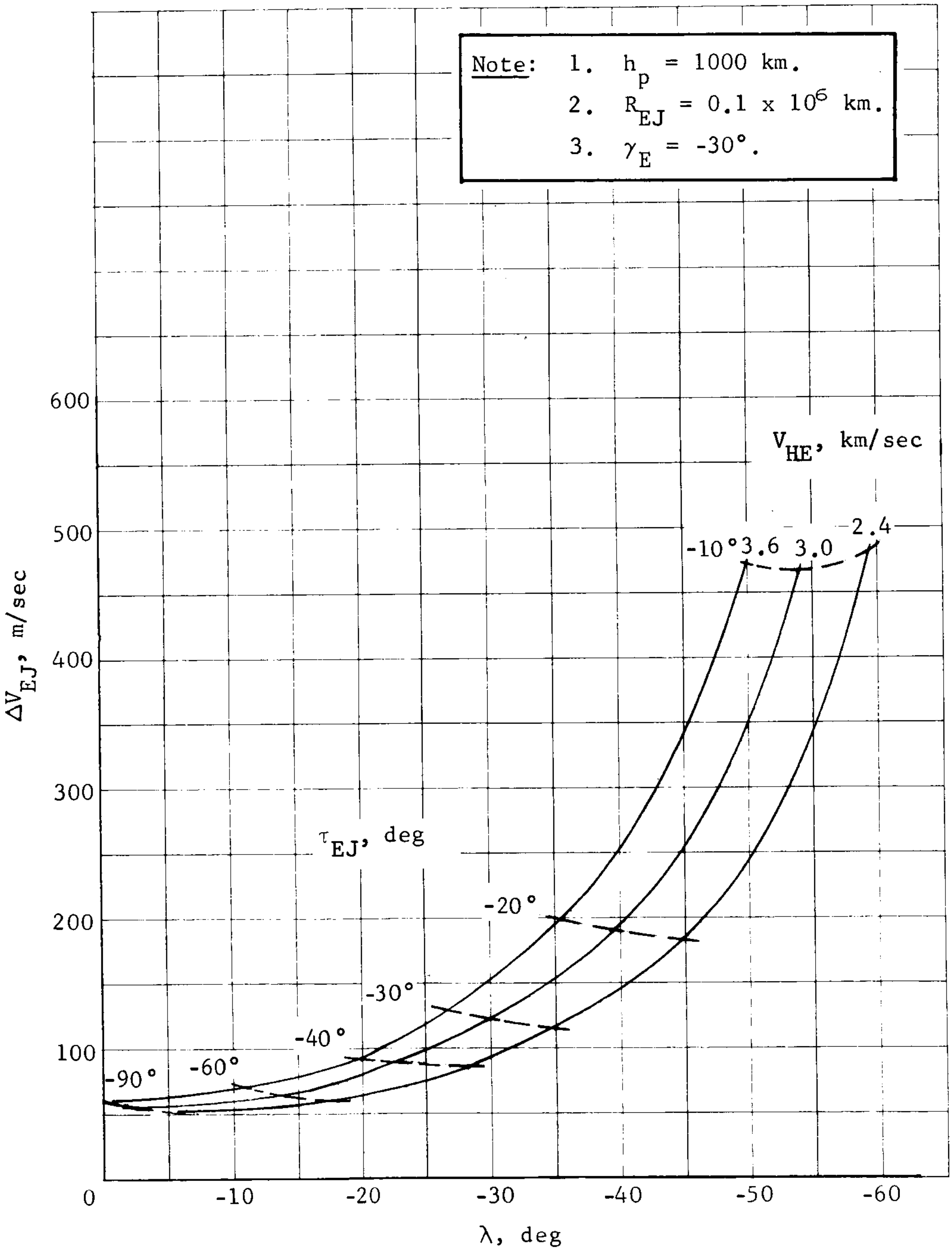

Figure A86.- Ejection ΔV Requirements

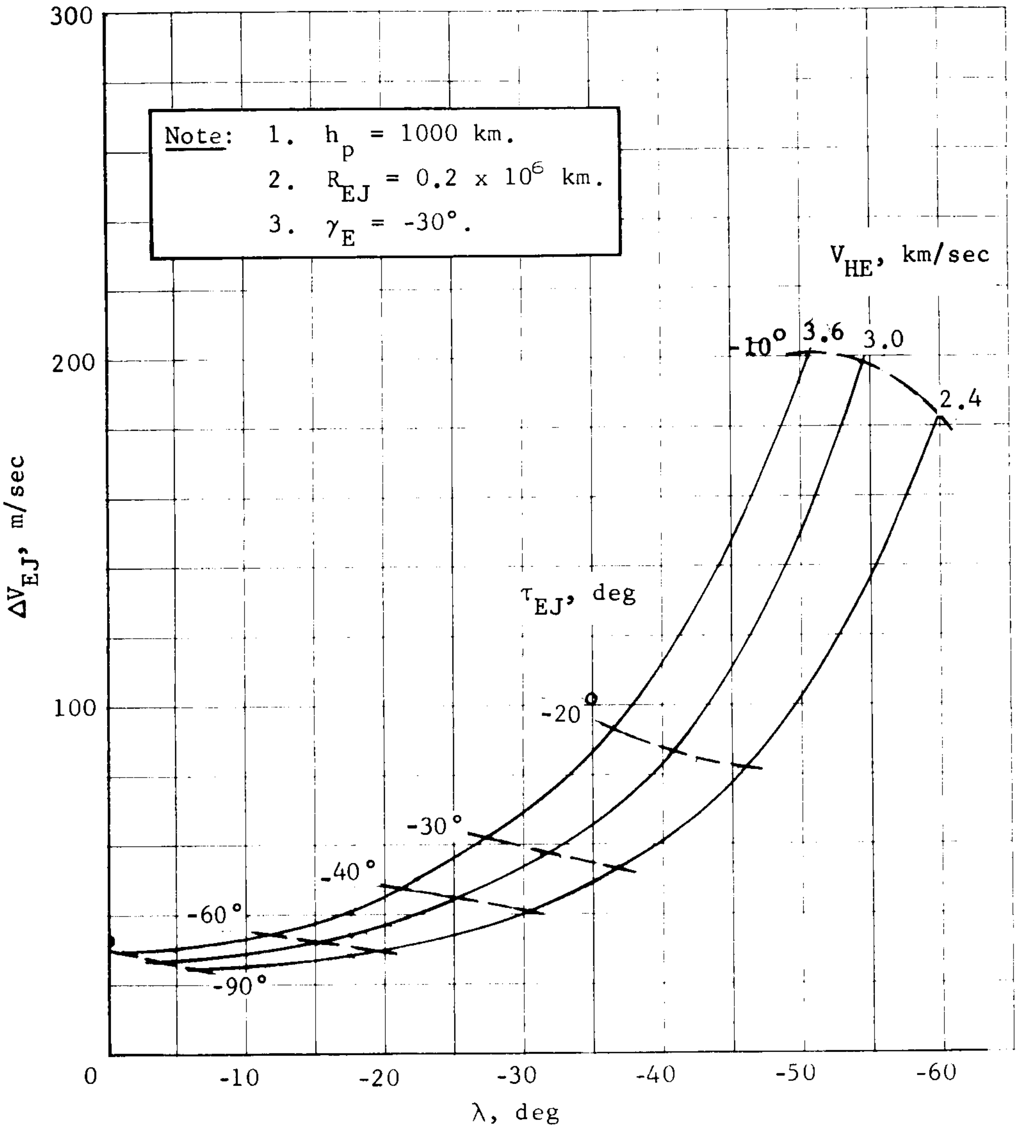

Figure A87.- Ejection ΔV Requirements

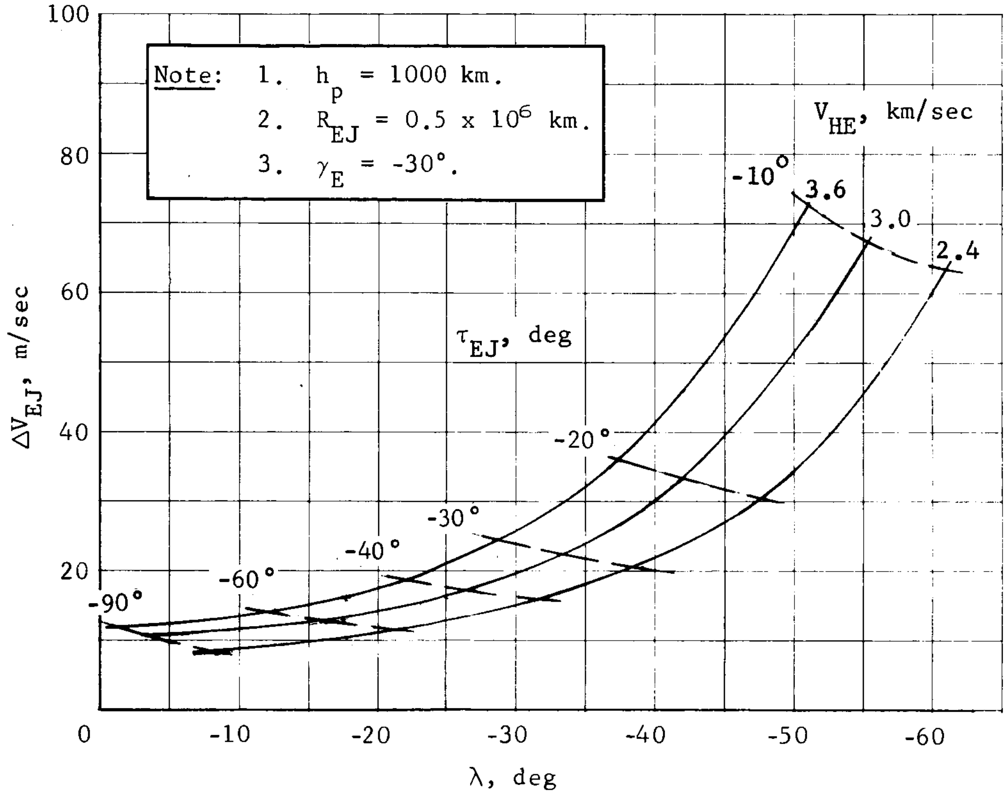

Figure A88.- Ejection ΔV Requirements

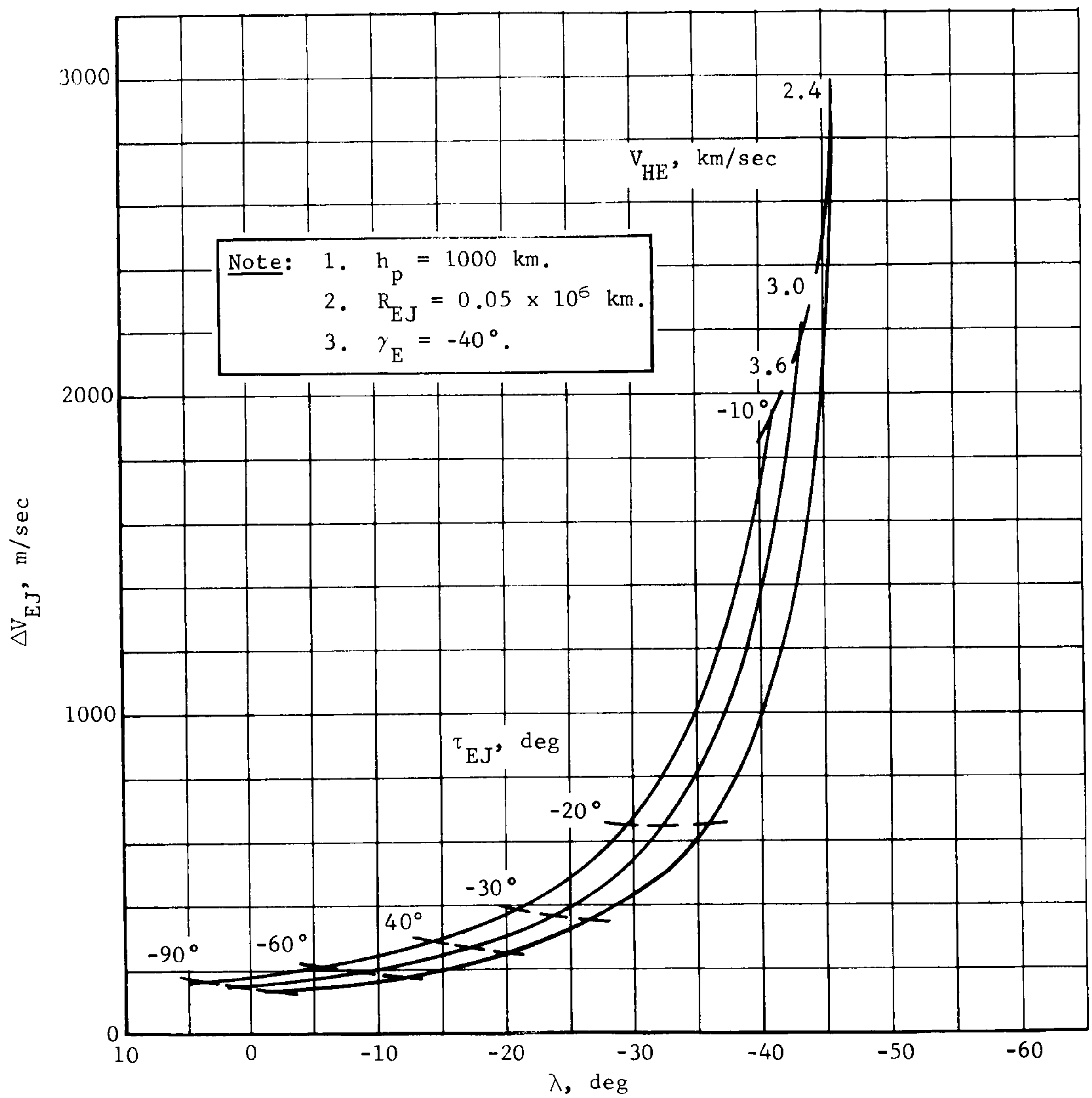

Figure A89.- Ejection ΔV Requirements

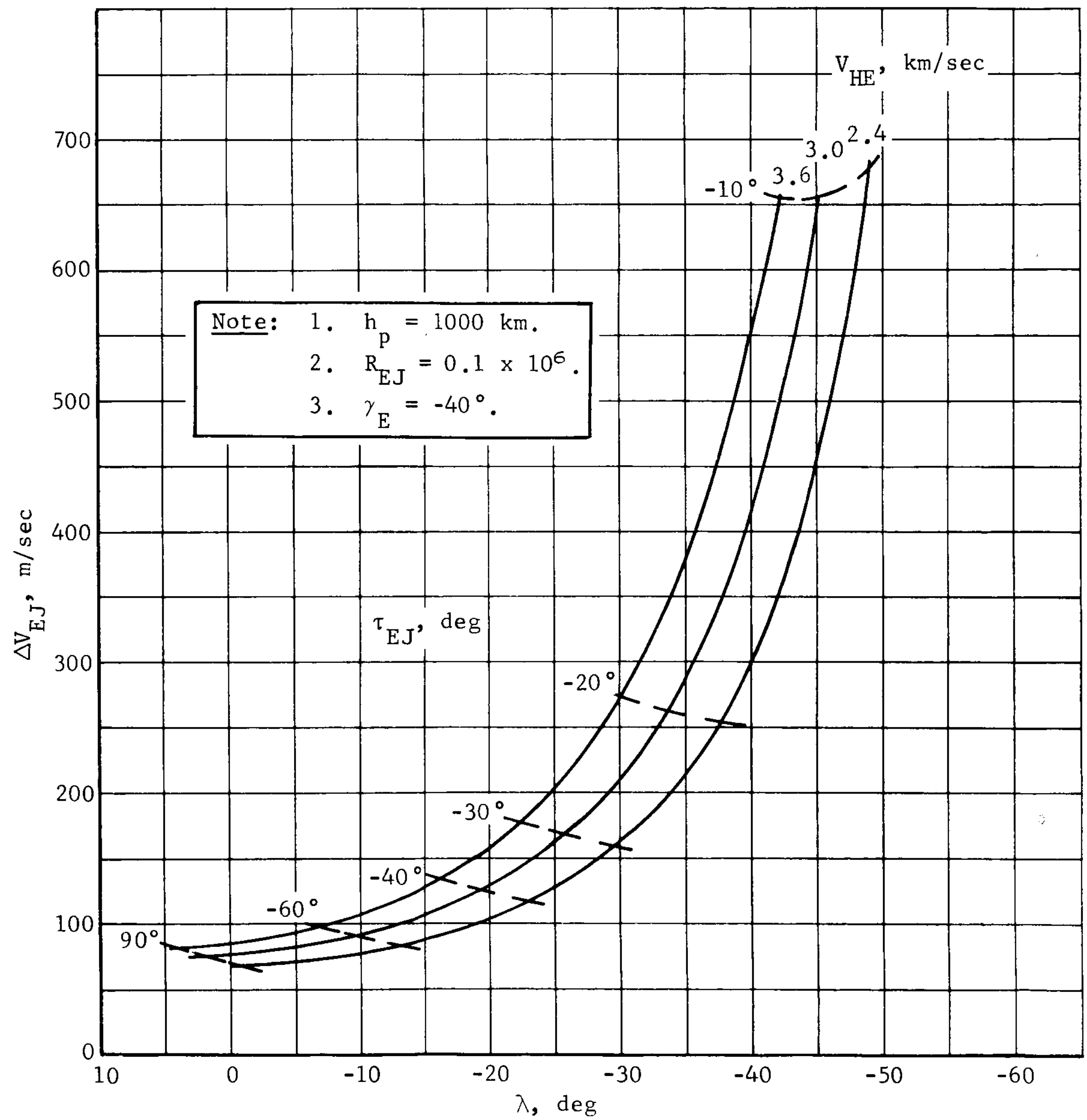

Figure A90.- Ejection ΔV Requirements

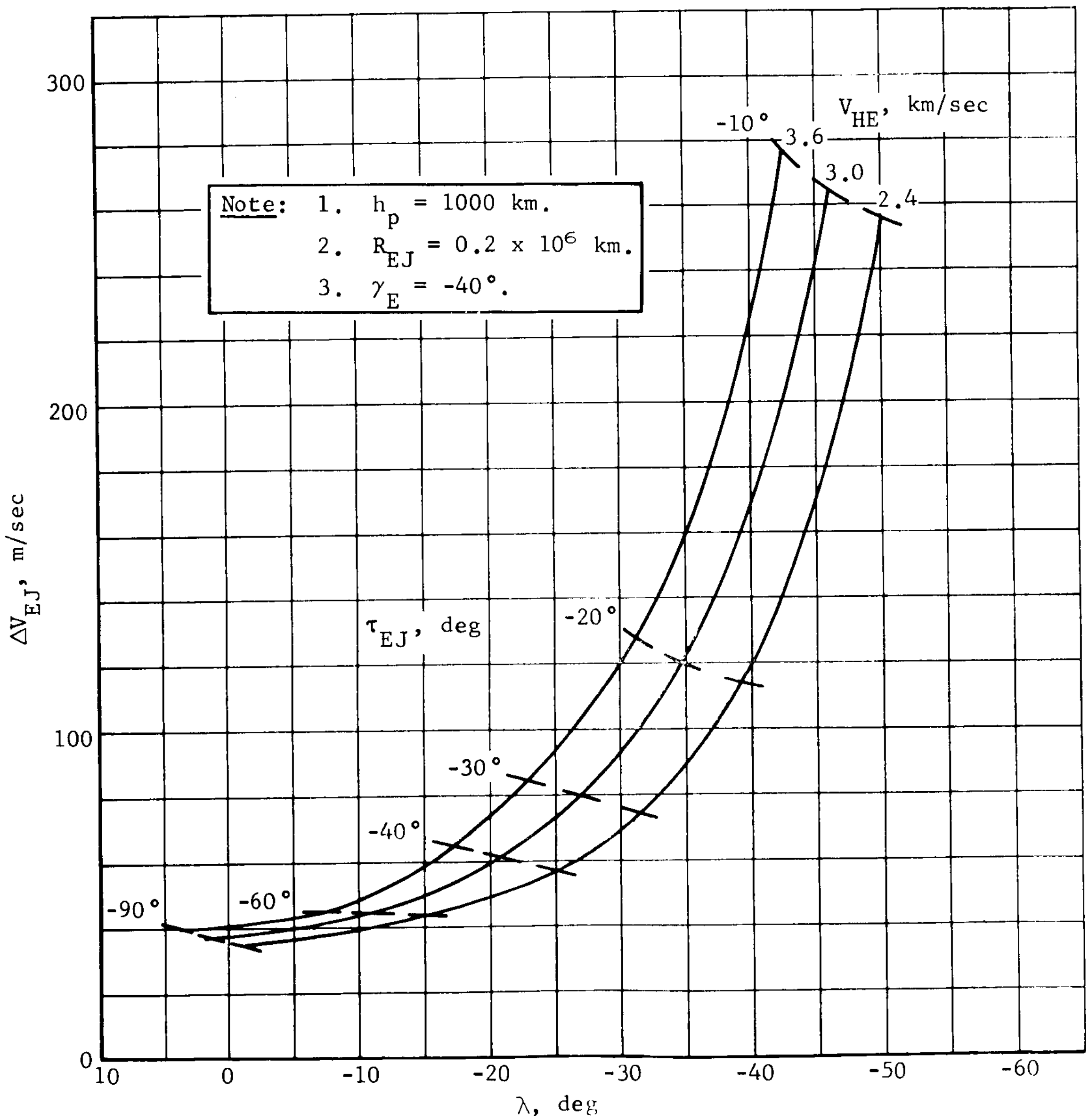

Figure A91.- Ejection ΔV Requirements

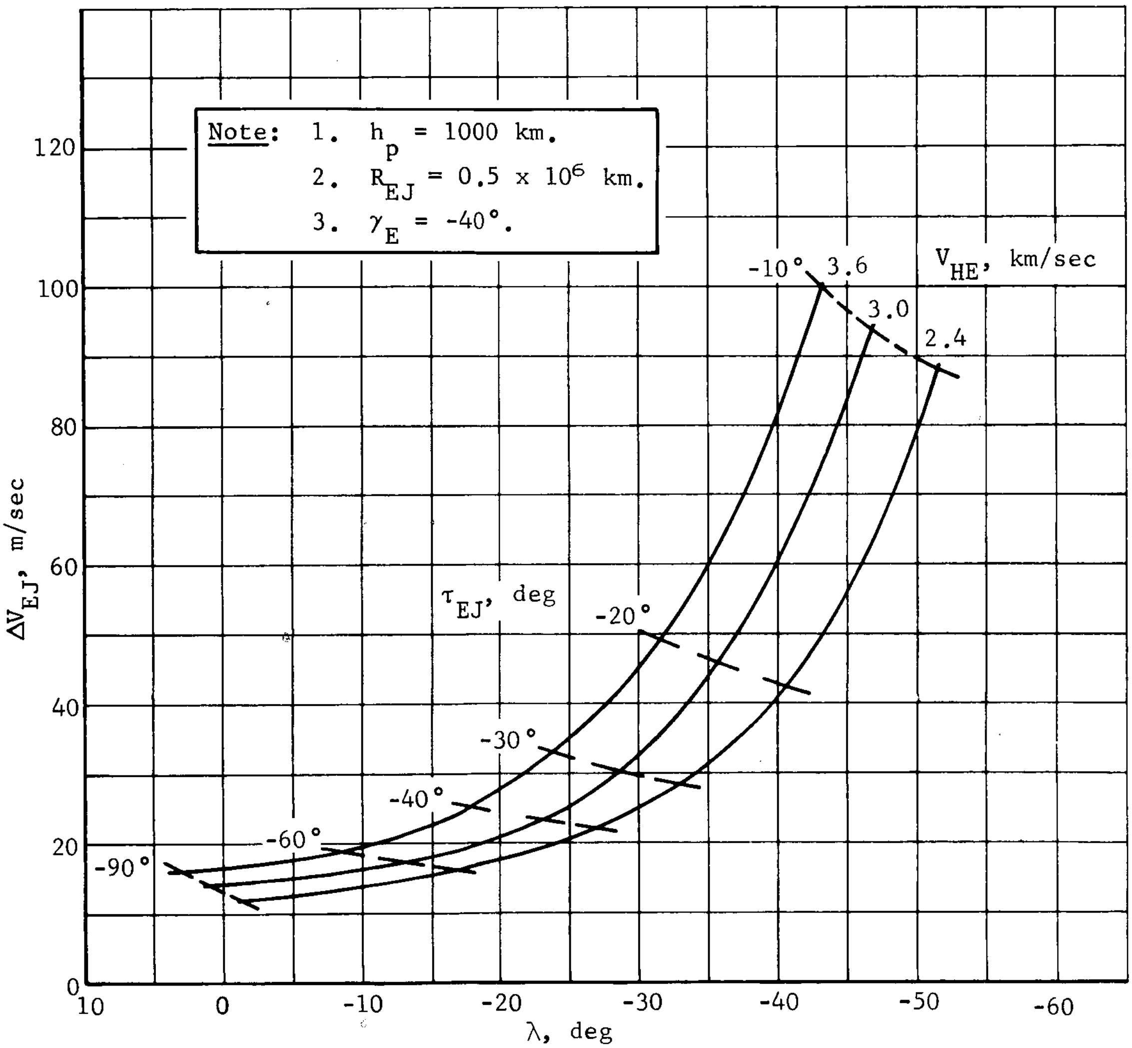

Figure A92.- Ejection ΔV Requirements

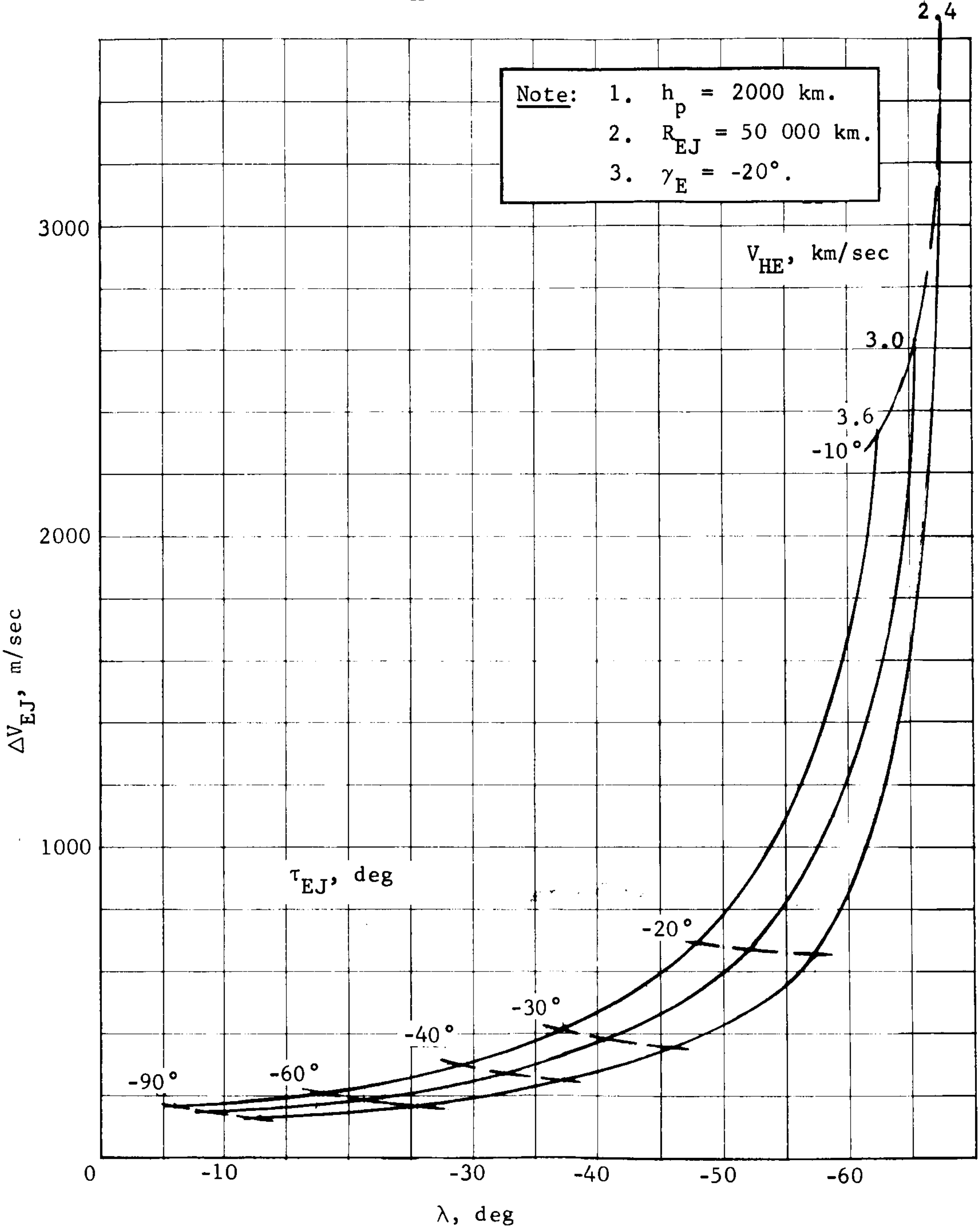

Figure A93.- Ejection ΔV Requirements

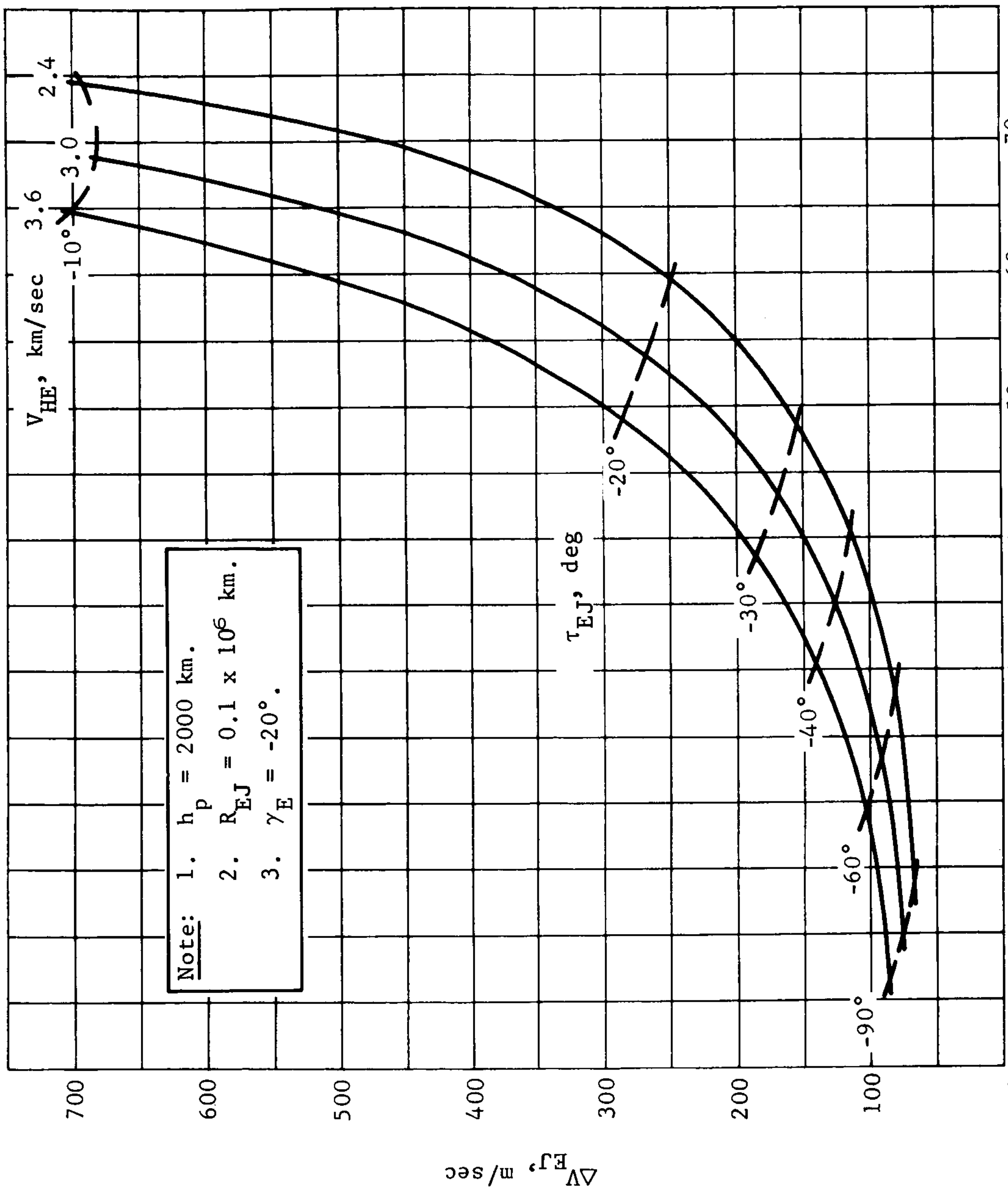

Figure A94.- Ejection ΔV Requirements

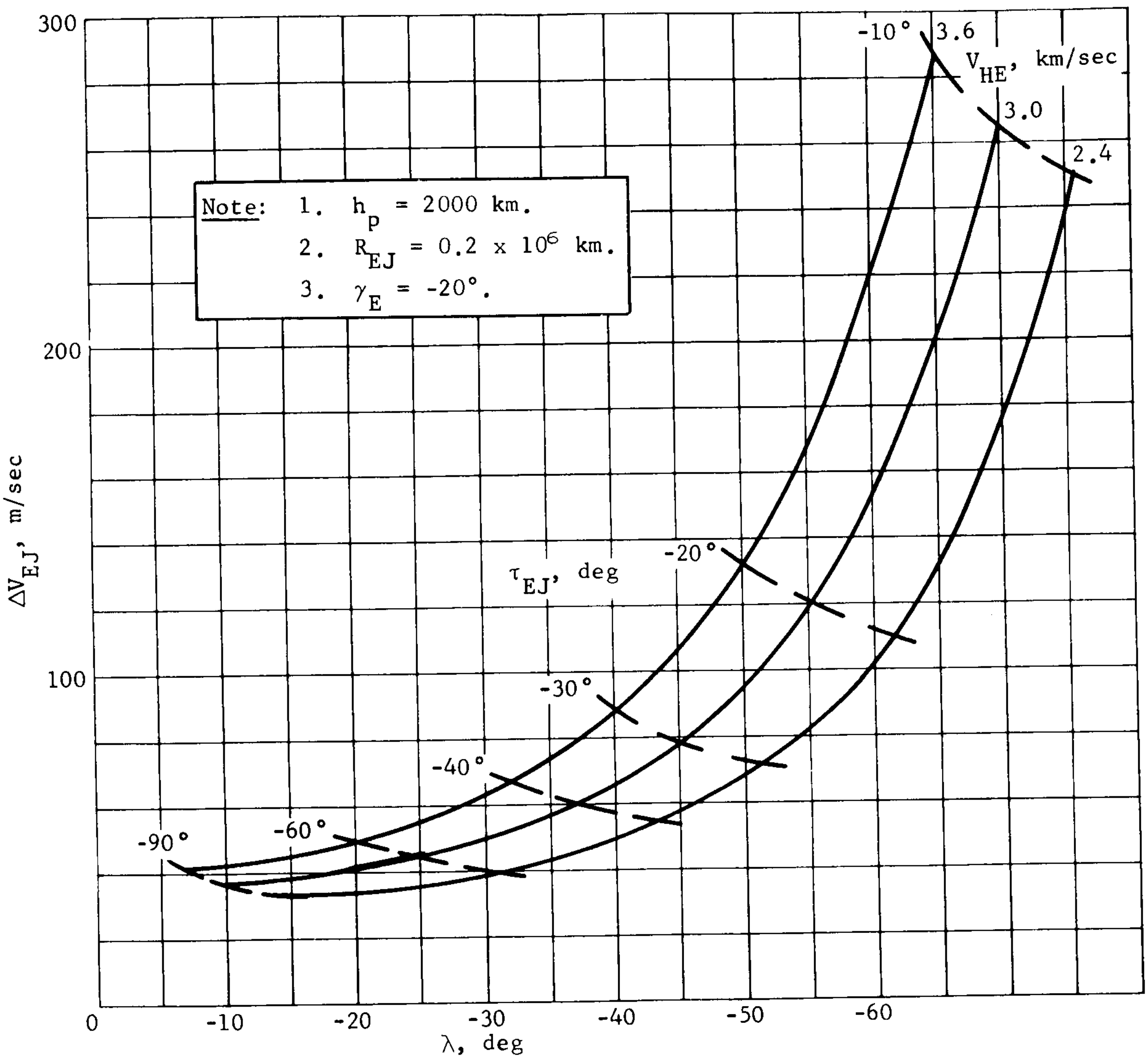

Figure A95.- Ejection ΔV Requirements

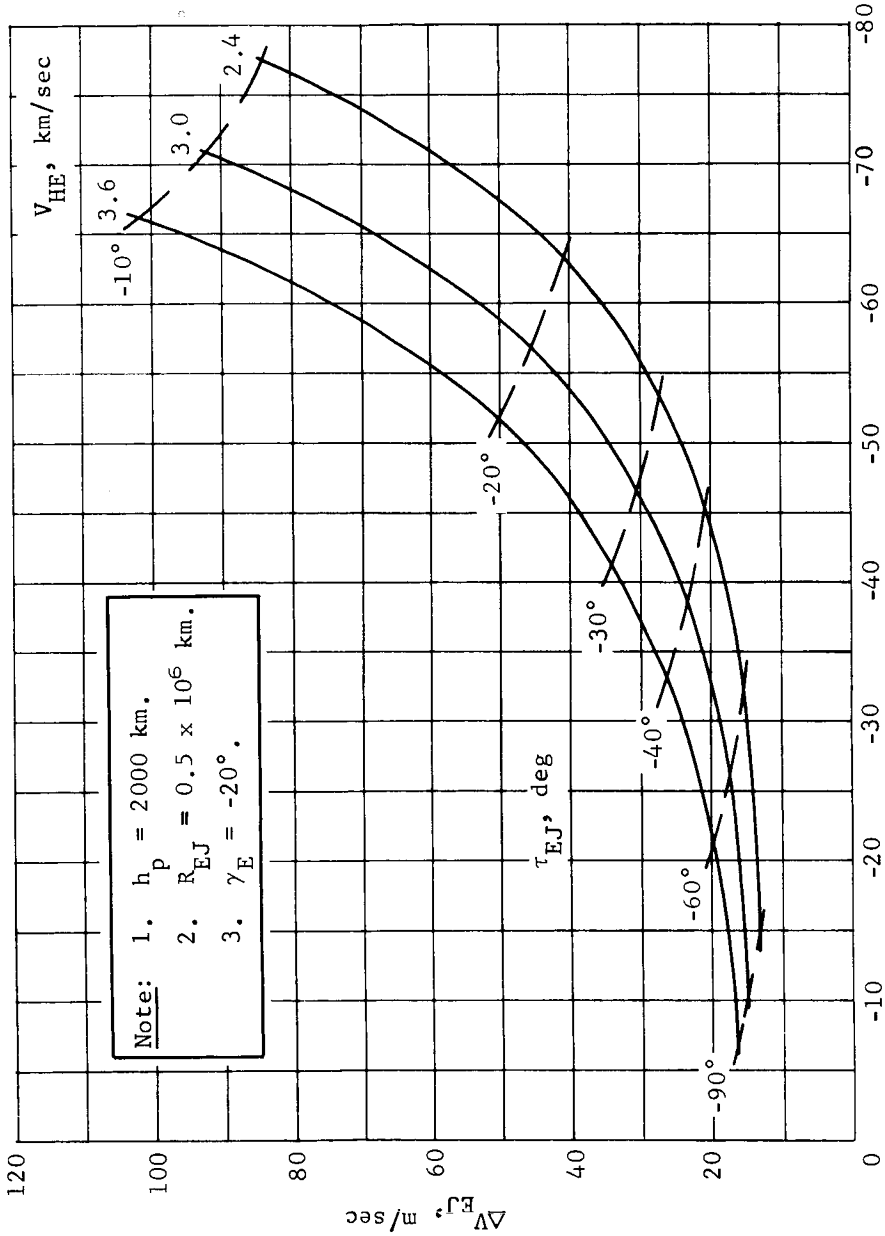

Figure A96.- Ejection ΔV Requirements

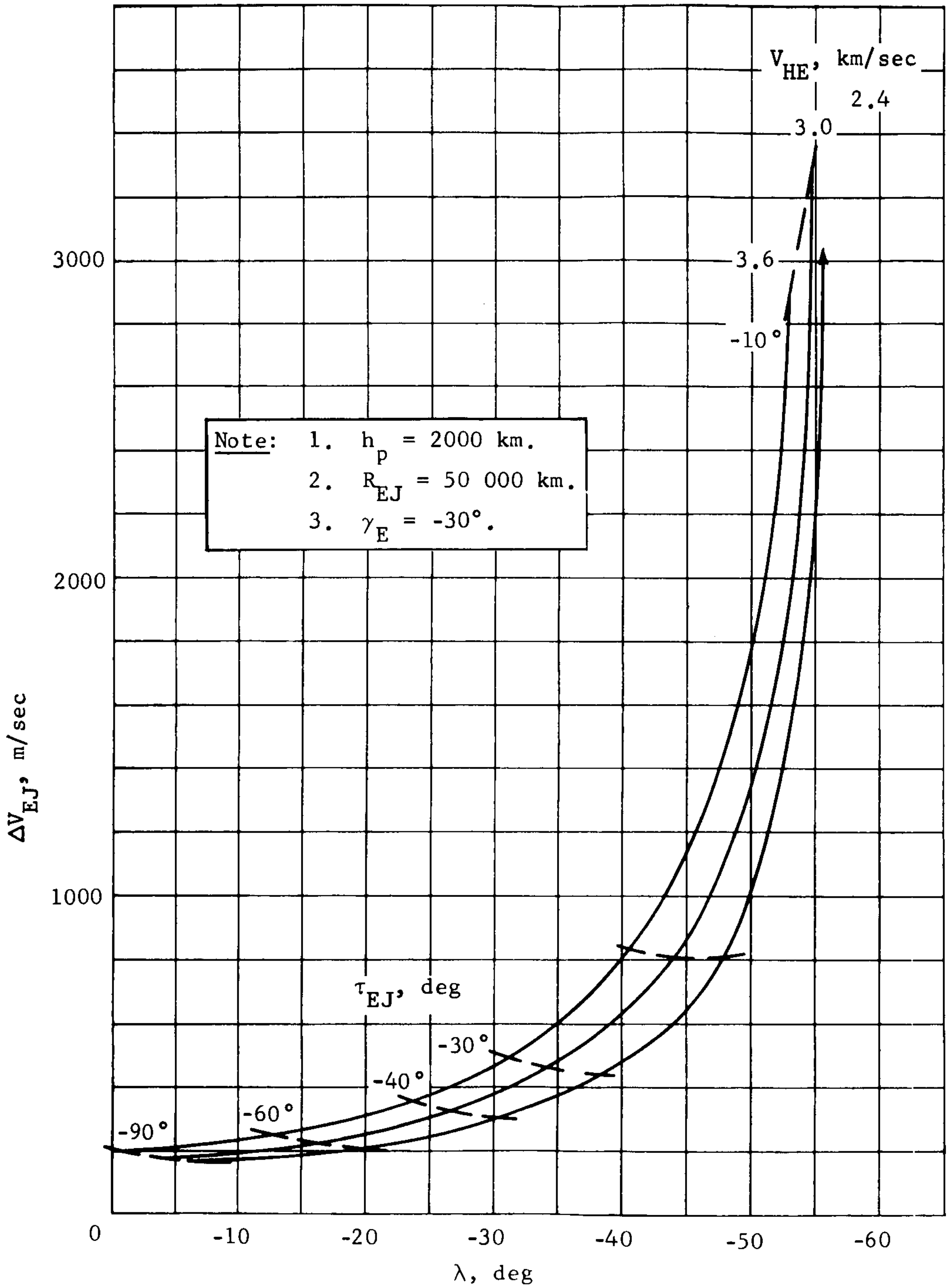

Figure A97.- Ejection ΔV Requirements

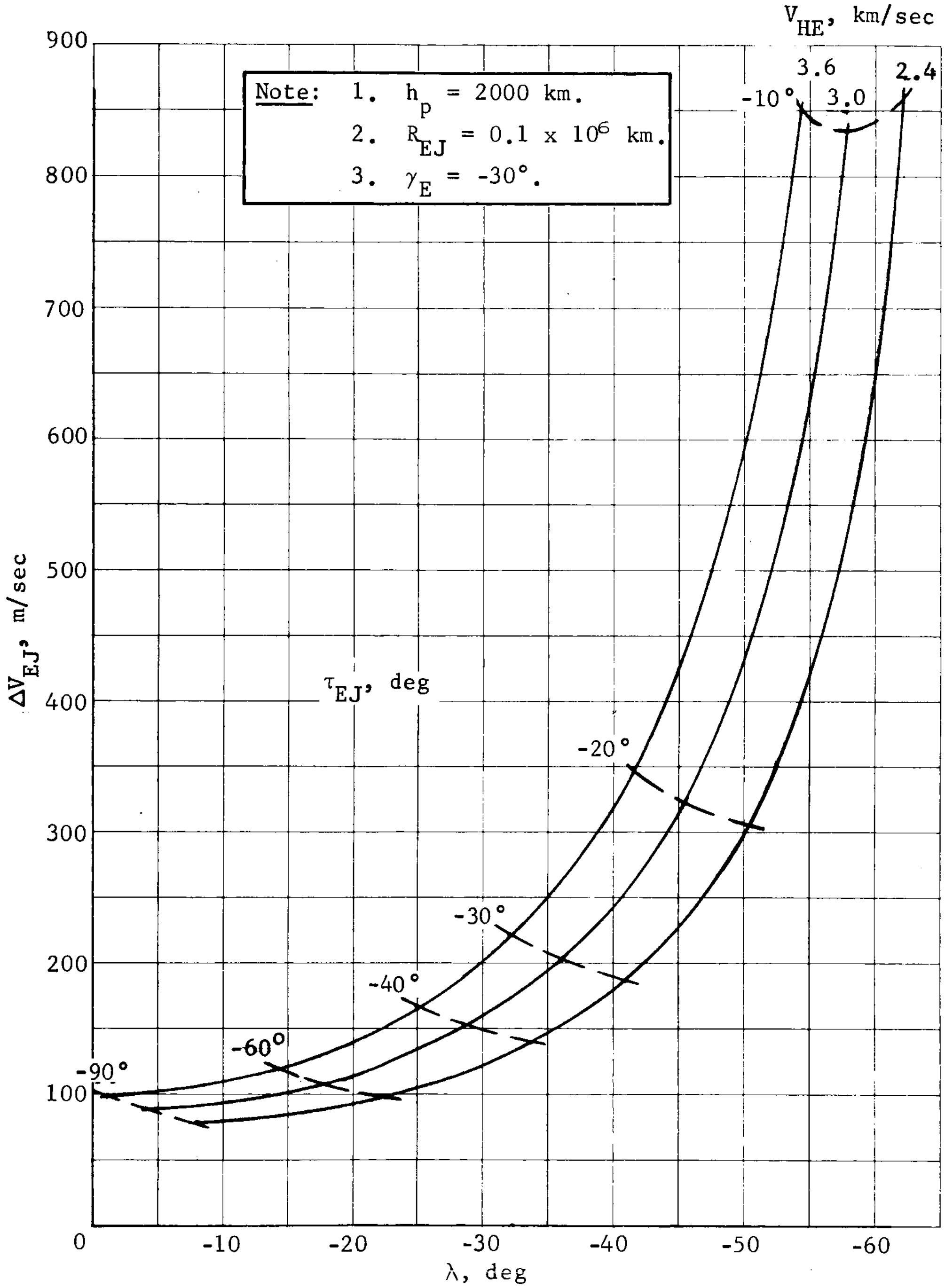

Figure A98.- Ejection ΔV Requirements

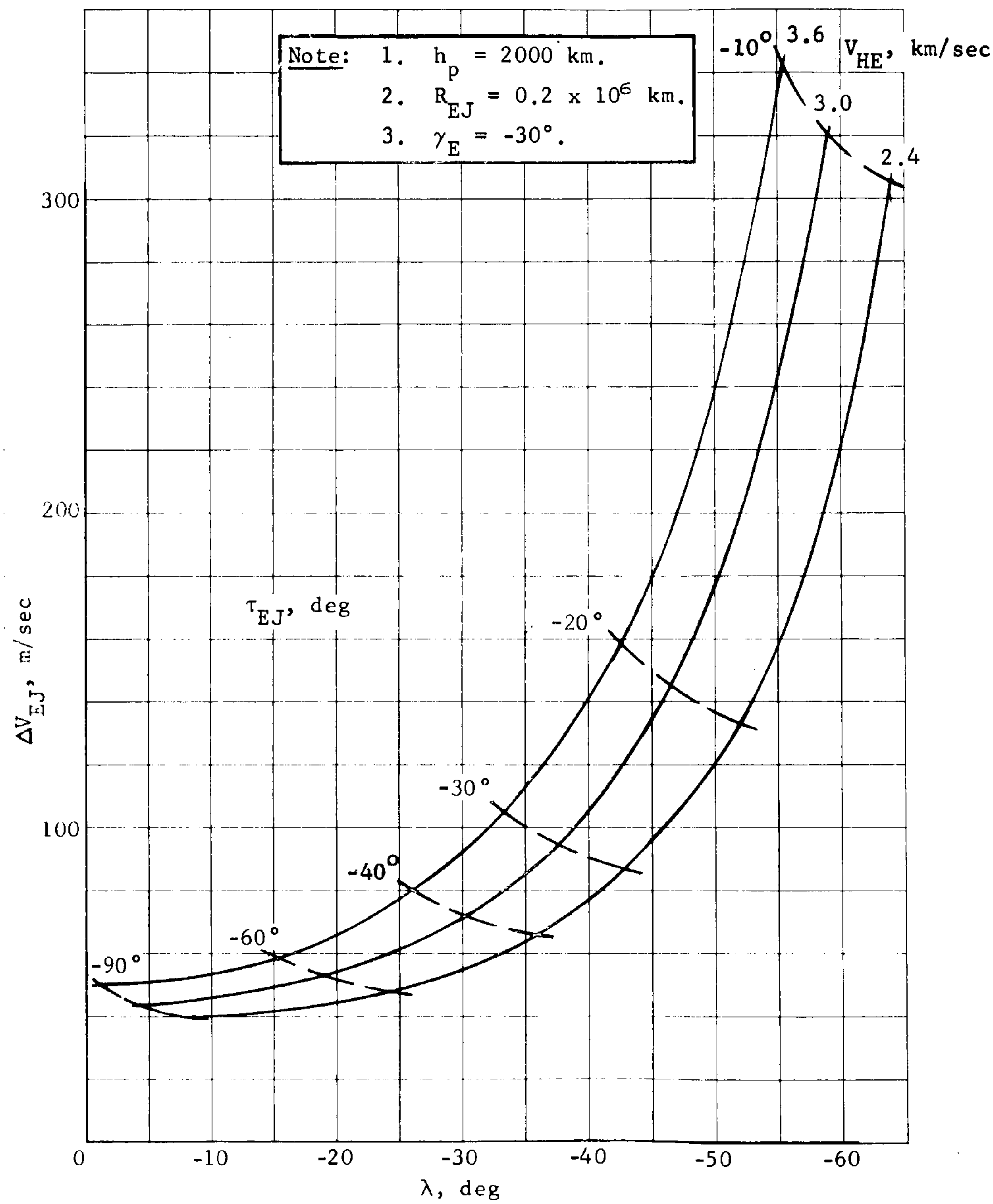

Figure A99.- Ejection ΔV Requirements

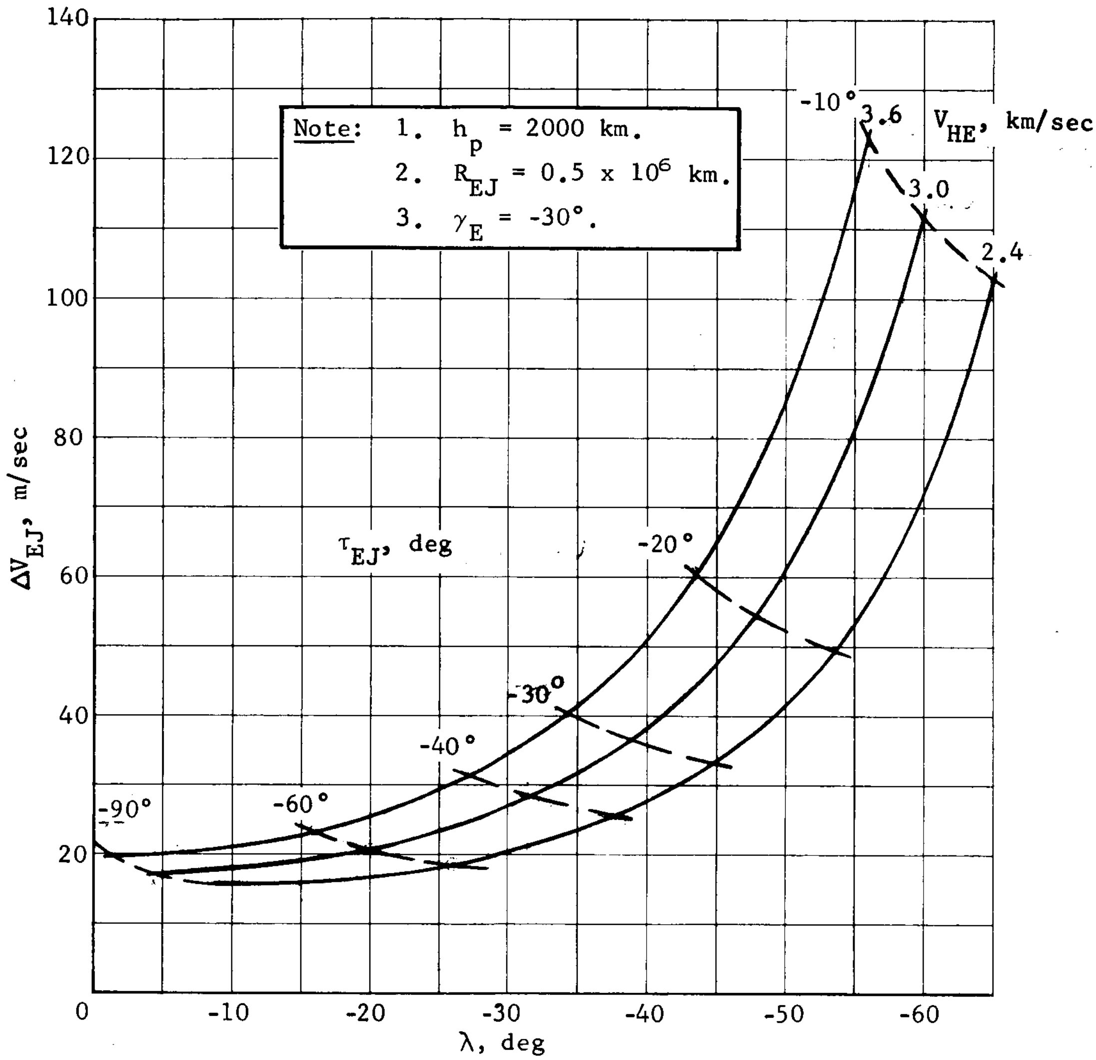

Figure A100.- Ejection ΔV Requirements

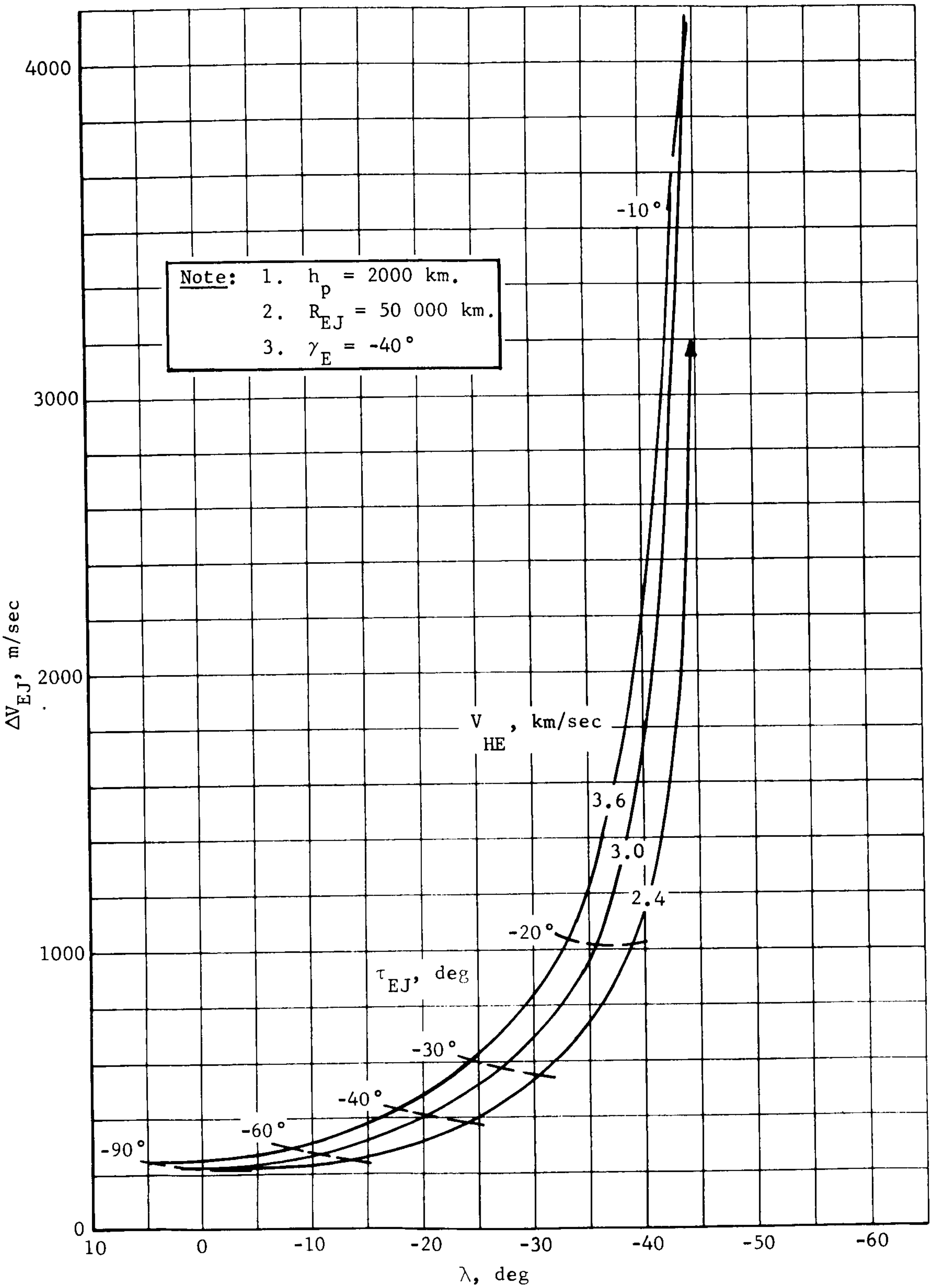

Figure A101.- Ejection ΔV Requirements

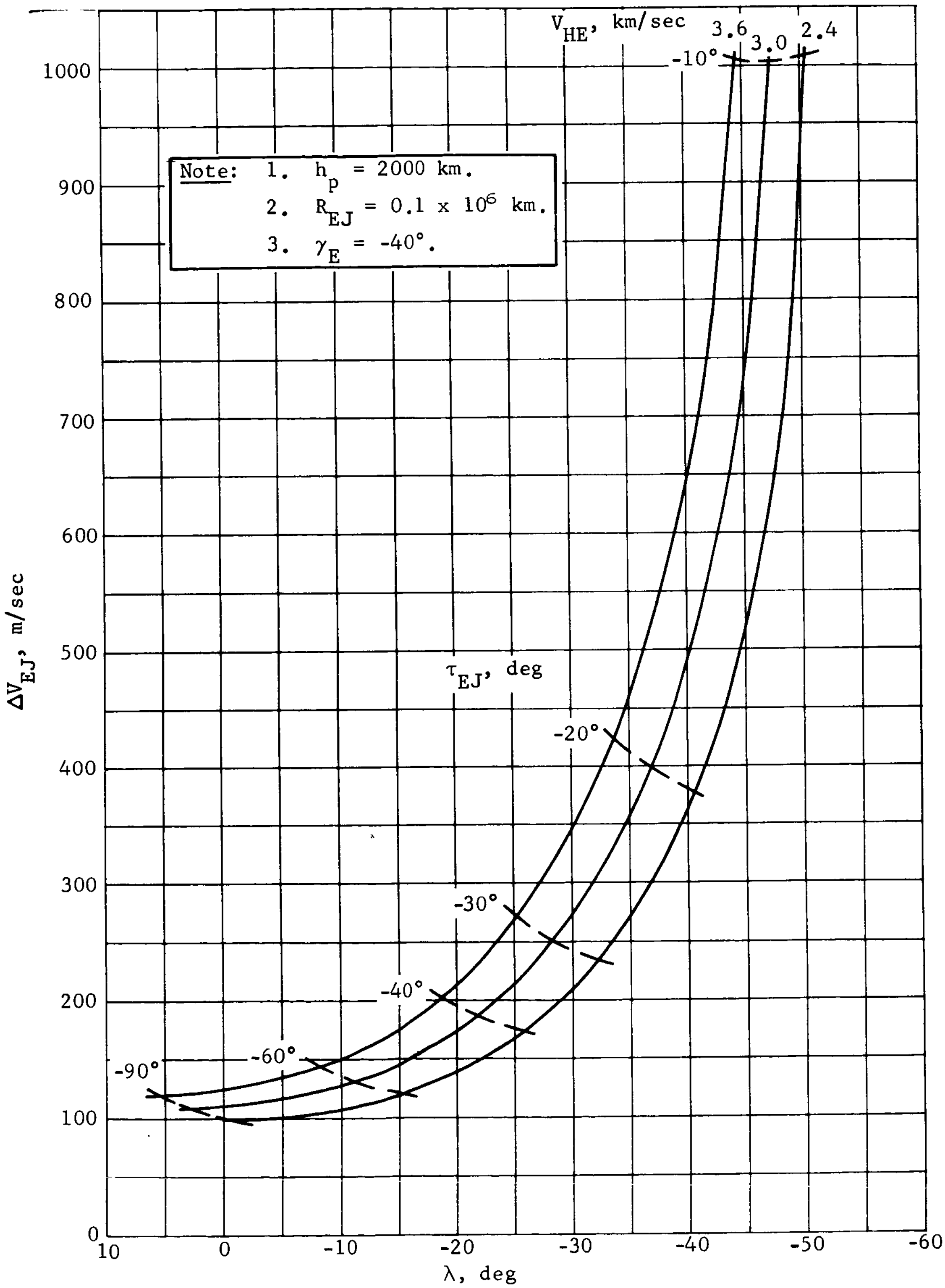

Figure A102.- Ejection ΔV Requirements

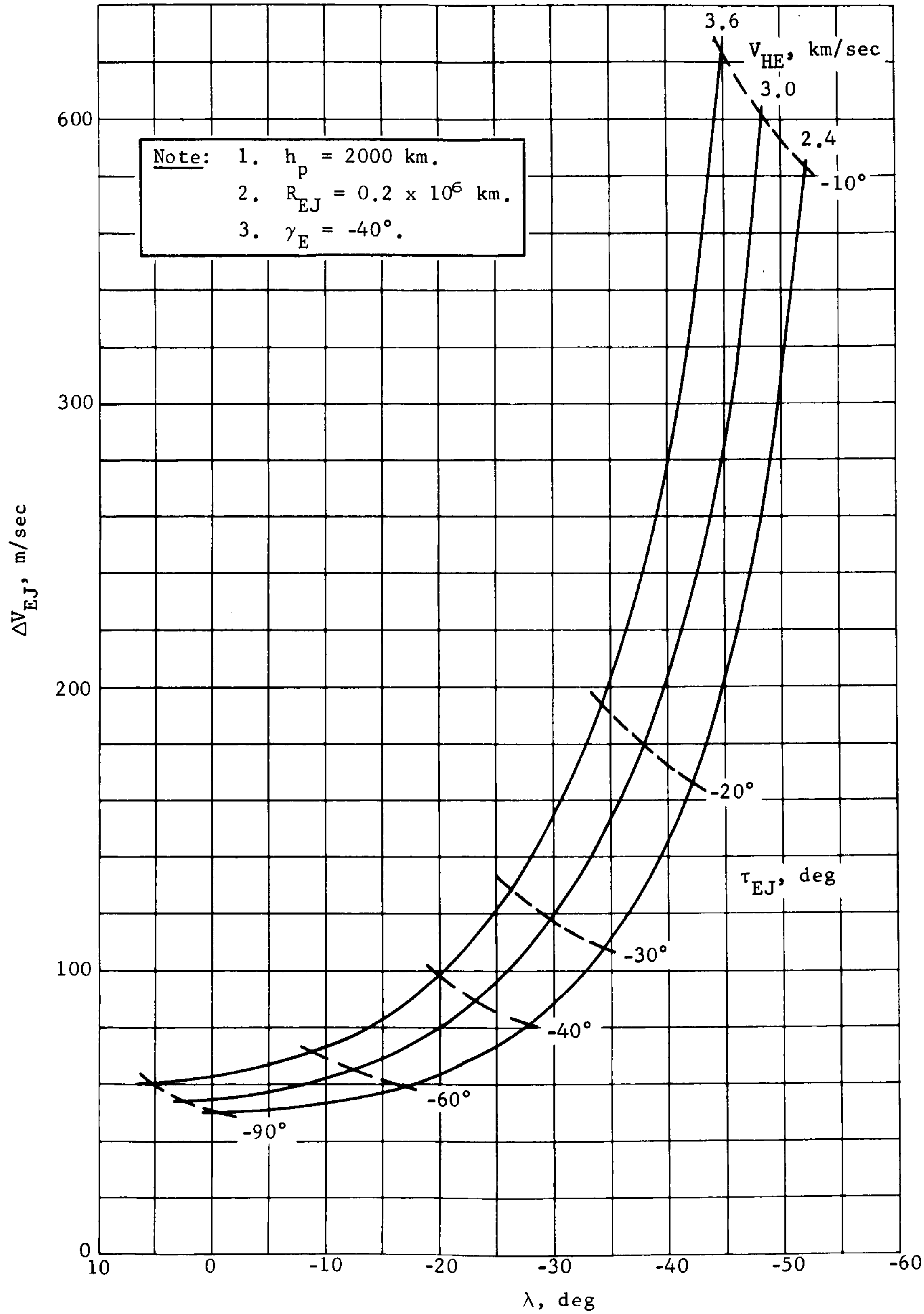

Figure A103.- Ejection ΔV Requirements

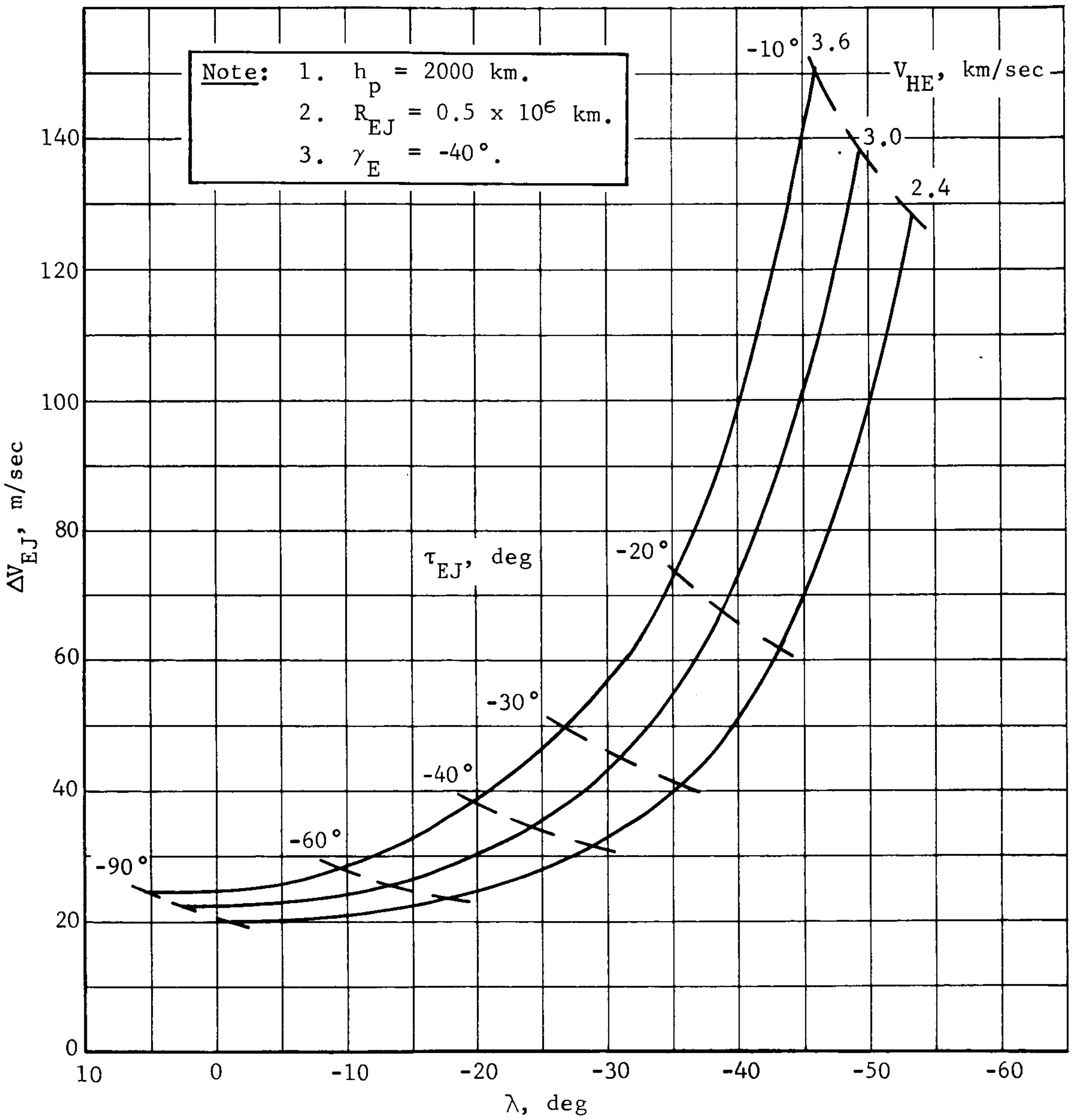

Figure A104.- Ejection ΔV Requirements

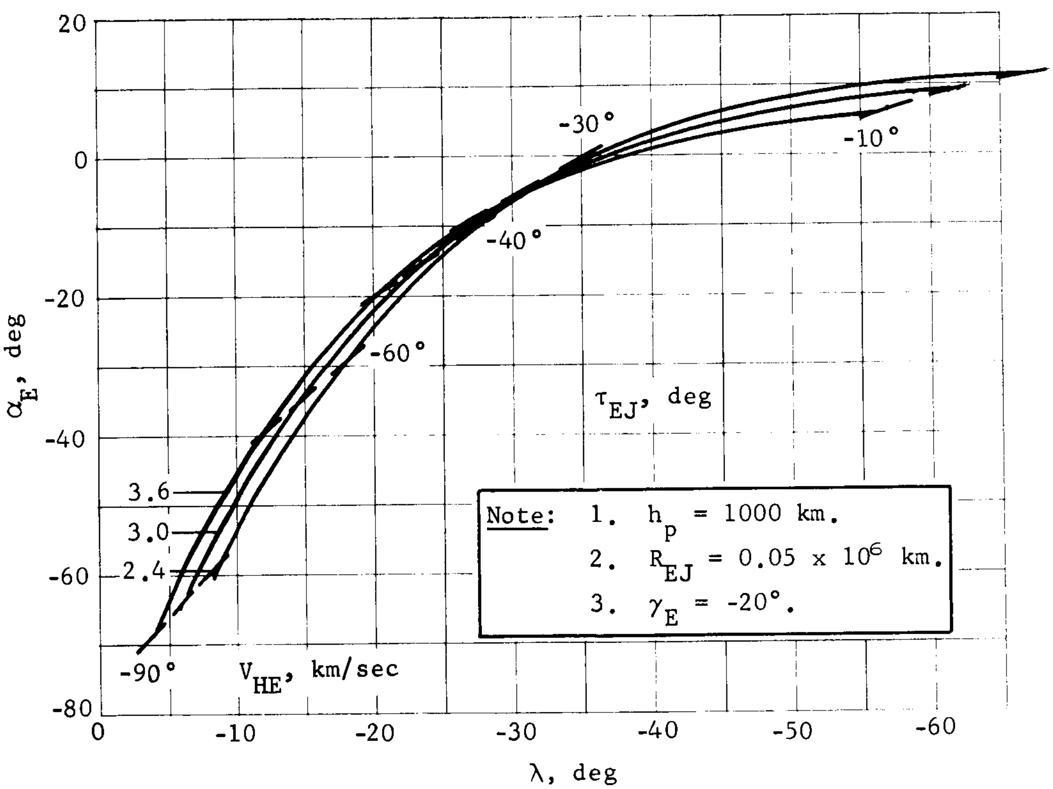

Figure A105.- Entry Angle of Attack (Direct Mode)

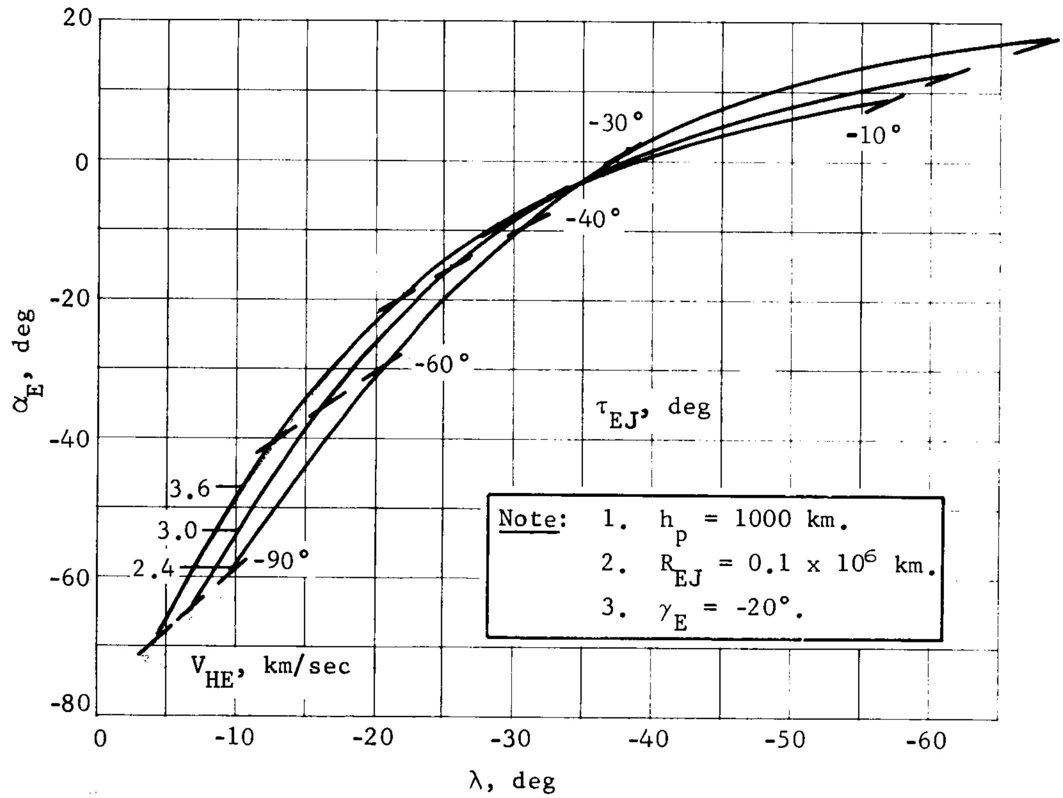

Figure A106.- Entry Angle of Attack (Direct Mode)

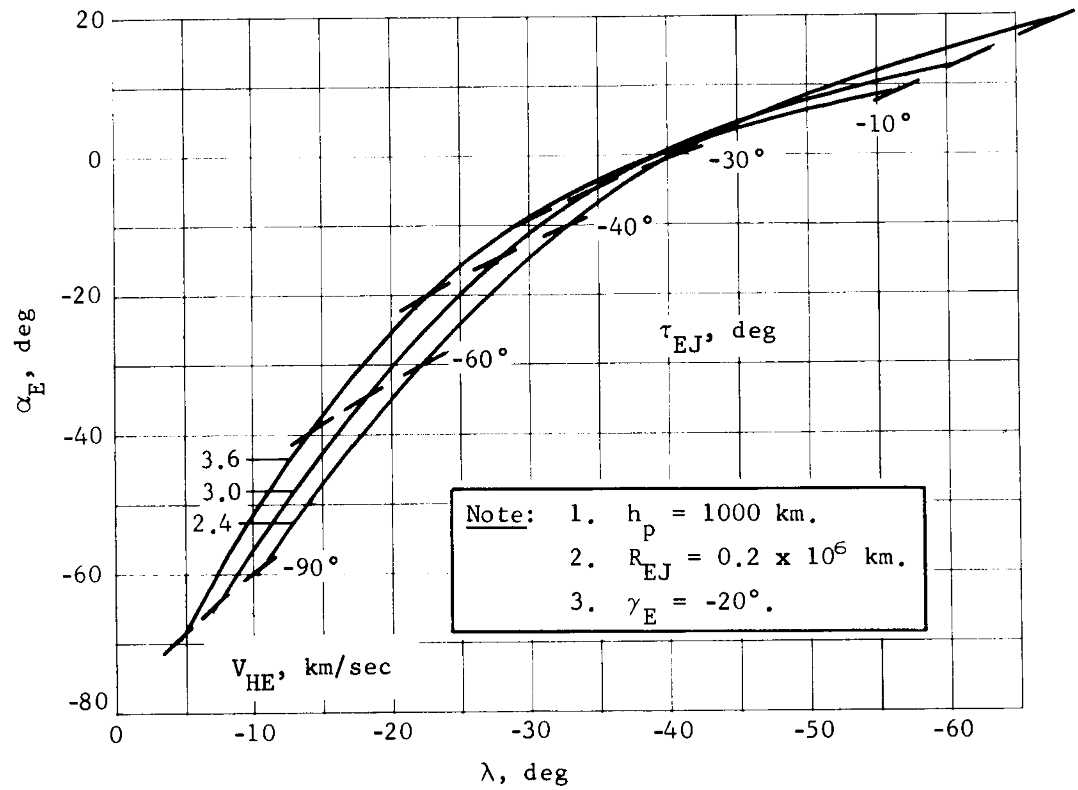

Figure A107.- Entry Angle of Attack (Direct Mode)

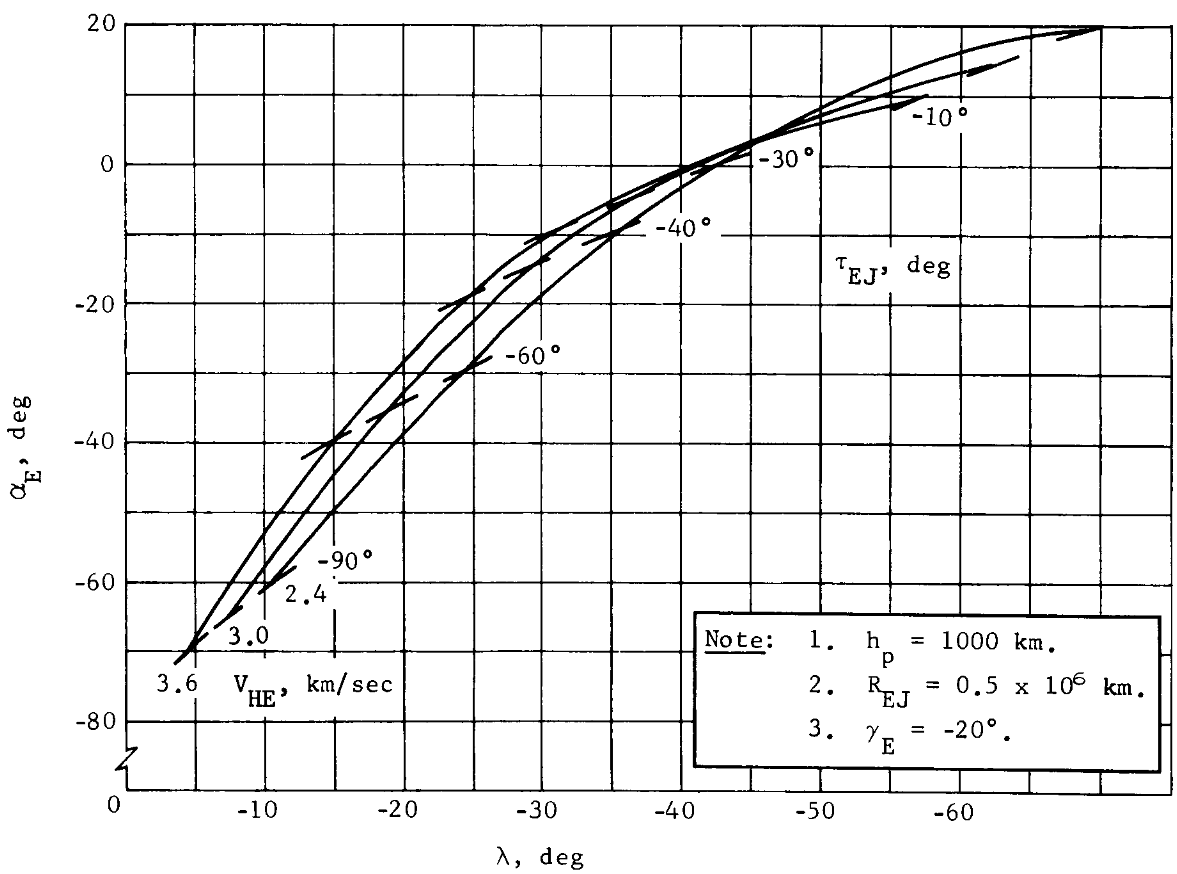

Figure A108.- Entry Angle of Attack (Direct Mode)

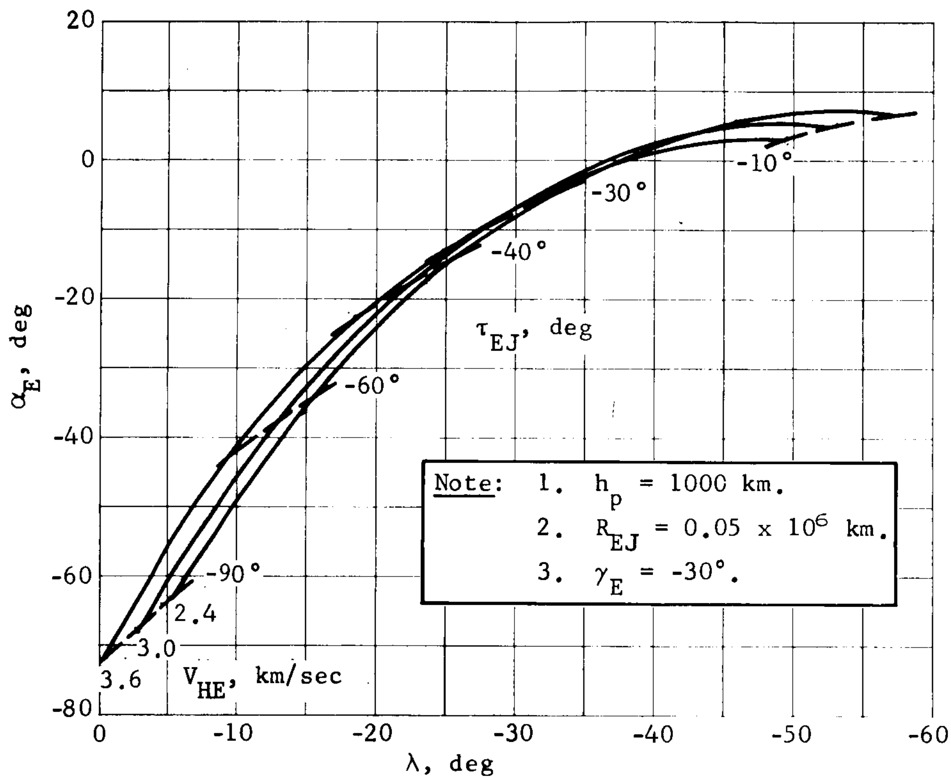

Figure A109.- Entry Angle of Attack (Direct Mode)

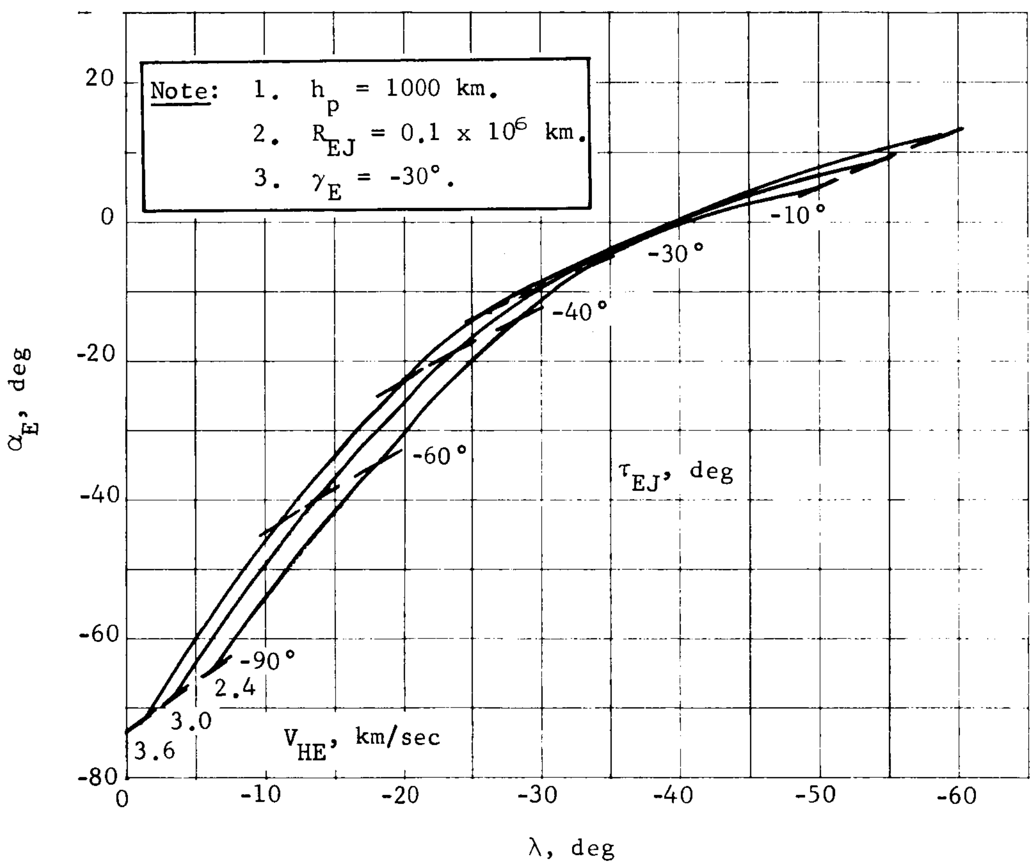

Figure A110.- Entry Angle of Attack (Direct Mode)

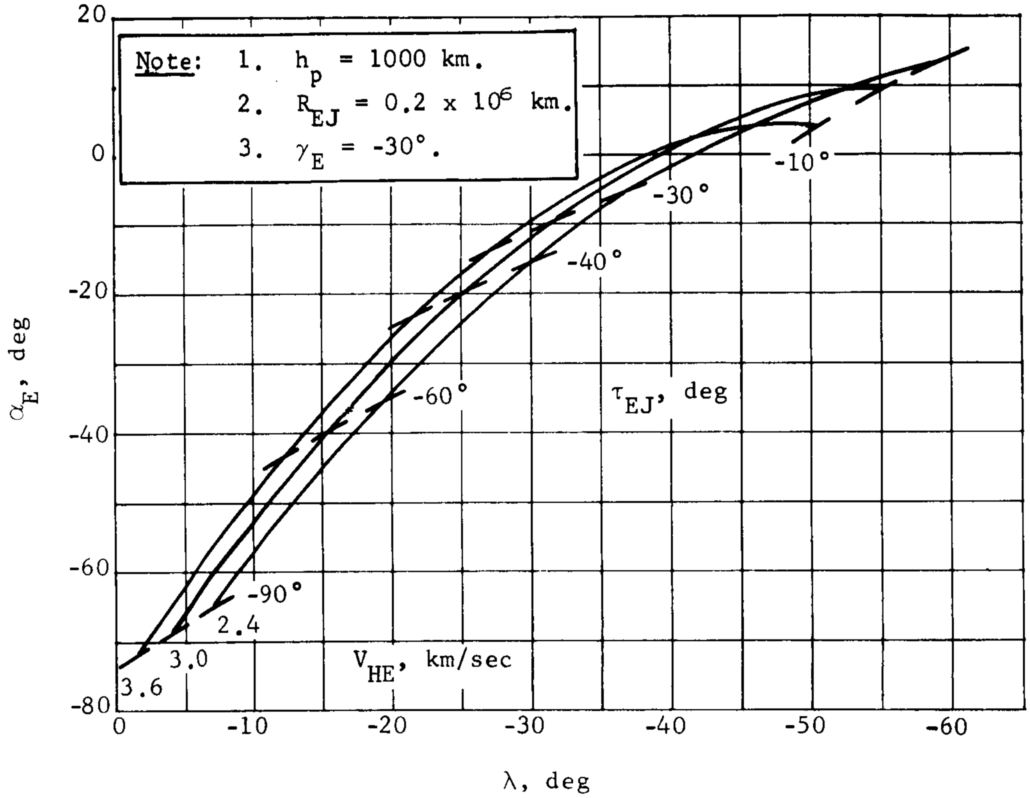

Figure A11.- Entry Angle of Attack (Direct Mode)

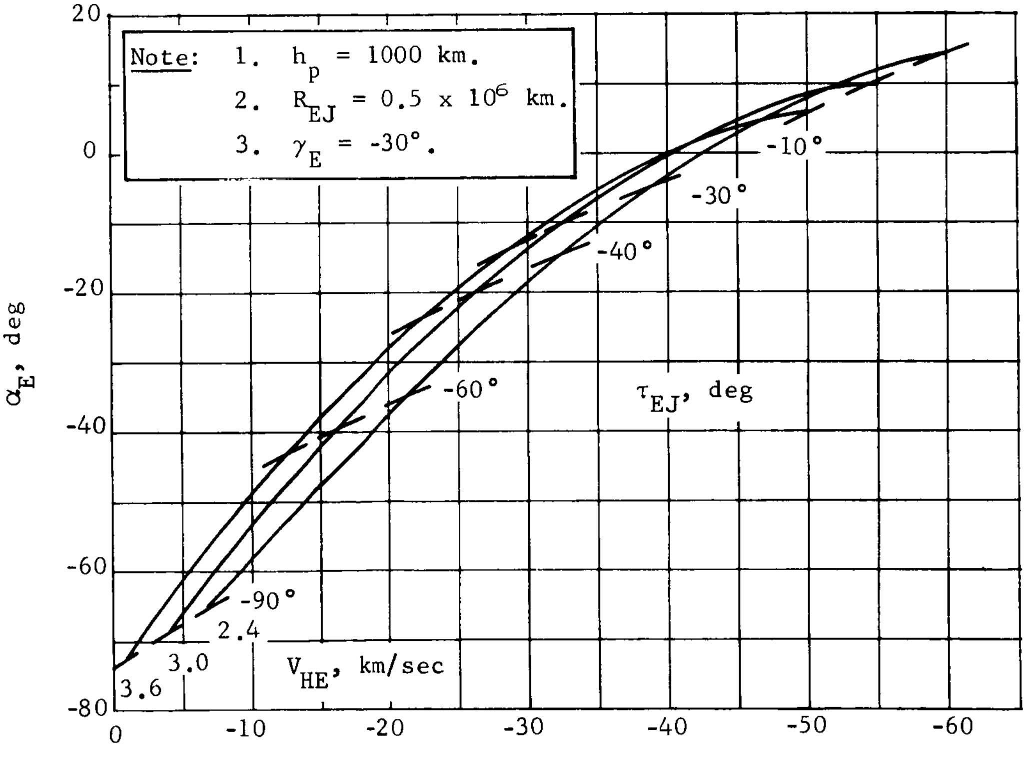

Figure A112.- Entry Angle of Attack (Direct Mode)

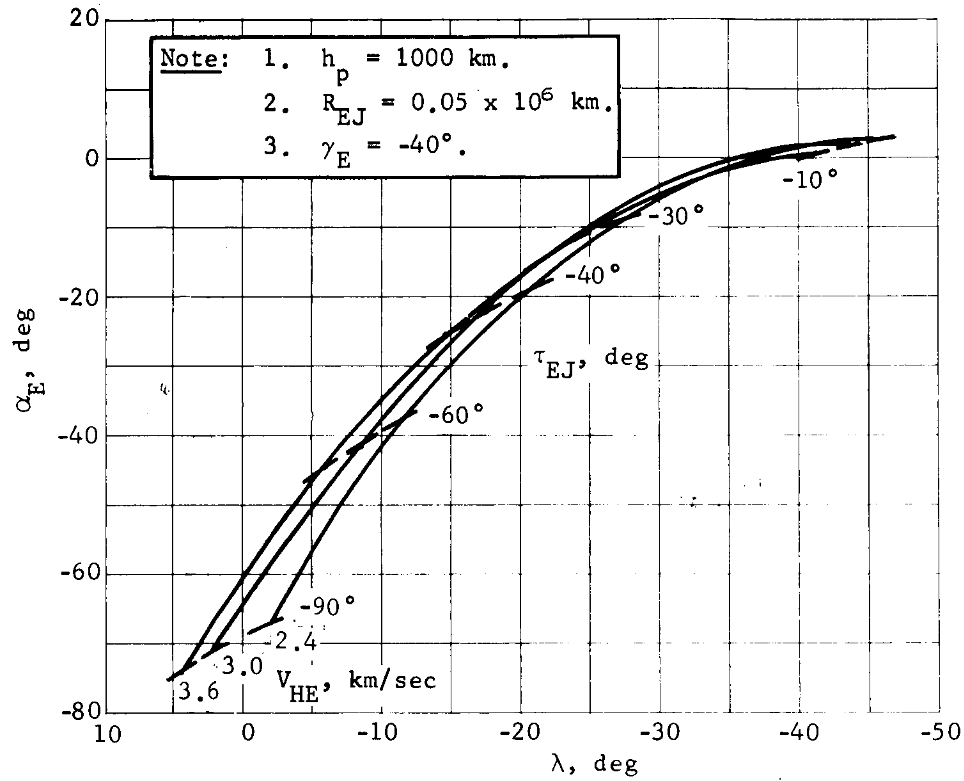

Figure A113.- Entry Angle of Attack (Direct Mode)

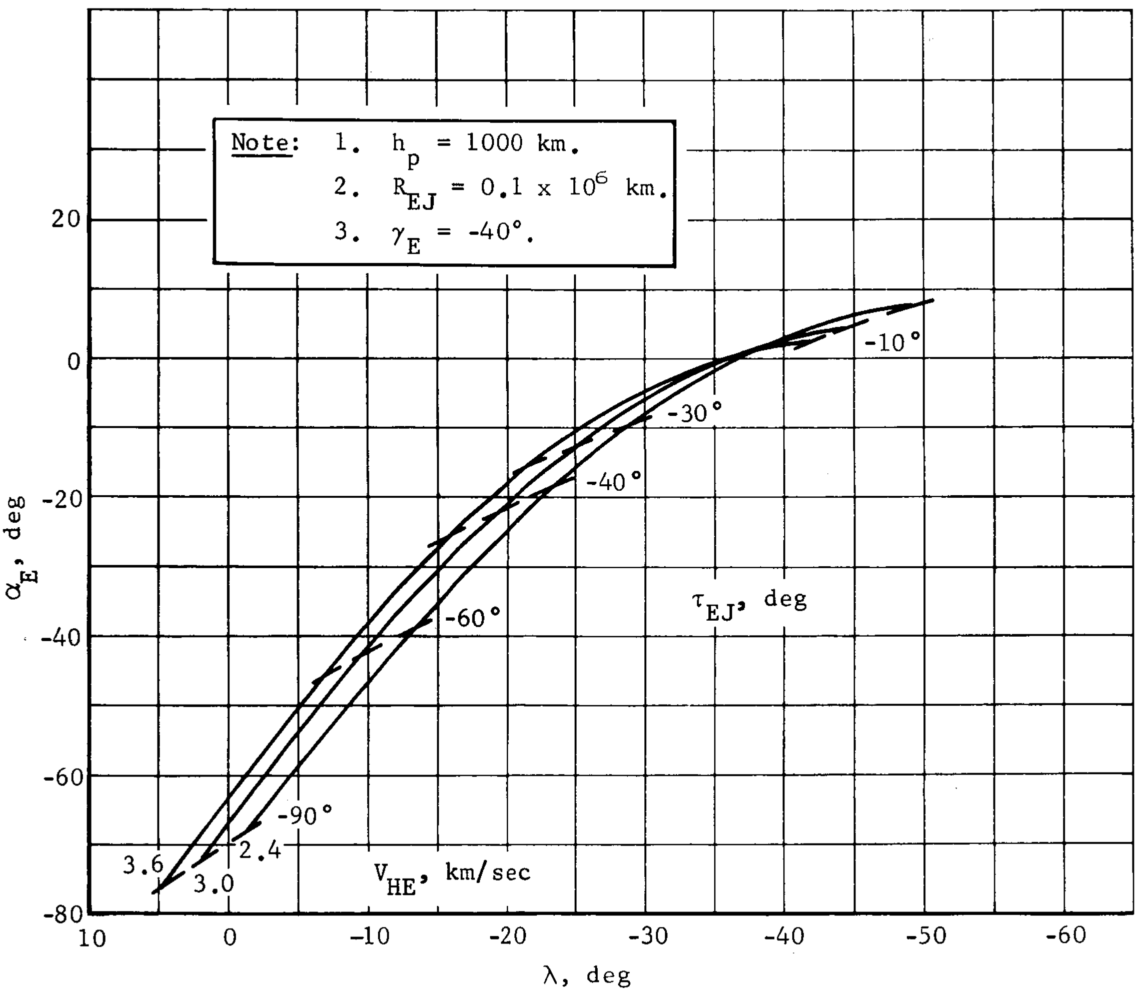

Figure A114.- Entry Angle of Attack (Direct Mode)

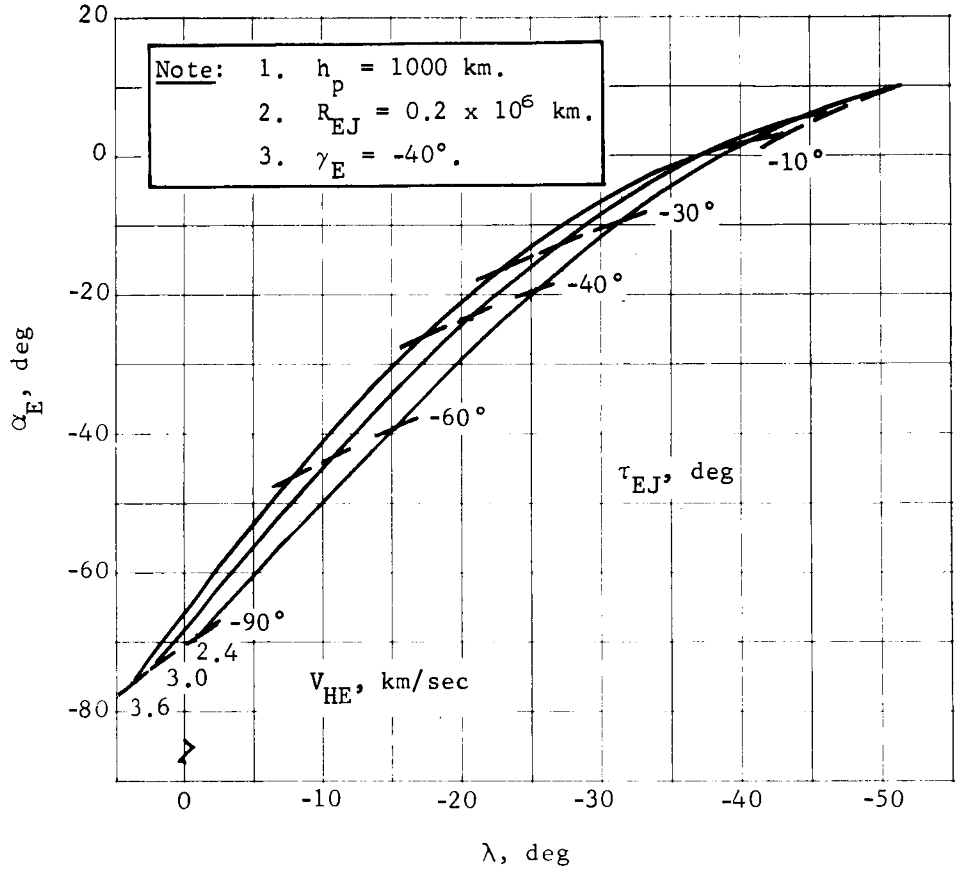

Figure A115.- Entry Angle of Attack (Direct Mode)

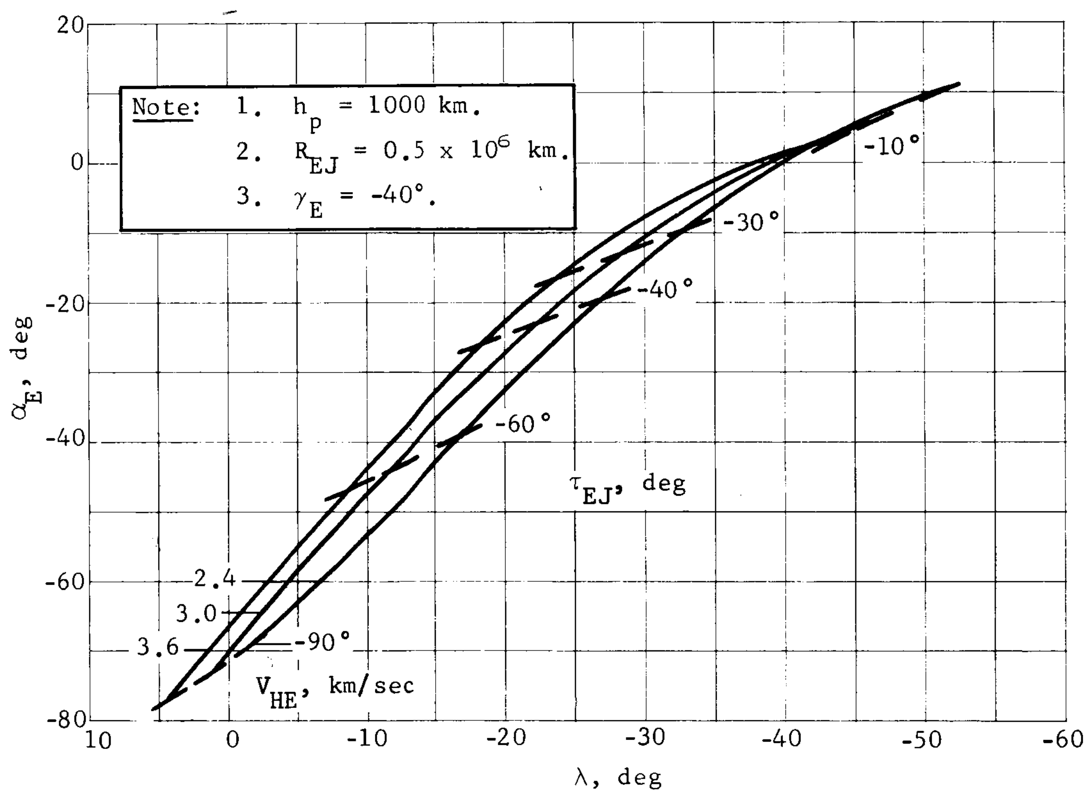

Figure A116.- Entry Angle of Attack (Direct Mode)

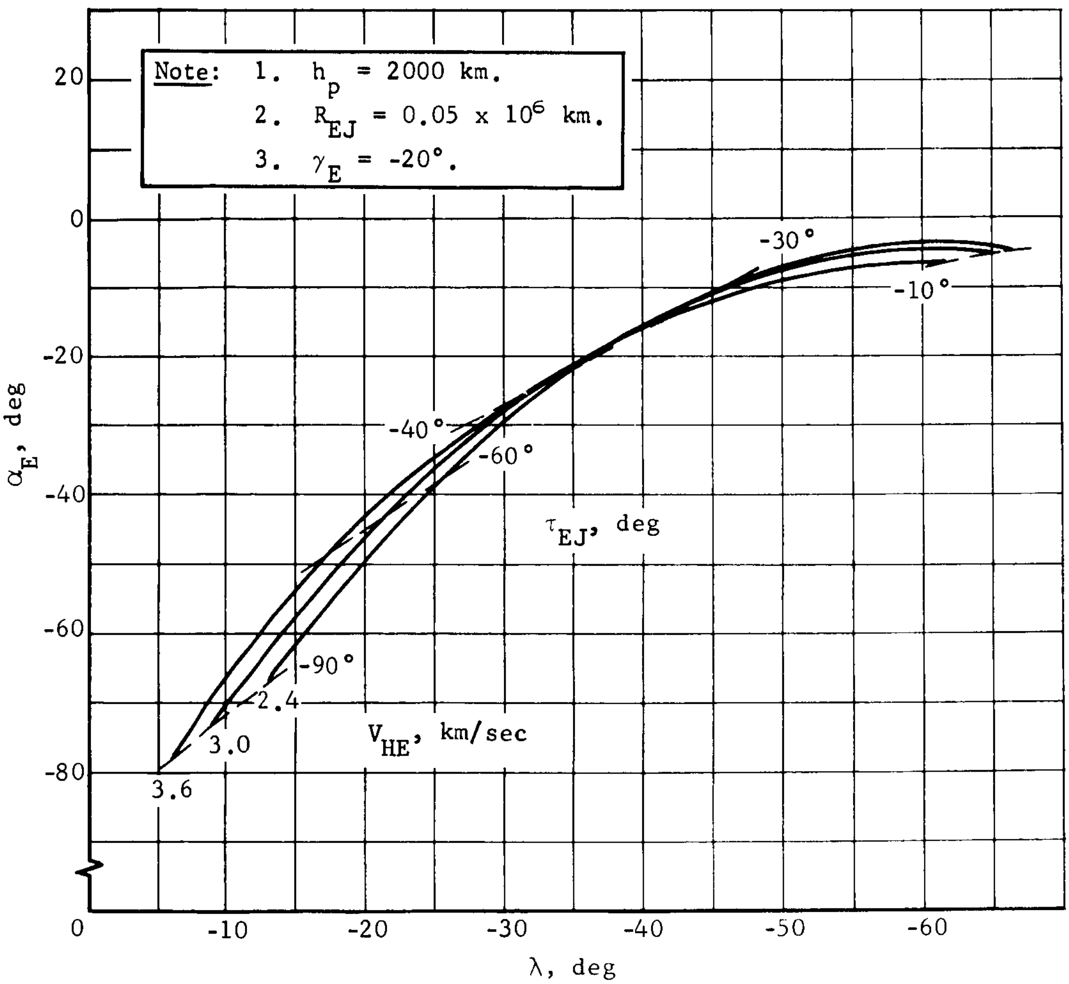

Figure A117.- Entry Angle of Attack (Direct Mode)

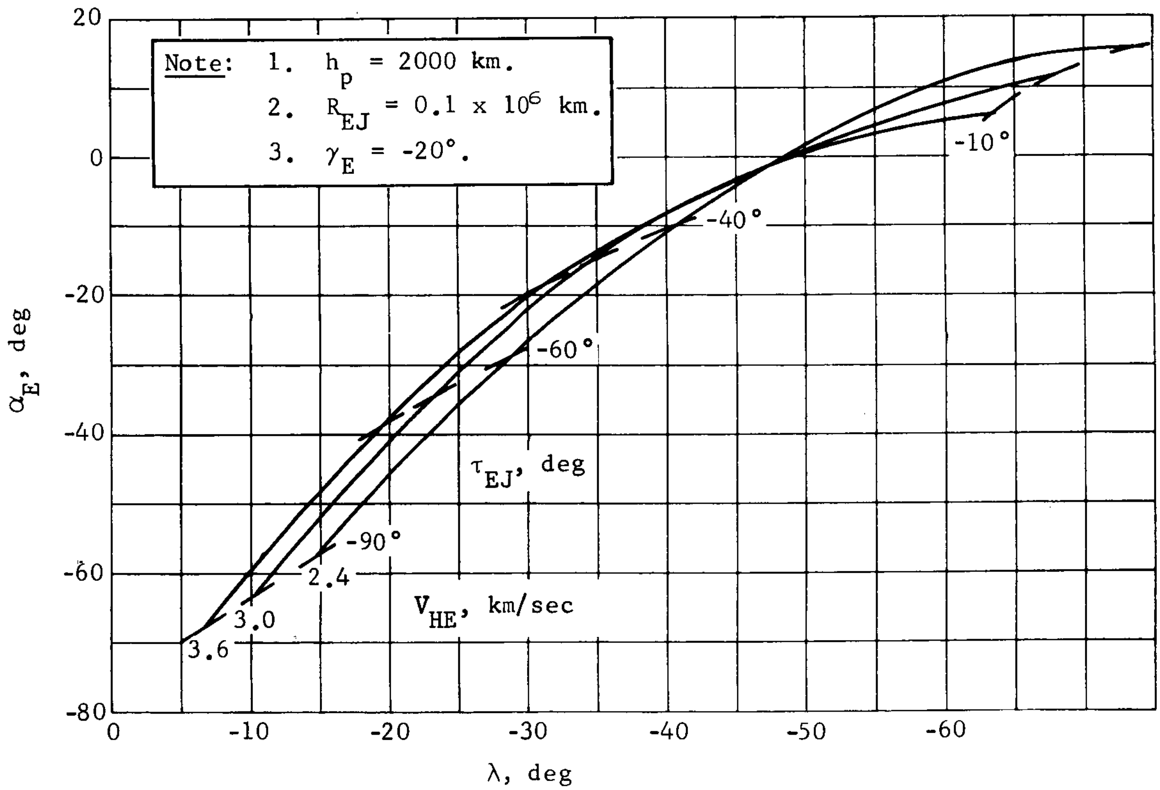

Figure A118.- Entry Angle of Attack (Direct Mode)

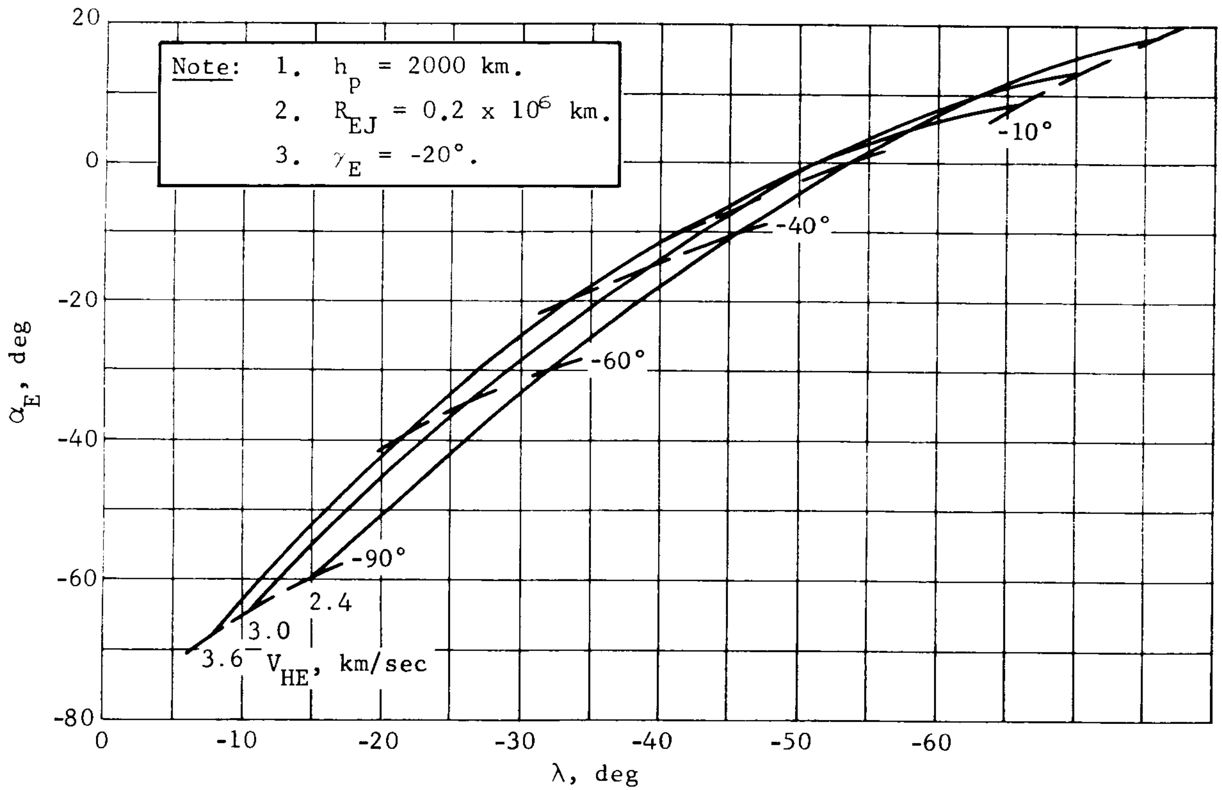

Figure A119.- Entry Angle of Attack (Direct Mode)

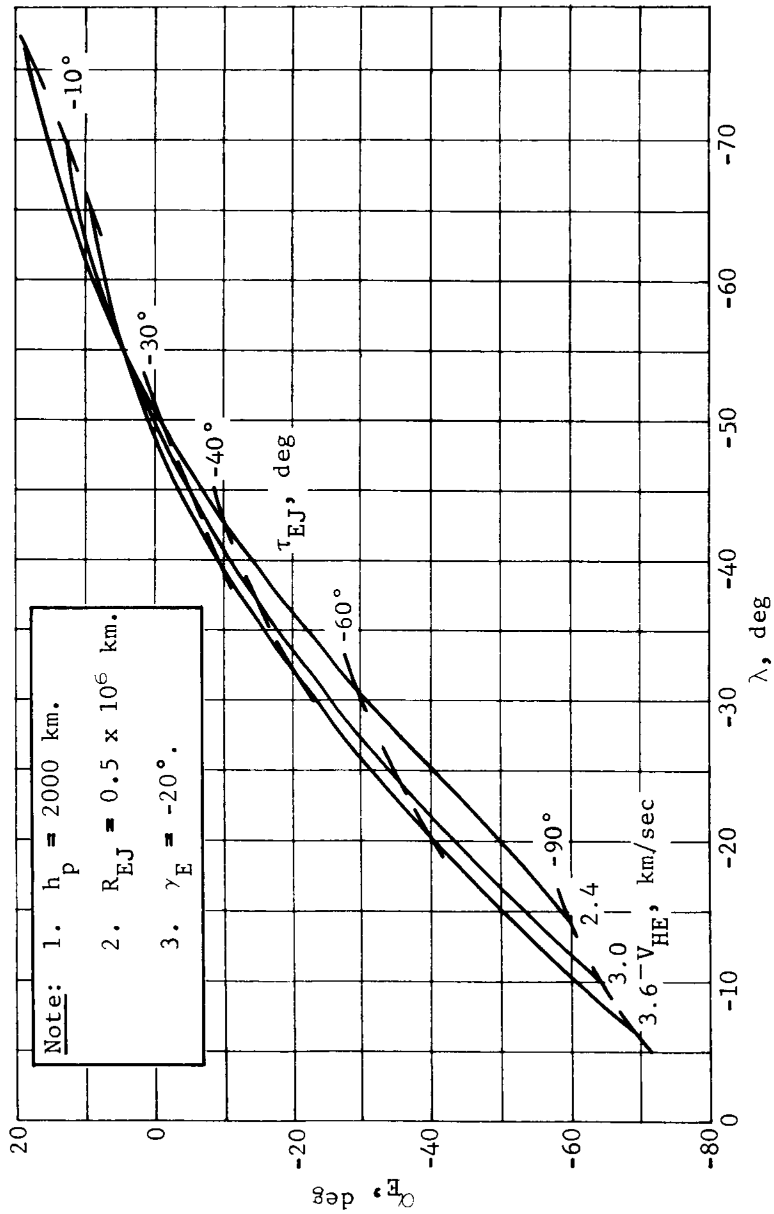

Figure A120.- Entry Angle of Attack (Direct Mode)

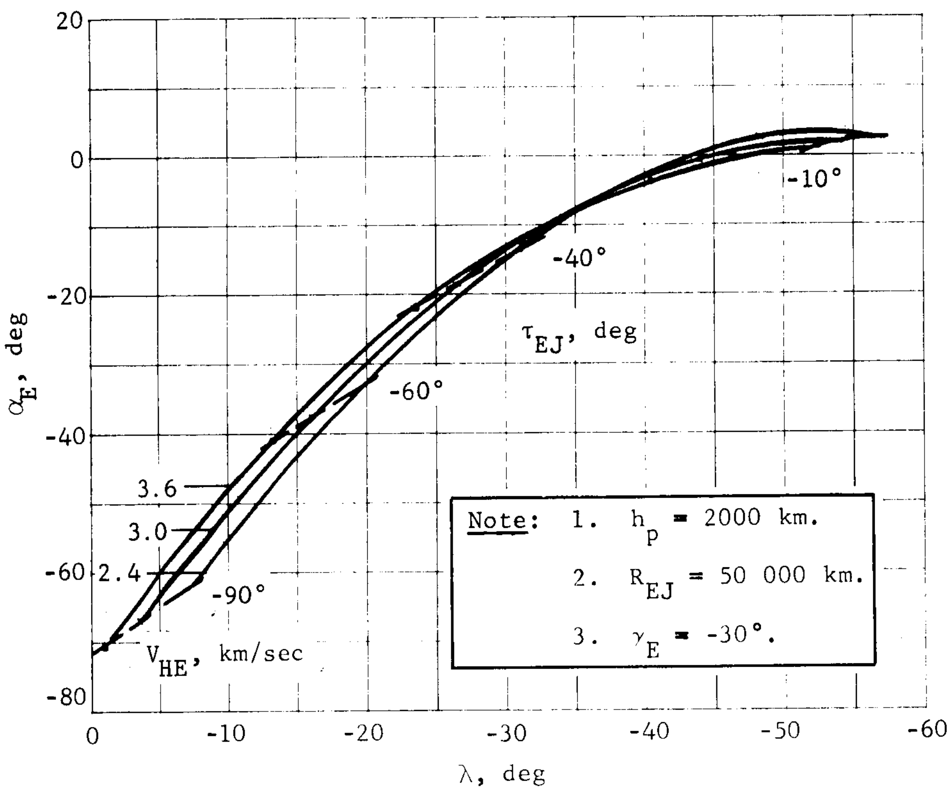

Figure A121.- Entry Angle of Attack (Direct Mode)

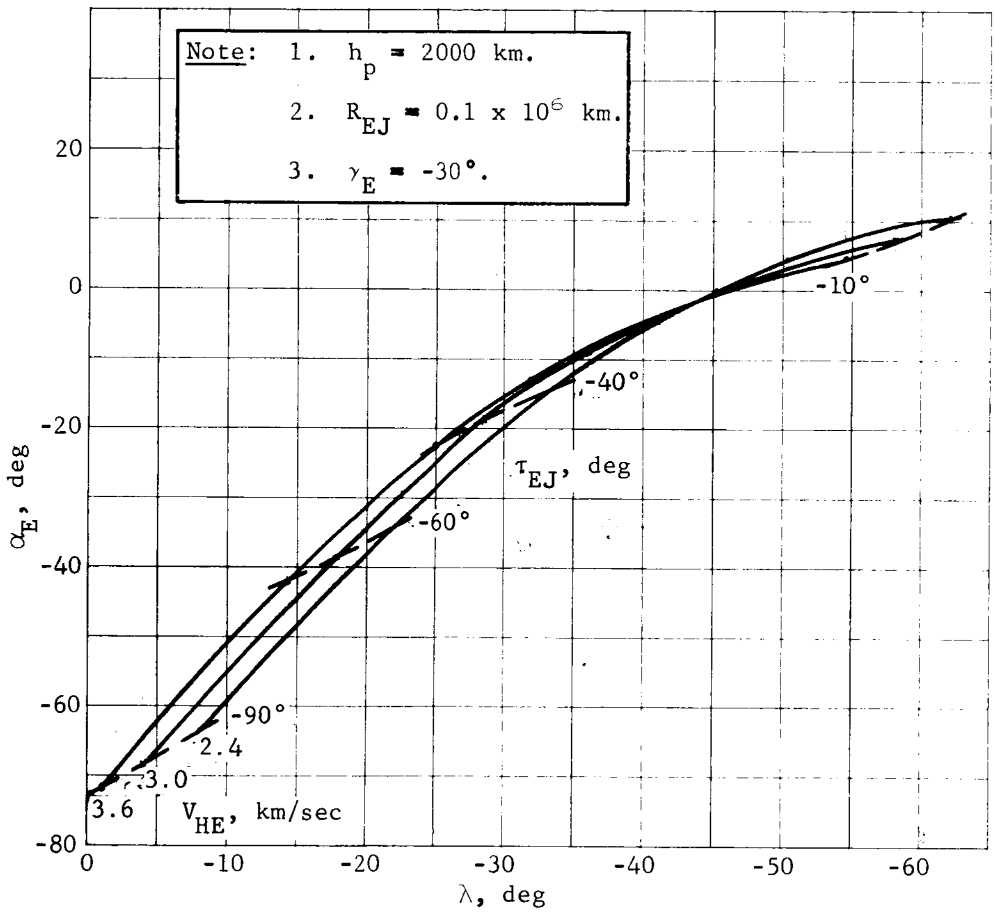

Figure A122.- Entry Angle of Attack (Direct Mode)

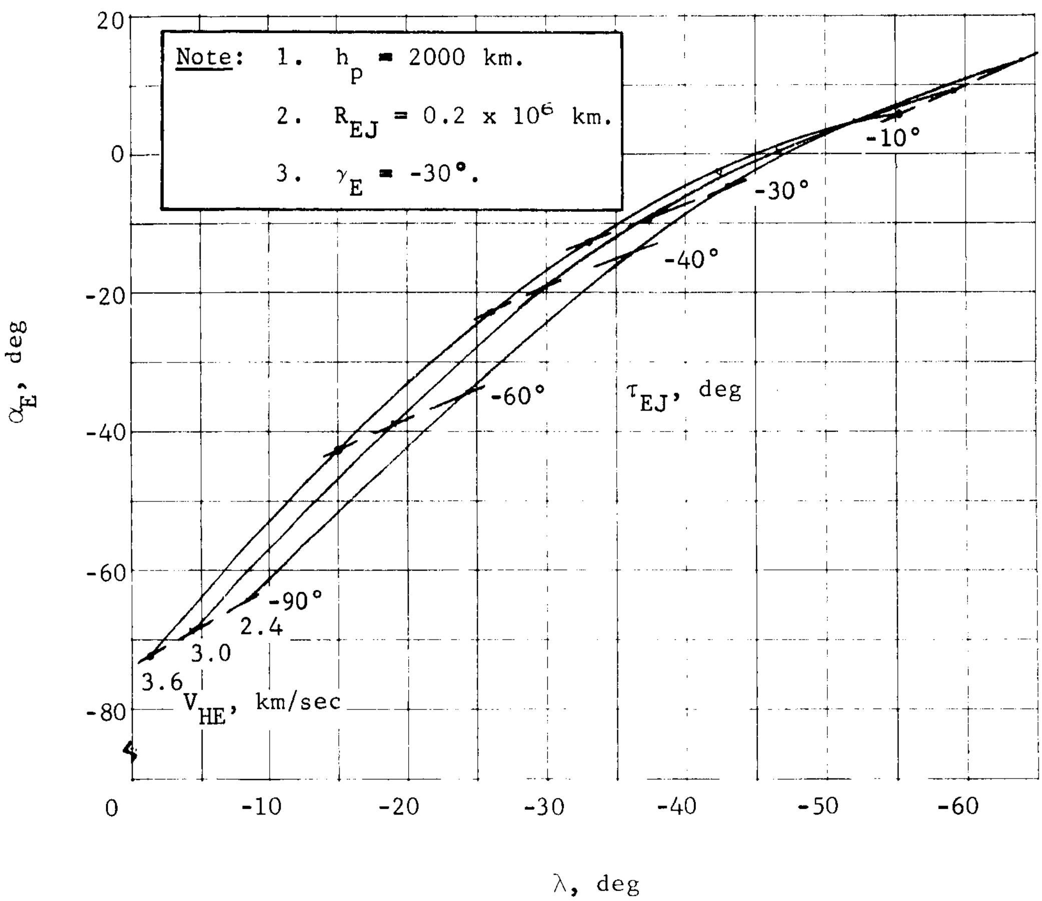

Figure A123.- Entry Angle of Attack (Direct Mode)

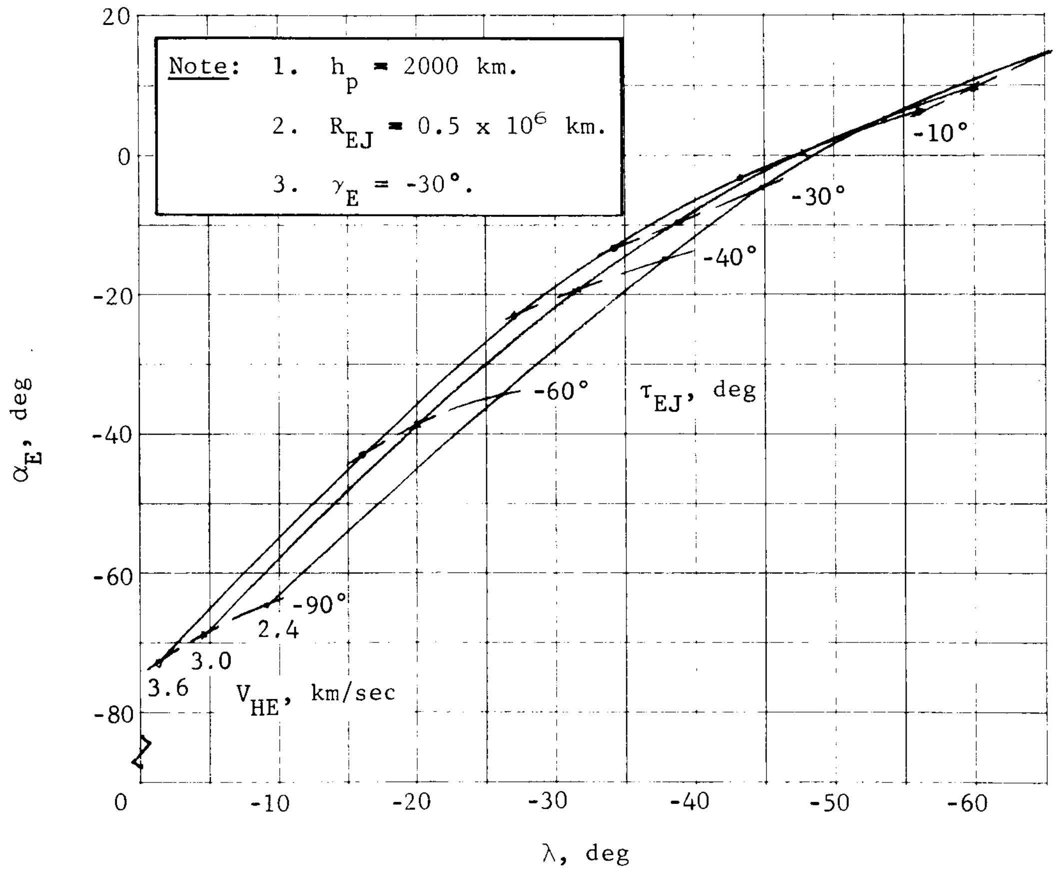

Figure A124.- Entry Angle of Attack (Direct Mode)

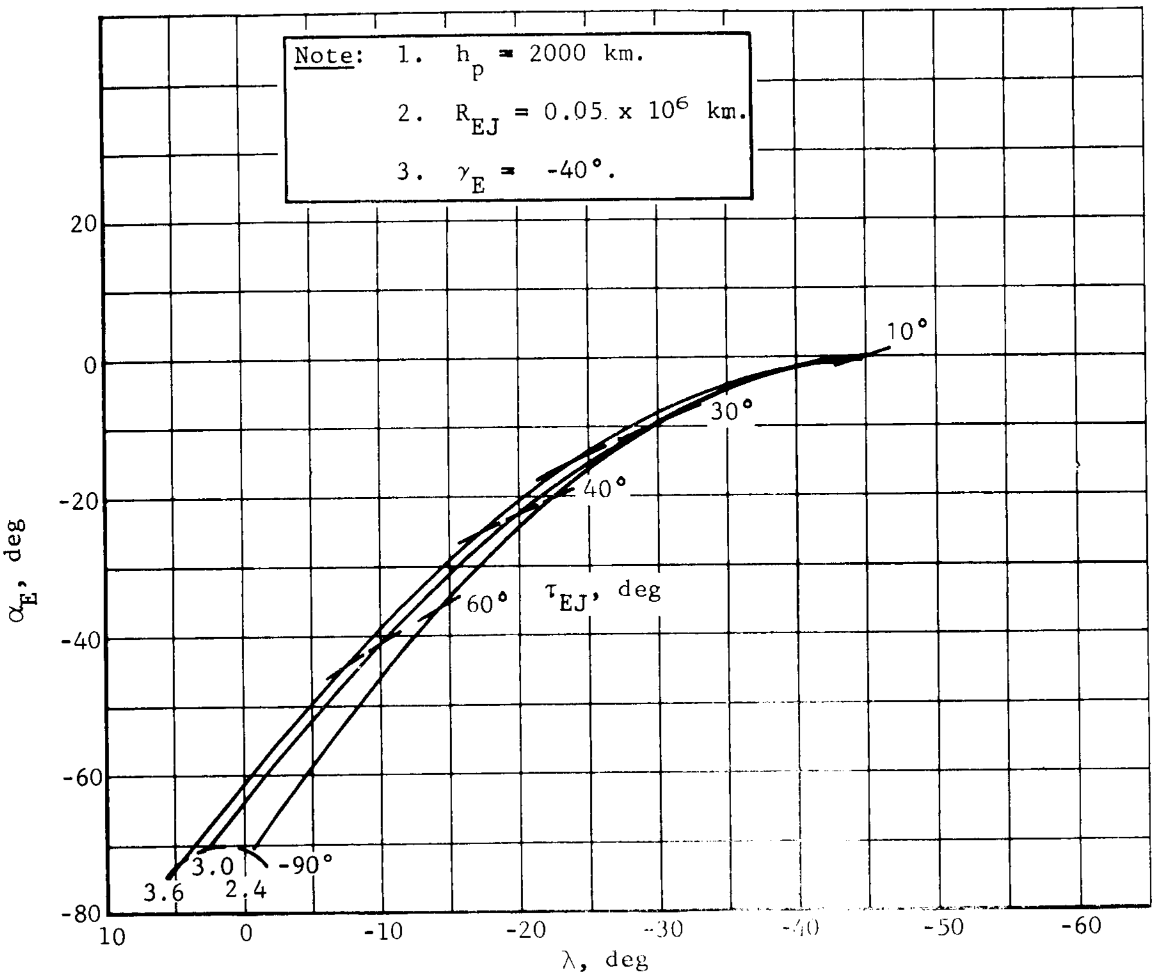

Figure A125.- Entry Angle of Attack (Direct Mode)

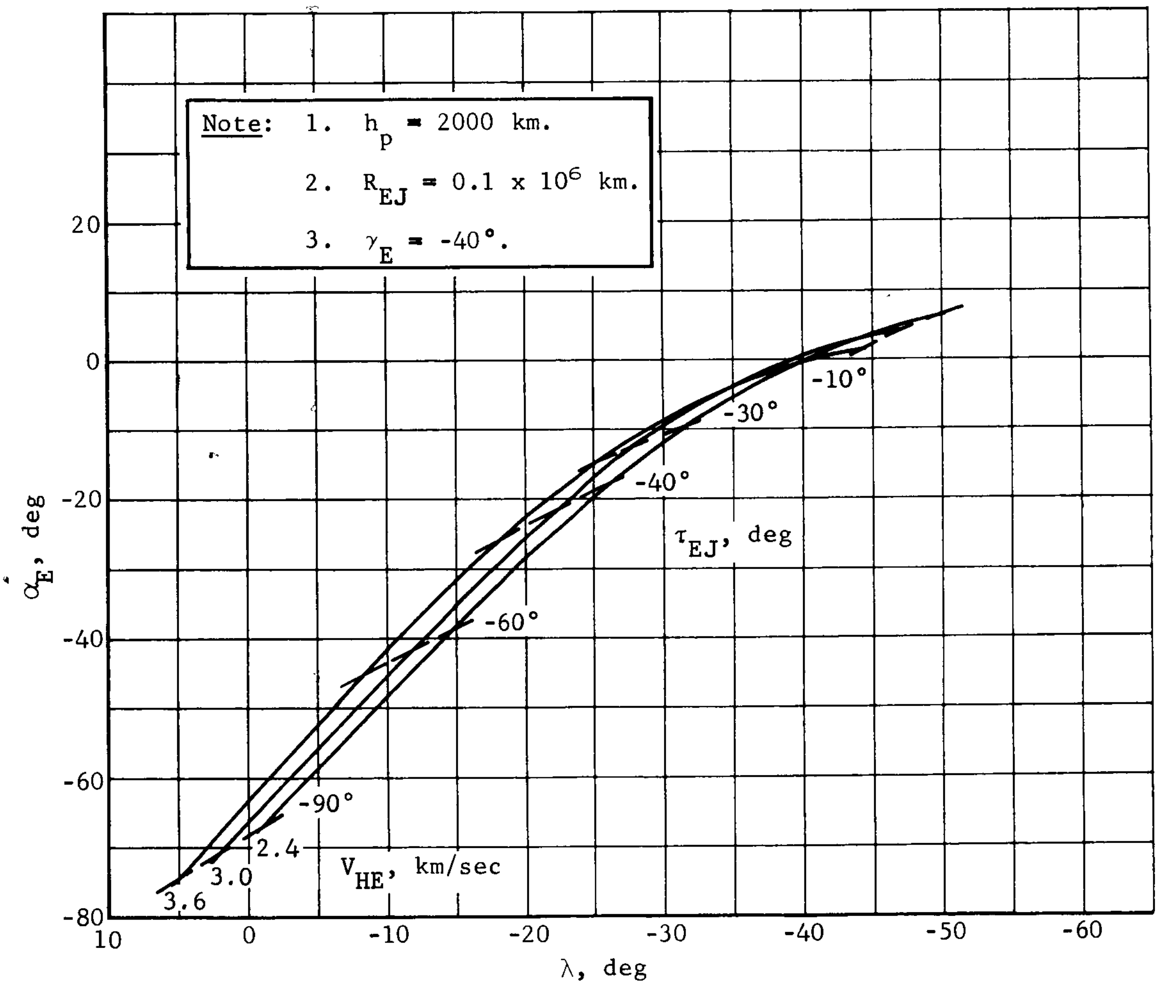

Figure A126.- Entry Angle of Attack (Direct Mode)

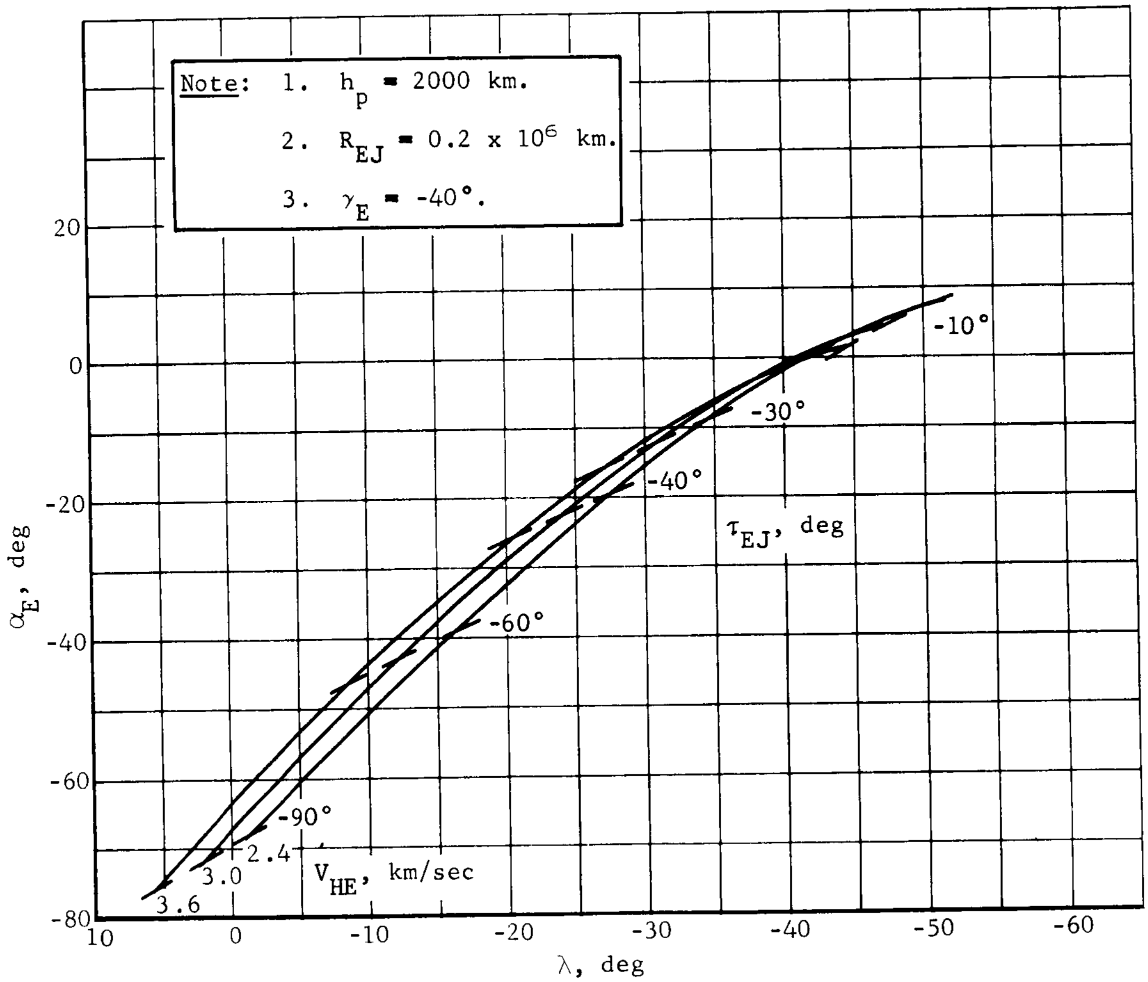

Figure A127.- Entry Angle of Attack (Direct Mode)

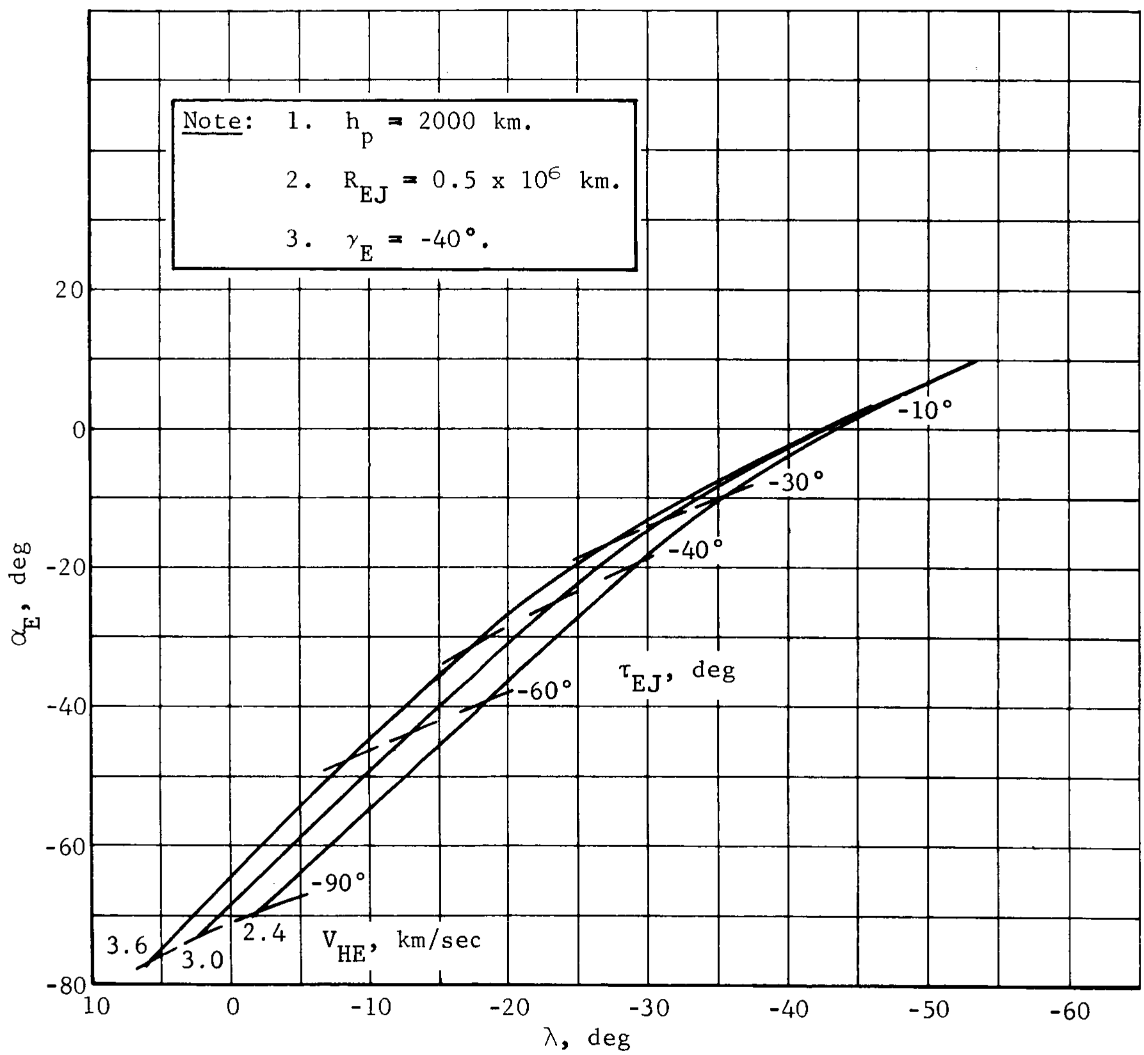

Figure A128.- Entry Angle of Attack (Direct Mode)

APPENDIX A

Relay Communication Link Constraints, Direct Mode

The geometry of the relay link during entry is shown in figure A129. The entry point is measured with respect to periapsis of the approach trajectory by β. The orbiter is shown lagging the capsule at the time of entry, that is a negative λ. The relay link antenna on the capsule is assumed along the longitudinal axis of the capsule. The capsule enters the atmosphere with a zero angle of attack. The system performance of the relay link is a function of range and antenna aspect angles (both capsule and orbiter). The capsule antenna aspect angle at entry, α_{CE}, is shown and is defined positive when measured counterclockwise from the capsule antenna centerline to the line of sight. The communication distance at entry, ρ_{CE}, is shown. Of importance in analyzing fading margin losses during entry is the angle the reflected signal from the Martian surface to the orbiter makes with the local vertical, θ_{FM}. This angle is almost always greatest at the time of entry. The fading margin losses become significant when θ_{FM} becomes greater than 60°. Also shown is the capsule antenna aspect angle at touchdown, $\alpha_{C_{TD}}$. This angle is a function of atmosphere encountered as well as β and λ. If an elevation mask at touchdown of 34° is assumed, then $\alpha_{C_{TD}}$ must be between -56° and 56° if the orbiter is to see the landing. The amount of intitial postlanding link time available is a maximum if $\alpha_{C_{TD}}$ is -56°, and zero if $\alpha_{C_{TD}}$ is 56°. Some initial link time is desirable to verify landing and also to get a few pictures out before the orbiter goes out of sight and the capsule goes into darkness. Near-equatorial landing sites 30° from the evening terminator are not in view of Earth. The λ is selected so that at least 5 min of initial link time is obtained with an elevation mask of 34° in the most critical atmosphere. The most critical atmosphere is VM-3 since the entry time is the longest.

All of the parameters discussed can be shown as a function of β and λ for a given approach trajectory. Boundaries are shown in figure A130 for an h_p of 1000 km and a V_{HE} of 3.0 km/sec. It should be recalled that β is directly a function of γ_E and the β corresponding to γ_E of -20°, -30°, and -40° are shown.

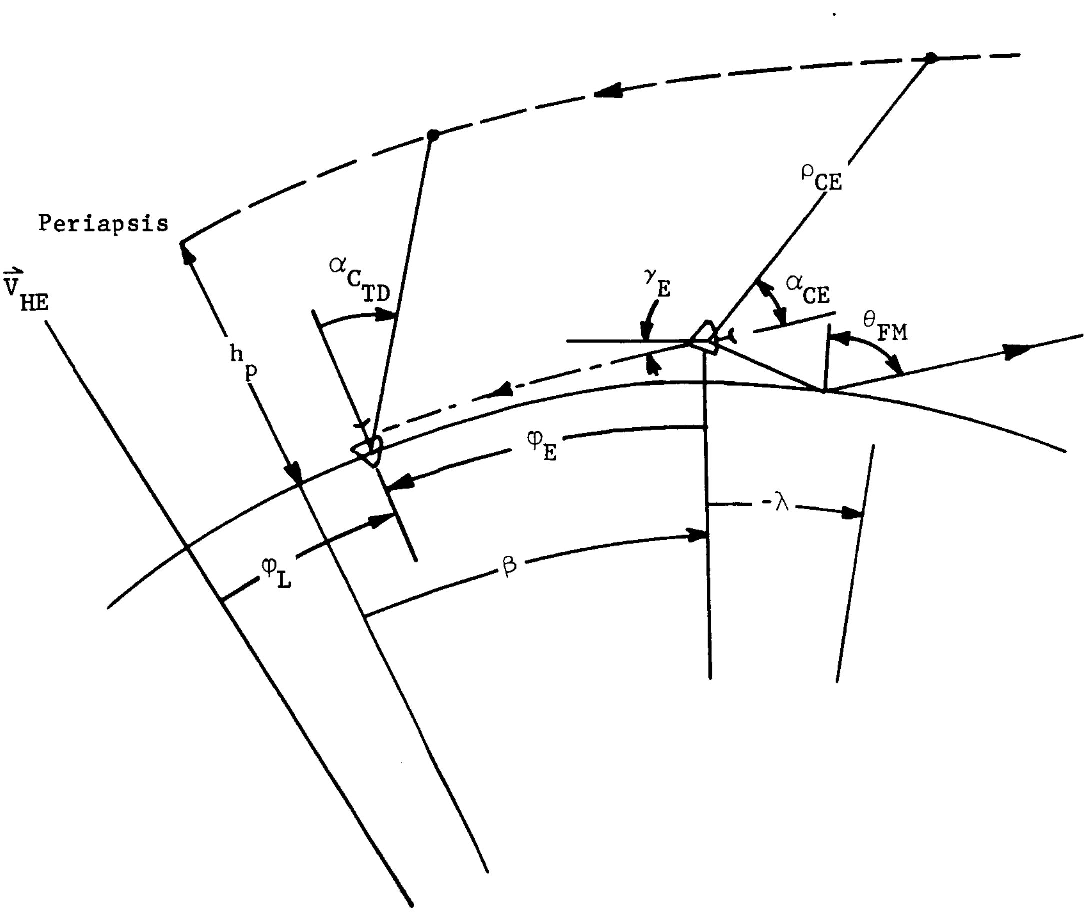

Figure A129.- Relay Communication Link during Entry

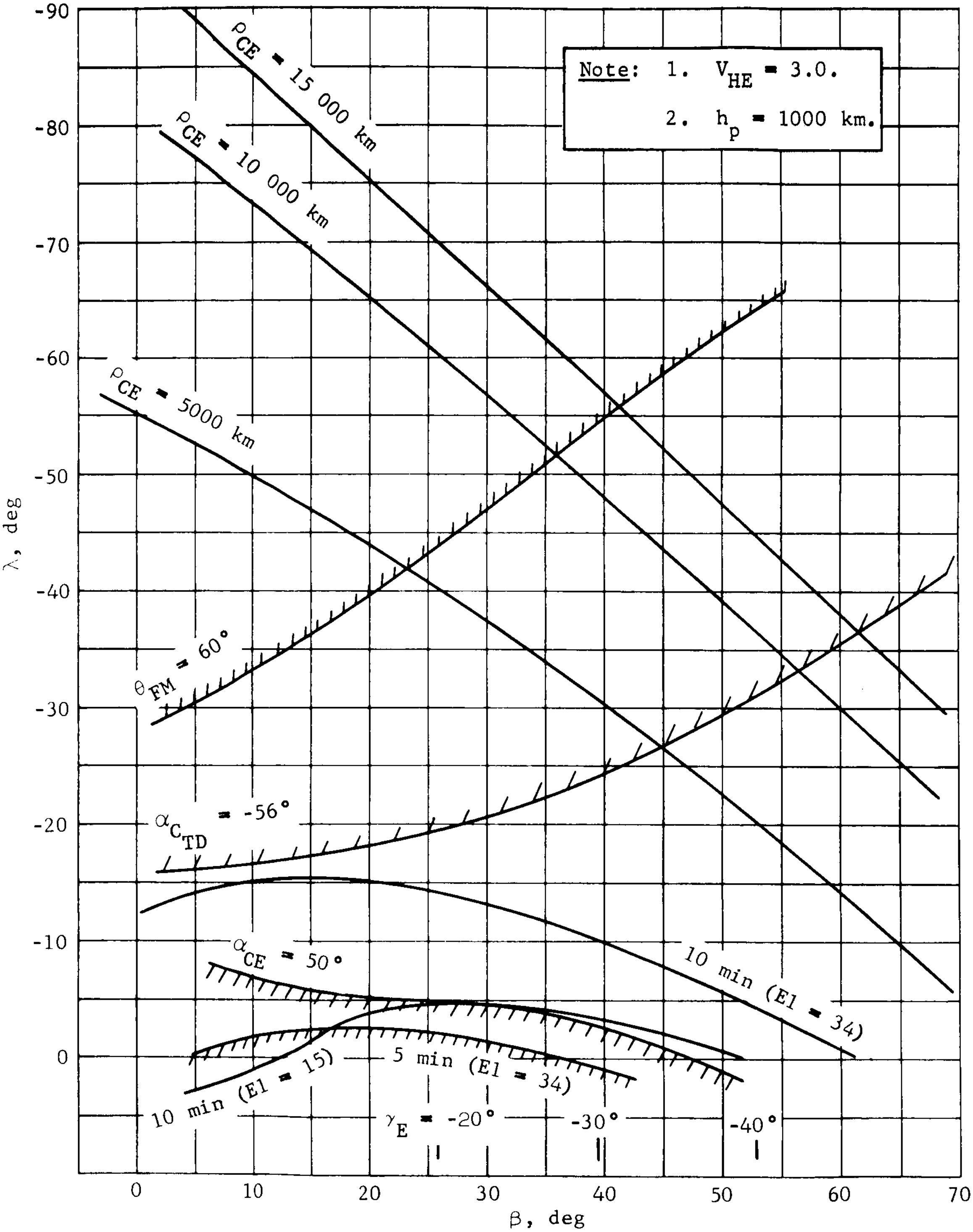

(a) No Overlay

Figure A130.- Relay Communication Link Boundaries (Direct Mode)

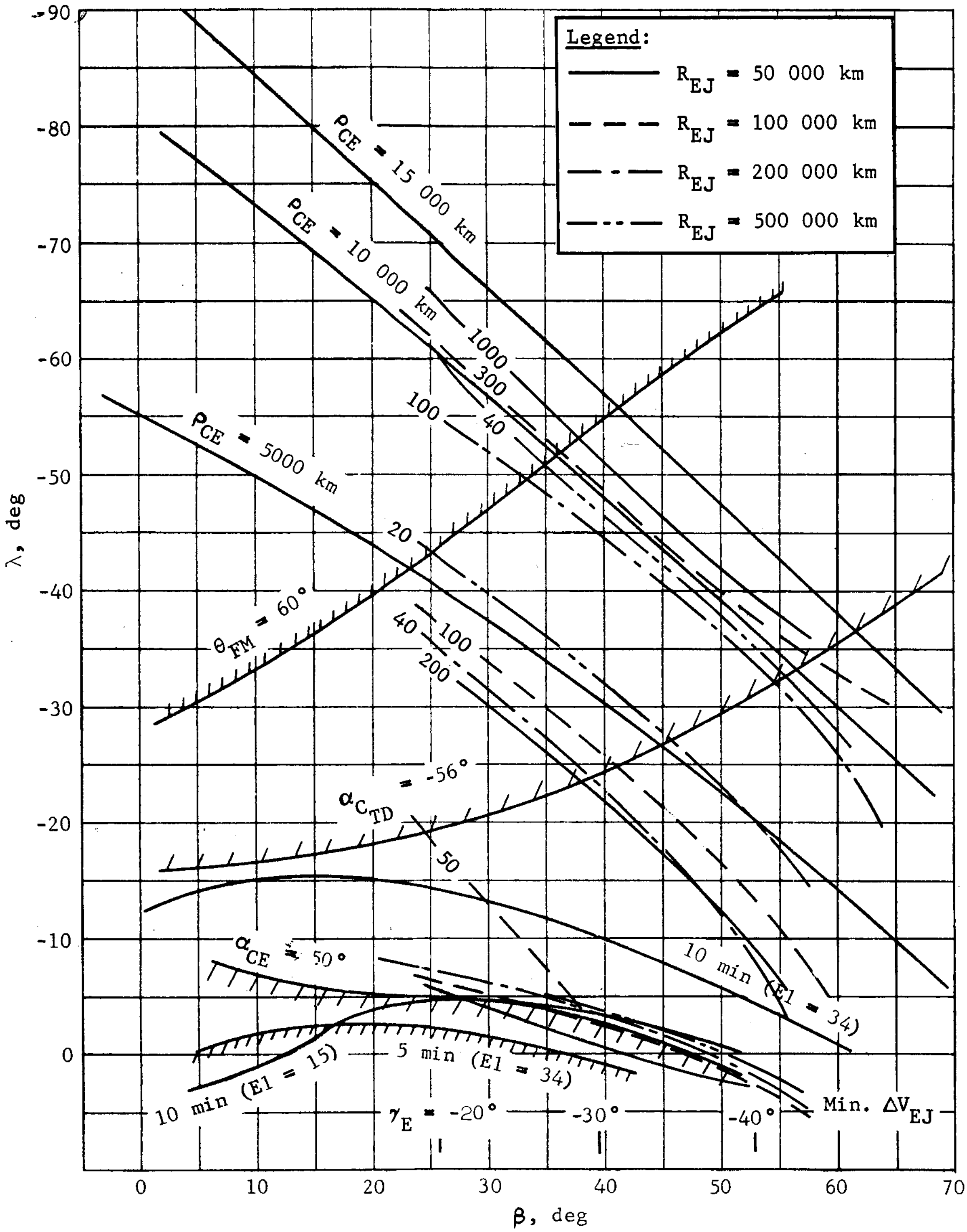

(b) Ejection ΔV (m/sec), Overlay 1

Figure A130.- Continued

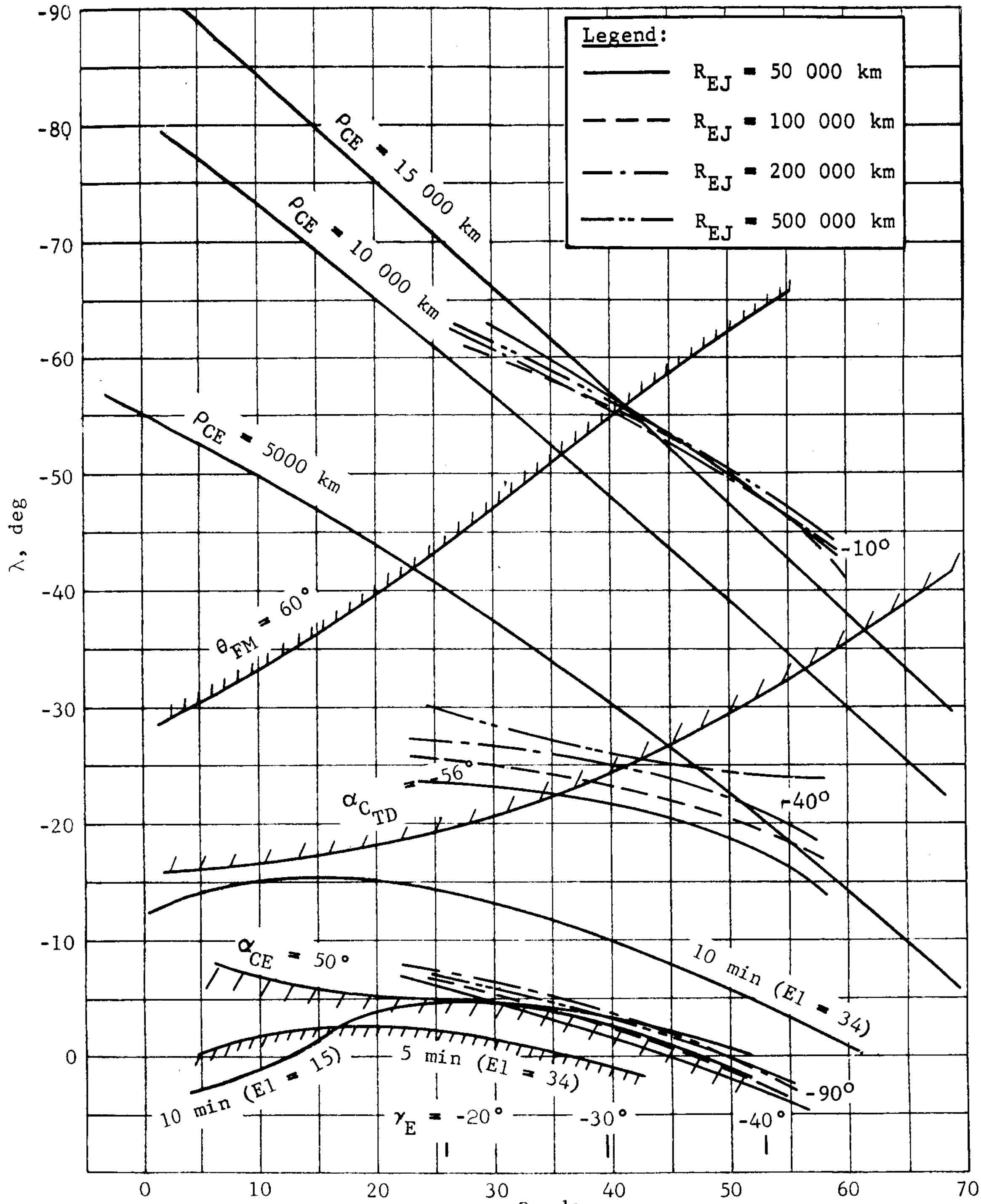

(c) Ejection Angle, τ_{EJ}, Overlay 2

Figure A130.- Continued

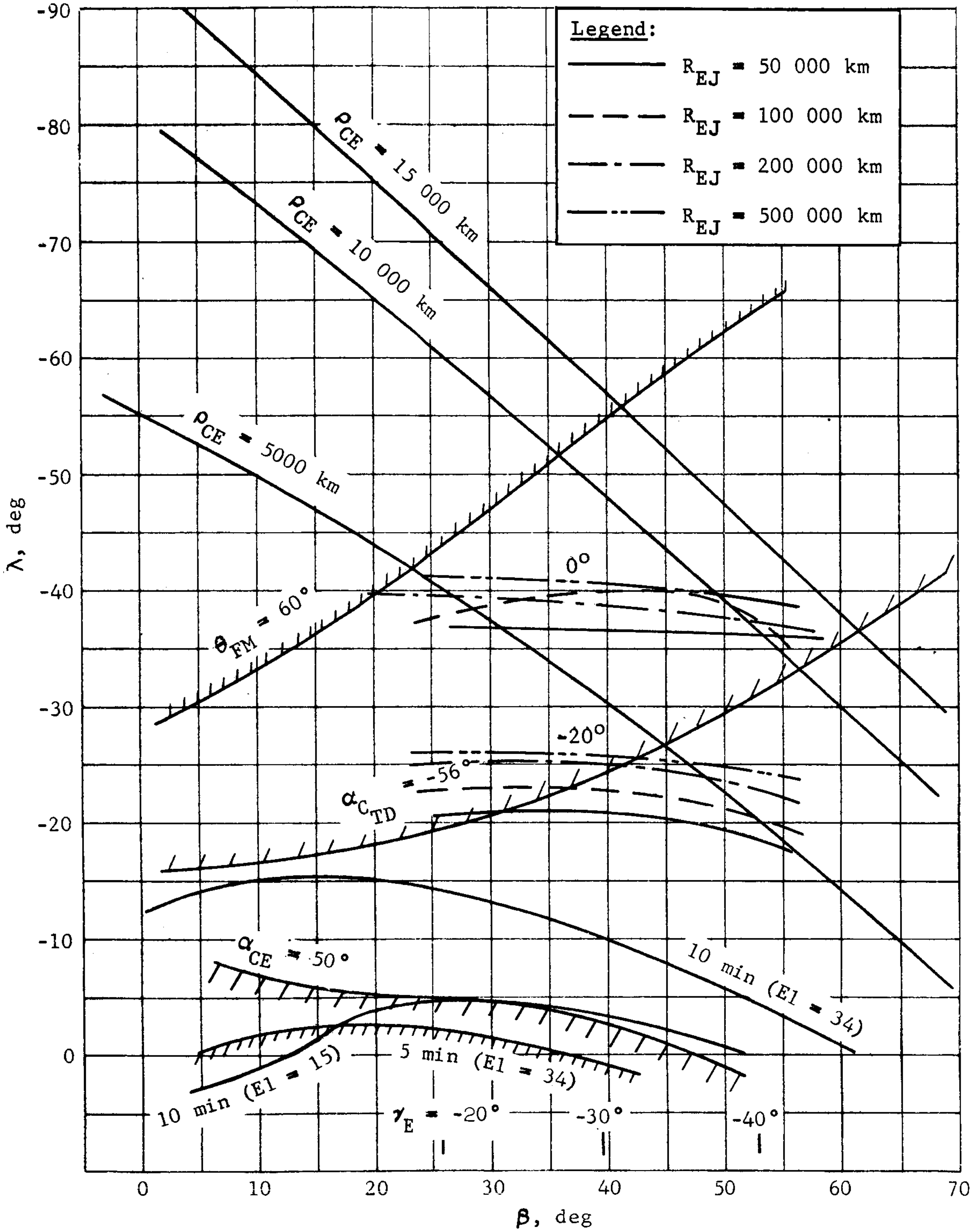

(d) Entry Angle of Attack, α_E, Overlay 3

Figure A130.- Concluded

The ρ_{CE} only becomes important for steeper γ_E. The $\alpha_{C_{TD}} = -56°$ boundary is always below the fading margin boundary and is below the ρ_{CE} of 5000 km boundary until a γ_E of about -34°. Over the range of γ_E considered in this study (-20° to -38°) the $\alpha_{C_{TD}}$ of -56° is taken to be the design upper limit on λ. The $\alpha_{C_{TD}}$ boundary is a function of atmosphere and VM-8, shortest entry time, is the limiting case. For a γ_E of -20° the allowable range of λ is -2.5° to -19.5°. For a γ_E of -38° the range of λ is about +4° to -22°. To keep the α_{CE} less than 50°, and thus the capsule beamwidth, with a γ_E of -20° the λ must be greater than -5°. Any λ above -14° would give at least 10 min of initial postland link time with an elevation mask of 34°.

The ejection ΔV requirements are given in overlay 1 (fig. A130). For a γ_E of -20° and an R_{EJ} of 100 000 km a λ of -17.5° is obtained with a ΔV_{EJ} of 50 m/sec. The ejection angle, τ_{EJ}, is shown in overlay 2 (fig. A130) and is seen to be always greater than -40° for the required range of λ. The minimum ΔV_{EJ} occurs very close to a τ_{EJ} of -90°. Section 3 of Appendix A shows that the entry dispersions due to pointing errors at ejection are minimized for τ_{EJ} of -90°. The entry angle of attack, α_E, is shown in overlay 3 (fig. A130). If a spin-stabilized system were used, the α_E would always be greater, in absolute value, than -20° for the selected range of λ.

Boundaries of communication parameters for V_{HE} of 2.4 and 3.6 km/sec are shown in figures A131 and A132. The $\alpha_{C_{TD}} = -56°$ boundary is almost unchanged with V_{HE} while the 5-min line lowers with increasing V_{HE}. The $\alpha_{CE} = 50°$ line raises with increasing V_{HE}. The effect of a higher periapsis altitude is shown in figure A133. The $\alpha_{C_{TD}} = -56°$ and $\alpha_{CE} = 50°$ are raised slightly.

APPENDIX A

The 5-min elevation of 34° line is below the λ scale and only the 10-min line is shown. The ρ_{CE} for a γ_E of -20° is still less than 5000 km. The major effect of higher h_p is longer initial postlanding link times.

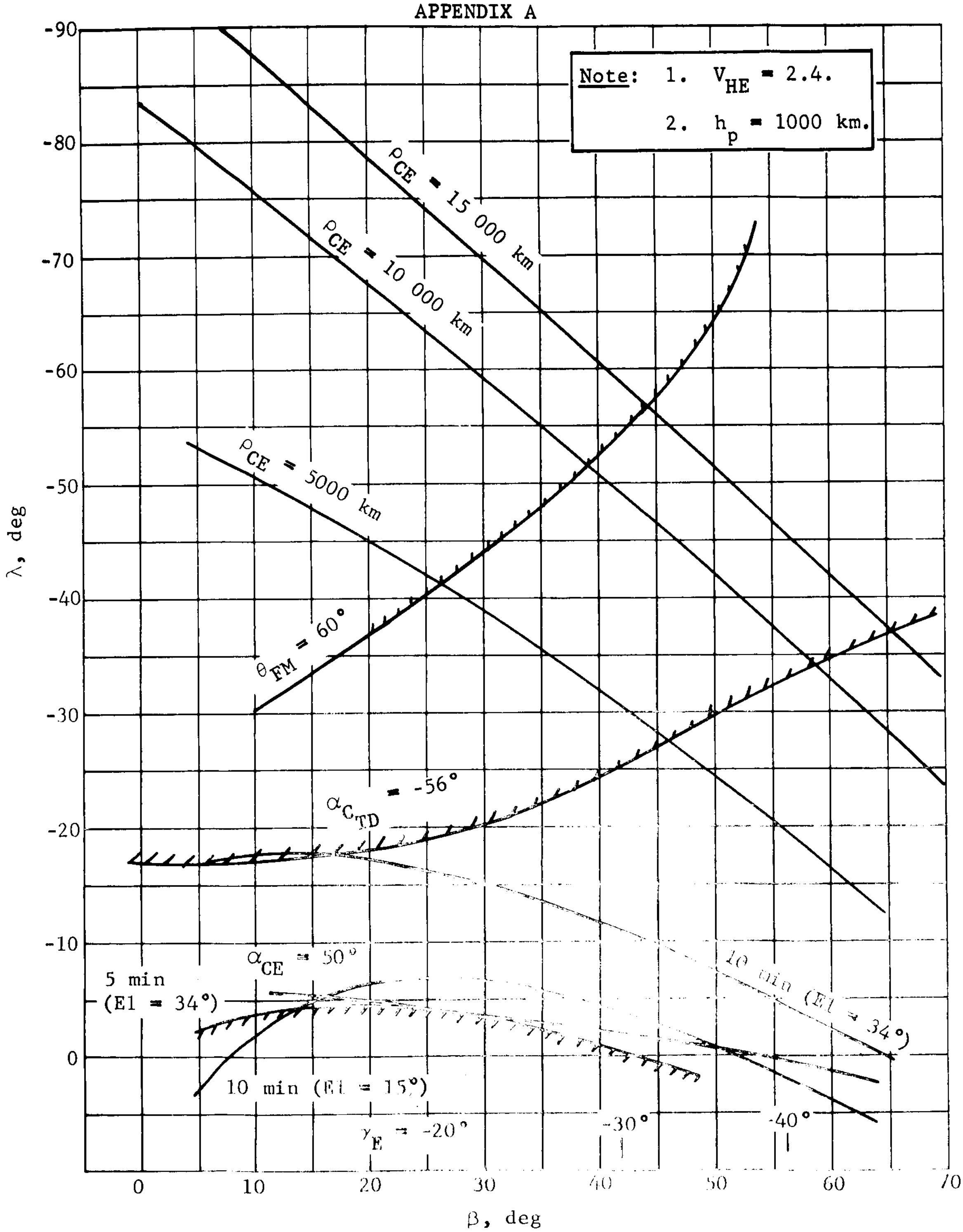

Figure A131.- Relay Communications Link Boundaries (Direct Mode)

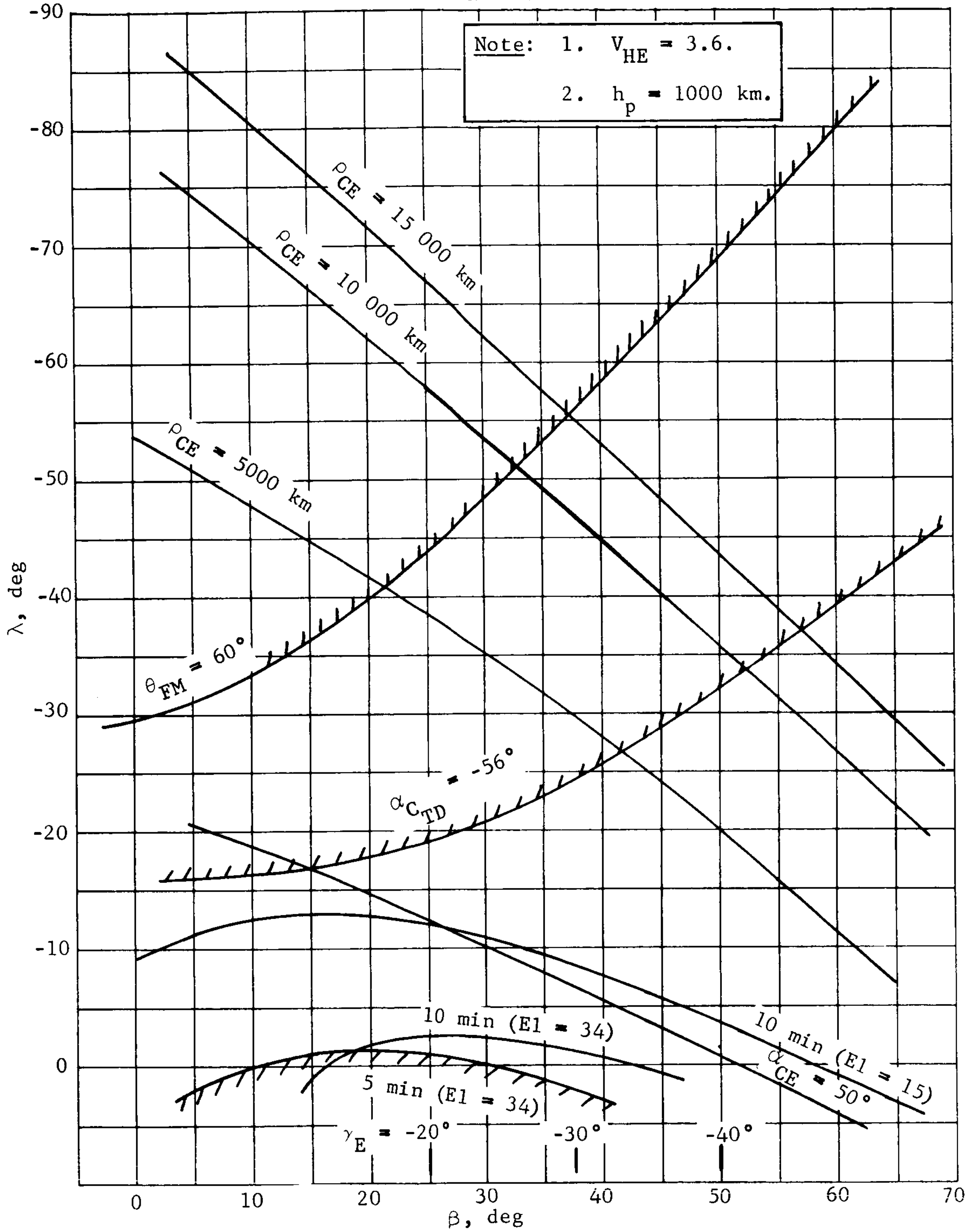

Figure A132.- Relay Communications Link Boundaries (Direct Mode)

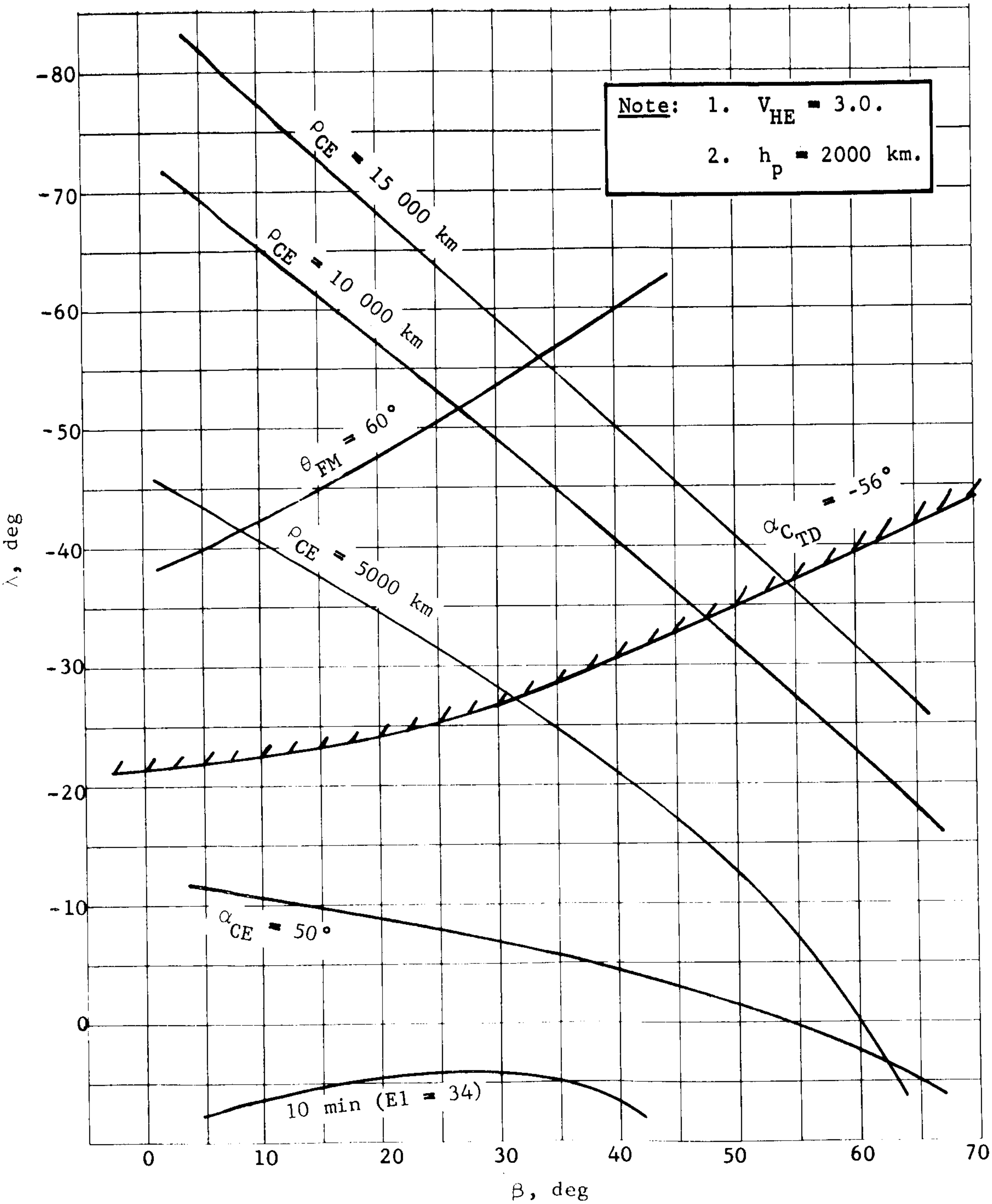

Figure A133.- Relay Communications Link Boundaries (Direct Mode)

APPENDIX A

Deorbit Requirements, Orbit Mode

The deorbit requirements are given for the two reference orbits: (1) 1000 x 33 070 km (e = 0.785, period = 24.62 hr), and (2) 1000 x 15 000 km (e = 0.614, period = 10.25 hr). For orbit (1) γ_E of -15.5°, -18.4°, and -20.3° are studied, and for orbit (2) γ_E of -15°, -17.7°, and -19.7°. The shallowest γ_E in both cases is 2.5° above the skipout boundary. The minimum γ_E is taken to be 5σ above the skipout boundary to reduce landing site dispersions. It is shown in section 3 of this appendix that the 1σ error in γ_E can be controlled to 0.5° for both orbits. The entry velocities are 15 000 fps and 14 400 fps, respectively, for orbits (1) and (2).

The minimum deorbit impulse, $\Delta V_{D_{min.}}$, is shown as a function of β and γ_E for both orbits in figure A134. The usefulness of using γ_E to increase the range of β is seen. Unlike the direct mode β can also be varied with deorbit impulse, ΔV_D. The $\Delta V_{D_{min.}}$ does not result in an acceptable relay link during entry for all β, however, and other deorbit maneuver strategies must be investigated. The allowable range of γ_E is limited on the shallow end by the skipout boundary and by the dispersions in γ_E due to navigation uncertainty at deorbit and maneuver execution errors. The maximum allowable γ_E for a given landed equipment weight is a function of design aeroshell diameter and is discussed in appendix B.

The deorbit true anomaly, θ_D, is shown for orbit (1) with a γ_E of -15.5° in figure A135 as a function of λ for β between 26° and 34°. The θ_D which results in $\Delta V_{D_{min.}}$ is shown. As pointed out previously, using $\Delta V_{D_{min.}}$ for every β does not result in a favorable relay communication link. For example, a β of 34° would result in a λ of -42.5° for the $\Delta V_{D_{min.}}$ strategy. This is shown to be unacceptable as discussed later. The curves terminate when θ_D is such that a parabolic transfer occurs from deorbit to entry. For θ_D greater than this cutoff the transfer is hyperbolic. Only elliptical deorbit trajectories were studied. If the λ were to be restricted to a maximum of -17.5° the θ_D variation is as shown.

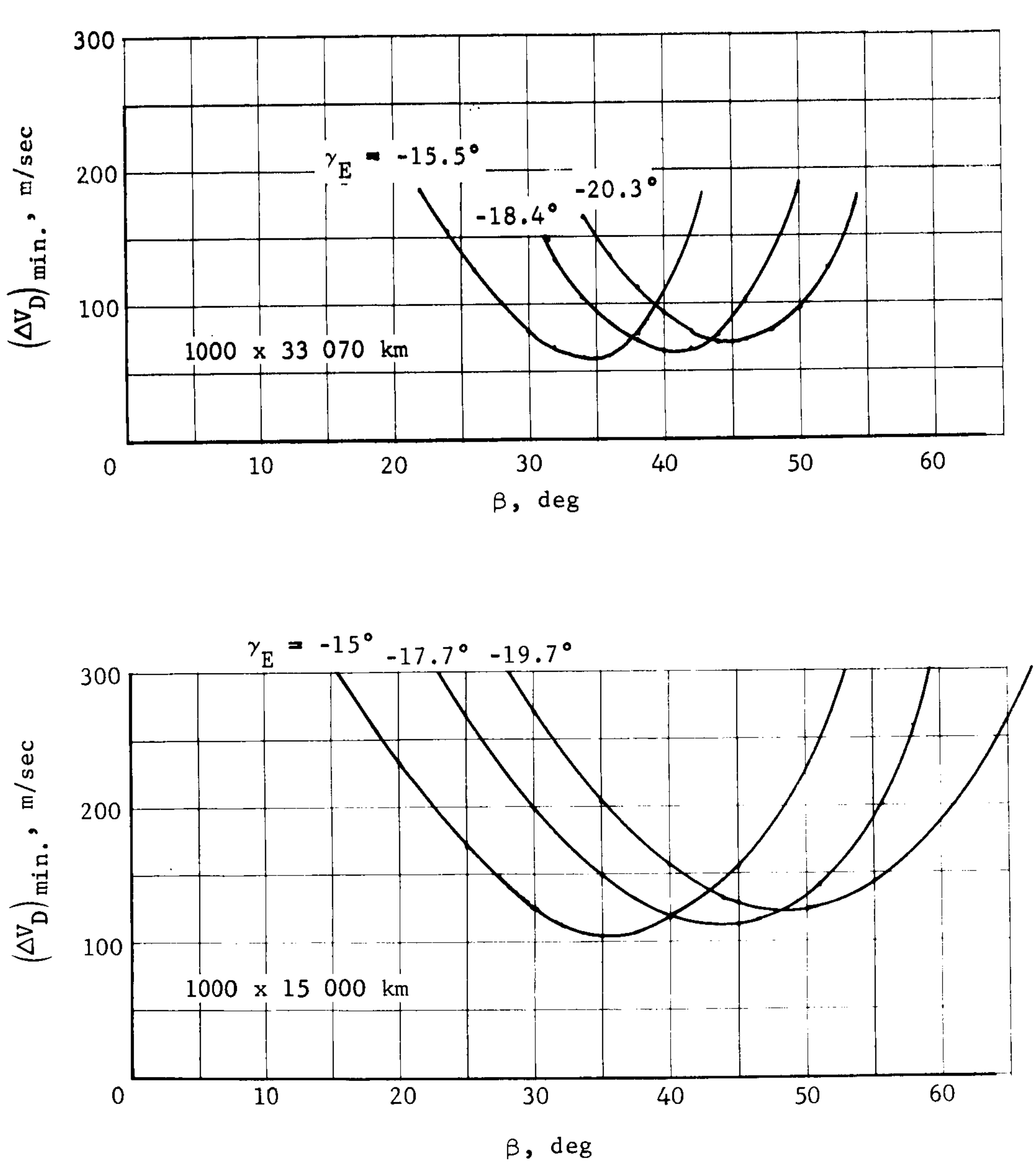

Figure A134.- Minimum ΔV_D Requirements

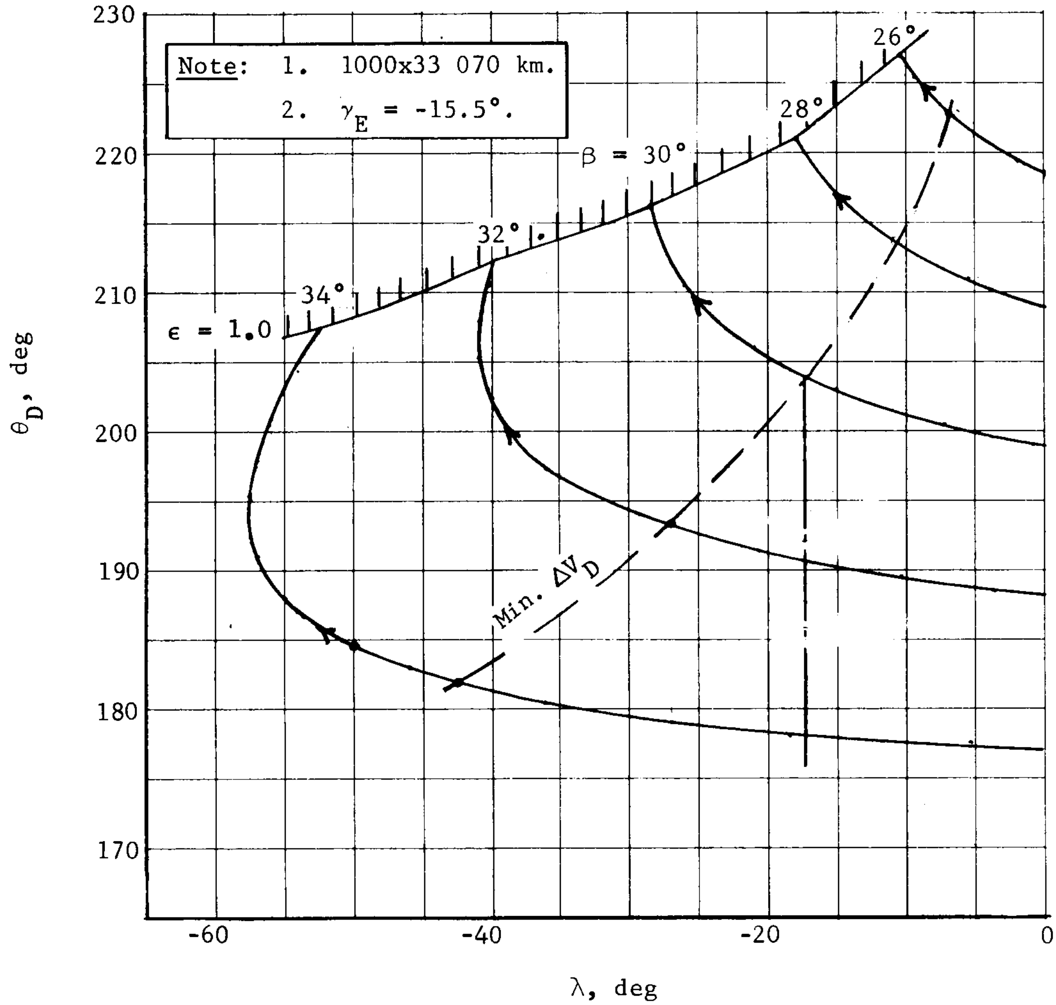

Figure A135.- True Anomaly versus Lead Angle

The ΔV_D variation with λ is shown in figure A136. Again the $\Delta V_{D_{min.}}$ line is shown. The variation of angle of attack at entry, α_E, assuming a spin stabilized capsule is shown in figure A137. It is seen that low β result in high α_E. The coast time, time from deorbit to entry, is very sensitive to β and is shown in figure A138. It is desirable to keep t_c under 8 hr for G&C considerations. The ΔV_D, α_E, and t_c are shown for γ_E of -18.4 and -20.3° in figures A139 thru A144. The curves are similar but the magnitude of β applicable increases with increasing γ_E. Similar data are presented for orbit (2) in figures A145 thru A154. The major difference between orbits (1) and (2) is that a coast time of 8 hr is not obtained with orbit (2) until large β. A ΔV_D requirement of 150 m/sec is reached before a t_c of 8 hr.

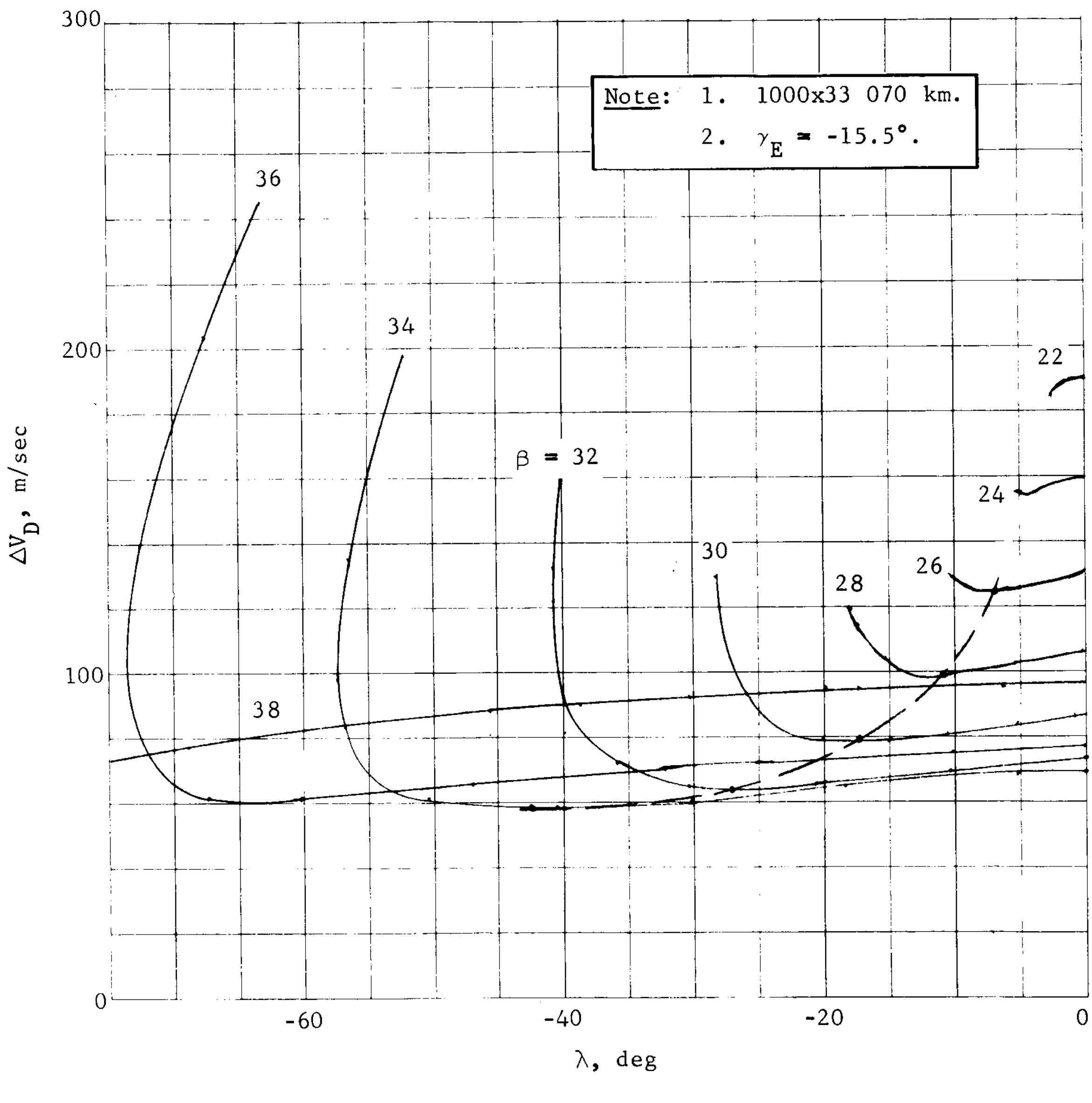

Figure A136.- ΔV_D versus Lead Angle

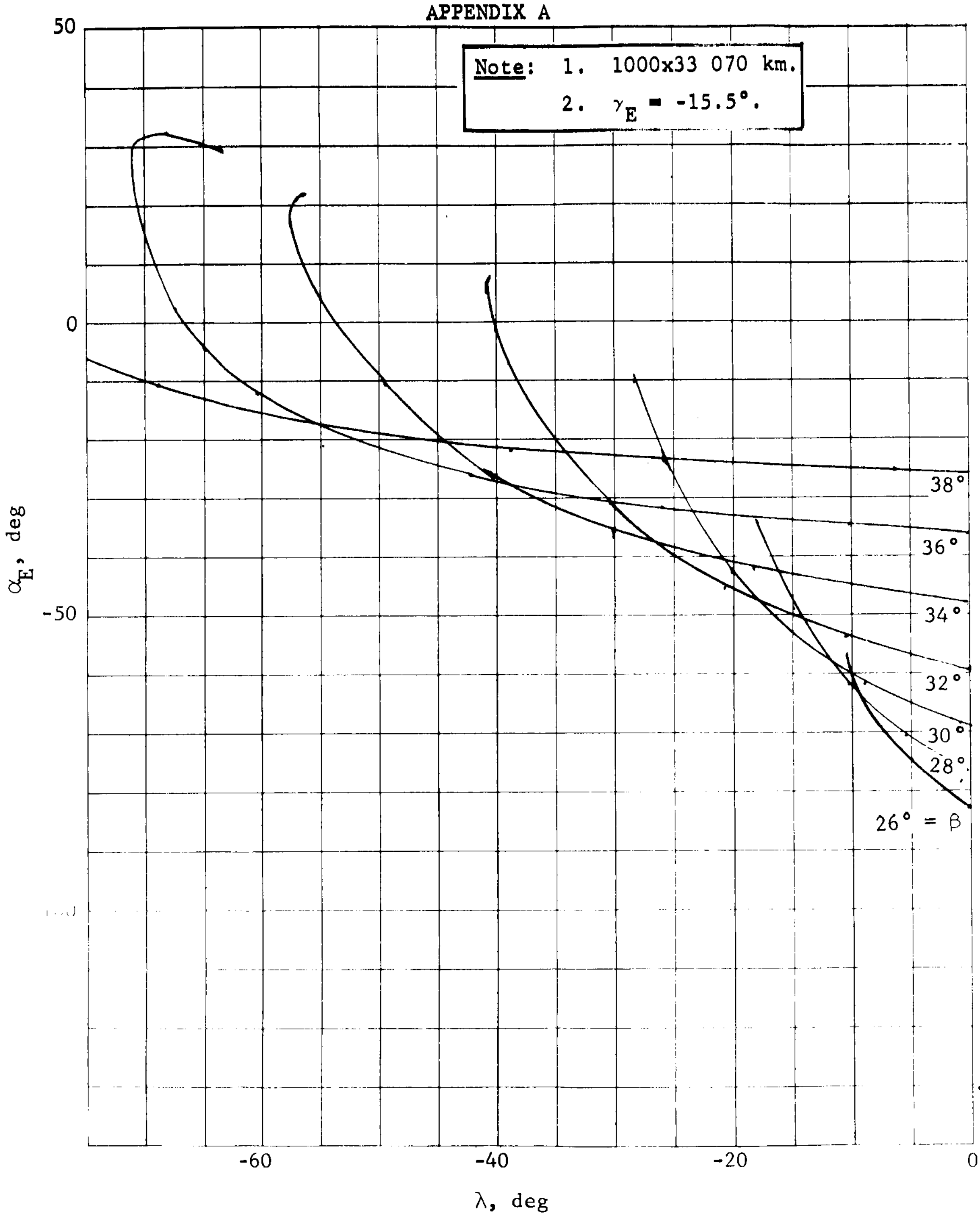

Figure A137.- Angle of Attack versus Lead Angle

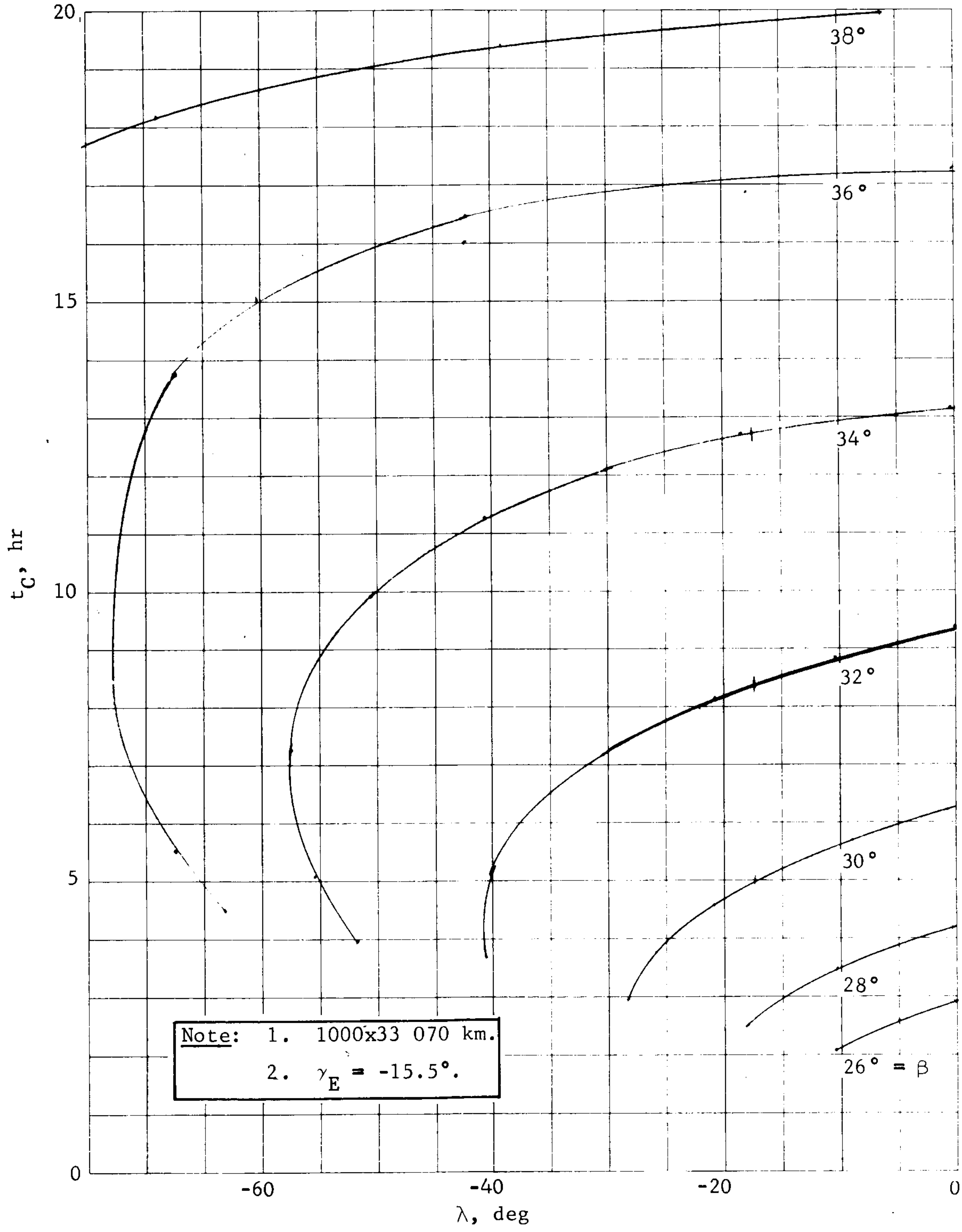

Figure A138.- Coast Time versus Lead Angle

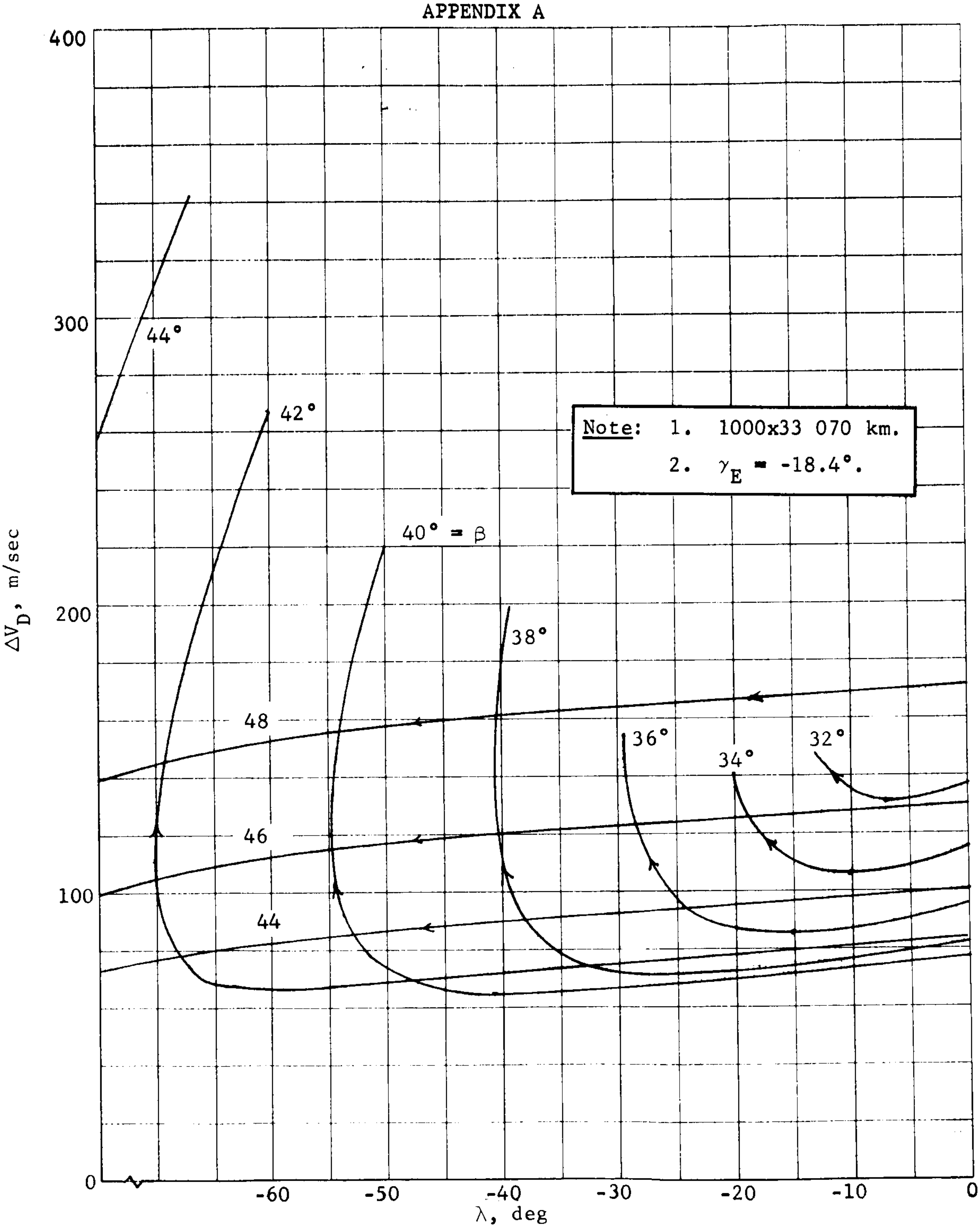

Figure A139.- ΔV_D versus Lead Angle

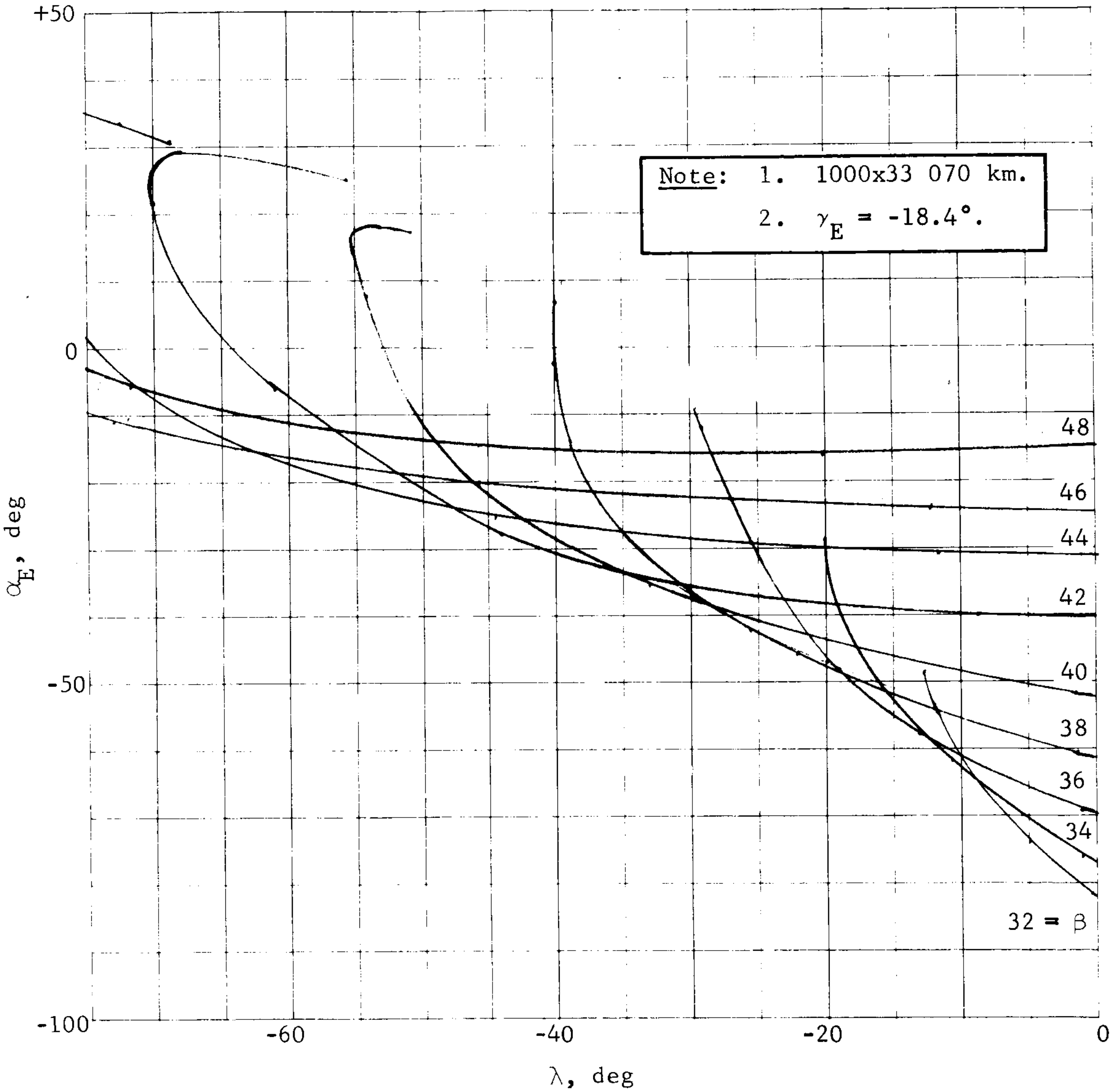

Figure A140.- Angle of Attack versus Lead Angle

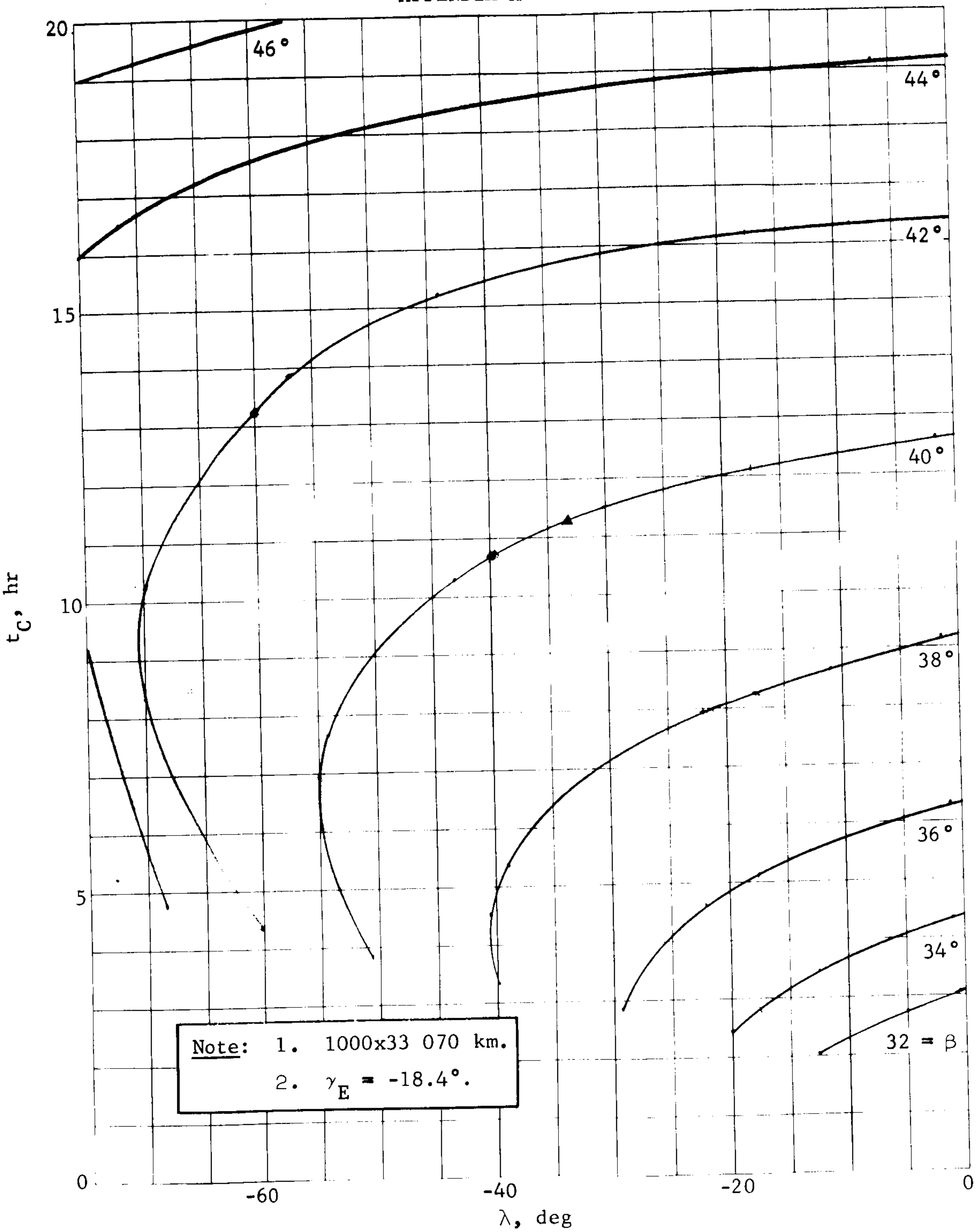

Figure A141.- Coast Time versus Lead Angle

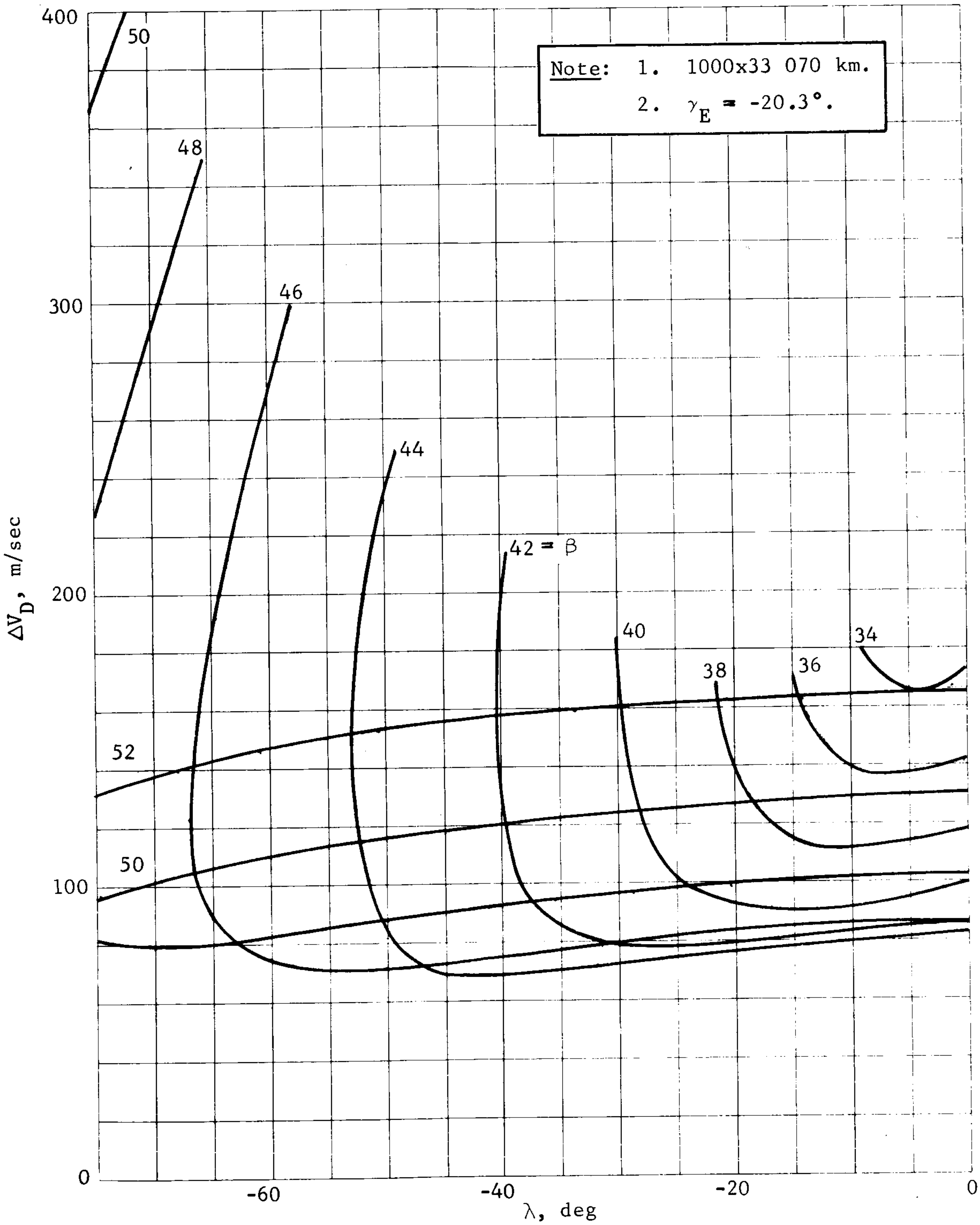

Figure A142.- ΔV_D versus Lead Angle

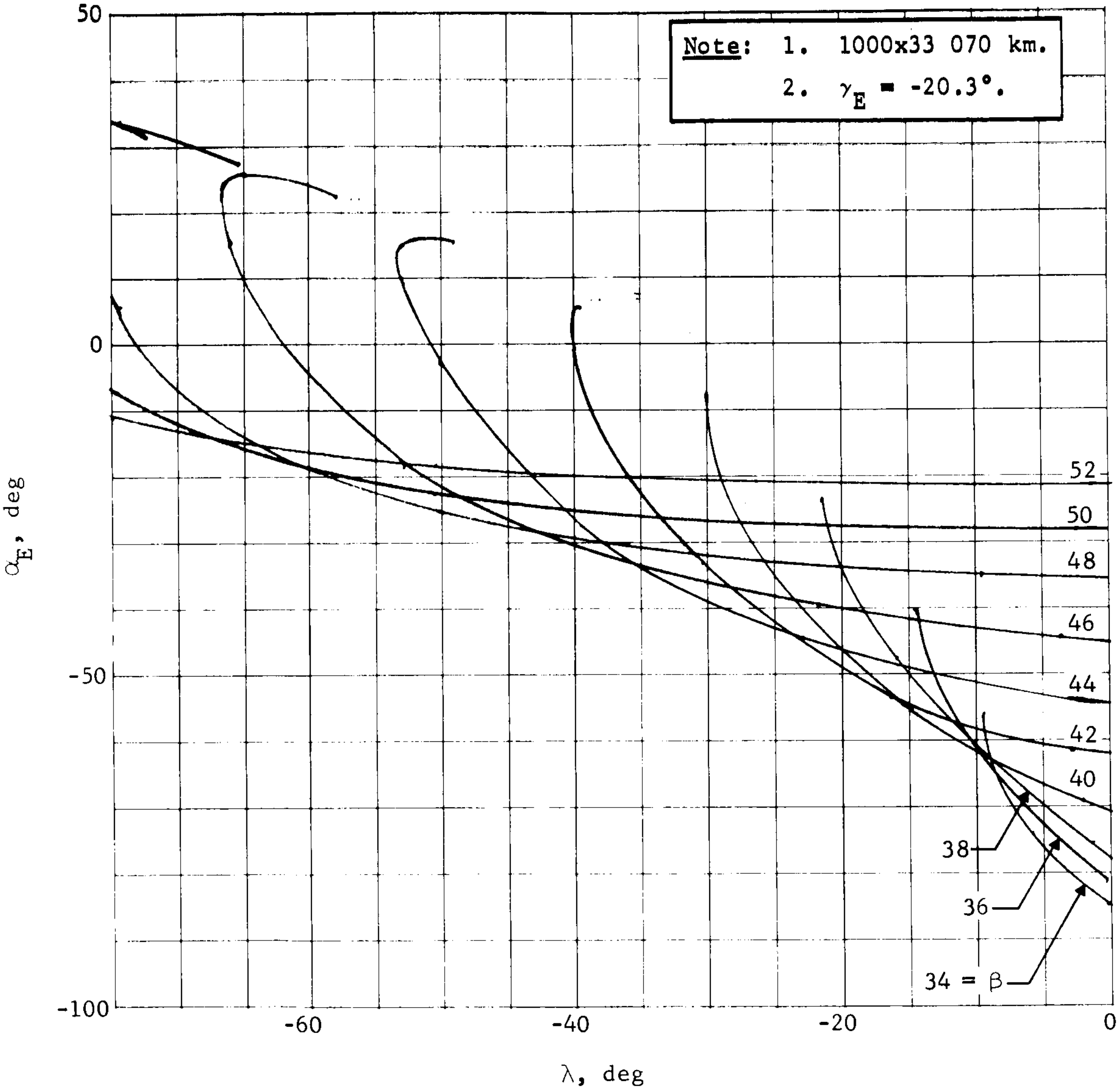

Figure A143.- Angle of Attack versus Lead Angle

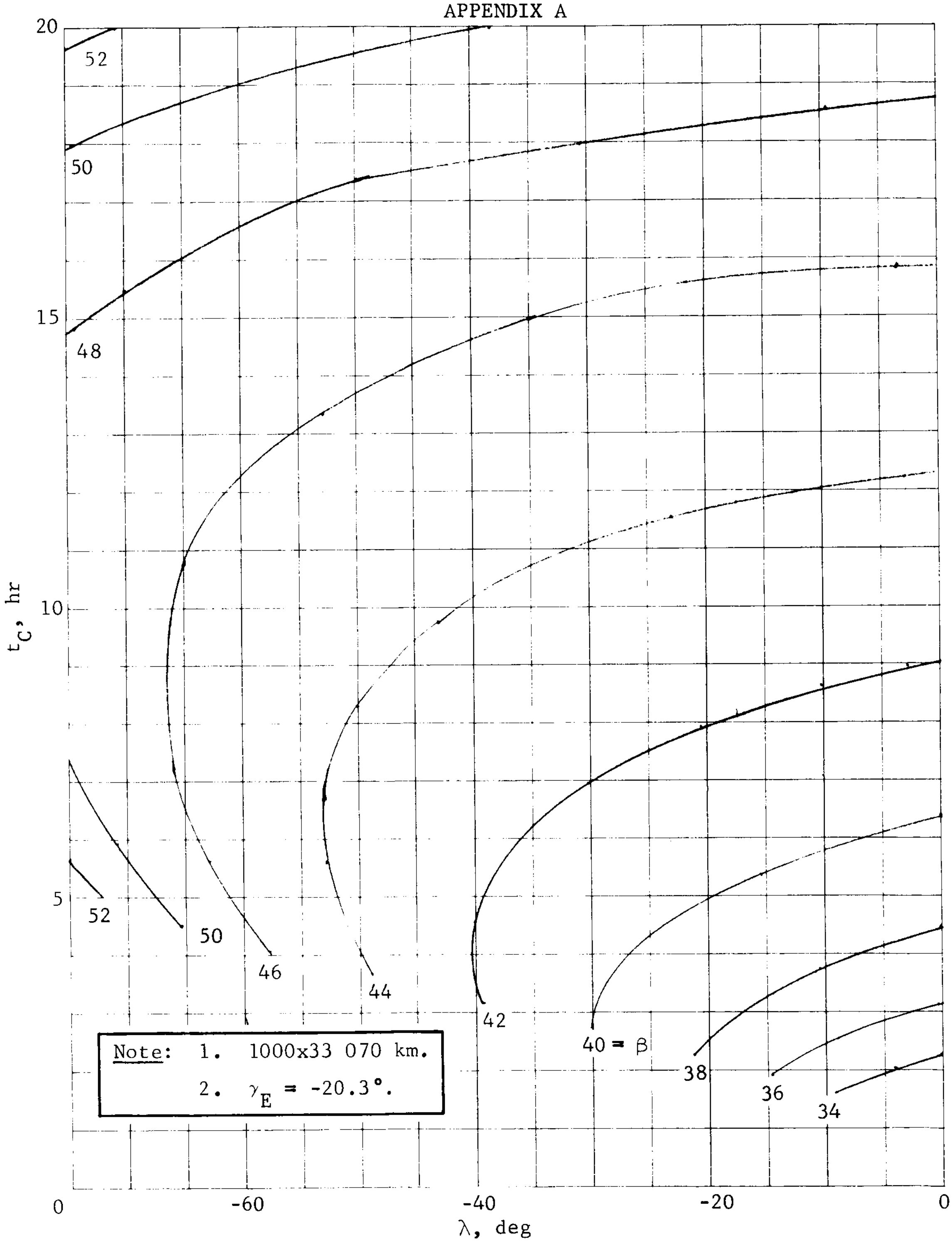

Figure A144.- Coast Time versus Lead Angle

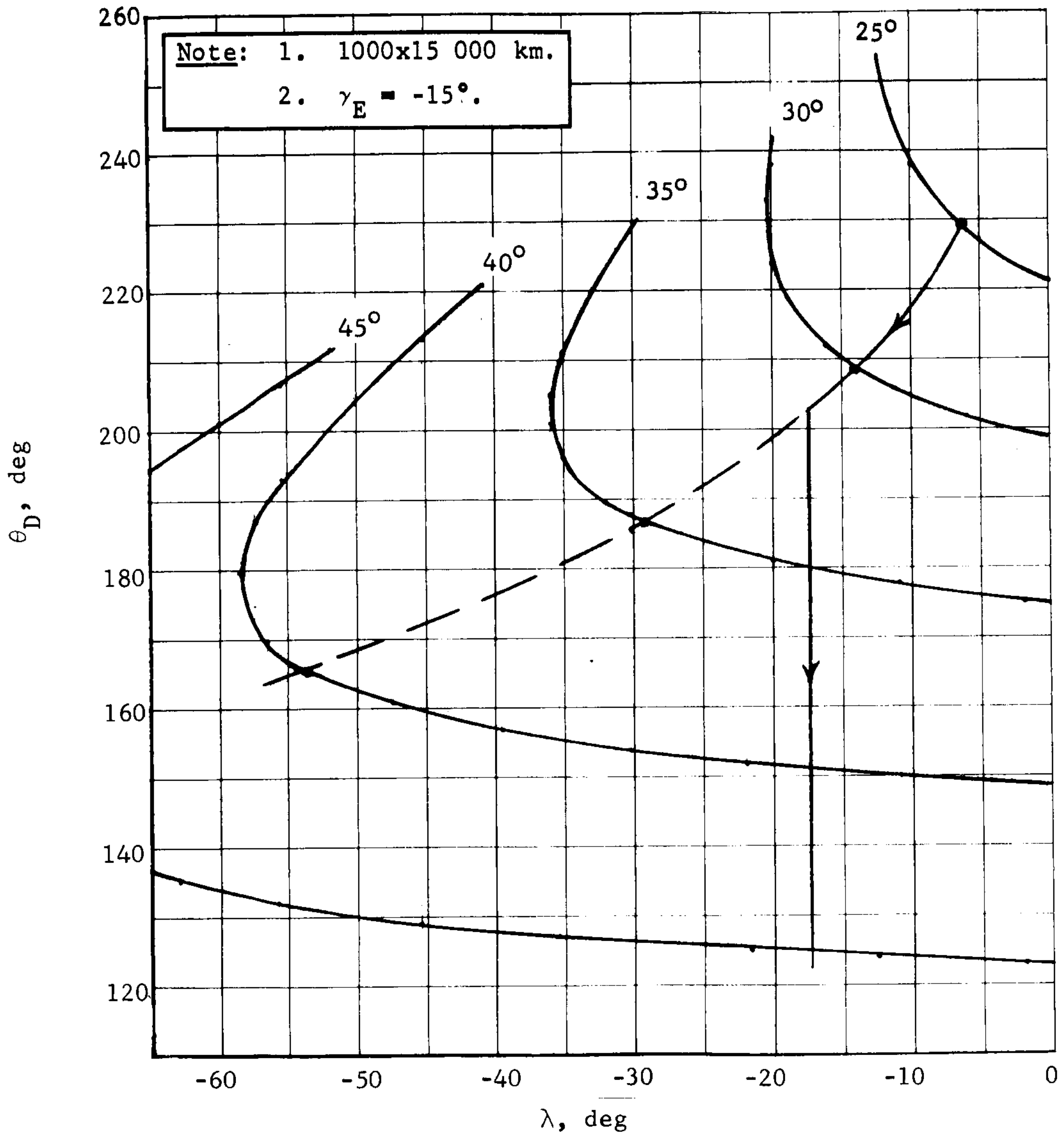

Figure A145.- True Anomaly versus Lead Angle

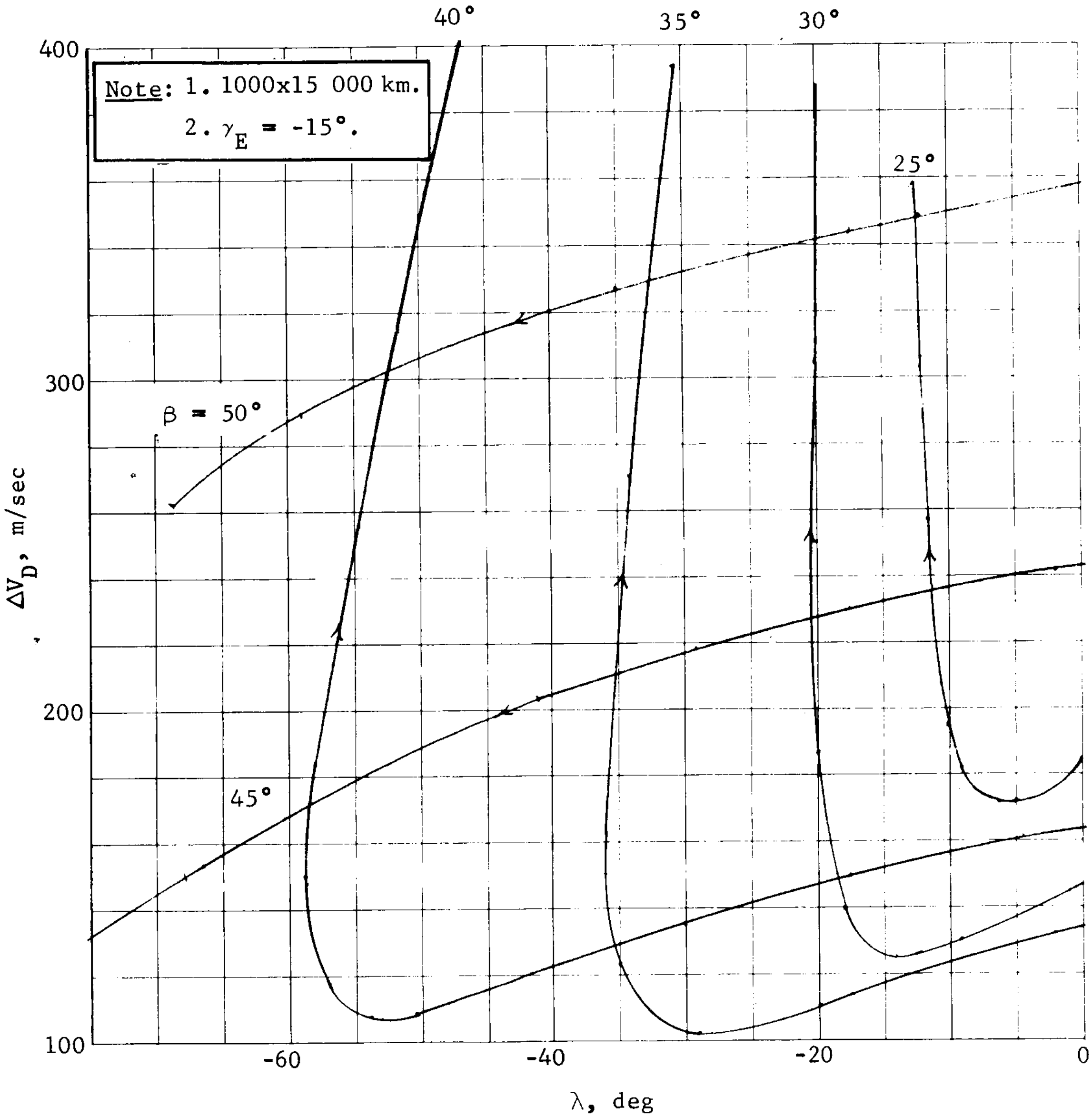

Figure A146.- ΔV_D versus Lead Angle

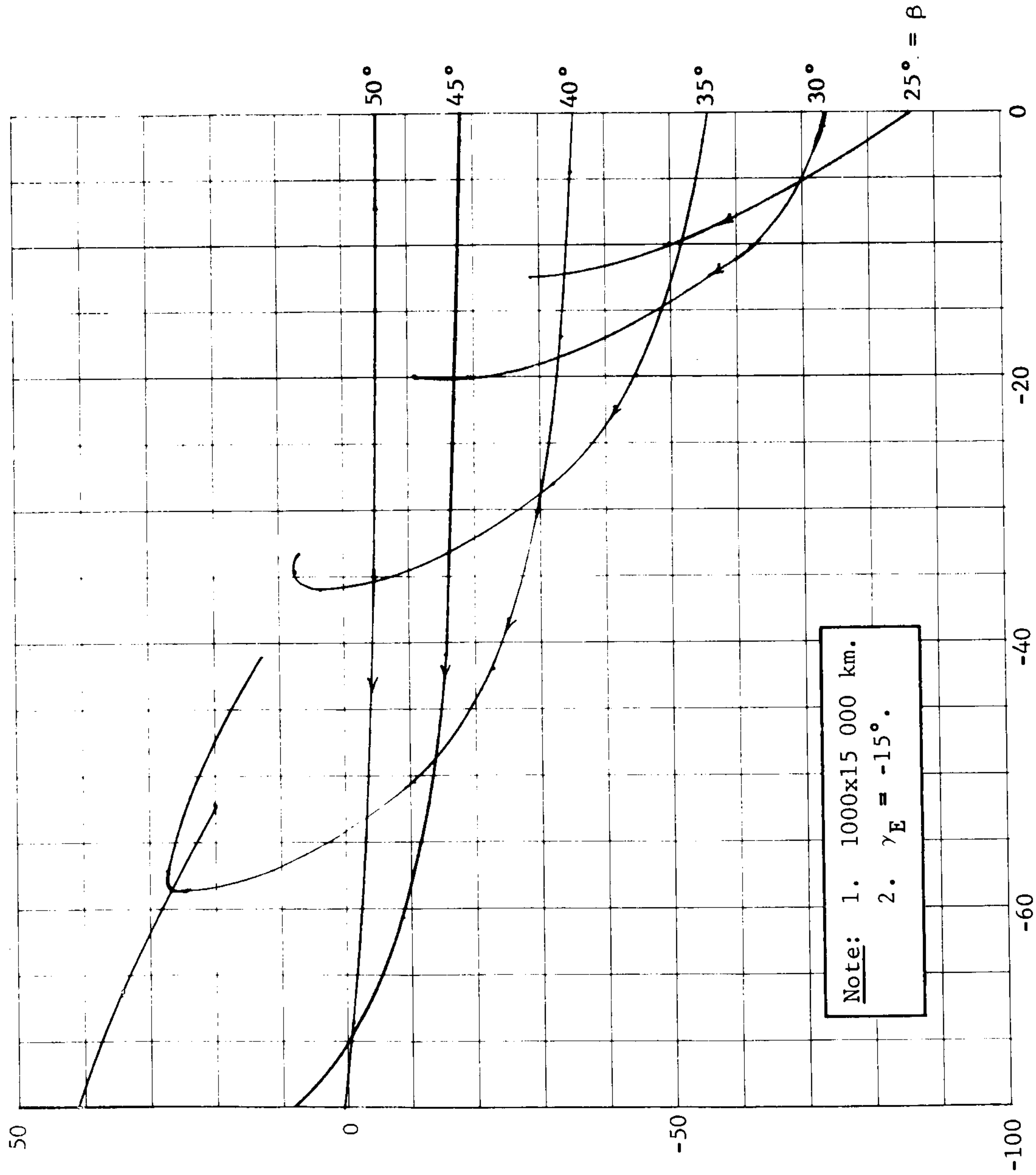

Figure A147.- Angle of Attack versus Lead Angle

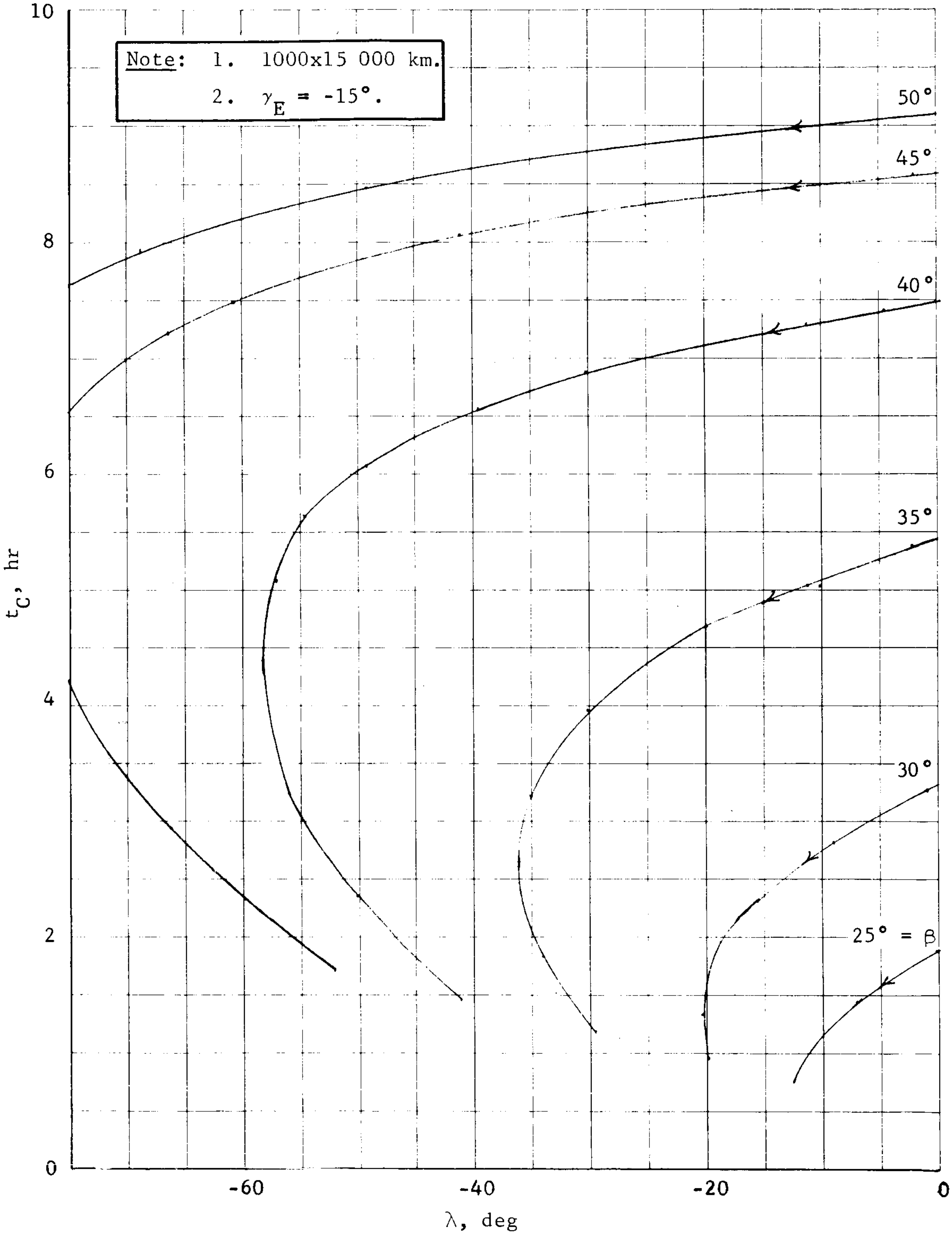

Figure A148.- Coast Time versus Lead Angle

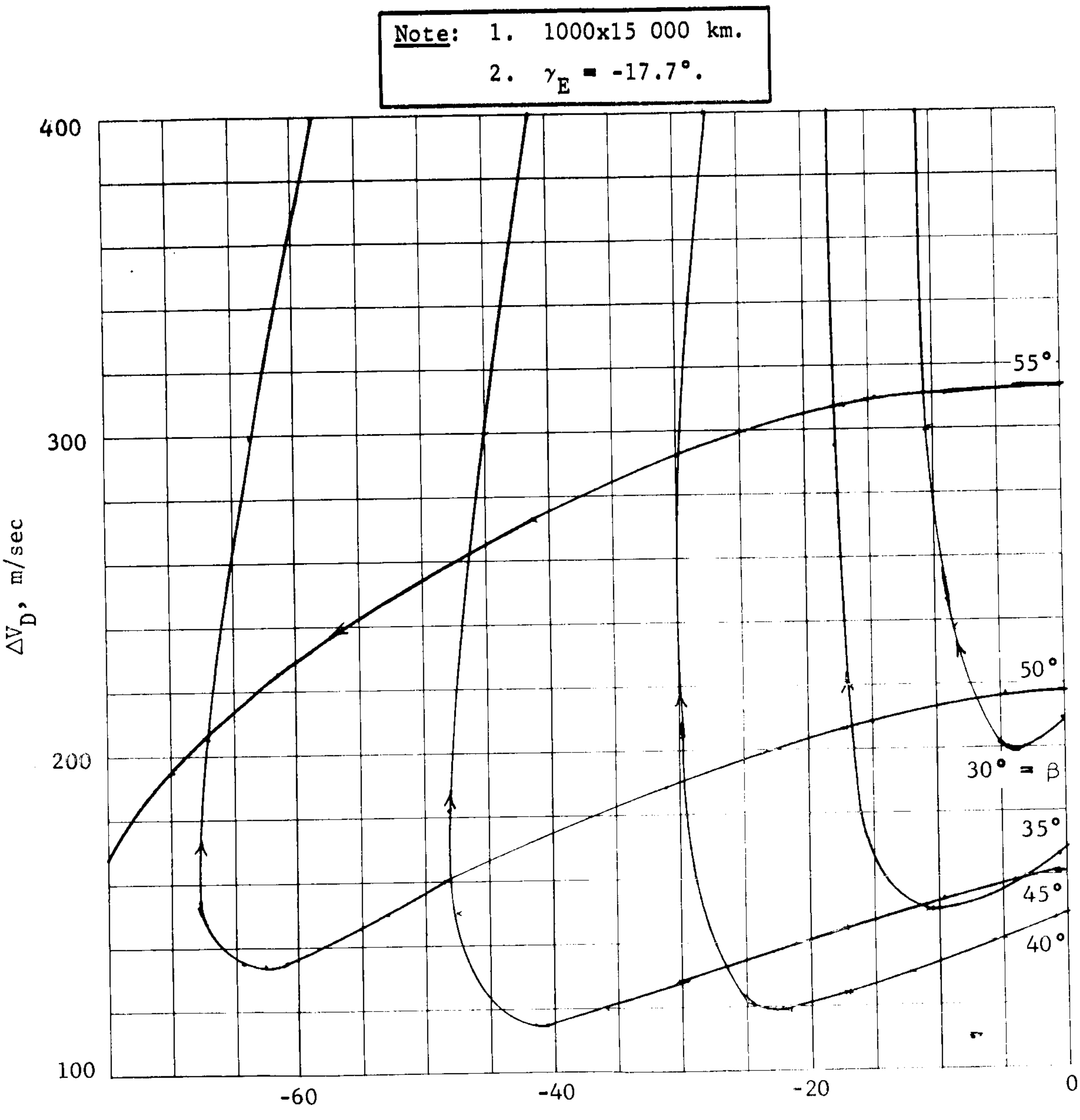

Figure A149.- ΔV_D versus Lead Angle

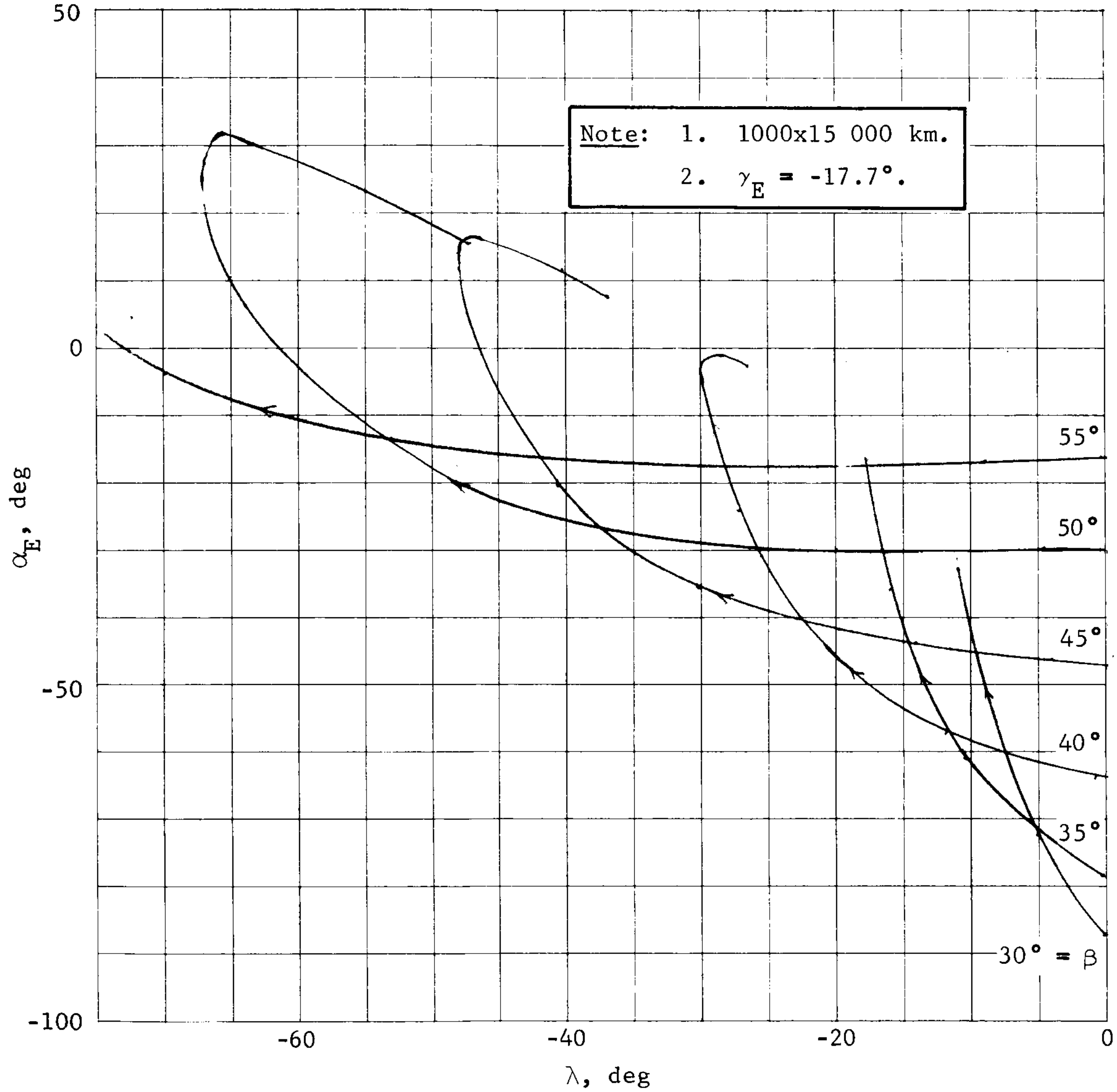

Figure A150.- Angle of Attack versus Lead Angle

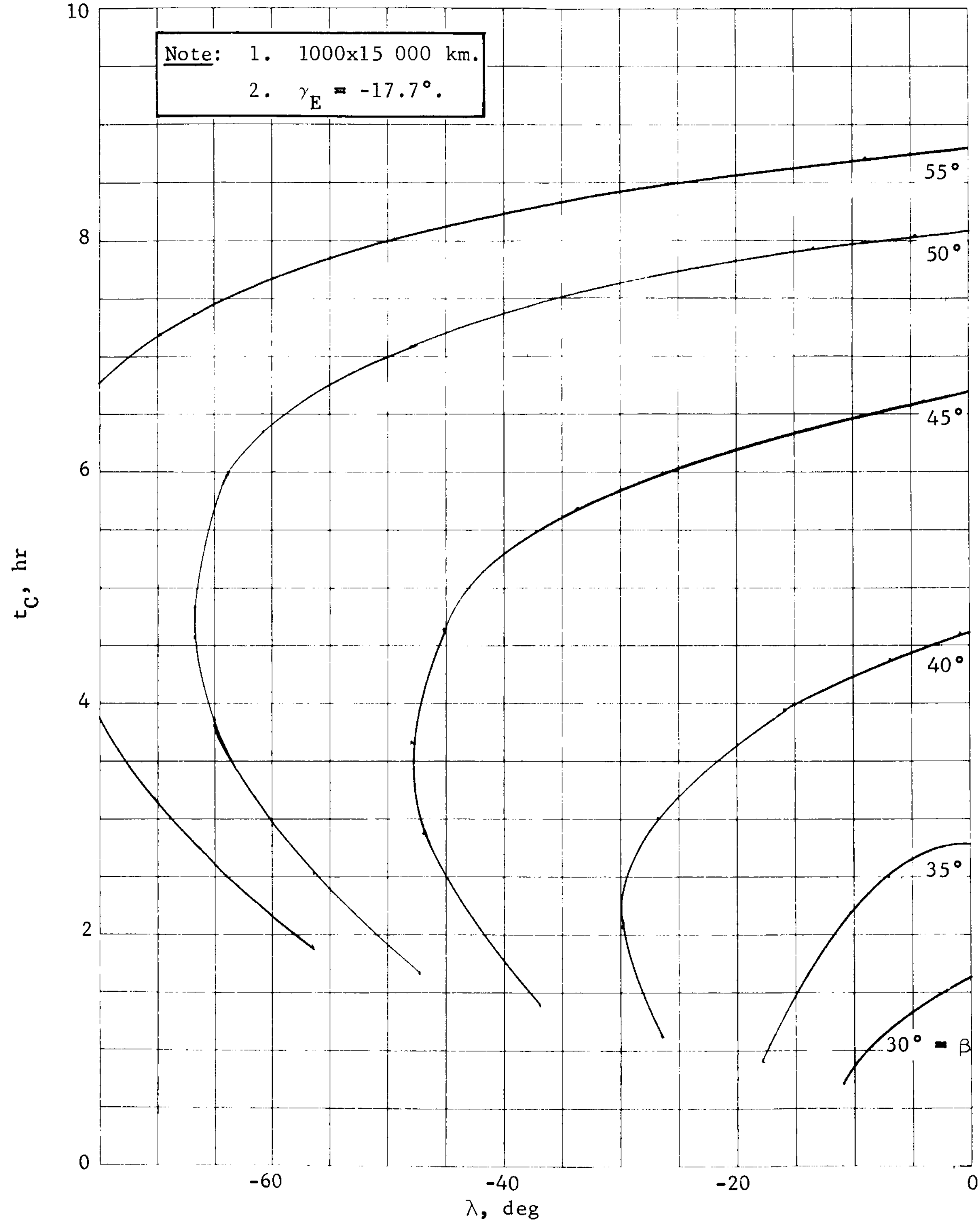

Figure A151.- Coast Time versus Lead Angle

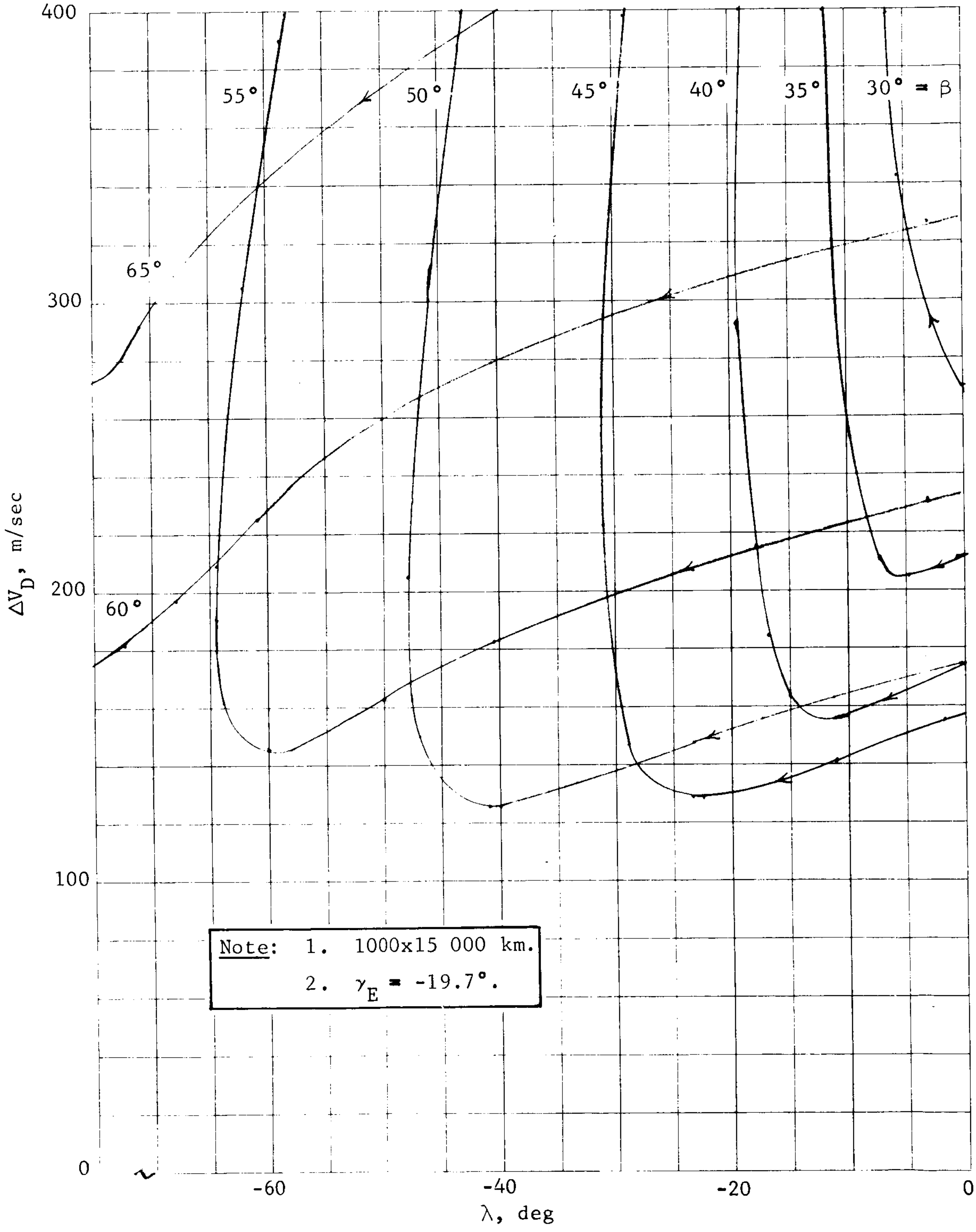

Figure A152.- ΔV_D versus Lead Angle

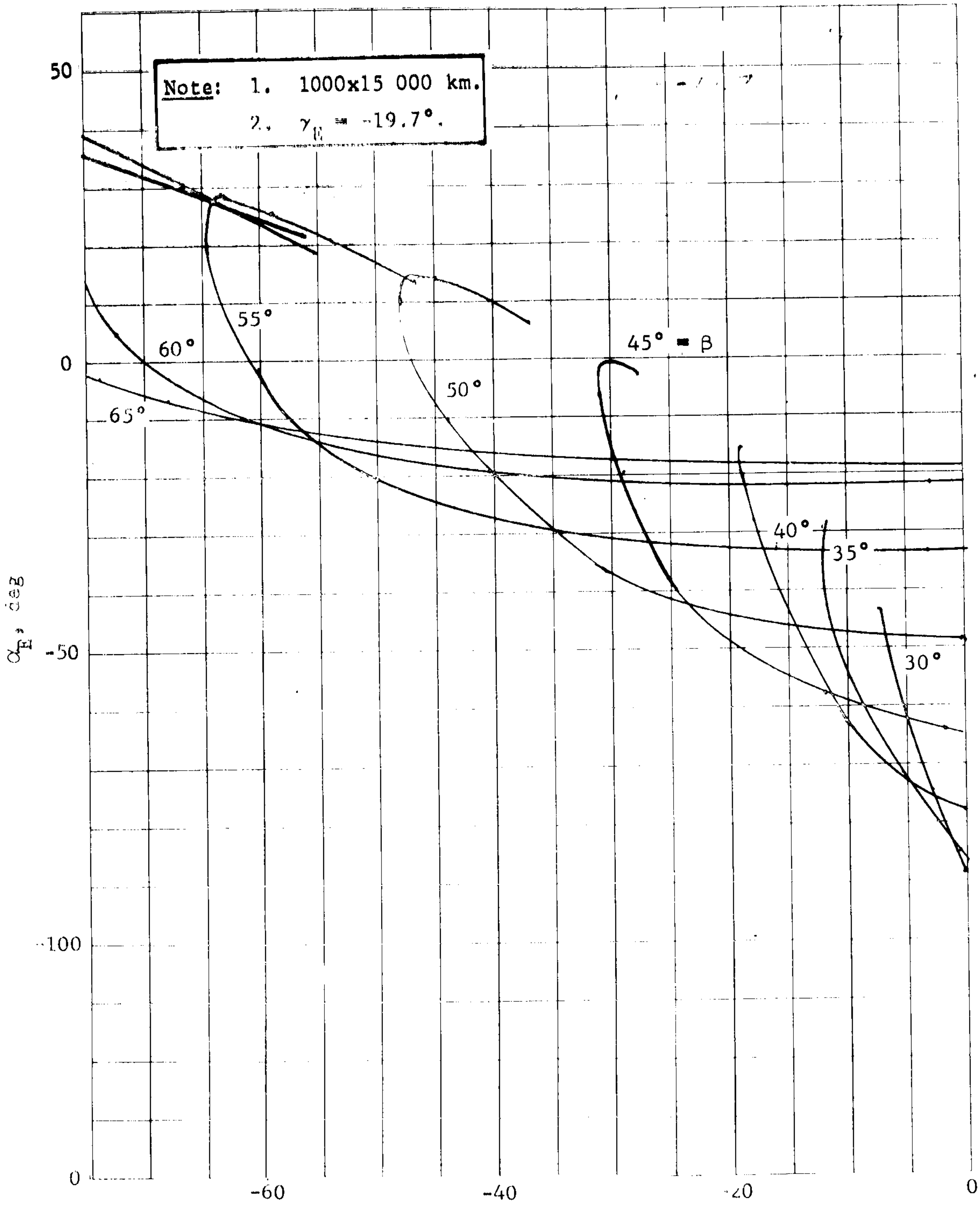

Figure A153.- Angle of Attack versus Lead Angle

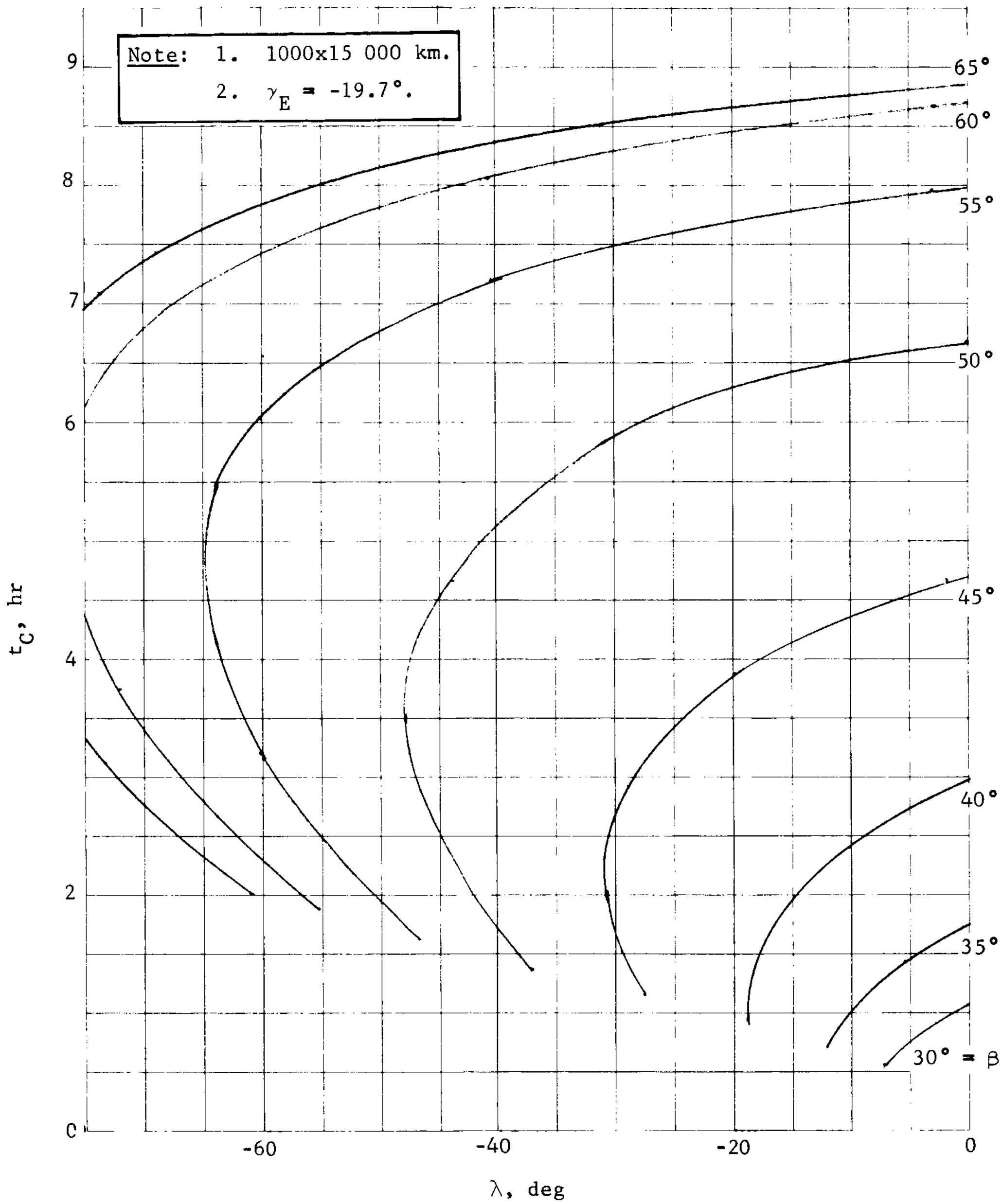

Figure A154.- Coast Time versus Lead Angle

Relay Communication Link Constraints, Orbit Mode

The geometry during entry is similar to the direct mode and figure A129 applies to the orbit mode. Again boundaries of ρ_{CE}, α_{CE}, $\alpha_{C_{TD}}$, and initial link time are shown as a function of β and λ in figure A155 for orbit (1). The γ_E is another independent parameter for the orbit mode.

The $\alpha_{C_{TD}}$ is a function of γ_E and atmosphere and is shown for a γ_E of -15.5° and -20.3° for the VM-8 atmosphere. The upper bound on λ is about -19° independent of β, while the lower bound varies between -9.5° and -5° as β increases from 20° to 40°. The selected deorbit maneuver strategy must keep λ in the proper range as a function of β. The ΔV_D is shown in overlay 1 (fig. A155) for a γ_E of -18.4°. For example, a variable ΔV_D of up to 120 m/sec would allow a β range from about 33.5° to 45.5°. The restriction on β to keep $|\alpha_E| < 30°$ is shown in overlay 2 (fig. A155). The upper limit on β for orbit (1) is determined by the t_c constraint and is shown in overlay 3. Boundary plots for orbit (2) are shown in figure A156, and it is seen that the allowable range of λ is similar to orbit (1). Overlays of ΔV_D, $|\alpha_E| < 30°$, and t_c are shown for a γ_E of -17.7°.

The allowable range of β as a function of γ_E, ΔV_D, and t_c is summarized in figure A157 for orbit (1). Any point inside the boundaries does correspond to an allowable λ. If 150 m/sec were provided and γ_E could be varied between -15.5° and -20°, the resulting range of β would be 24.2° to 41.2°, a $\Delta\beta$ of 17°. A similar plot is shown for orbit (2) in figure A158. If 150 m/sec were provided and γ_E could be varied between -15° and -20°, the resulting range of β would be 27.2° to 49.8°, a $\Delta\beta$ of 22.6°. The β flexibility of orbit (2) is thus greater mainly due to the t_c constraint which is critical for orbit (1).

The minimum allowable nominal γ_E is shown in figures A157 and A158 based on the error analysis that follows. The maximum allowable nominal γ_E such that a 3σ error in γ_E does not exceed -18° is also shown. The allowable range of β for the 1000x33 070-km orbit is 27 to 35° with a ΔV_D of 120 m/sec. The nominal β is 31°. Employing γ_E steeper than -16° or using higher ΔV_D does not significantly increase the capability for this orbit. The allowable range of β for the 1000x15 000-km orbit is 26 to 34°, with a ΔV_D of 150 m/sec. The nominal β is 34°.

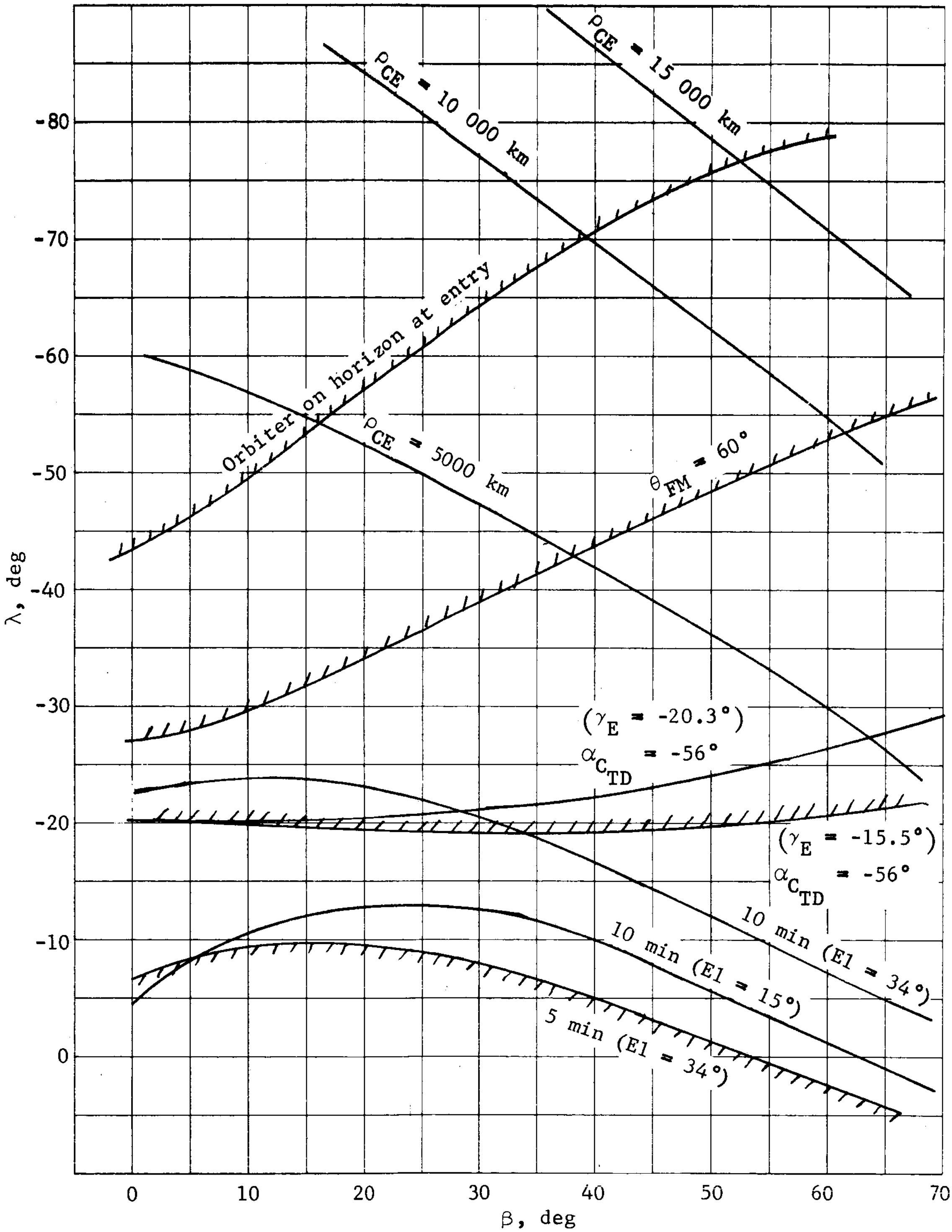

(a) No Overlay

Figure A155.- Relay Communication Link Boundaries (Orbit Mode), 1000x33 070 km

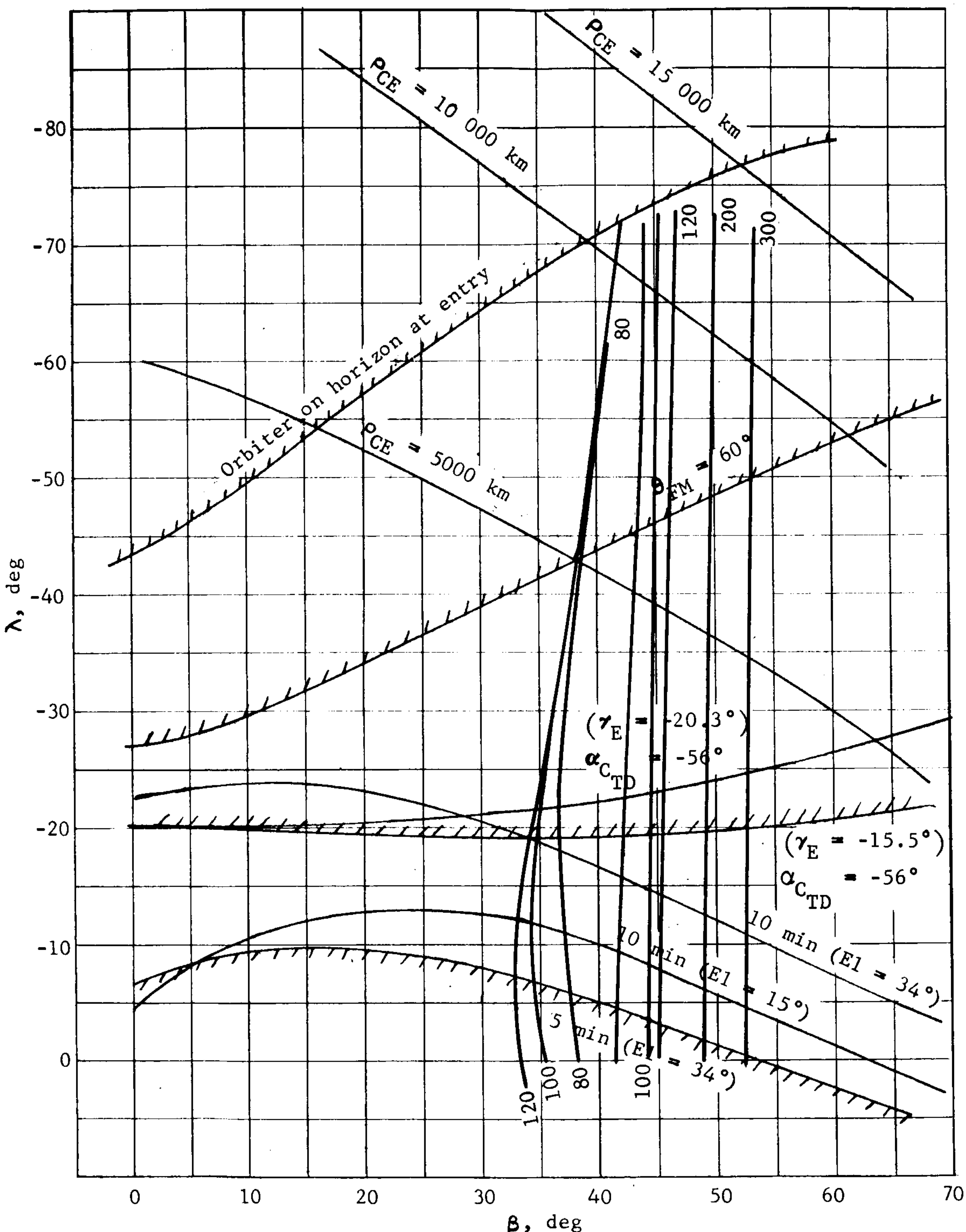

(b) ΔV_D, m/sec, Overlay 1 (γ_E = -18.4°)

Figure A155.- Continued

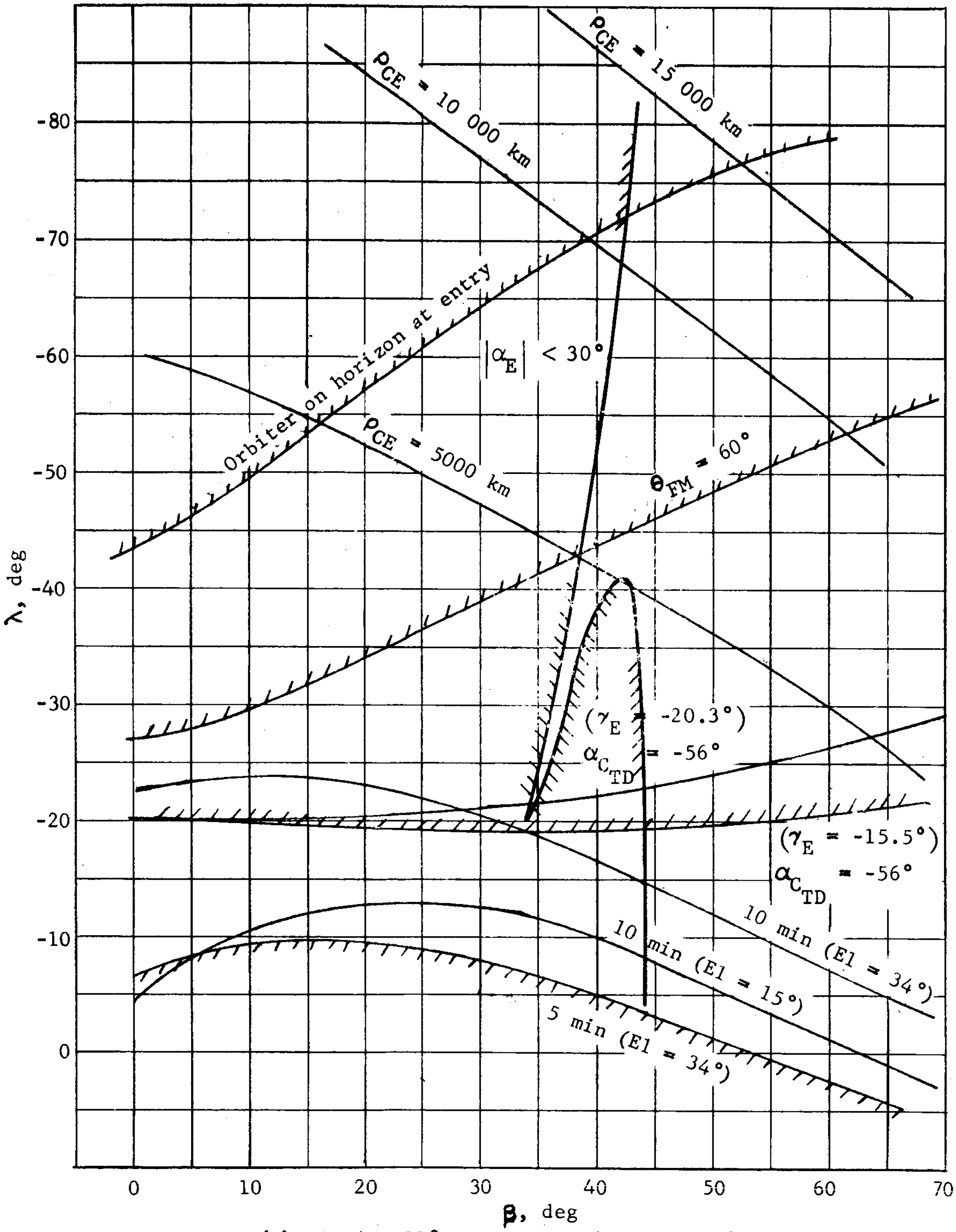

(c) $|\alpha_E| < 30°$, Overlay 2 (γ_E = -18.4°)

Figure A155.- Continued

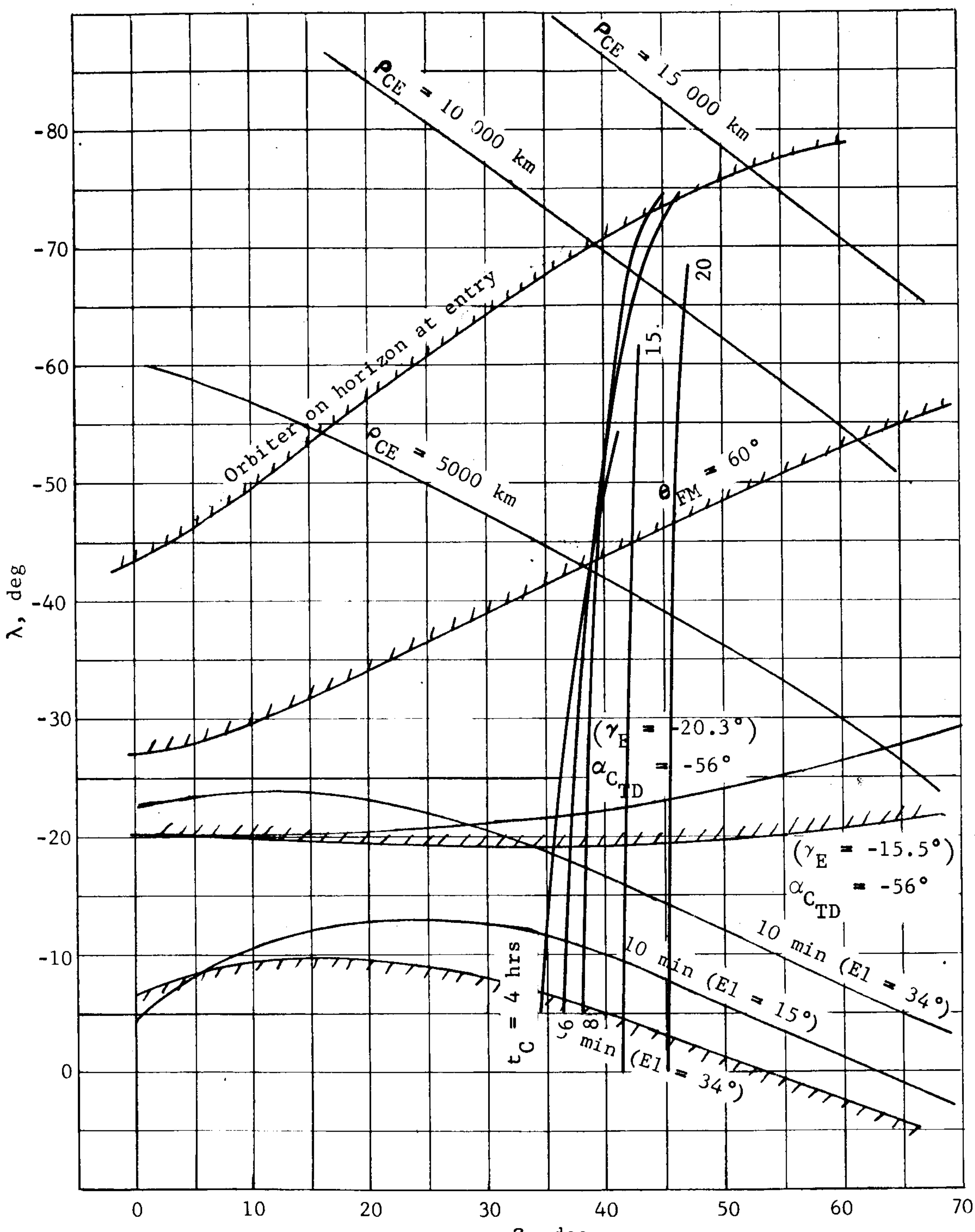

(d) t_c, hr, Overlay 3 (γ_E = -18.4°)

Figure A155.- Concluded

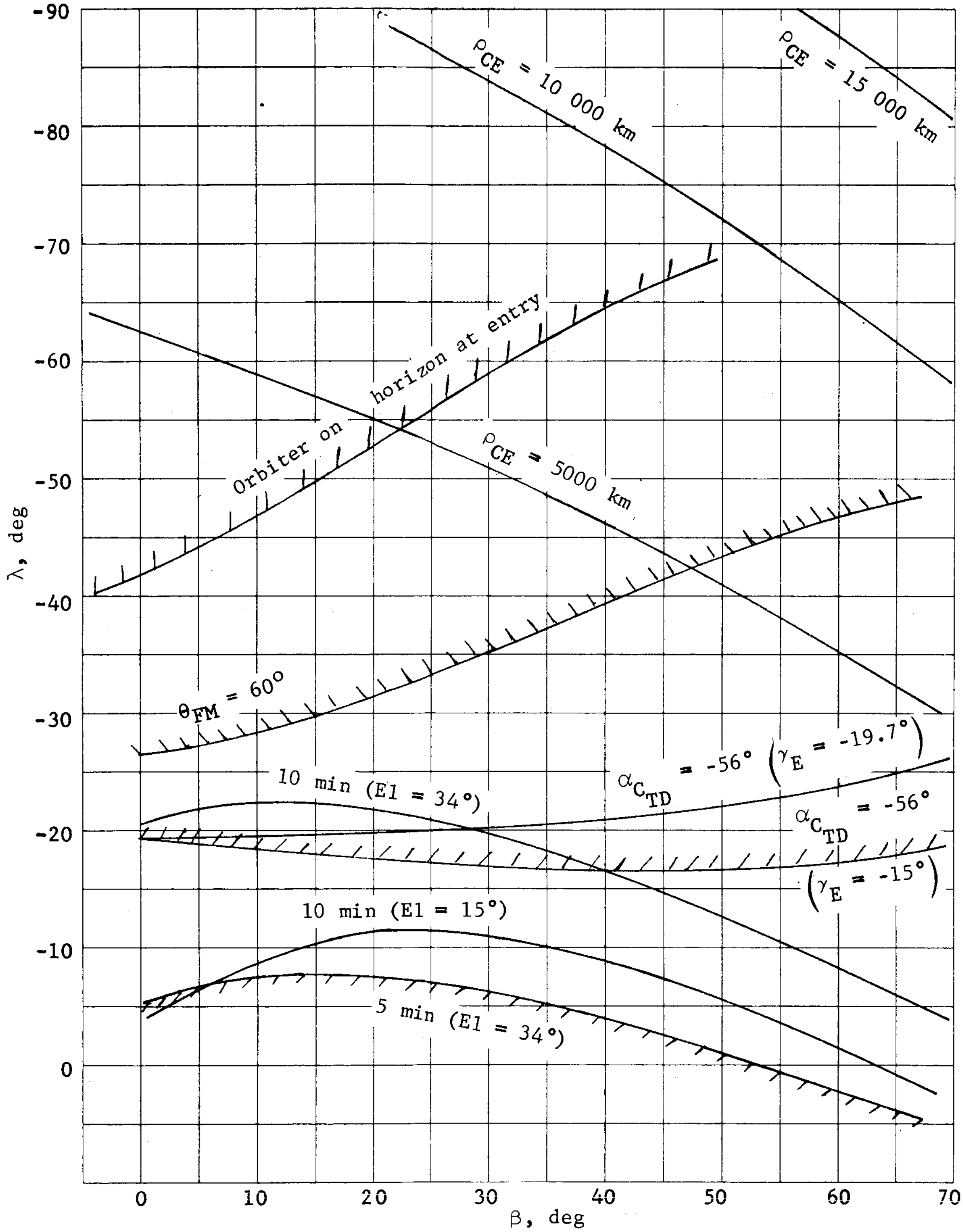

(a) No Overlay

Figure A156.- Relay Communication Link Boundaries (Orbit Mode), 1000x15 000 km

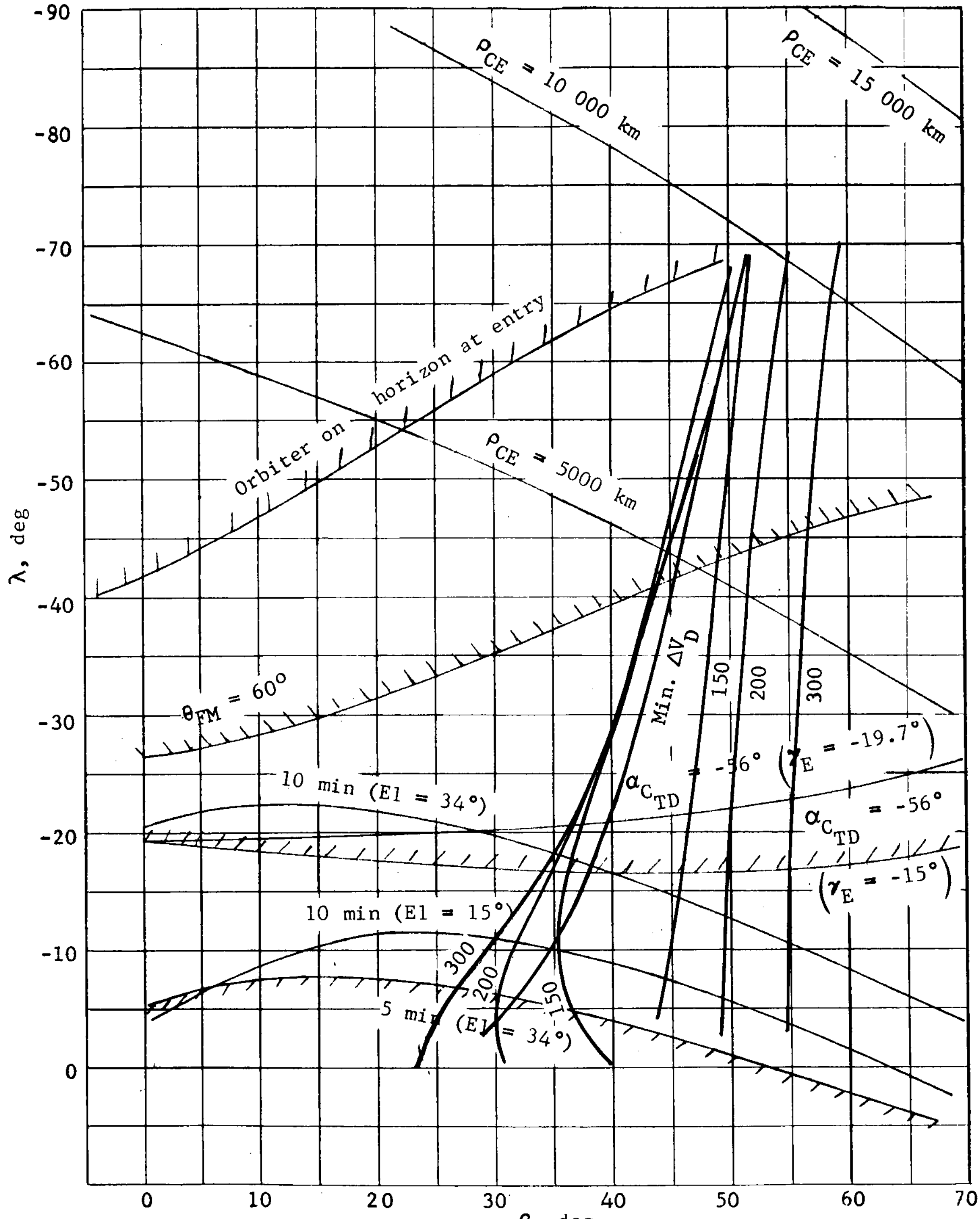

(b) ΔV_D, m/sec, Overlay 1 (γ_E = -17.7°)

Figure A156.- Continued

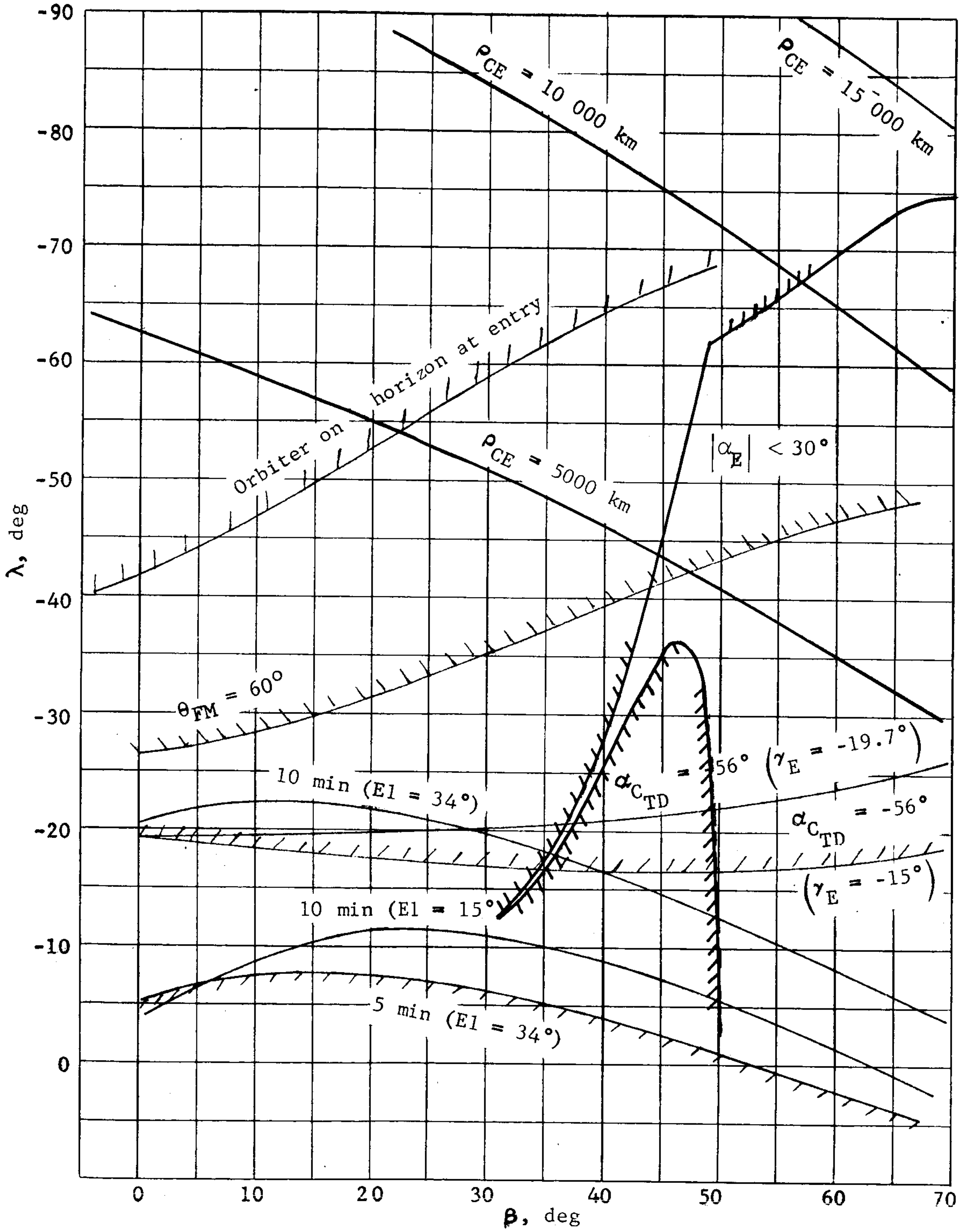

(c) $|\alpha_E| < 30°$, Overlay 2 (γ_E = -17.7°)

Figure A156.- Continued

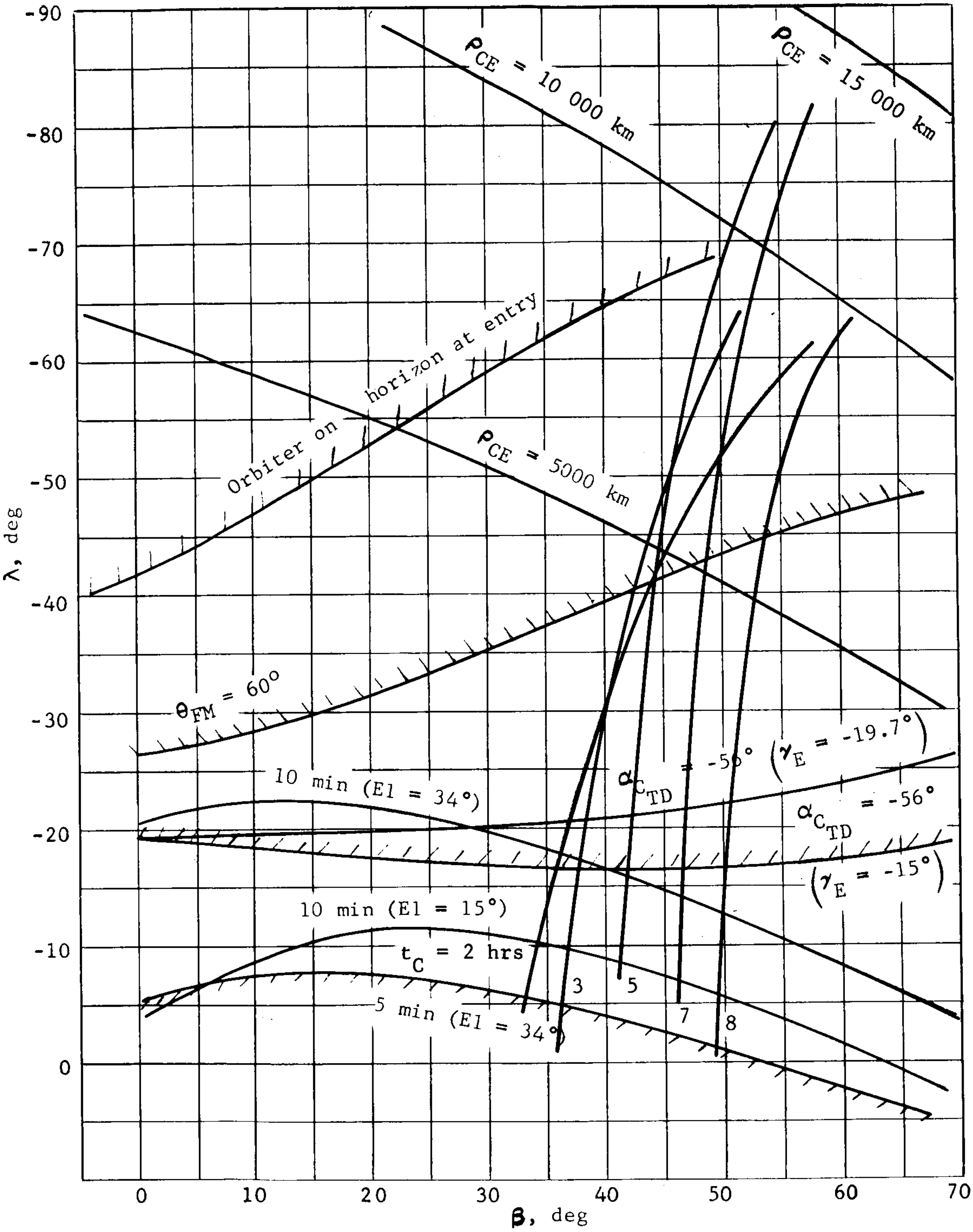

(d) t_c, hr, Overlay 3 (γ_E = -17.7°)

Figure A156.- Concluded

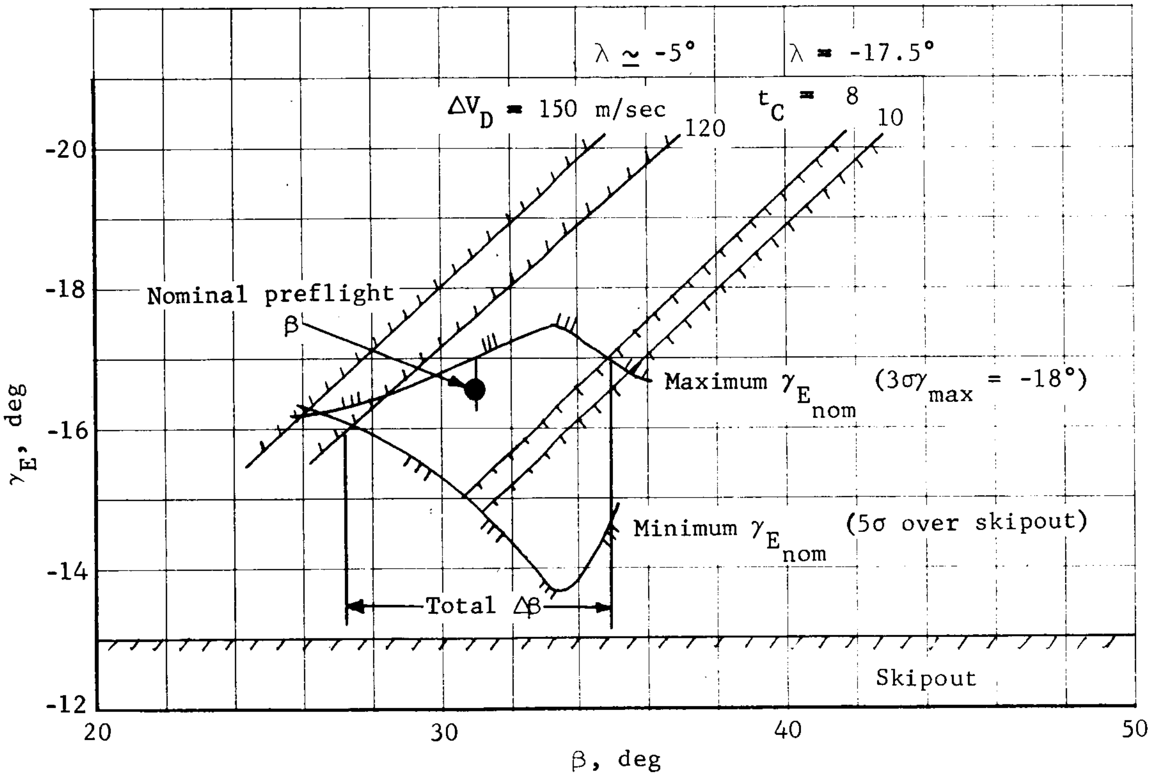

Figure A157.- Summary of Entry Locations (Orbit Mode), 1000x33 070 km

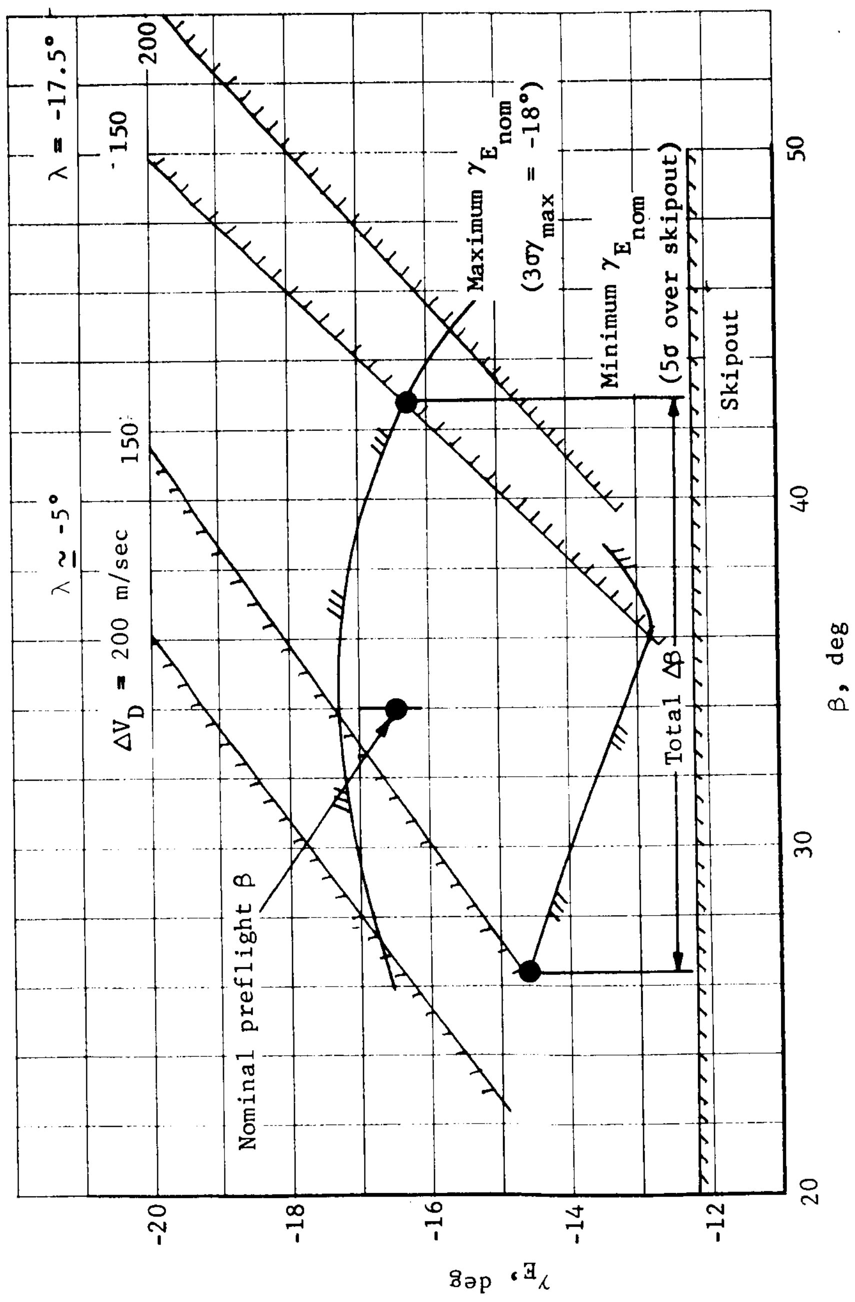

Figure A158.- Summary of Entry Locations (Orbit Mode), 1000x15 000 km

APPENDIX A

Landing Site Flexibility, Direct Mode

The first subsection has shown that the entry location parameter, β, is restricted to about 27° (±2°) for a γ_E of -21°. This is the nominal γ_E for the direct mode based on the error analysis presented in section 3 of this appendix.

The basic energy contours for the 1973-I launch opportunity are shown in figure A159. Also given is an overlay for ZAP angle and δ_{HE} angle. The ZAP angle is the angle between the hyperbolic excess velocity vector and the Mars-to-sun vector. The δ_{HE} angle is the declination of the $\vec{V}_{HE}$ with respect to the Martian equator. These two angles together position the $\vec{V}_{HE}$ with respect to the sun or the evening terminator. Any approach trajectory must pass through a given $\vec{V}_{HE}$. A family of approach trajectories with different inclinations to the equator are thus possible.

The locations of the sun (assumed on the equator), evening terminator, and a line 30° from the evening terminator are given in figure A160. The first overlay shows the total allowable variation of the $\vec{V}_{HE}$ during the launch opportunity where the C_3 has been limited to 30 km ^{2}/sec^2 and the V_{HE} has been limited to 3.5 km/sec. The central angle between the $\vec{V}_{HE}$ and the landing site, φ_L, is a function of V_{HE} and γ_E and is given by the sum of β and τ' minus the downrange angle traversed during entry, about 12°. For a γ_E of -21° the angle φ_L is about 78° for a V_{HE} of 3.5 km/sec and 68° for a V_{HE} of 2.4 km/sec. Based on this angle the allowable landing sites, corresponding to the total variation of $\vec{V}_{HE}$, with respect to the evening terminator and the equator are shown. It must be remembered that for any given $\vec{V}_{HE}$ the locus of possible landing sites is a circle about the $\vec{V}_{HE}$ with a φ_L between 68° and 78° depending on the magnitude of V_{HE}. To land at the equator 30° from the evening terminator the $\vec{V}_{HE}$ must be in the eastern section of the allowable $\vec{V}_{HE}$ region and the orbiter inclination must be low, less than 20°. To have a high inclination orbit, for a good mapping mission, and also a landing site 30° from the terminator, the $\vec{V}_{HE}$ must be in the western tip of the allowable $\vec{V}_{HE}$ region. The latitude of the landing site is high, greater than 60°.

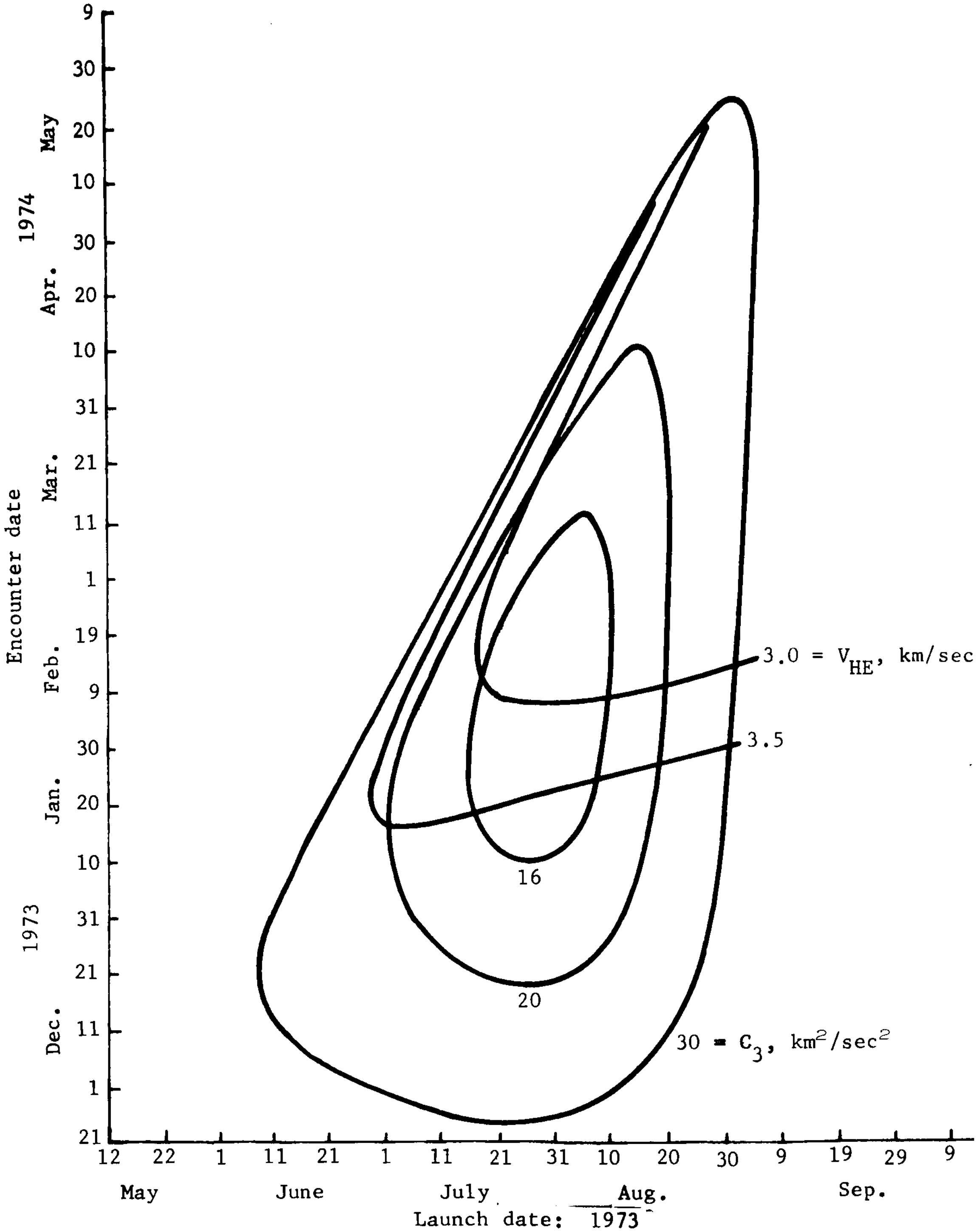

(a) No Overlay

Figure A159.- 1973-I Energy Contours

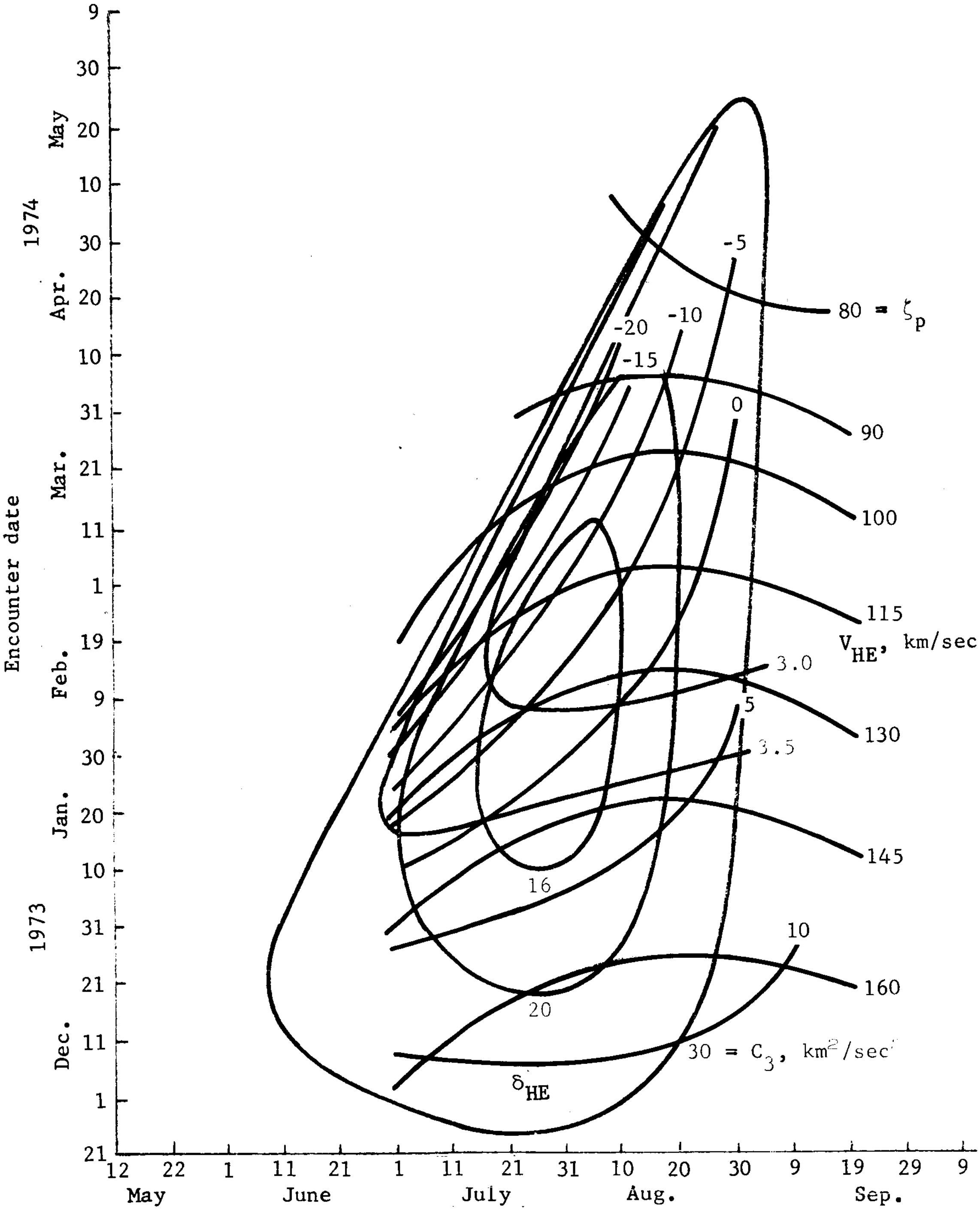

(b) V_{HE} Overlay

Figure A159.- Concluded

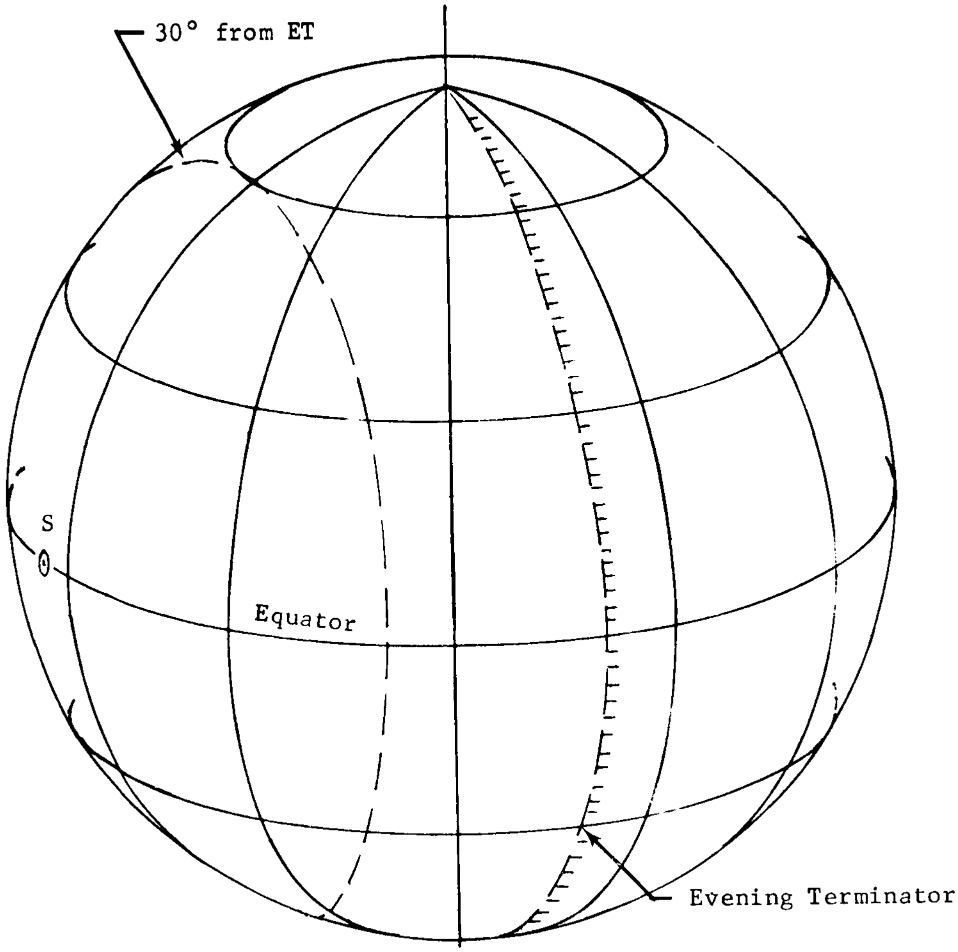

(a) No Overlay

Figure A160.- Targeting Capability (1973-I)

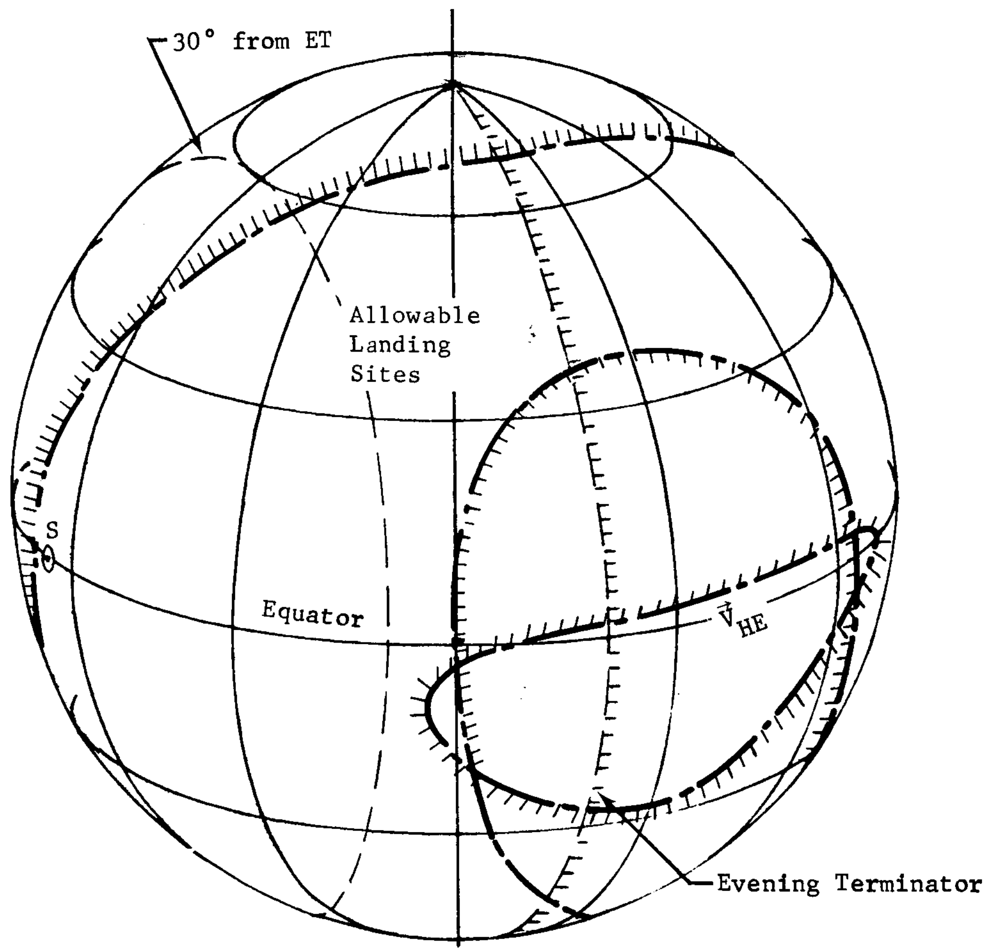

(b) Overlay 1

Figure A160.- Continued

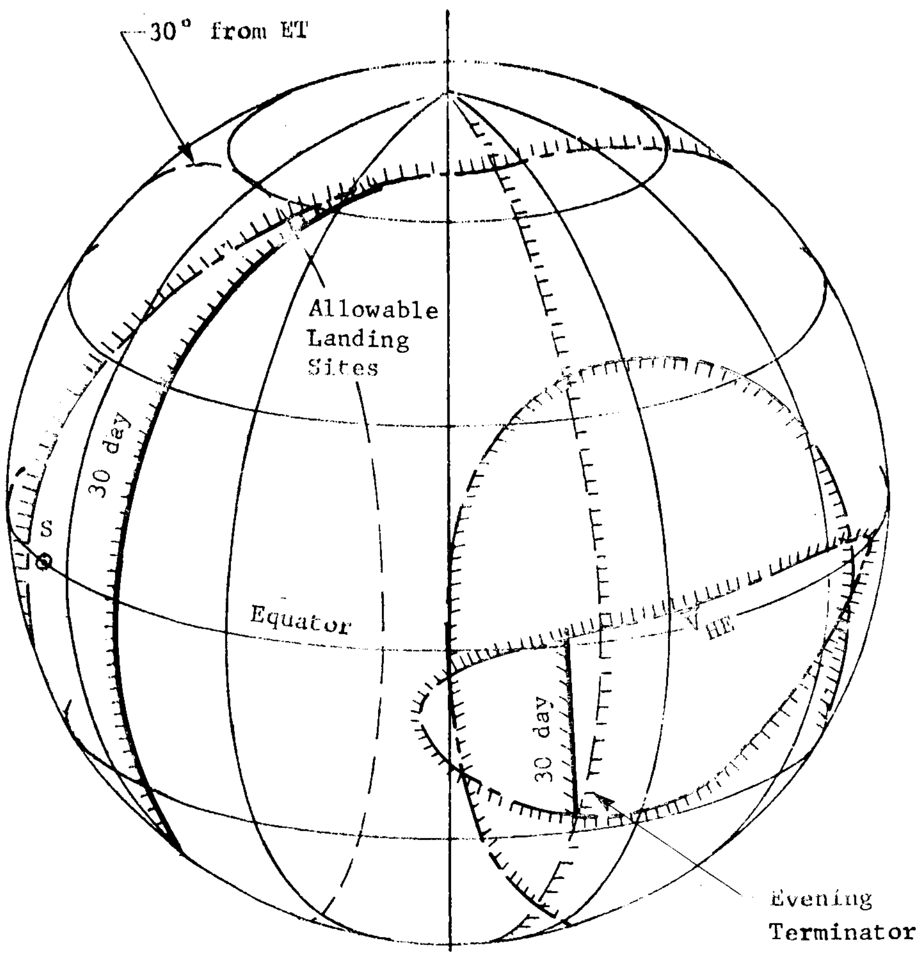

(c) Overlays 1 and 2

Figure A160.- Continued

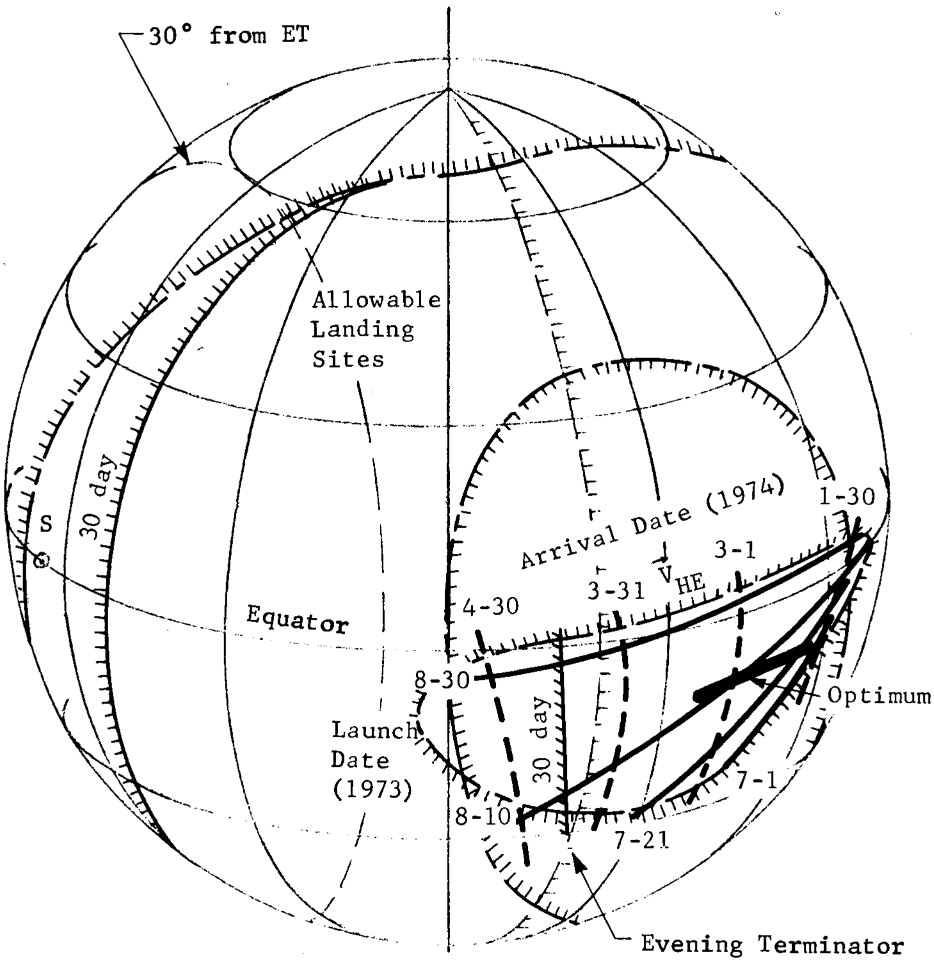

(d) Overlays 1, 2, and 3

Figure A160.- Concluded

APPENDIX A

There is no way of getting both high inclination orbits and near-equatorial landing sites with the direct mode. The effect of a 30-day launch period requirement on the allowable V_{HE} region and the degradation in allowable landing sites is shown in overlay 2 (fig. A160). The allowable $\bar{V}_{HE}$ region is tied back to specific launch and arrival dates in overlay 3. Also shown is the launch period discussed in section 1, which optimizes capsule system weight in orbit.

The above discussion has not mentioned longitude control, only latitude and orientation with respect to the terminator. Longitude control is possible through the selection of encounter time of day. If there were no restriction on encounter time of day, full 360° coverage is possible. However, if the orbit insertion maneuver must be made in view of Goldstone, the allowable encounter time is reduced to about 10 hr and the allowable range of longitudes to about 150°. If the capsule ejection maneuver were to occur about 8 hr before encounter and it too had to be viewed from Goldstone, the allowable longitude range is reduced to about 30°. The DSN tracking of Mars is shown in figure A161 for two dates.

Once a desirable landing site is selected (latitude, longitude, and distance from the terminator) there is no capability to change it before capsule ejection.

Landing Site Flexibility, Orbit Mode

Earlier it has been shown that the β range for the 1000 x 33 070-km orbit is between 24° and 32° for a γ_E of -15.5° and a ΔV_D capability of 150 m/sec. The β range for the 1000 x 15 000-km orbit is between 27° and 40° with a γ_E of -15° and a ΔV_D also of 150 m/sec. Using the extreme values of β, 24° and 40°, and assuming a downrange angle during entry of 16°, the possible landing area shown in overlay 1 (fig. A160) is expanded by at most 6° in all directions. This assumes that the orbiter periapsis is the same as the periapsis of the approach hyperbola. The allowable landing area can be expanded greatly by shifting periapsis at orbit insertion.

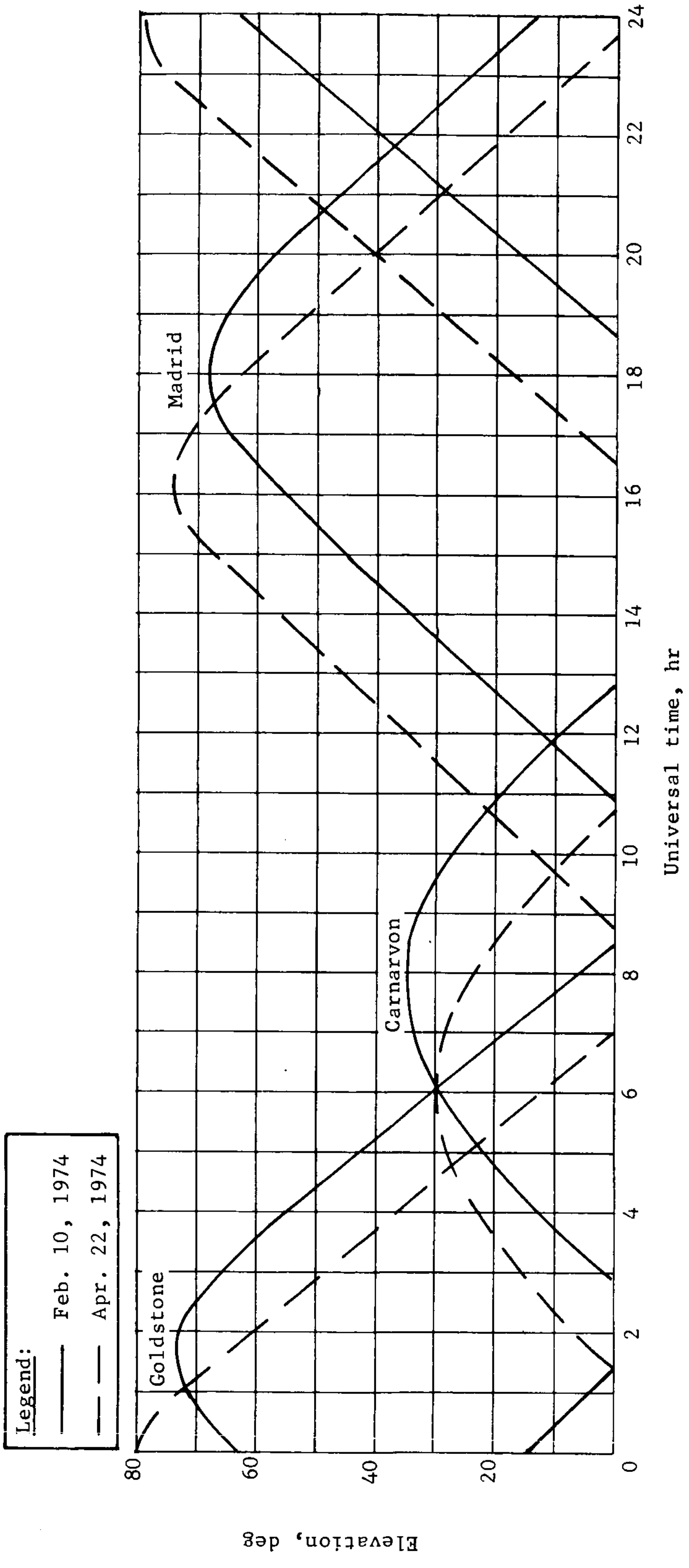

Figure A161.- DSN Tracking of Mars

APPENDIX A

The added orbit insertion requirements for periapsis shift are shown in figure A162 as a function of periapsis shift, $\Delta\omega$, for both orbits. The variation with V_{HE} is slight for $\Delta\omega$ less than 60°. Orbit shifts up to 40° can be obtained with 320 m/sec for orbit (1) and 230 m/sec for orbit (2).

The $\Delta(\Delta V_{O.I.})$ shown are minimum in that for a given $\Delta\omega$ the approach trajectory periapsis altitude is adjusted to give the minimum ΔV required. The point on the approach trajectory where insertion occurs is very close to the tangency point between the approach trajectory and the resulting orbit. For negative shifts insertion occurs before periapsis of the approach trajectory and for positive shift afterwards.

The required periapsis shift to land 30° from the evening terminator at latitudes of 0 and 30° is shown in figure A163 as a function of launch and arrival date. The shifts are shown for a nominal β of 31°, which corresponds to the 1000x33 070-km orbit. If the shift is desired for a nominal β of 34°, merely add 3° to the curves shown. The allowable $\Delta\beta$ range can be used to reduce the periapsis shift requirement.

High inclination orbits that have landing sites 30° from the terminator and near the equator are possible with the orbit mode through periapsis shift. In fact the required region of $\vec{V}_{HE}$ on overlay 1 (fig. A160) corresponds to a low magnitude of V_{HE}, around 2.5, so that added ΔV could be used for shifts.

The orbit mode has longitude control through (1) orbital period (2) number of orbits before deorbit; and (3) β variation (amount of longitude control depends on orbit inclination).

To land at a preselected distance from the evening terminator there must be an allowable range of β that is sufficient to cancel out the error in periapsis location. This error is due to two sources: (1) navigation uncertainty at the time of the calculation of the required orbit insertion maneuver; and (2) error in the execution of the orbit insertion maneuver. If the navigation uncertainty is as large as 300 km, the resulting $\Delta\beta$ required would be about 12°. There is another feature of targeting unique to the orbit mode. If a desired longitude is to be reached after a given number of orbits, enough $\Delta\beta$ capability must be available to cancel out the time phasing error due to period errors in the orbit. Even if an orbit trim maneuver is made there still will be some period error. The ability of β variation to cancel out these errors is of course greater for low inclination orbits.

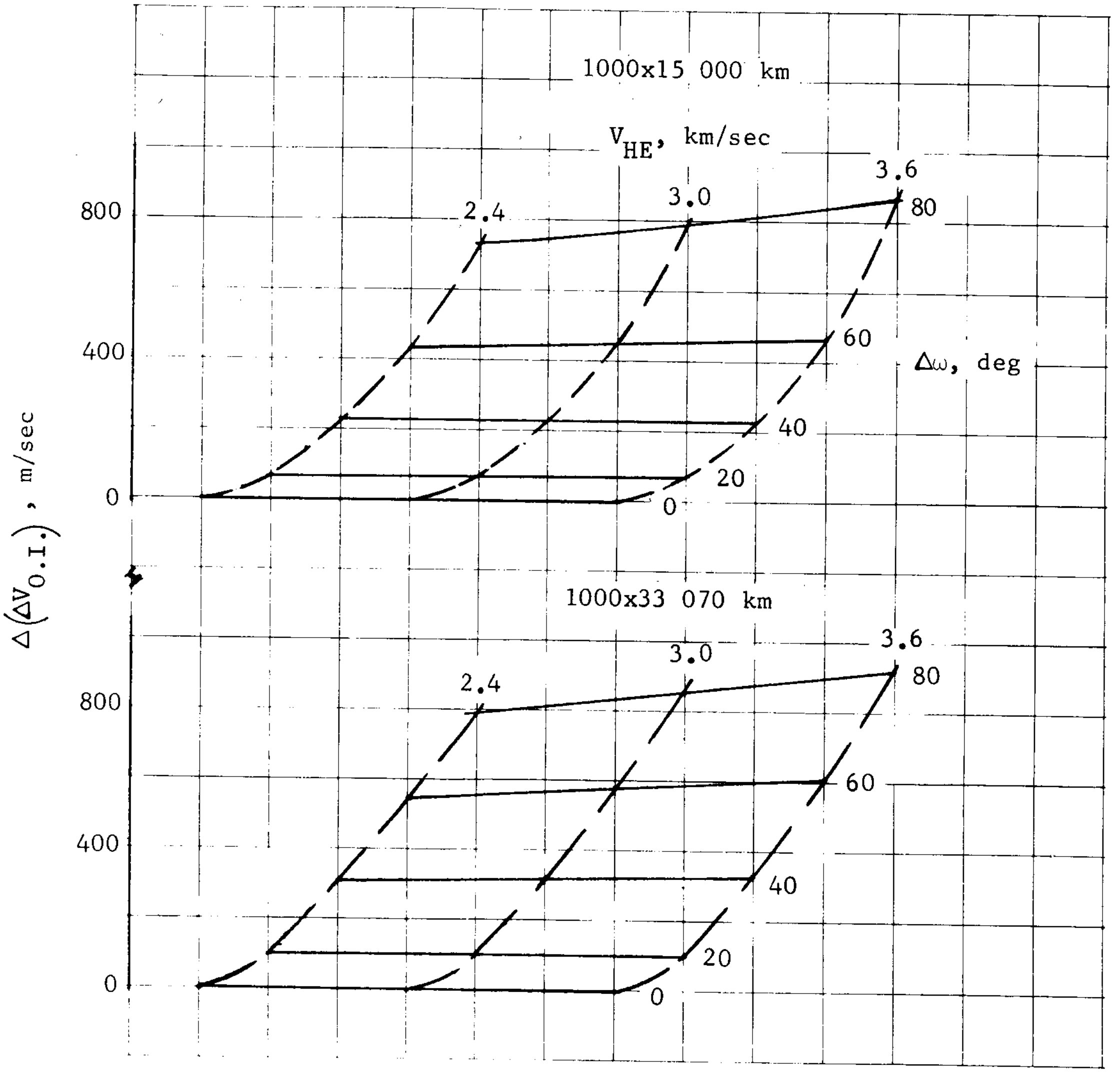

Figure A162.- Periapsis Shift Velocity Requirements

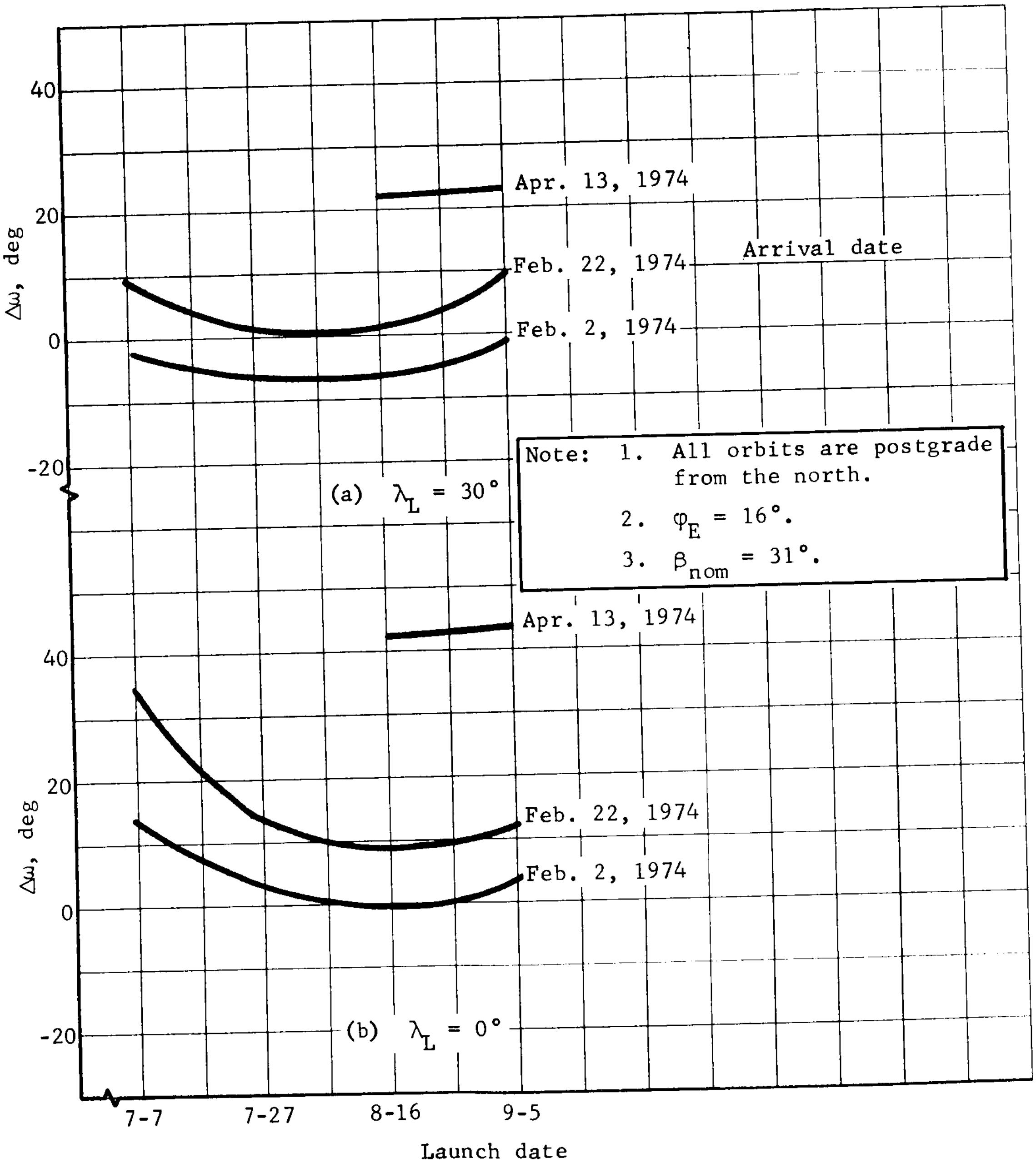

Figure A163.- Periapsis Shift Requirements to Land 30° from Evening Terminator

APPENDIX A

The major advantage of the orbit mode is its ability to survey candidate landing sites from orbit before a deorbit maneuver is made.

APPENDIX A

This page intentionally left blank.

APPENDIX A

3. ERROR ANALYSIS

The error sources considered for both the direct and orbit modes are (1) navigation uncertainty at ejection or deorbit and (2) ejection error, both pointing and impulse. The most important error at the time of entry for mission planning purposes is the error in entry flight path angle, γ_E. The high sensitivity of landed equipment weight to γ_E for the direct mode is shown in Appendix B. The downrange angle, φ_E, and crossrange angle, X_R, errors at entry are also presented. An error in φ_E is equivalent to an error in entry location parameter, β. The method for propagating φ_E through the atmosphere to obtain landing footprints is presented.

Entry Dispersions Due to Navigation Uncertainty, Direct Mode

The navigation uncertainty at the time of capsule ejection is expressed in terms of an uncertainty in the impact parameter, b, and time of periapsis passage, t_p. The maximum 3σ error in t_p is about 4 minutes. The effect of this error source on γ_E and φ_E is negligible and can be neglected. With Earth-based tracking, the 1σ error in b is shown in figure A164 as a function of time before periapsis. The upper bound on the present DSN capability is felt to be the maximum curve, while the projected capability in the early 1970s is felt to be near the minimum curve. The improvement comes about mainly through the improved ephemeris of Mars. The ability to reduce the error in b to about 5 km (1σ) through onboard guidance is discussed in Appendix D. The error in b does not decrease much until about a day before periapsis. This rapid improvement is caused by the gravitational bending of the trajectory by Mars. The times at which the trajectory enters the Martian sphere of influence are shown as a function of V_{HE}. Also shown are the times corresponding to a V_{HE} of 3.0 km/sec for capsule ejection distances of 50 000 and 100 000 km. The error in b at any R_{EJ} was taken to be at the time corresponding to a V_{HE} of 3.0 km/sec independent of the actual value of V_{HE}.

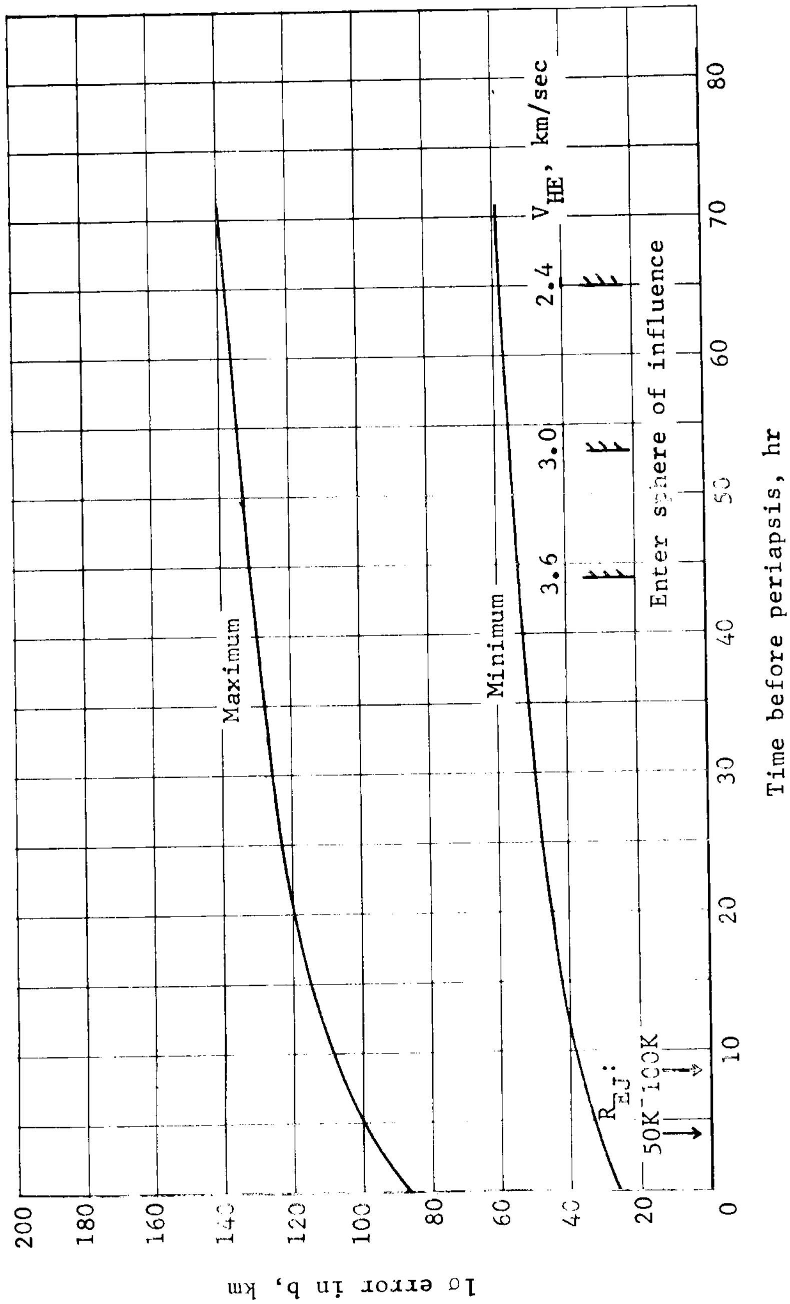

Figure A164.- Earth-Based Tracking

APPENDIX A

Analytical expressions were derived for $\partial\gamma_E/\partial b$ and $\partial\varphi_E/\partial b$ as functions of R_{EJ}, τ_{EJ}, ΔV_{EJ}, V_{HE}, h_p, and the nominal values of γ_E and φ_E. Typical results of the 3σ γ_E error are shown as a function of R_{EJ} in figure A165 for the assumed maximum and minimum error in b. The effect of τ_{EJ} is seen to be significant for lower R_{EJ}. Section 2 of this appendix shows that the τ_{EJ} is always greater, in absolute value, than -40°, and the variation of 3σ γ_E between -40 and -90° is small. From section 2, it is recalled that minimum ΔV_{EJ} occurs near a τ_{EJ} of -90°. The effect of V_{HE} is shown in figure A166 for a τ_{EJ} of -40°. The sensitivity of γ_E to an error in b is shown as a function of V_{HE} and γ_E in figure A167. The sensitivity increases rapidly with shallower γ_E. To investigate the magnitude of b error over which the partials are applicable (i.e., the nonlinearity effect), trajectories with perturbed periapsis altitude were run as shown by the solid line in figure A168. The $\partial\gamma_E/\partial r_p$ is just the product of $\partial\gamma_E/\partial b$ and $\partial b/\partial r_p$. The $\partial b/\partial r_p$ is a function of h_p and V_{HE} and, for the example shown, is 1.14. Good agreement is obtained for Δh_p or Δb less than 100 km.

The 3σ error in downrange angle, φ_E, is shown in figure A169 for the maximum navigation errors as a function of R_{EJ}. The effect of V_{HE} and γ_E are shown. The sensitivity of φ_E to b is shown in figure A170. The $\partial\varphi_E/\partial b$ is approximately 1.4 times as great as the $\partial\gamma_E/\partial b$. The nonlinearity effects are shown in figure A171. The ratio of crossrange error, X_R, to error in b is shown as a function of V_{HE} and γ_E in figure A172. This assumes that the error in the b plane is spherically distributed.

The expression for $\partial\gamma_{LE}/\partial b$ reduces to the following for small ΔV_{EJ}:

$$\partial\gamma_{LE}/\partial b = \frac{V_{HE}}{r_E\left(V_{HE}^2 + \frac{2\mu}{r_E}\right)\sin r_E}$$

where r_E is the entry radius.

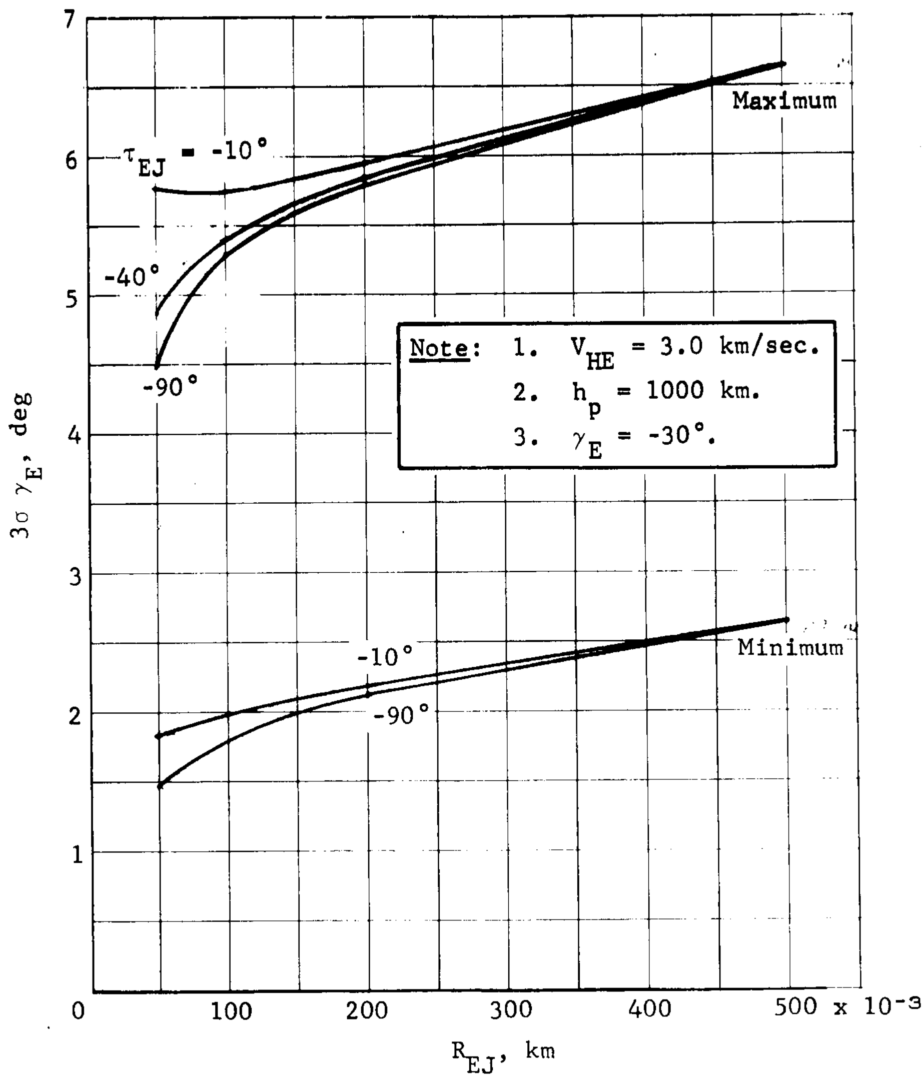

Figure A165.- Error due to Navigation, Entry Flightpath Angle

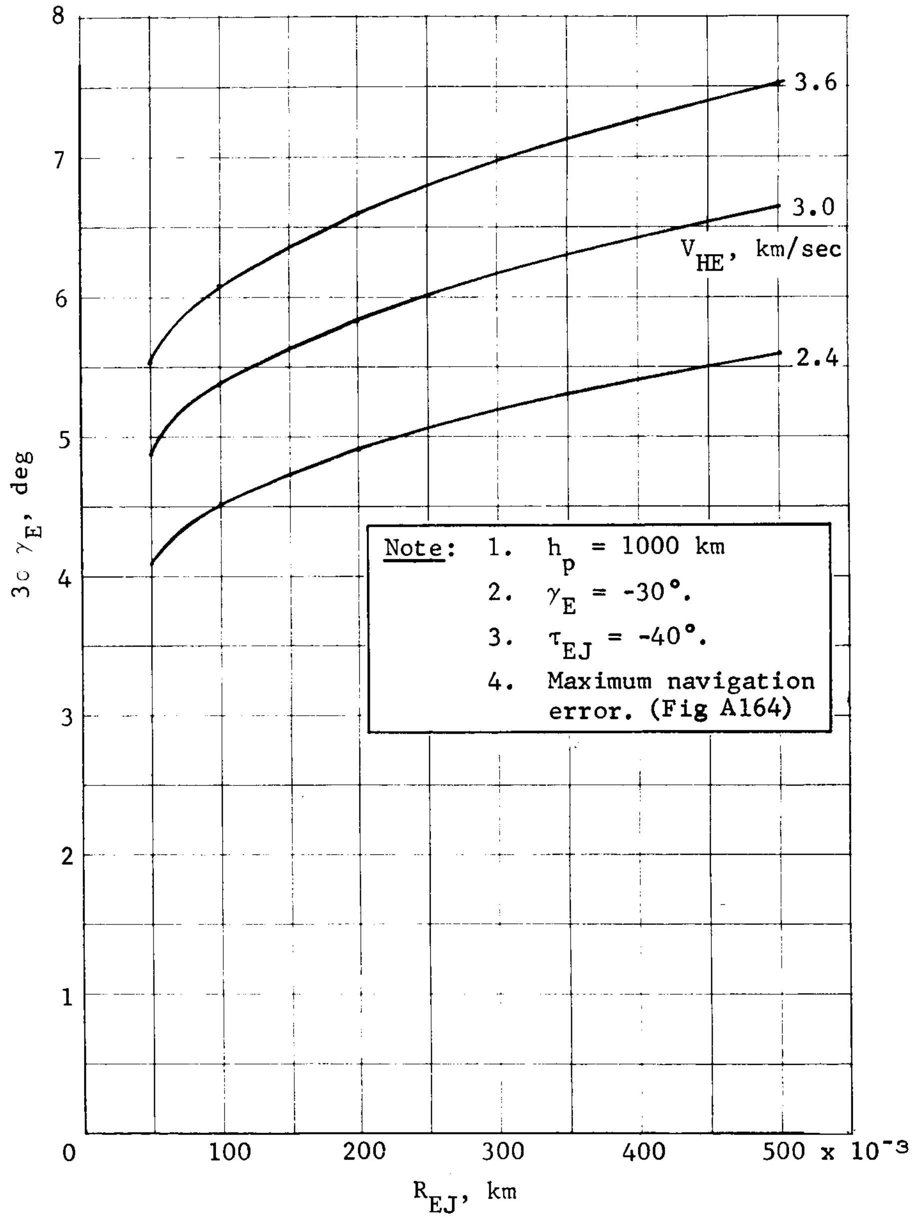

Figure A166.- Error due to Naviagtion, Entry Flightpath Angle

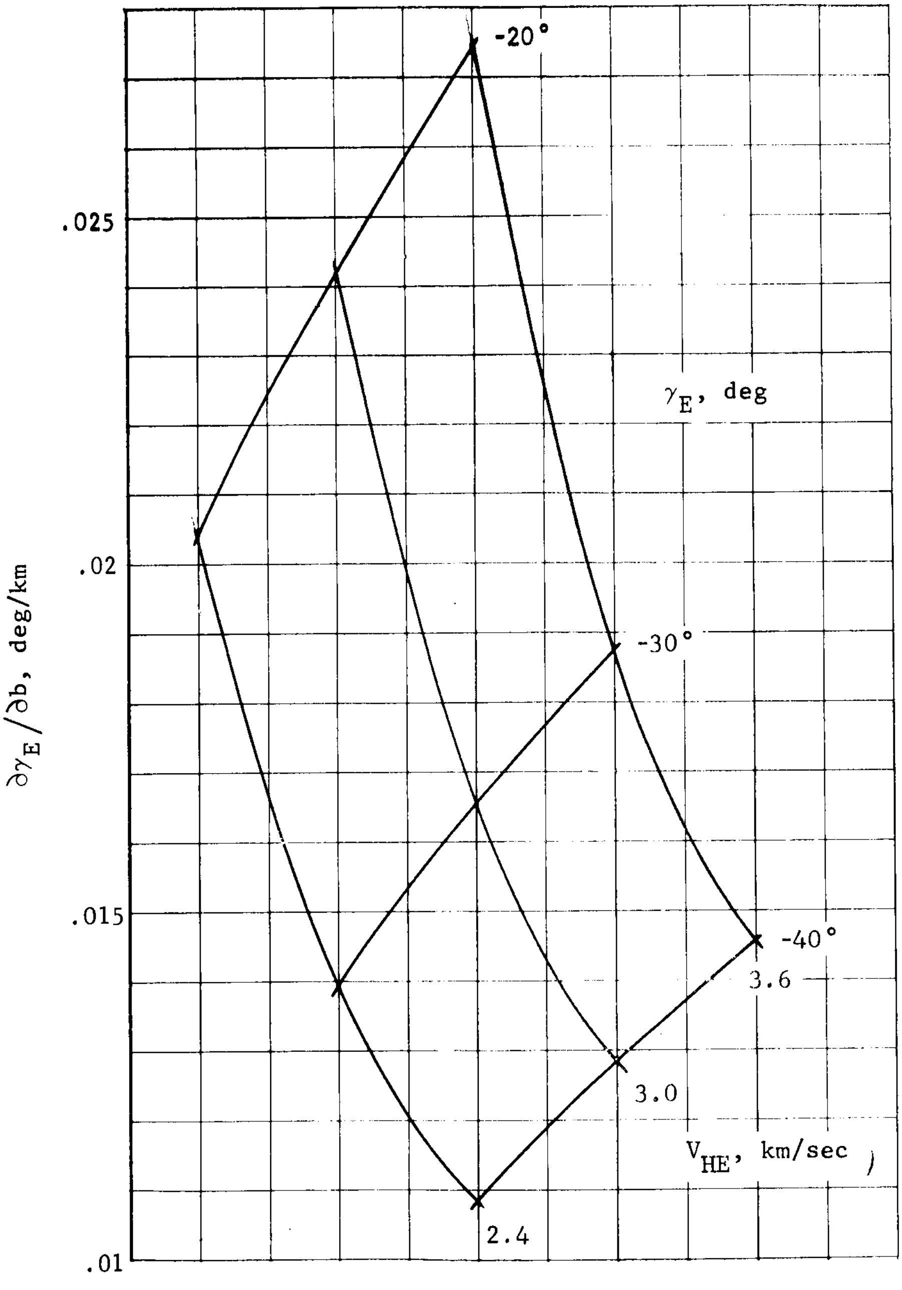

Figure A167.- Sensitivity to Navigation Error, Direct Mode, Entry Flightpath Angle

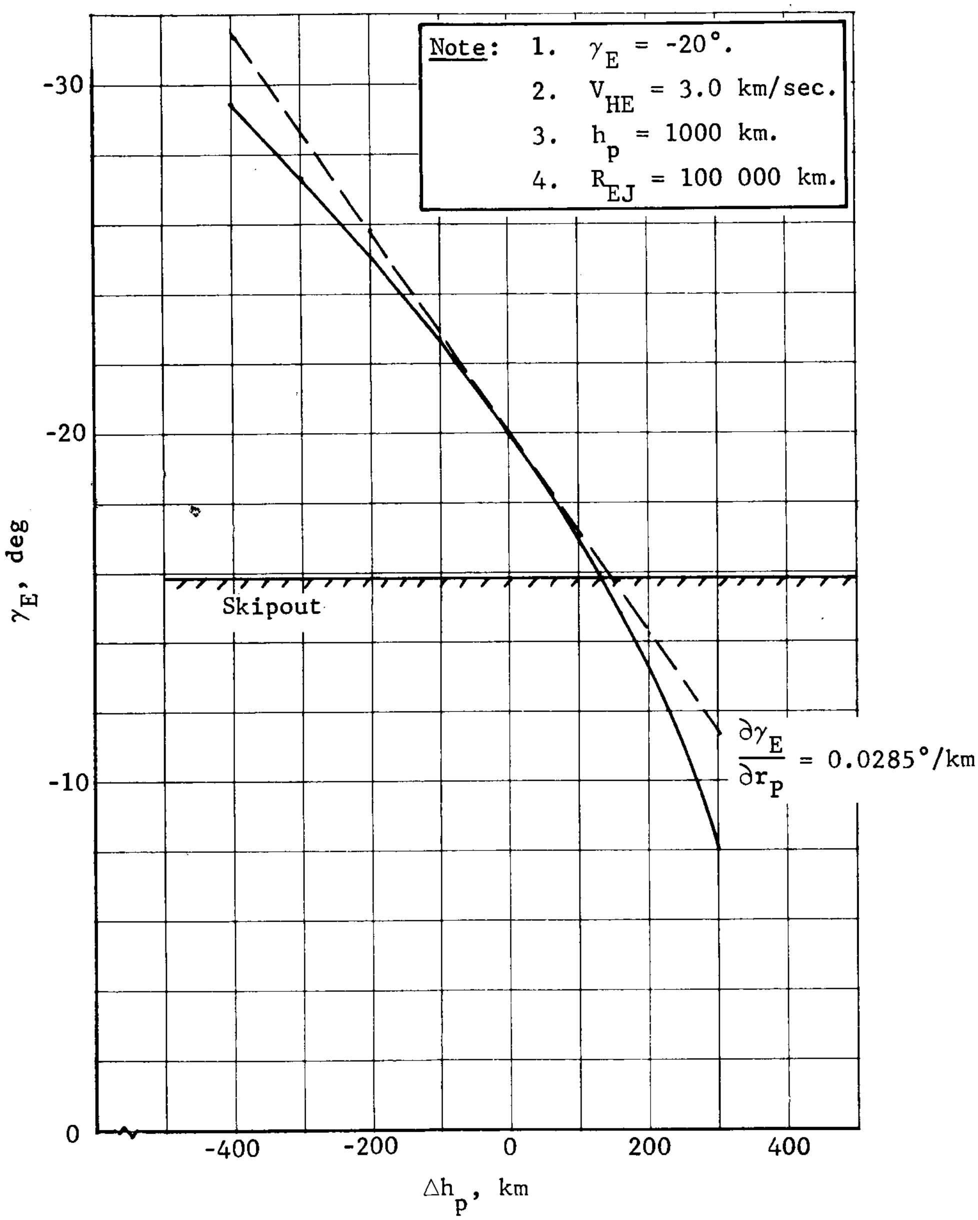

Figure A168.- Nonlinearity Effects, Entry Flightpath Angle

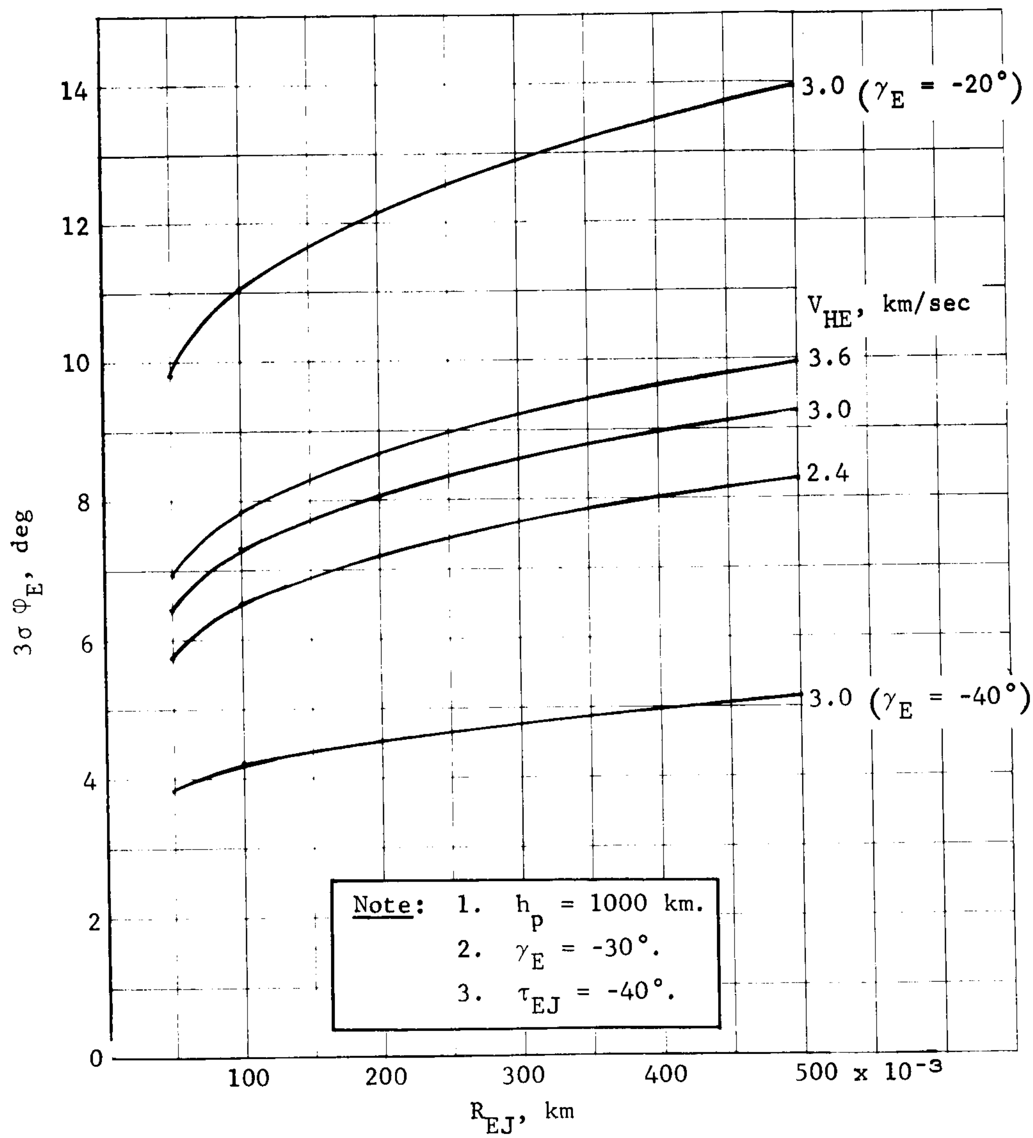

Figure A169.- Maximum Error due to Navigation, Downrange Angle

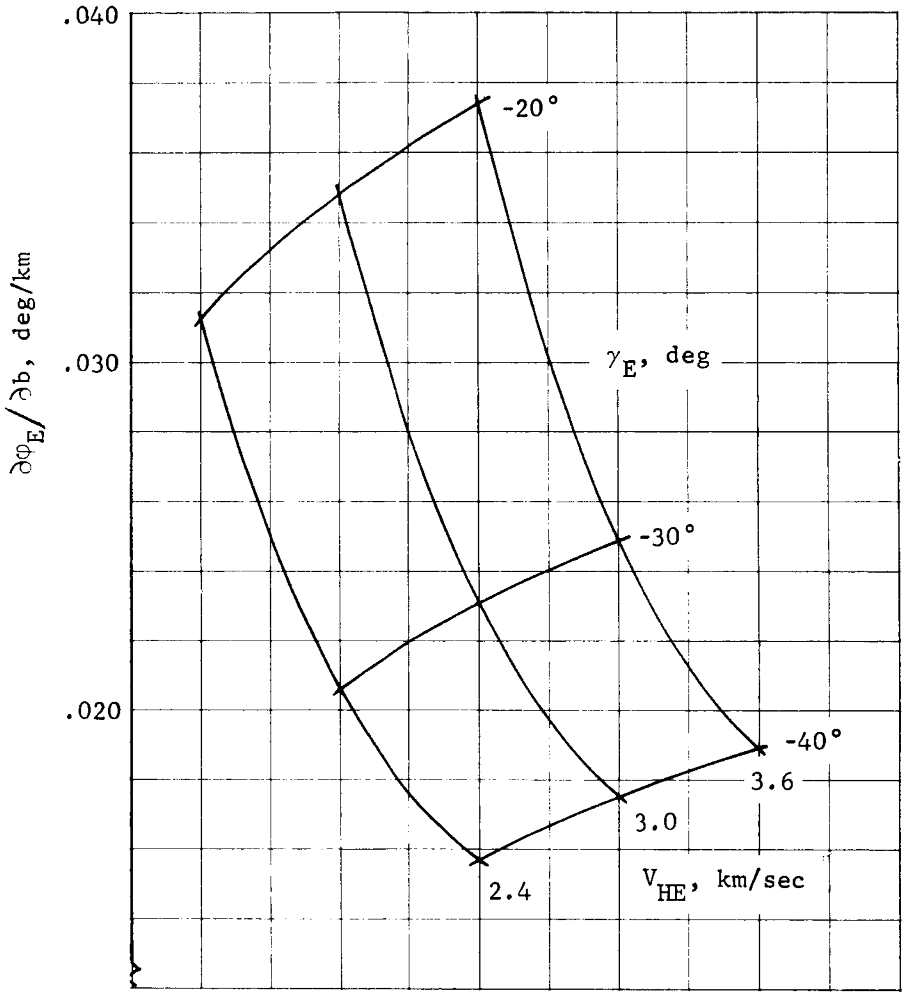

Figure A170.- Sensitivity to Navigation Errors, Direct Mode, Downrange Angle

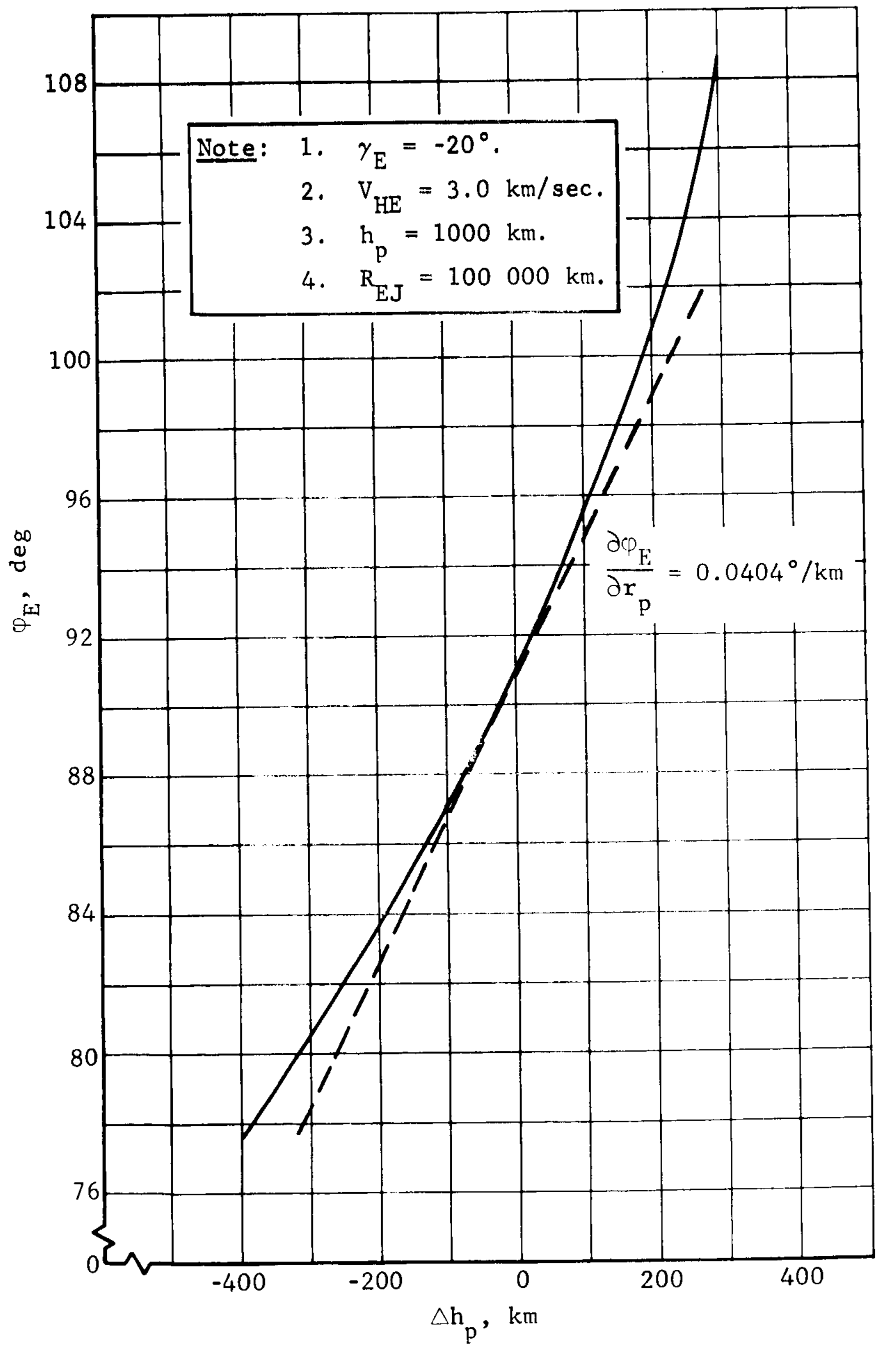

Figure A171.- Nonlinearity Effects, Downrange Angle

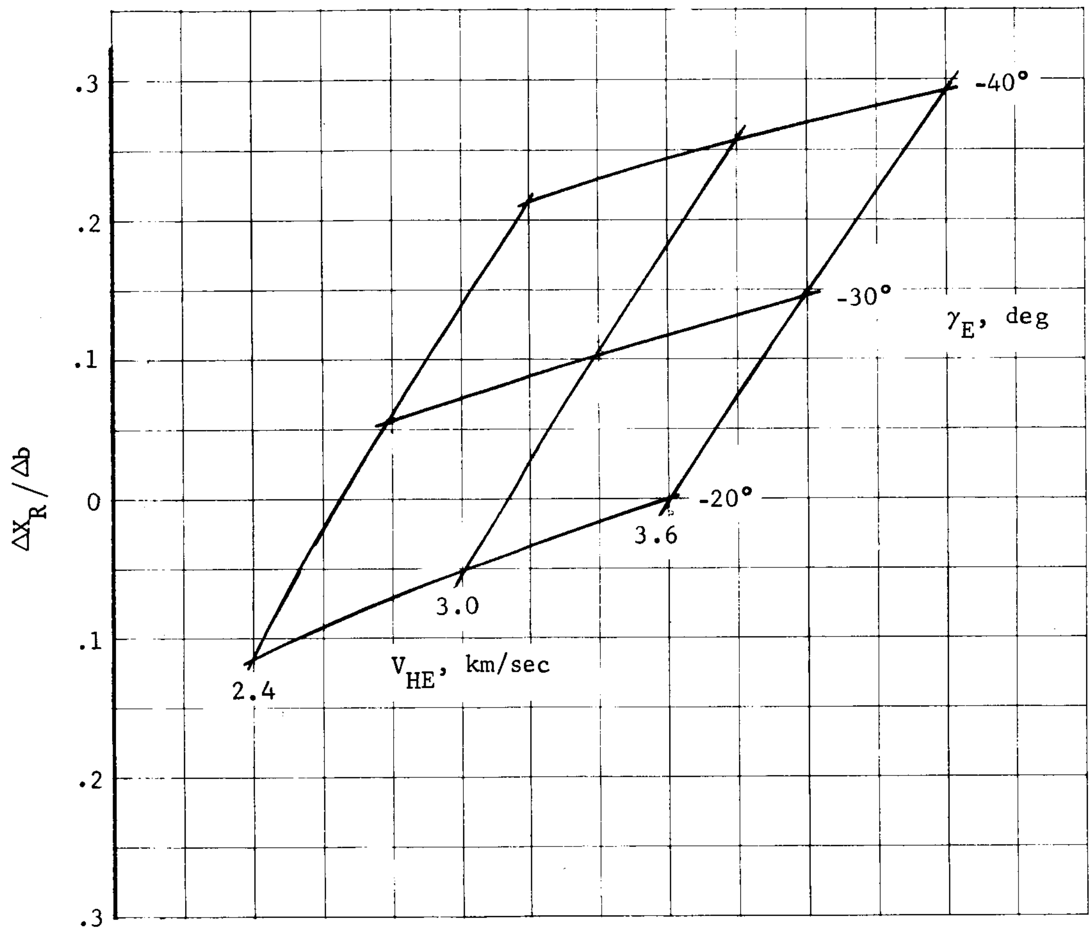

Figure A172.- Cross range error, Direct Mode, 50 000 < R_{EJ} < 500 000 km

APPENDIX A

Entry Dispersion Due to Ejection Maneuver Errors, Direct Mode

The ejection maneuver errors comprise a pointing error and an impulse error. A fixed entry altitude computer program was constructed, which propagates these errors from ejection to entry. The entry dispersions due to pointing are most sensitive to the ejection angle, τ_{EJ}. The 1σ error in γ_E due to a 1σ pointing error of 0.5° is shown as a function of τ_{EJ} in figure A173. The error is shown for a nominal γ_E of -30°, an h_p of 1000 km, and a V_{HE} of 3.0 km/sec. For a given τ_{EJ} the $\sigma\gamma_E$ increases with decreasing R_{EJ}. As mentioned before, the τ_{EJ} is always greater, in absolute value, than -40° to keep the ΔV_{EJ} requirements reasonable and to obtain reasonable lead angles, λ, at entry. The maximum $\sigma\gamma_E$ is, for an R_{EJ} of 50 000 km, 0.4°. The effect of nominal γ_E is slight as shown in figures A174 and A175 for γ_E of -20 and -40°. The effect of V_{HE} is also slight as seen in figures A176 and A177 for V_{HE} of 2.4 and 3.6 km/sec.

The dispersion in γ_E due to a 1σ impulse error of 0.33% of the nominal value is shown in figure A178 as a function of τ_{EJ}. It is seen to be almost independent of τ_{EJ} and nearly a constant value of 0.1°. The variation with nominal γ_E is again negligible.

The dispersion in φ_E as a function of τ_{EJ} is shown in figure A179 for a 1σ pointing error of 0.5°. It is again about 1.4 times the corresponding error in γ_E. The dispersion in φ_E due to an impulse error is almost invariant with τ_{EJ} and is about 0.14°. The dispersion in X_R is shown in figure A180 and is about half the downrange error.

The dispersions in γ_E due to the three error sources discussed is used to determine the minimum nominal γ_E possible as well as the 3σ dispersions about this nominal. The minimum nominal γ_E is defined to be 5σ above the skipout boundary and is shown in figure A181. It is shown as a function of the 1σ error in γ_E due to an error in b, evaluated for a γ_E of -30°.

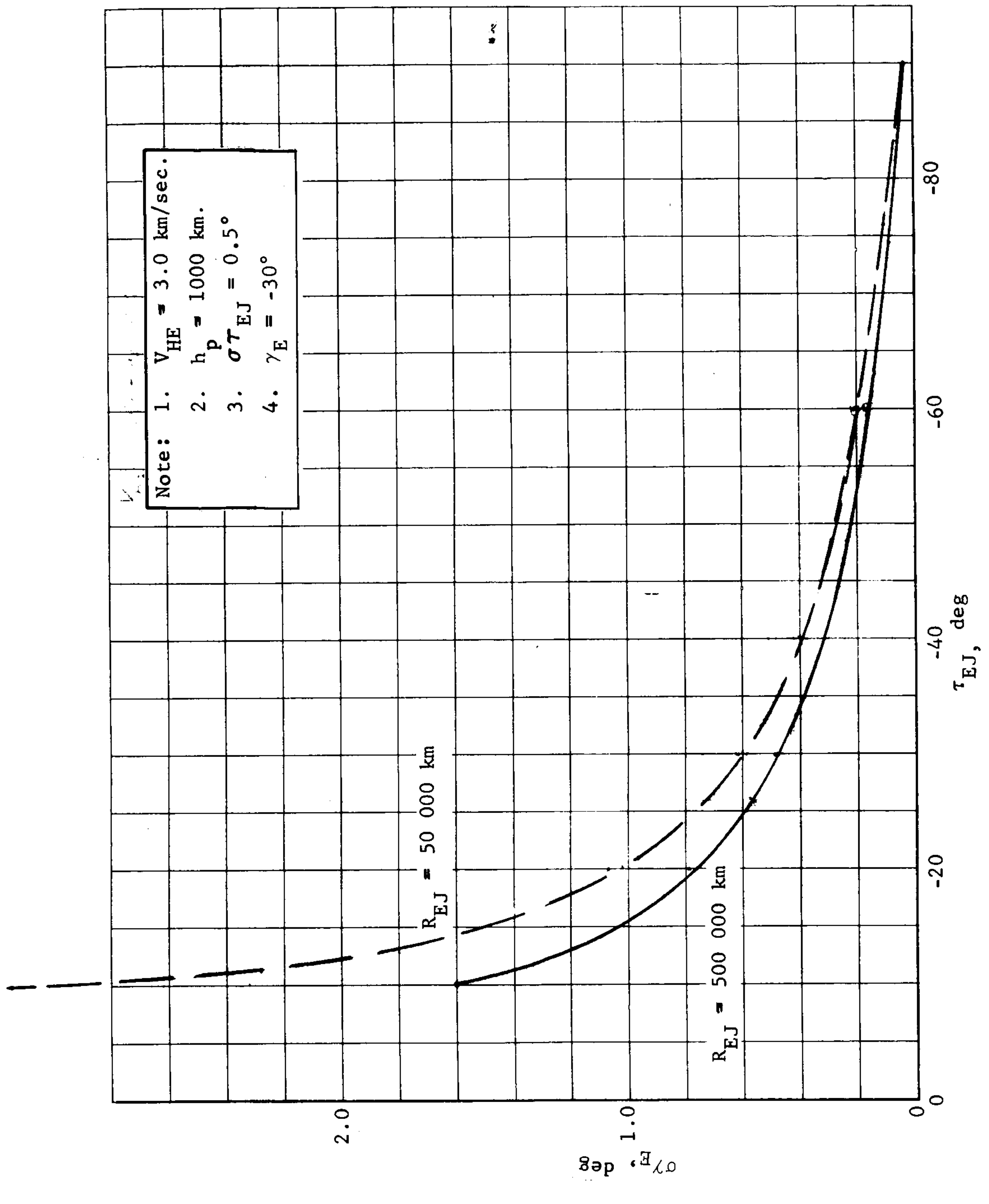

Figure A173.- Entry Flightpath Angle Dispersion versus Ejection Angle, Direct Mode

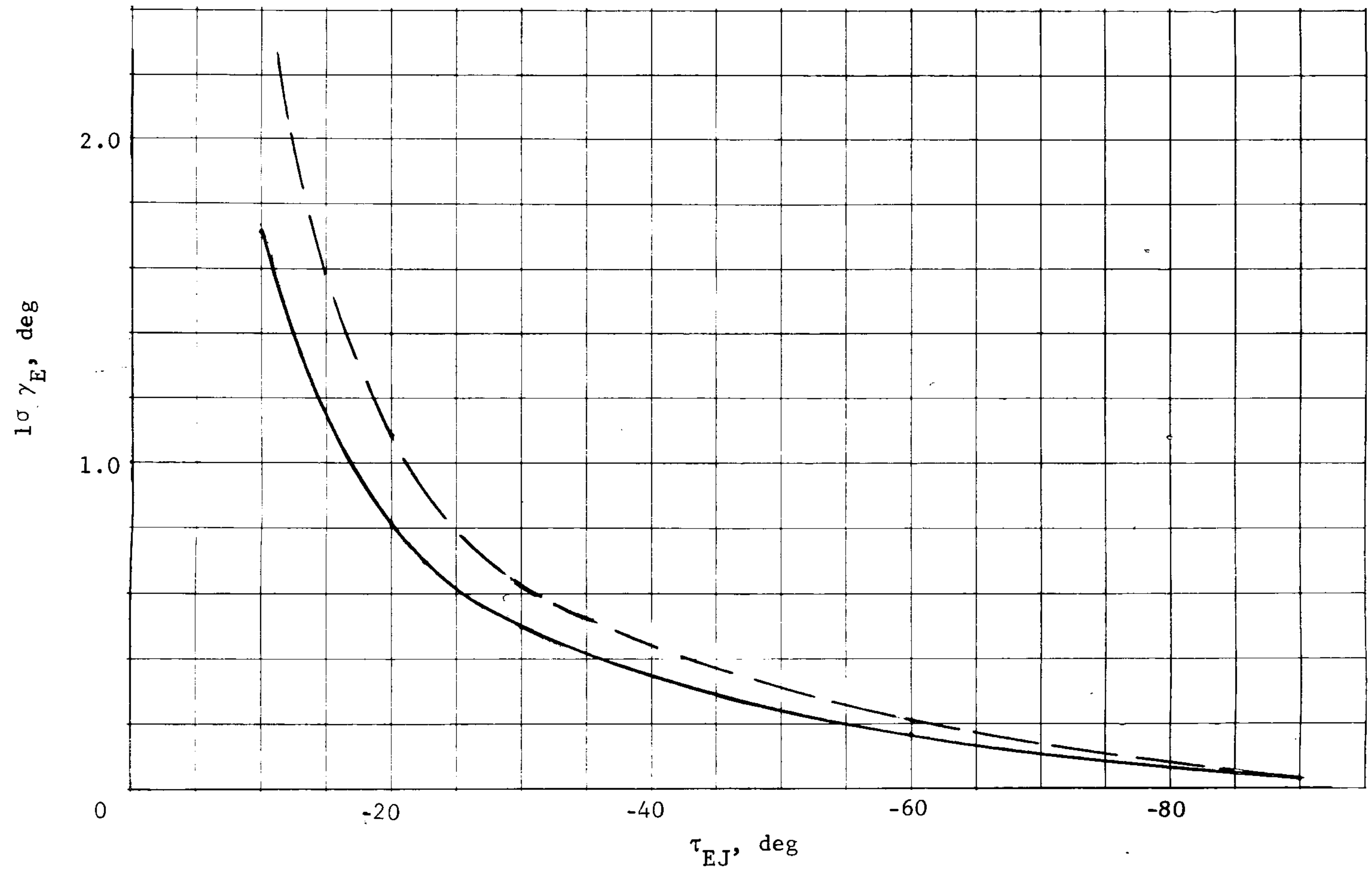

Figure A174.- Entry Flightpath Angle Dispersion versus Ejection Angle, Direct Mode, V_{HE} = 3.0 km/sec, γ_E = -40°

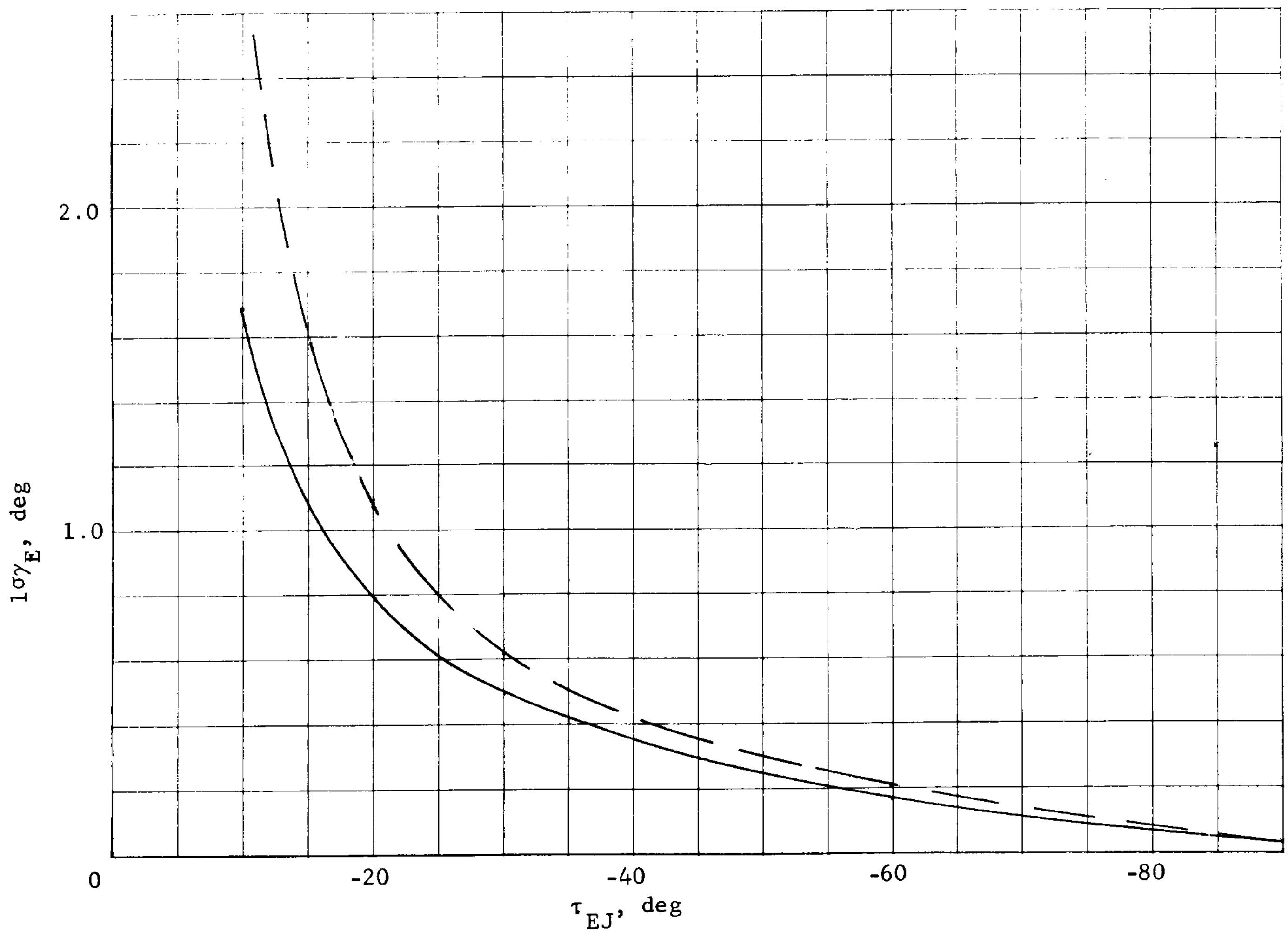

Figure A175.- Entry Flightpath Angle Dispersion versus Ejection Angle, Direct Mode, $V_{HE} = 3.0$ km/sec, $\gamma_E = -20°$, $\sigma\tau_{EJ} = 0.5°$

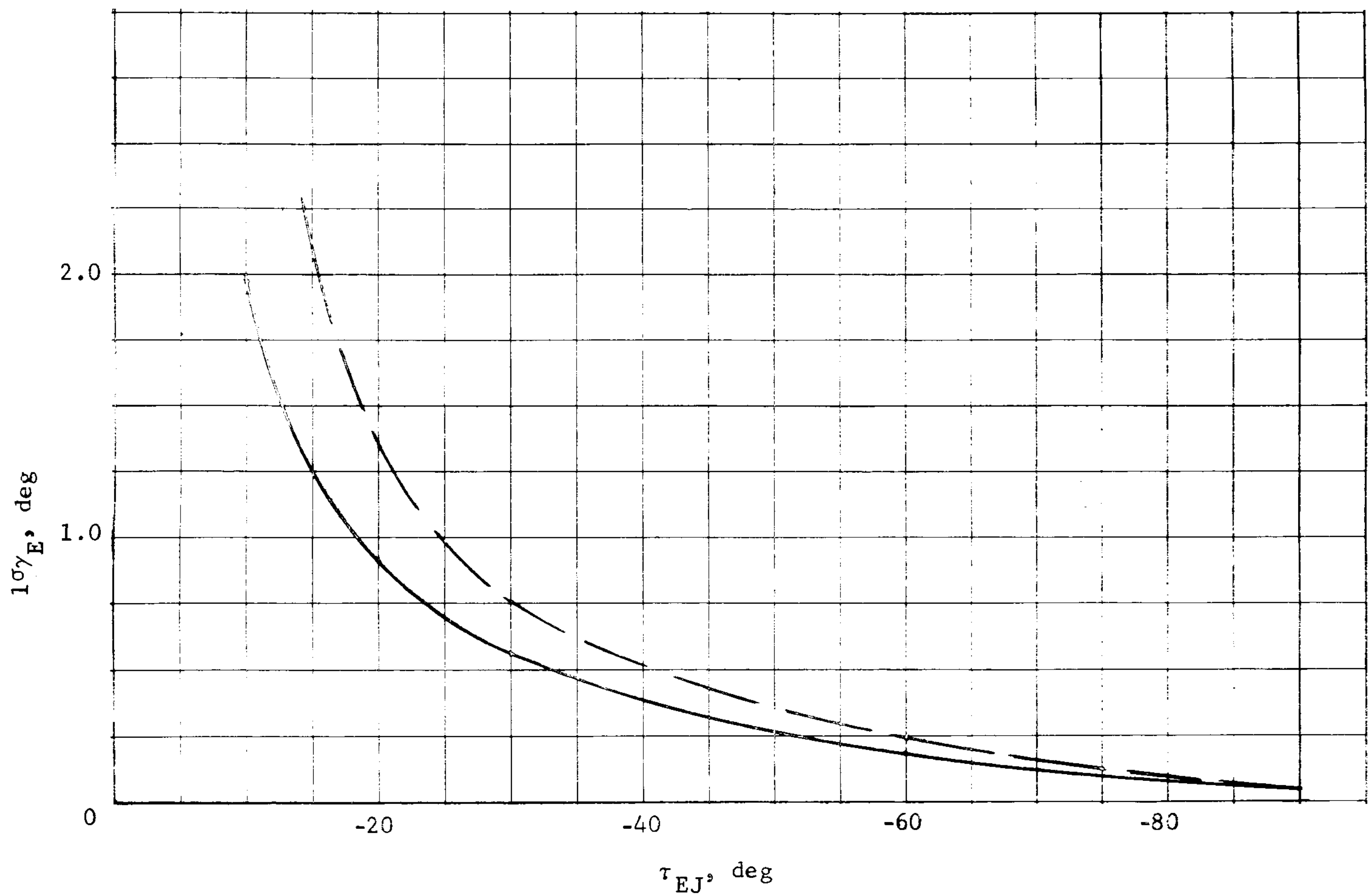

Figure A176.- Entry Flightpath Angle Dispersion versus Ejection Angle, Direct Mode, V_{HE} = 2.4 km/sec, γ_E = -30°

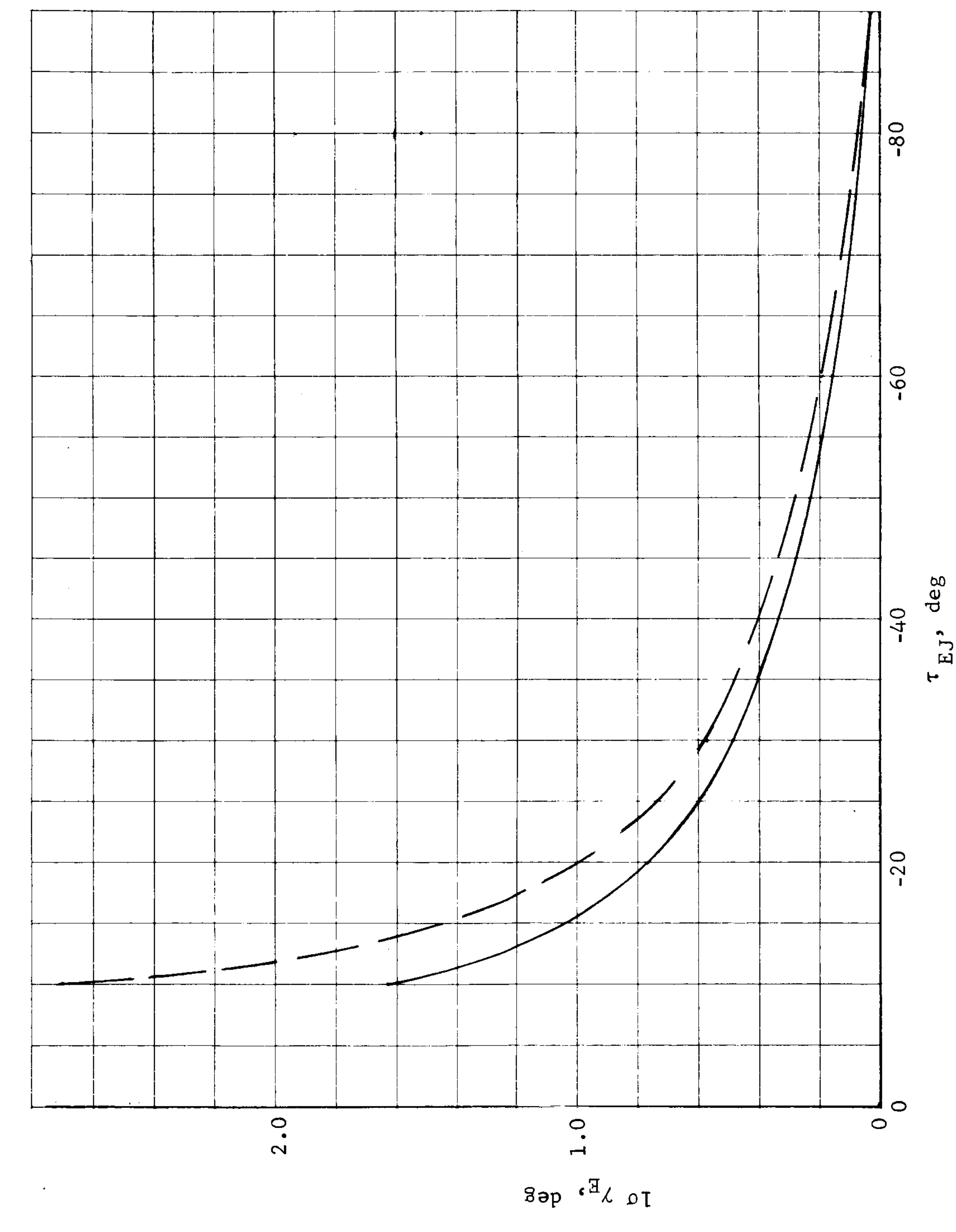

Figure A177.- Entry Flightpath Angle Dispersion versus Ejection Angle, Direct Mode, V_{HE} = 3.6 km/sec, γ_E = -30°

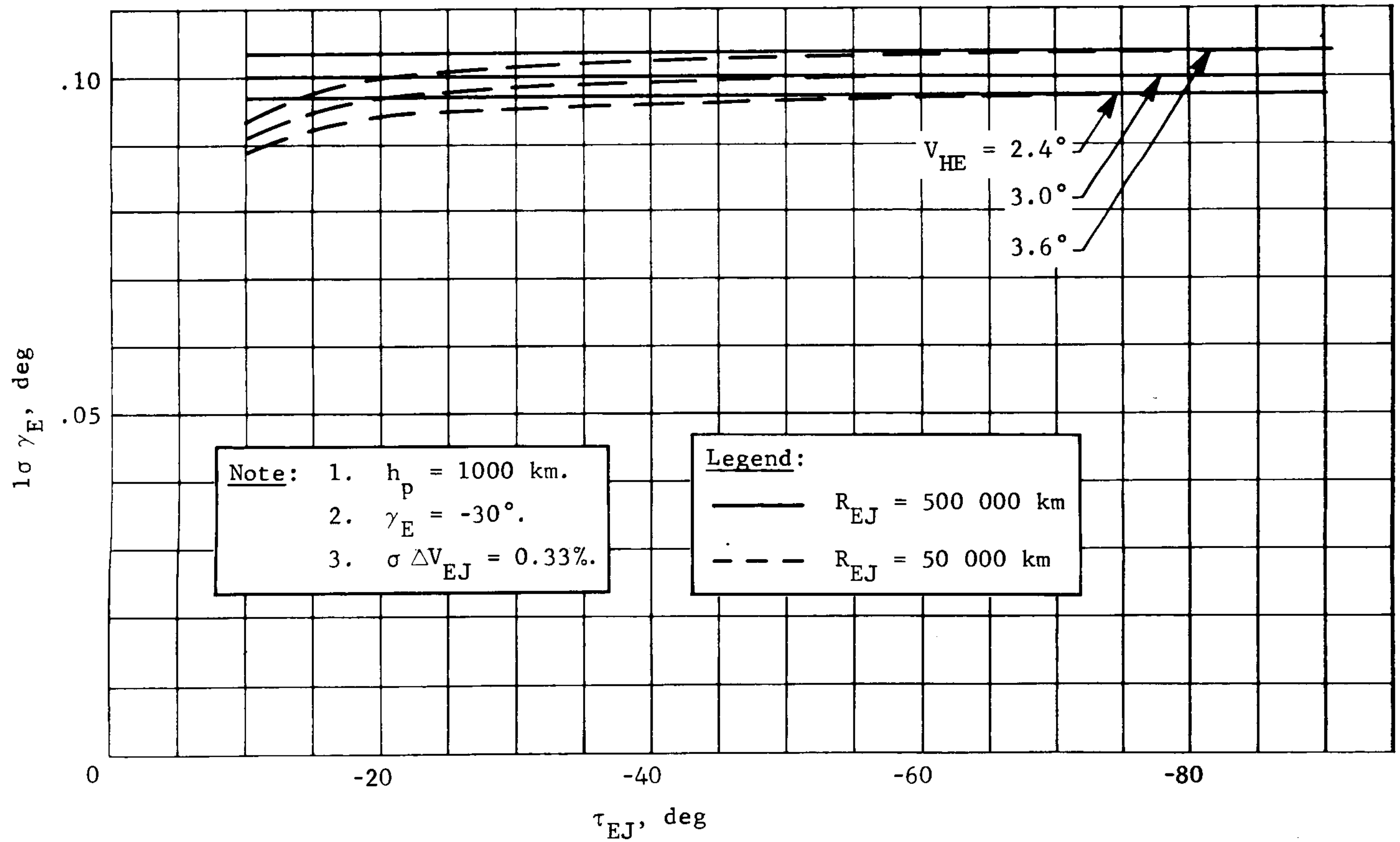

Figure A178.- Dispersion in Entry Flightpath Angle due to an Impulse Error

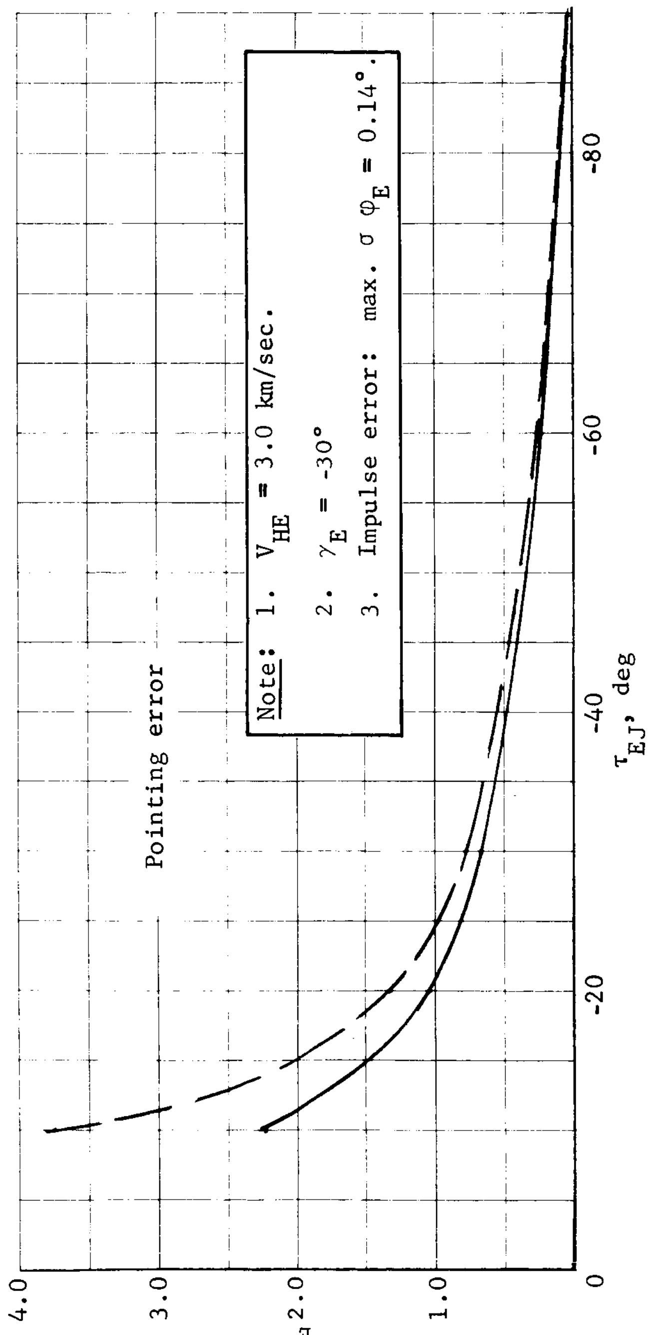

Figure A179.- Dispersion in Downrange Angle as a Function of Ejection Angle

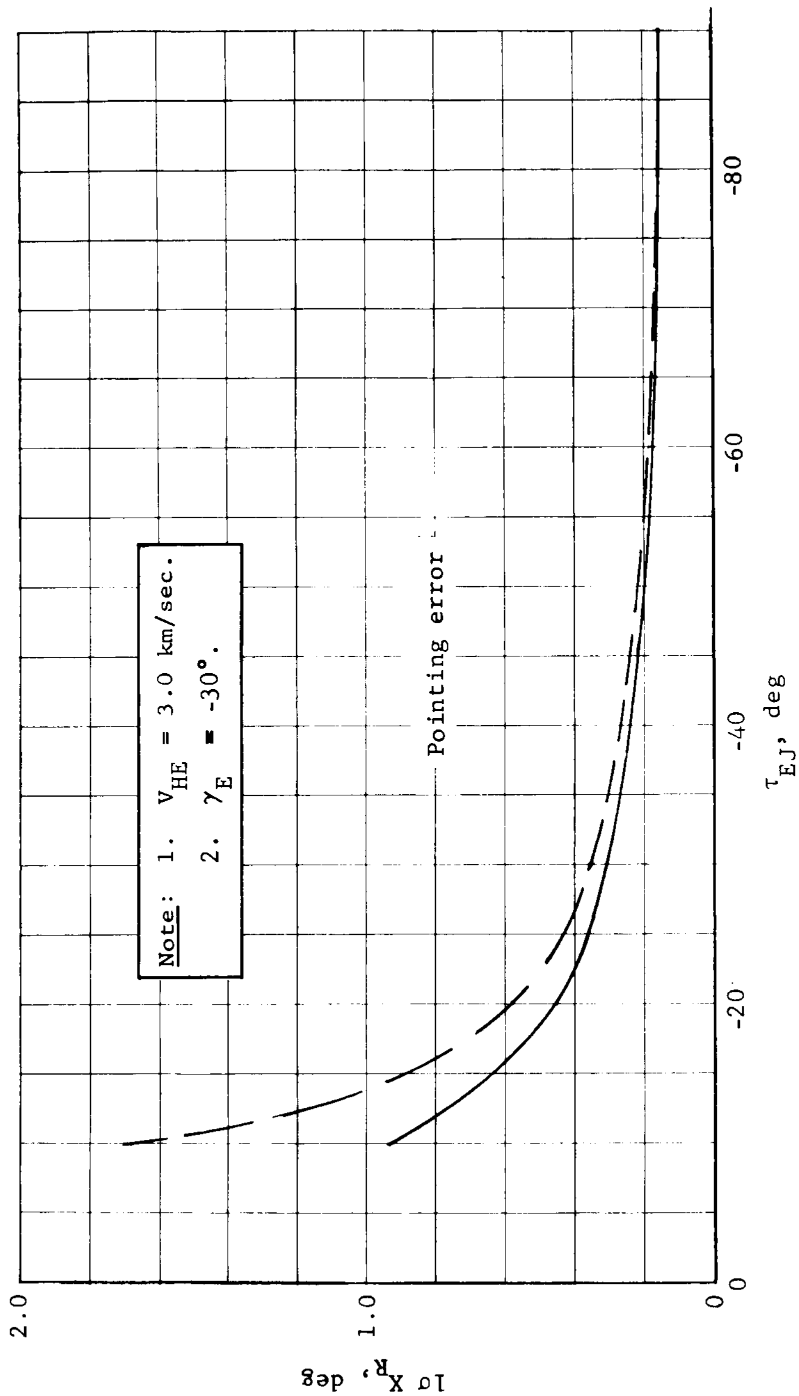

Figure A180.- Dispersion in Crossrange Angle as a Function of Ejection Angle

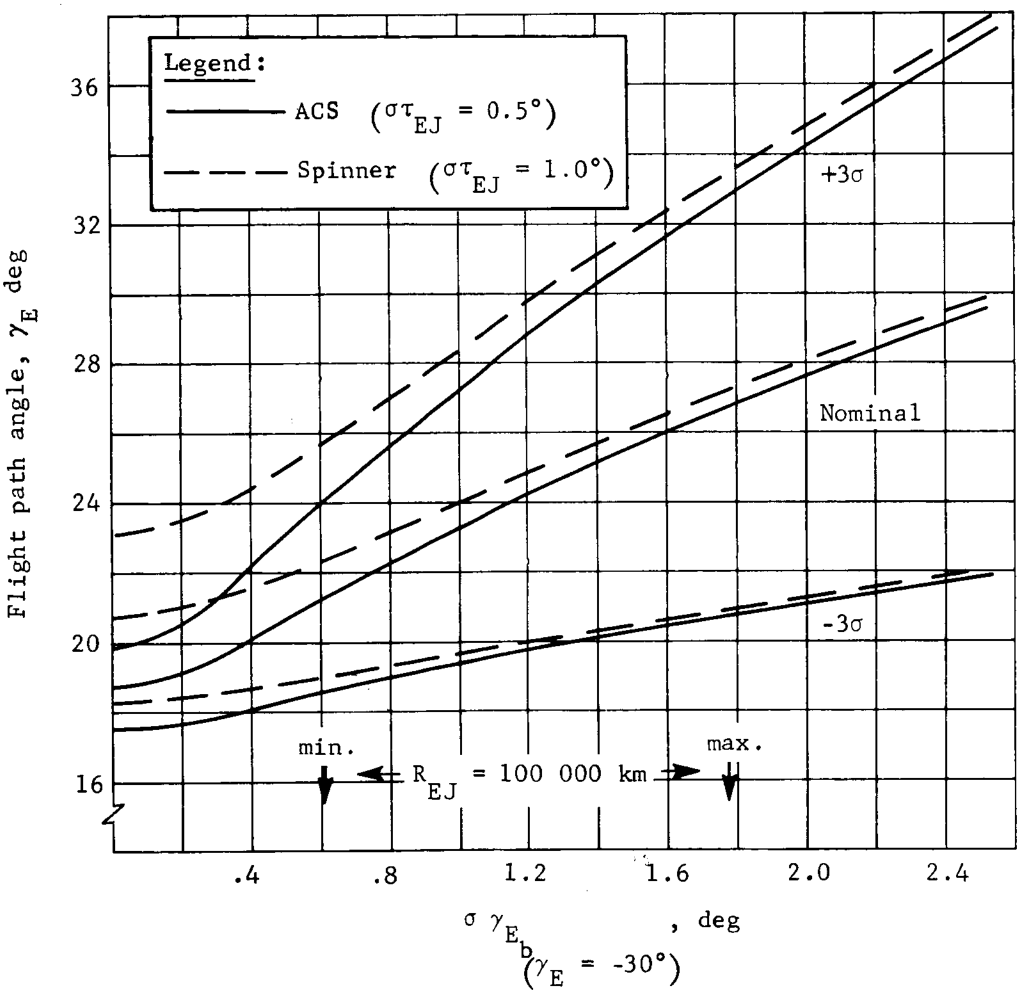

Figure A181.- Direct Mode Entry Corridor

For the ACS, the $\sigma\tau_{EJ}$ was taken to be 0.5°, and for the spinner 1.0°. For example, if the R_{EJ} is 100 000 km and the V_{HE} is 3.0 km/sec, the error in b is 106 and 37 km for the maximum and minimum curves. Independent of nominal γ_E, the $\partial\gamma_E / \partial b$ is read from figure A167 for a γ_E of -30° as 0.01655°/km. The resulting $\sigma\gamma_E$ due to an error in b evaluated at a γ_E of -30° is 1.75 and 0.61° for the maximum and minimum curves, respectively. The corresponding minimum nominal γ_E for the ACS case is -26.7 and -21.3°.

Entry Dispersions Due to Navigation Uncertainty, Orbit Mode

The navigation uncertainty for the orbit mode case is analyzed differently from the direct mode. A covariance matrix of orbital elements is assumed after at least four orbits of Earth-based tracking. The standard deviation of the orbital elements is taken to be σ_a = 3.33 km, σ_e = 0.33 x 10^{-4}, σ_{tp} = 1.67 sec, σ_ω = 0.007°, σ_Ω = 0.141°, and σ_i = 0.026°. The reference plane used is the plane in the sky. This is the plane that is normal to the Earth to Mars line of sight. Based on the assumed covariance matrix, the position and velocity errors as a function of true anomaly of deorbit, θ_D, can be found for a given nominal inclination to the plane in the sky, i_{PIS}.

The position errors are shown in figure A182 for the 1000x 33 070-km orbit for the θ_D range between 160 and 240°. The axis system is as shown with the Z_M-axis always toward the deorbit point and with the Y_M-axis opposite the angular momentum vector. Curves are shown for i_{PIS} of 5 and 60°, which considered all six orbital element errors. It is seen that the X_M error is lower for the i_{PIS} of 60°, while the out of plane error Y_M is larger. The Z_M error is unaffected by i_{PIS}. Also shown is the variation of the position errors if only the in-plane orbital element errors are considered, i.e., σ_a, σ_e, and σ_{tp}. The X_M component is reduced while the Z_M component is unchanged. There is no error out of the plane. Section 2 of this appendix has shown that the reference deorbit maneuver strategies always have θ_D greater than 180° and less than 240°.

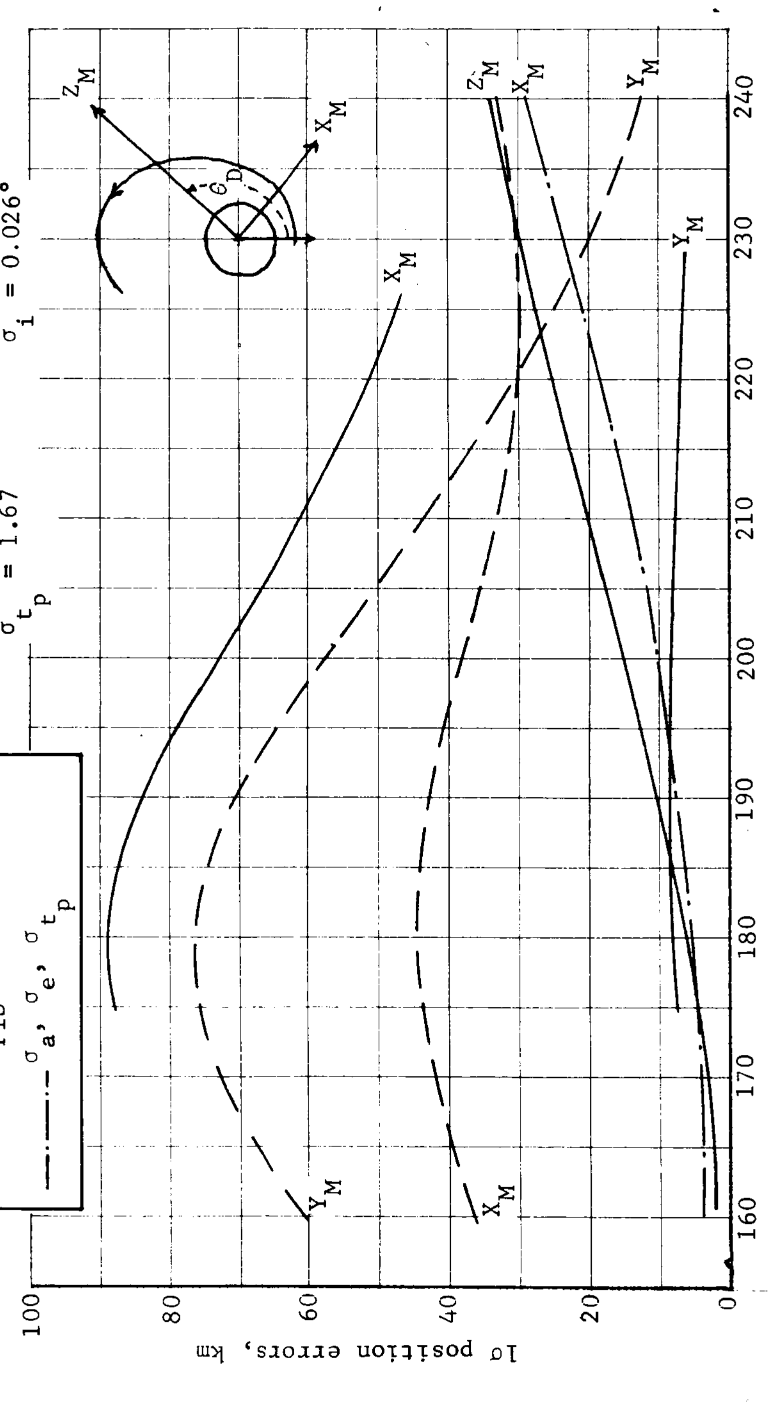

Figure A182.- Position Uncertainties at Deorbit, 1000x33 000-km Orbit

APPENDIX A

The sensitivity of γ_E to errors in X_M and Z_M is roughly the same magnitude and increases with θ_D in this range. The sensitivity of γ_E to an error in Y_M is zero.

The velocity errors are shown as a function of θ_D in figure A183 for the same i_{PIS} as above. Again the $\dot{X}_M$ error is lower for the i_{PIS} of 60°, while the $\dot{Y}_M$ is larger. The velocity component in the radial direction is also lower for the i_{PIS} of 60°. If only the in-plane orbital element errors are considered, the $\dot{X}_M$ is reduced to nearly zero, and the $\dot{Z}_M$ component is also reduced. The sensitivity of γ_E to an error in $\dot{X}_M$ is at least a factor of 10 greater than the sensitivity to error in $\dot{Z}_M$. The sensitivity to $\dot{X}_M$ decreases with increasing θ_D.

The position and velocity errors are shown for the 1000x15 000-km orbit in figures A184 and A185. Only an i_{PIS} of 60° and the in-plane case are shown. All the position components are lower than for the 1000x33 070-km orbit. The $\dot{X}_M$ component is lower but the $\dot{Y}_M$ and $\dot{Z}_M$ components are larger. The γ_E sensitivity to $\dot{X}_M$ is more critical, however, and the resulting γ_E error due to the total covariance matrix of position and velocity is lower for the smaller orbit.

The error in γ_E is shown as a function of θ_D in figure A186 for both orbits with an i_{PIS} of 60°. The γ_E is -15.5° for the 1000x33 070-km orbit and -15° for the 1000x15 000-km orbit. The range of entry location parameter, β, corresponds to that discussed in section 2 of this appendix. A minimum clearly occurs at a θ_D of 180°. Also shown is the effect of only considering in-plane errors, which reduces the dispersion in γ_E. If near-equatorial landing sites 30° from the evening terminator are desired in the 1973 launch period, the required orbits will have a high inclination to the plane in the sky, greater than 60°. For this reason, the final analysis of entry corridors is based on an i_{PIS} of 60°. For each β there corresponds a specific θ_D for the reference deorbit maneuver strategy as described in section 2 of this appendix.

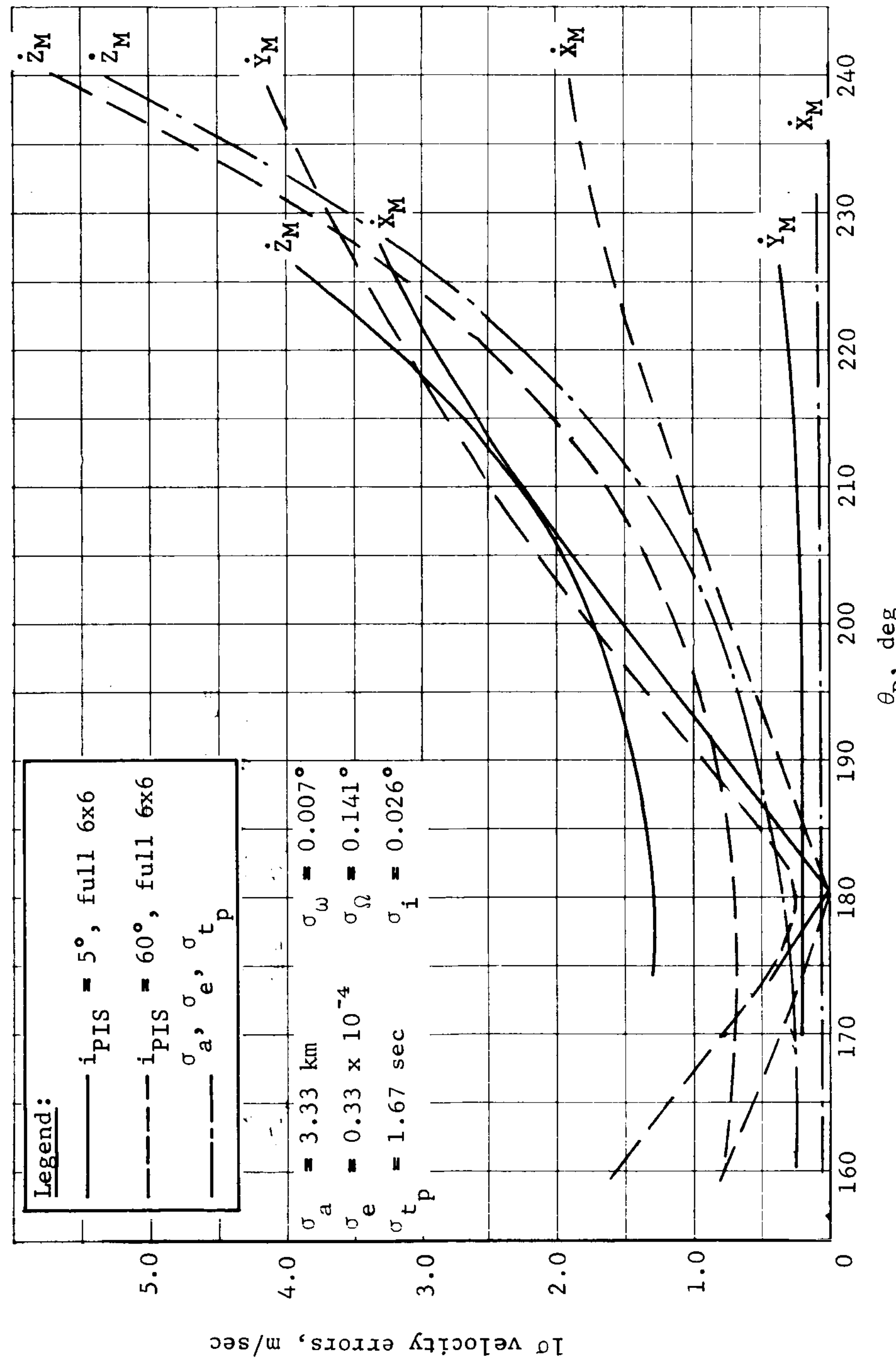

Figure A183.- Velocity Uncertainties at Deorbit, 100x33 700-km Orbit

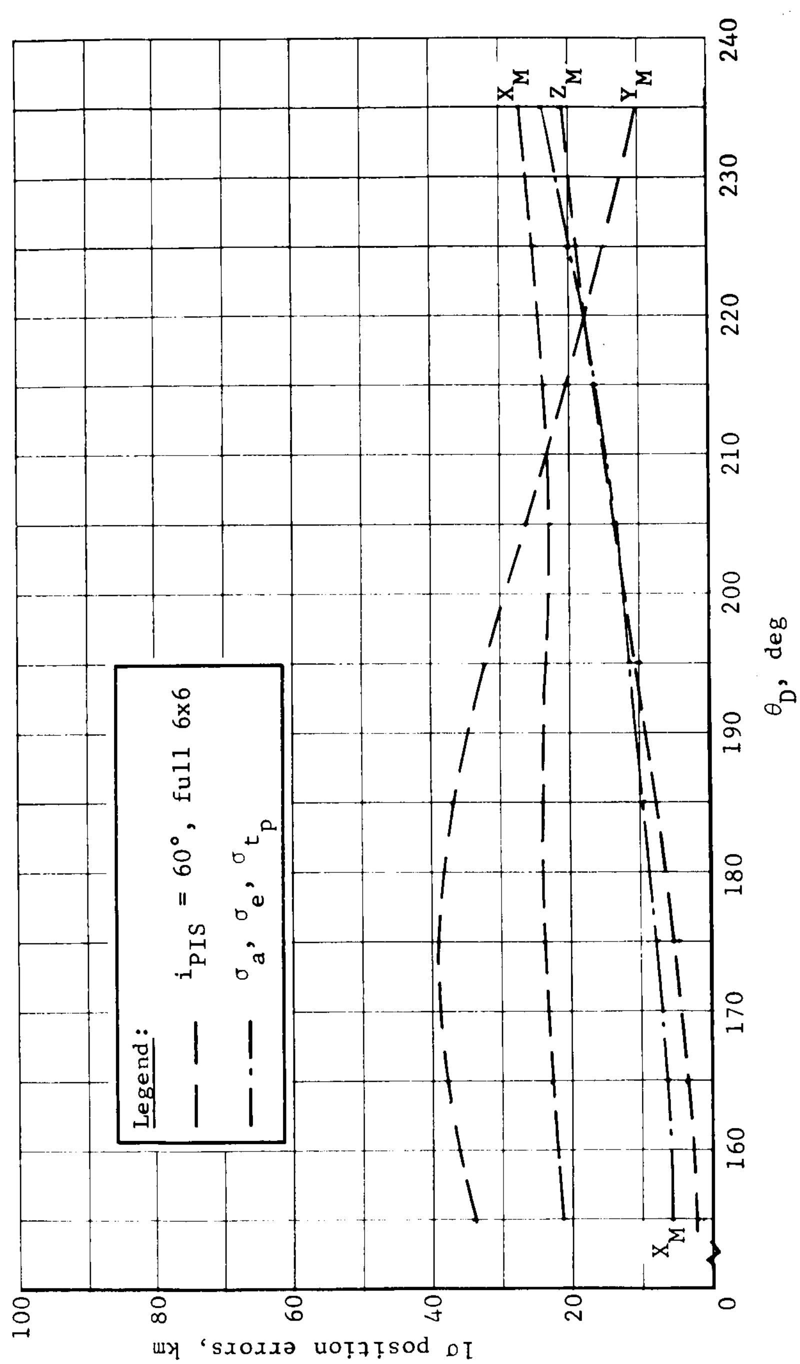

Figure A184.- Position Uncertainties at Deorbit, 1000x15 000-km Orbit

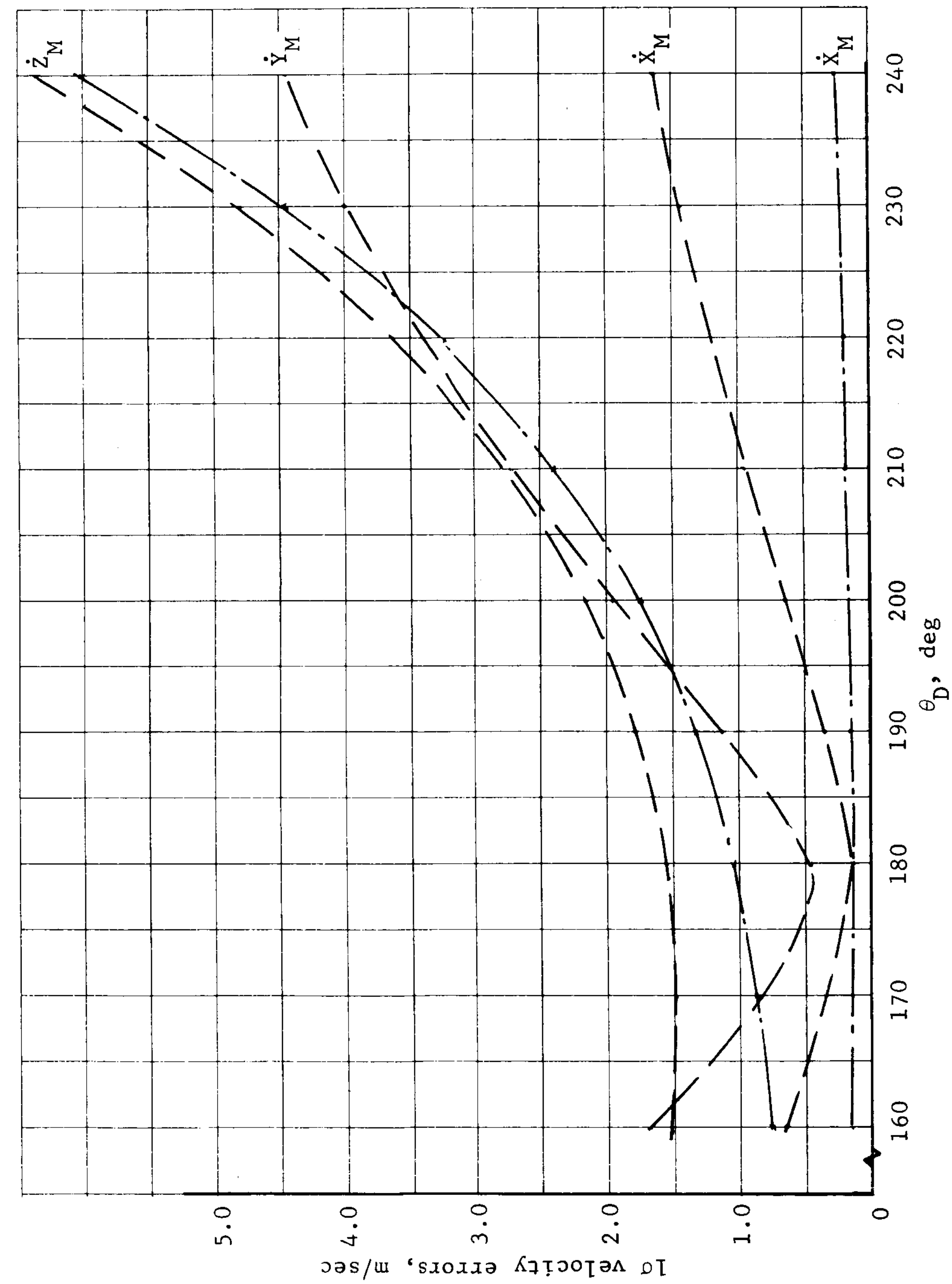

Figure A185.- Velocity Uncertainties at Deorbit, 1000x15 000-km Orbit

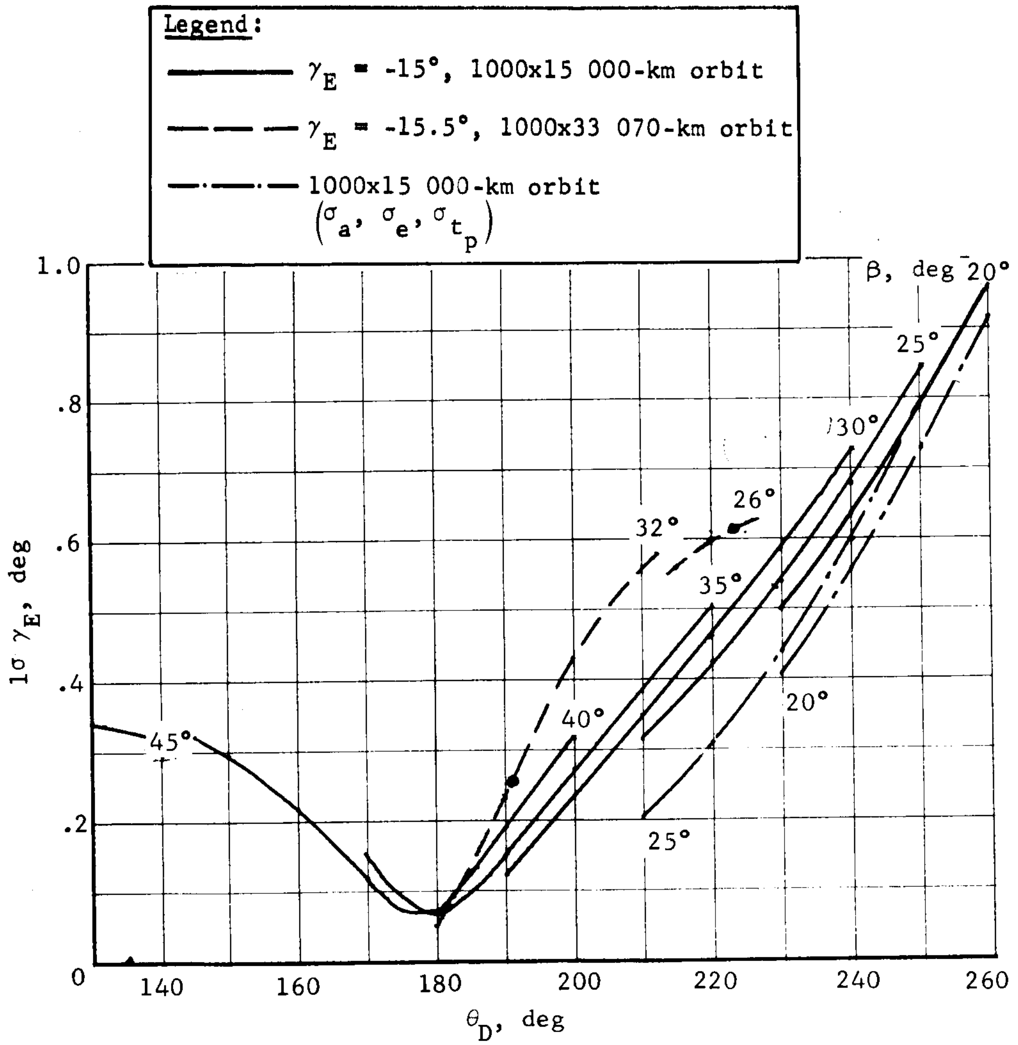

Figure A186.- Entry Flightpath Angle Dispersion versus True Anomaly of Deorbit, (i_{PIS} = 60°)

APPENDIX A

For the 1000x15 000-km orbit with a β of 25°, the θ_D that corresponds to minimum ΔV_D is 229°. The corresponding error in γ_E is 0.53°. The error decreases as β increases. As a comparison of the effect of i_{PIS}, figure A187 is shown for an i_{PIS} of 5°. Whereas the dispersion in downrange angle, φ_E, for the direct mode is approximately 1.4 times the corresponding dispersion in γ_E, for the orbit mode, the dispersion in φ_E is about twice the dispersion in γ_E. The dispersion in X_R due to navigation error is small compared to the dispersion due to execution errors and is not presented. The dispersions for steeper nominal γ_E are slightly less than those presented.

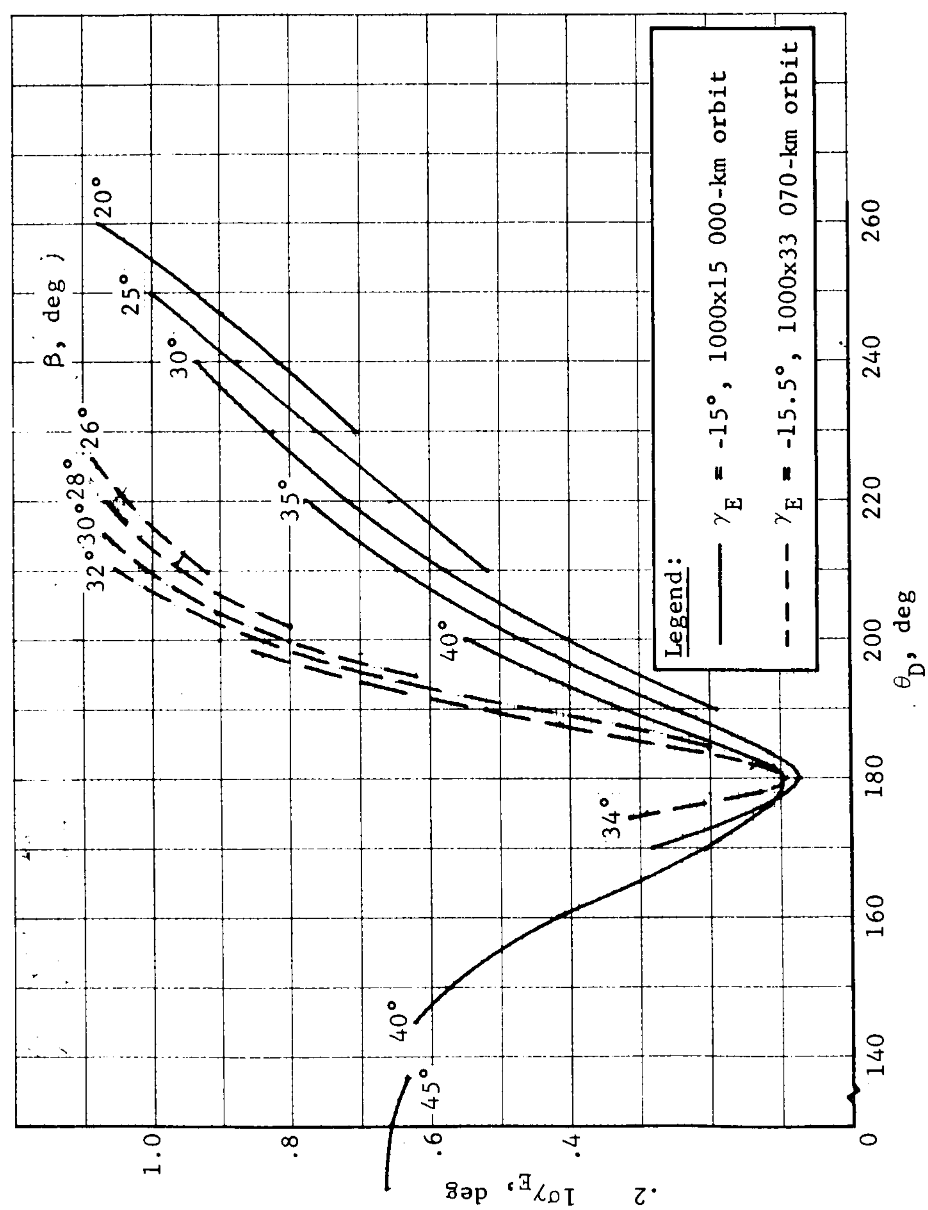

Figure A187.- Entry Flightpath Angle Dispersion versus True Anomaly of Deorbit, i_{PIS} = 5°

APPENDIX A

Entry Dispersions Due to Deorbit Maneuver Errors, Orbit Mode

The entry dispersions due to pointing are shown as a function of ΔV_D rather than τ_{EJ}. The dispersion in γ_E due to pointing is shown in figure A188 for the 1000x33 070-km orbit with a γ_E of -15.5°. The dispersion is seen to be minimum near minimum ΔV_D. The dashed line shows the variation of ΔV_D with β for the reference deorbit maneuver strategy. The maximum error in γ_E occurs for a β of 34°, and is 0.12°. The dispersion due to an impulse error of 0.33% of the nominal ΔV_D is almost invariant with ΔV_D and is about 0.09°. The dispersion in φ_E is shown in figure A189, and, as with the dispersions due to navigation errors, the error in φ_E is about twice the error in γ_E. The dispersion in X_R is shown in figure A190 and is a maximum of 0.066°, for a β of 26°. The dispersion in γ_E, φ_E, and X_R is shown for a γ_E of -18.4° in figures A191 thru A193. For the reference deorbit maneuver strategy, the dispersions are nearly the same as for the shallower γ_E.

The dispersion in γ_E is shown for the 1000x15 000-km orbit with a γ_E of -15° in figure A194. The maximum dispersion occurs again at the higher β because the deorbit maneuver strategy deviates from minimum ΔV_D. The maximum dispersion is about 0.5° due to pointing and 0.08° due to impulse. The dispersions in γ_E, φ_E, and X_R are shown for a γ_E of -17.7° in figures A195 thru A197.

The total dispersion in γ_E due to the three error sources discussed above is shown as a function of β in figure A198 for both orbits. The ΔV_D limits and coast time limit are obtained from figures A162 and A163 of section 2 of this appendix. The total dispersion for the 1000x15 000-km orbit is less than 0.5° for all β with a ΔV_D capability of 150 m/sec. To keep the total dispersion less than 0.5° for the 1000x33 070-km orbit, the β must be above 29°. The $\Delta\beta$ capability for the large orbit then is only about 3°. The total dispersion in γ_E as a function of β is similar for steeper nominal γ_E but is a little lower.

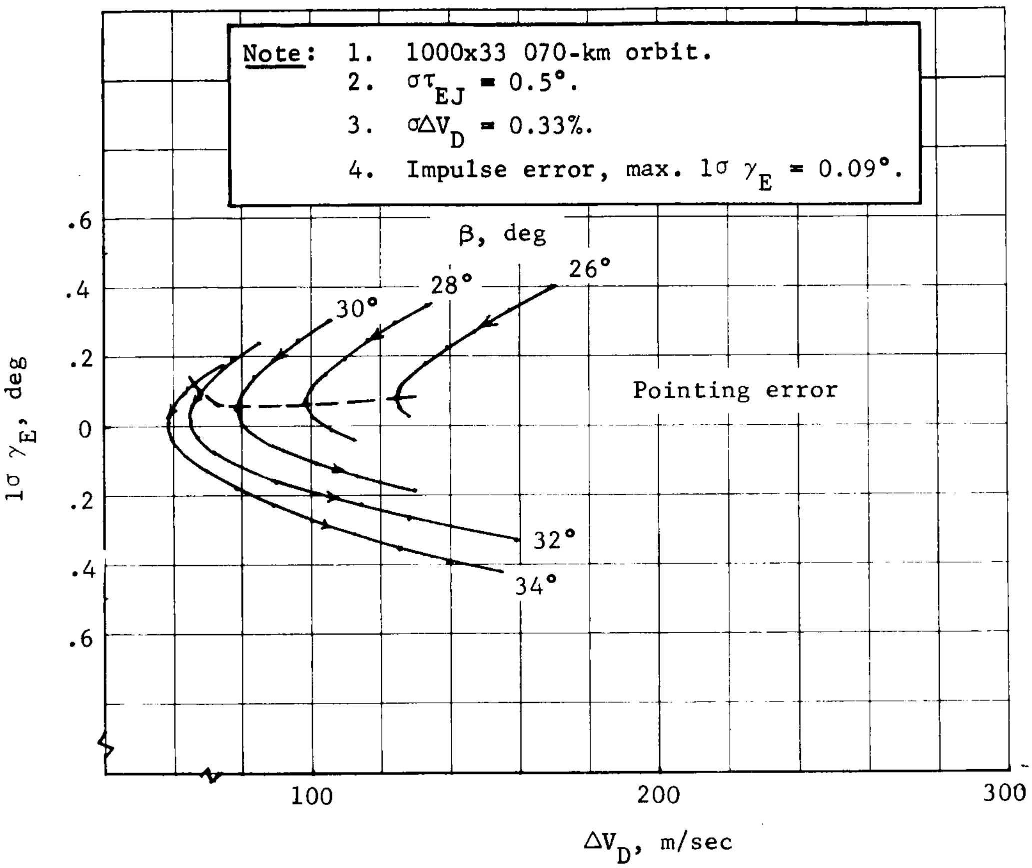

Figure A188.- Dispersion in Entry Flightpath Angle due to Pointing, γ_E = 15.5°

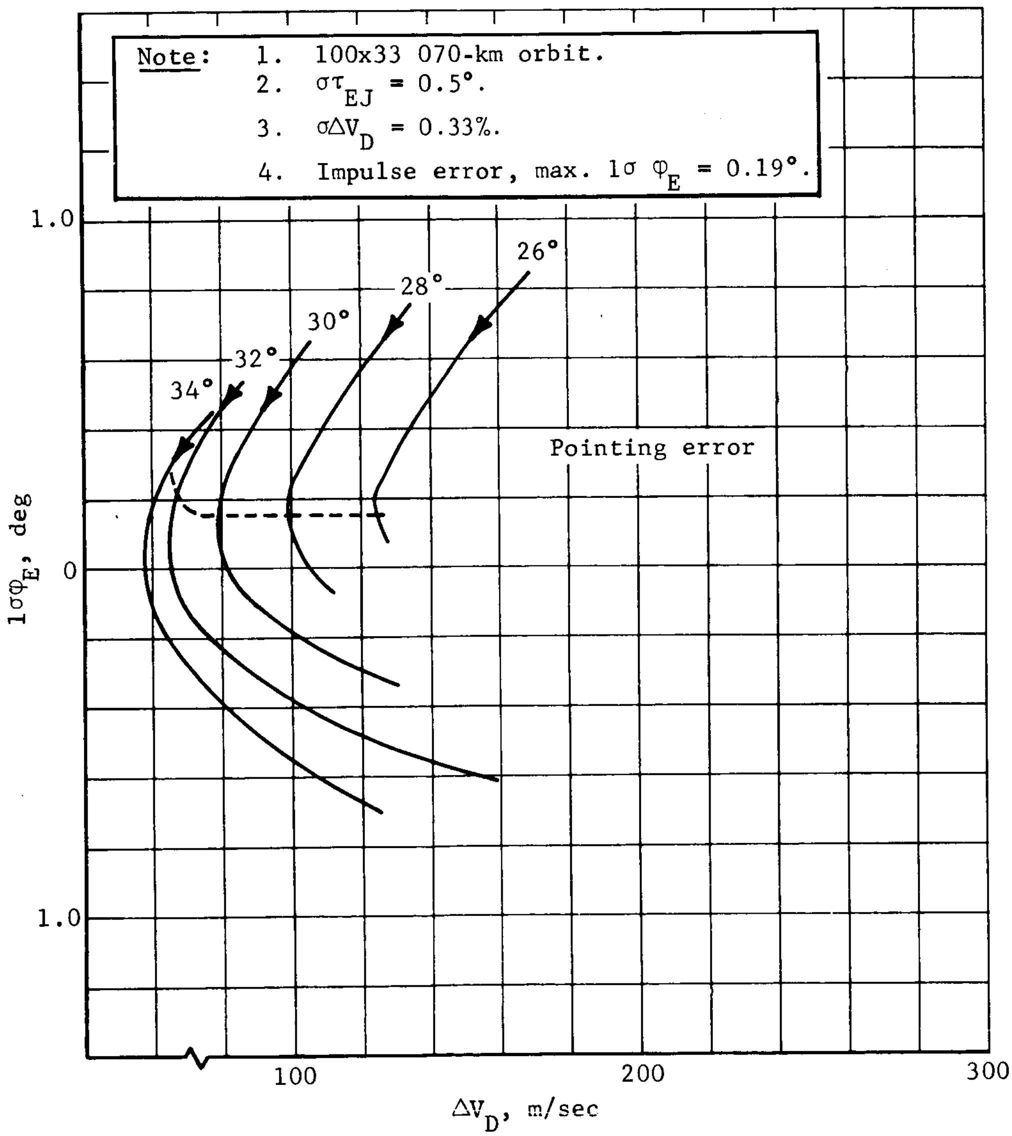

Figure A189.- Dispersion in Downrange Angle due to Pointing, γ_E = -15.5°

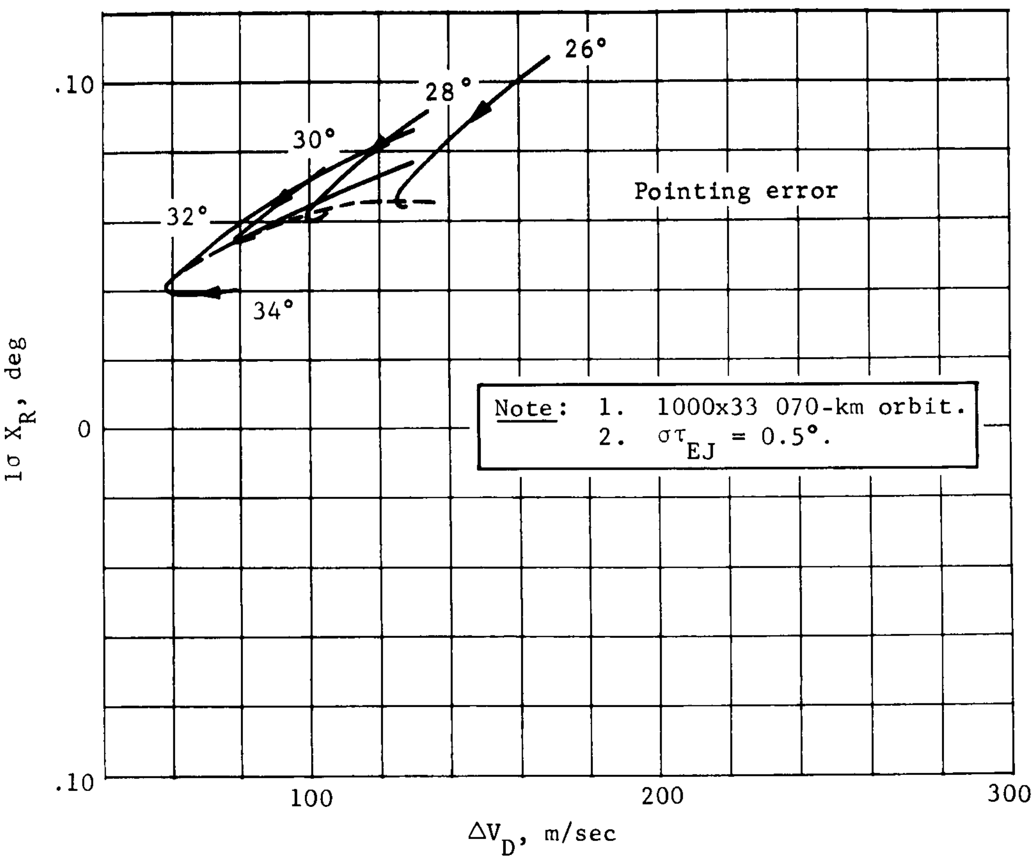

Figure A190.- Dispersion in Crossrange Angle due to Pointing, γ_E = -15.5°

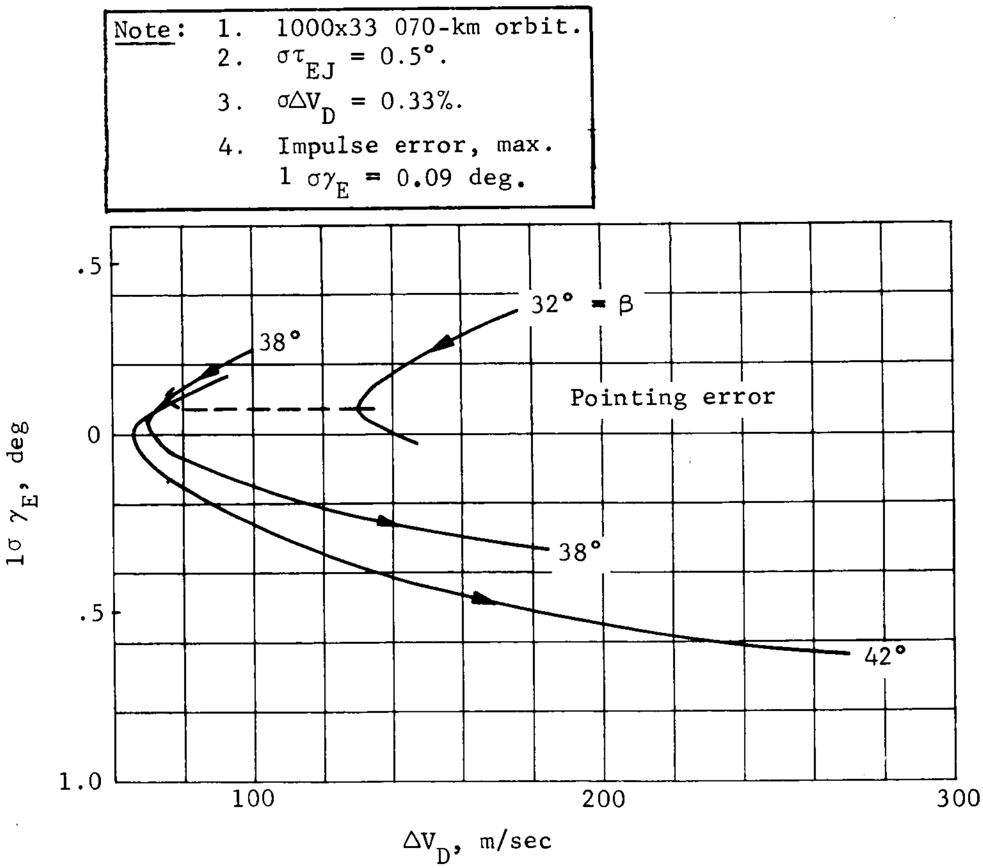

Figure A191.- Dispersion in Entry Flightpath Angle due to Pointing, $\gamma_E = -18.4°$

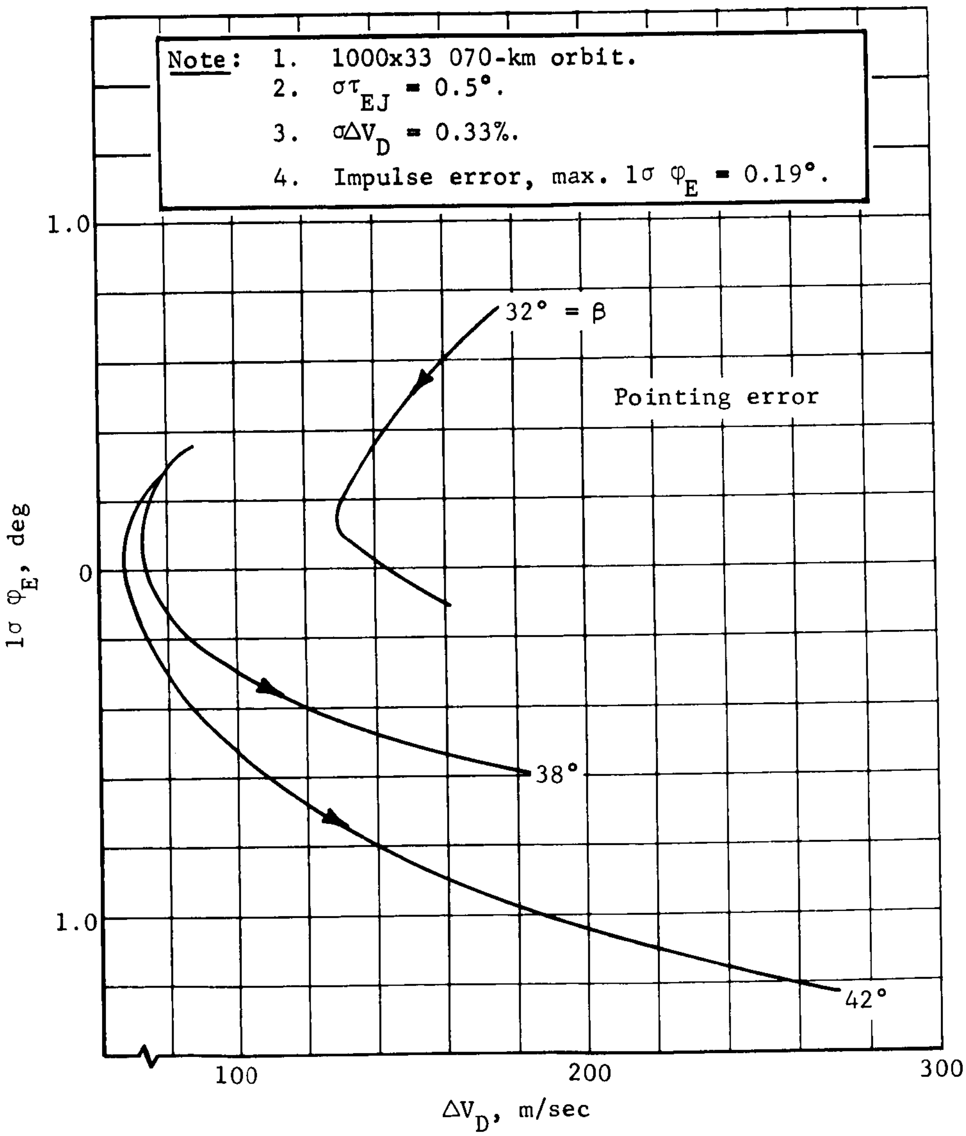

Figure A192.- Dispersion in Downrange Angle due to Pointing, γ_E = -18.4°

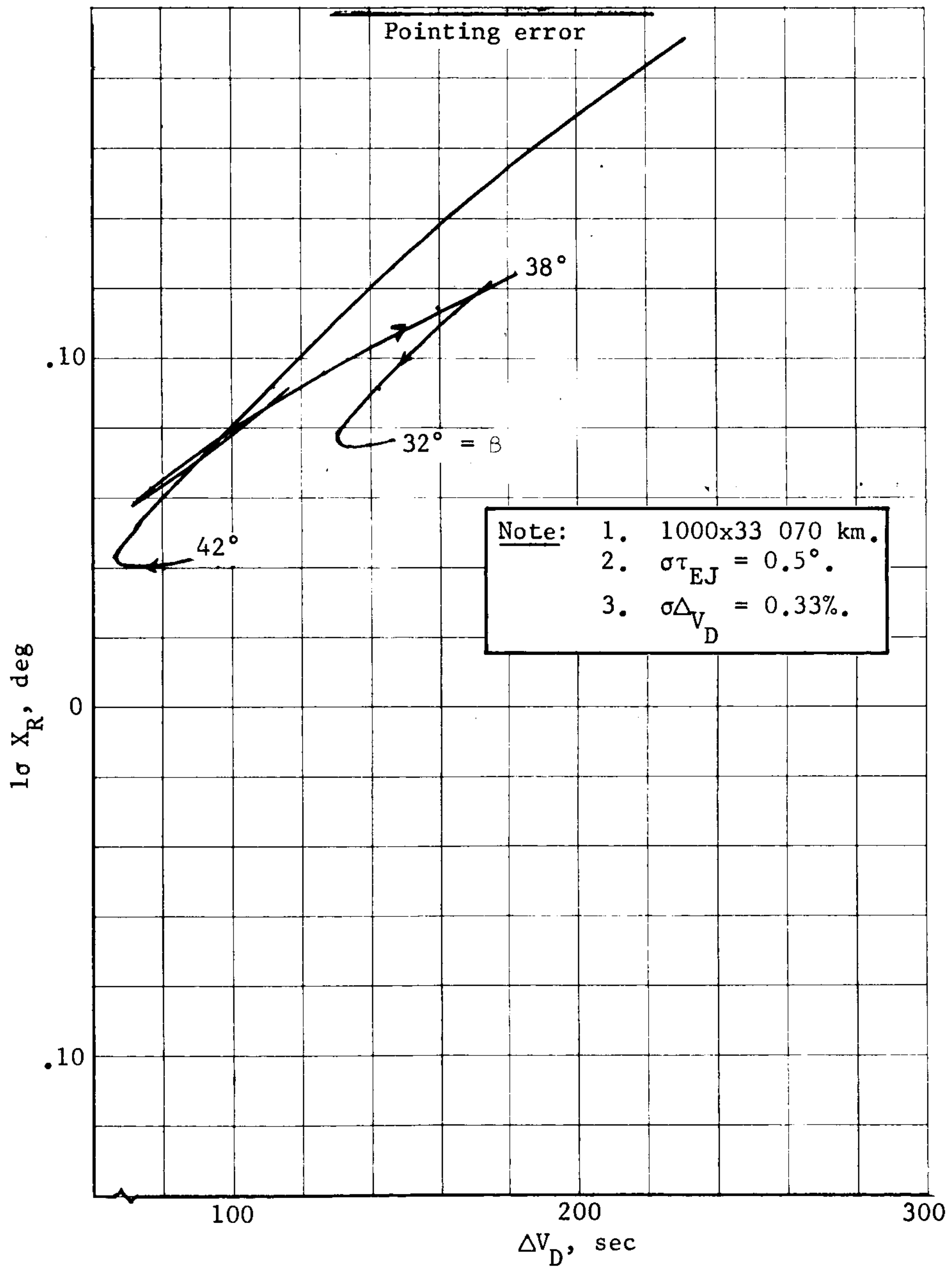

Figure A193.- Dispersion in Corssrange Angle due to Pointing, γ_E = -18.4°

Note: 1. 1000x15 000-km orbit.
2. $\sigma\tau_{EJ} = 0.5°$.
3. $\sigma\Delta V_D = 0.33\%$.
4. Impulse error, max. $1\sigma\ \gamma_E = 0.08°$.

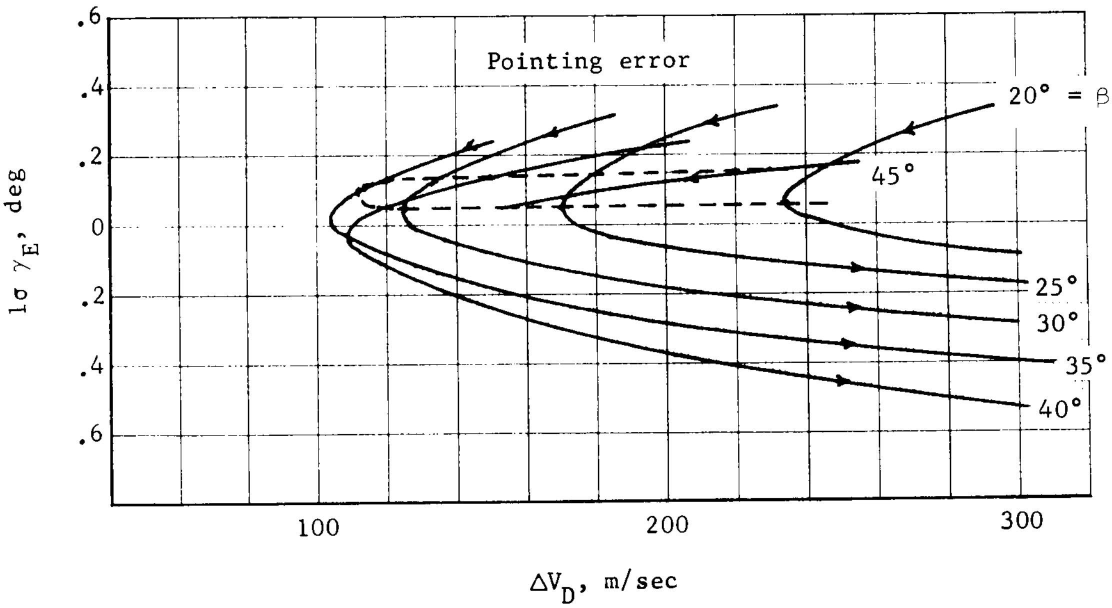

Figure A194.- Dispersion in Entry Flightpath Angle due to Pointing, $\gamma_E = -15°$

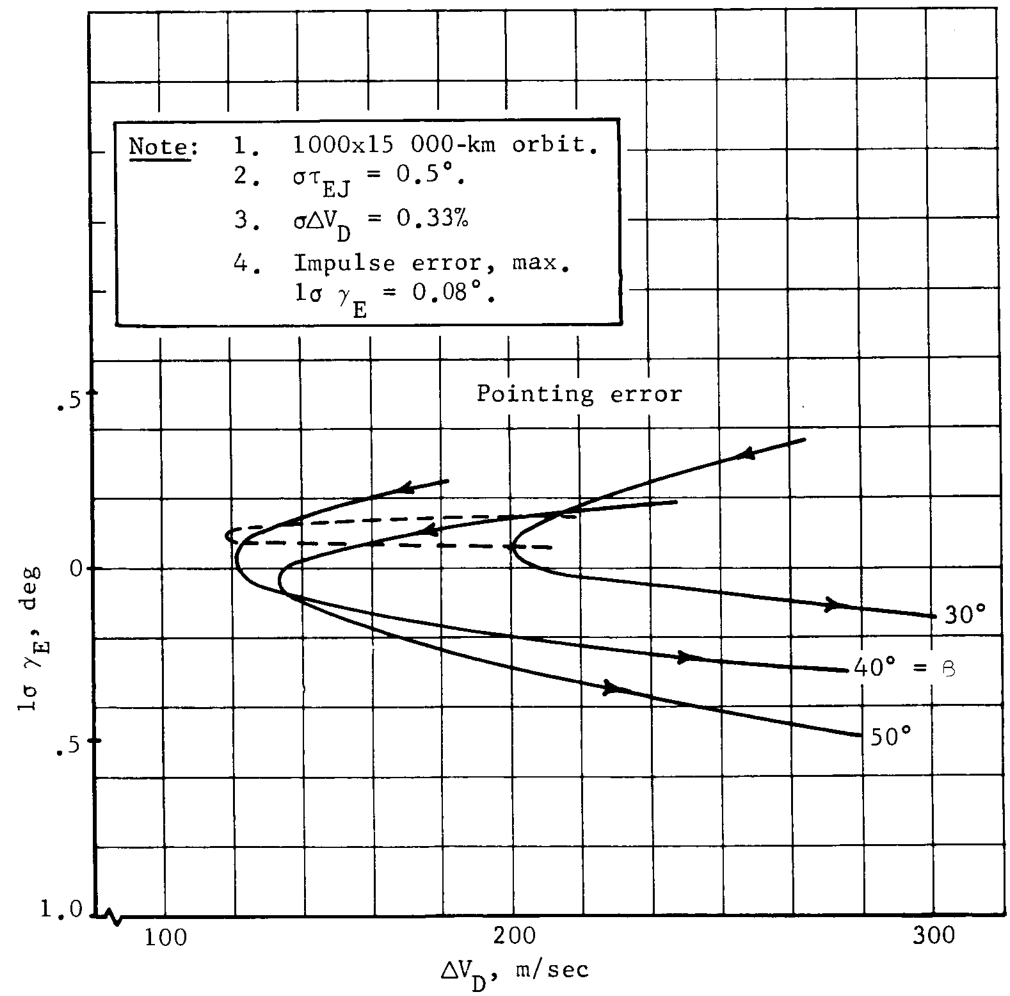

Figure A195.- Dispersion in Entry Flightpath Angle due to Pointing, γ_E = -17.7°

Note: 1. 1000x15 000-km orbit.
2. $\sigma\tau_{EJ} = 0.5°$.
3. $\sigma\Delta V_D = 0.33\%$.
4. Impulse error, max. $1\sigma\ \varphi_E = 0.20°$.

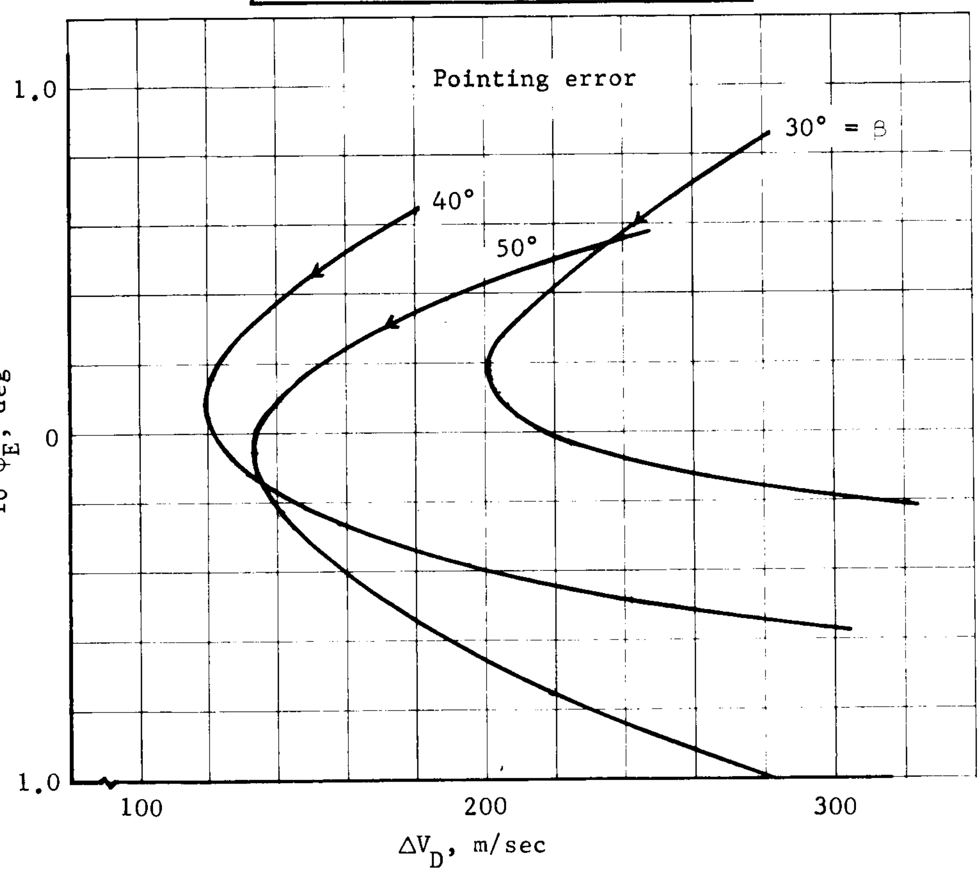

Figure A196.- Dispersion in Downrange Angle due to Pointing, $\gamma_E = 17.7°$

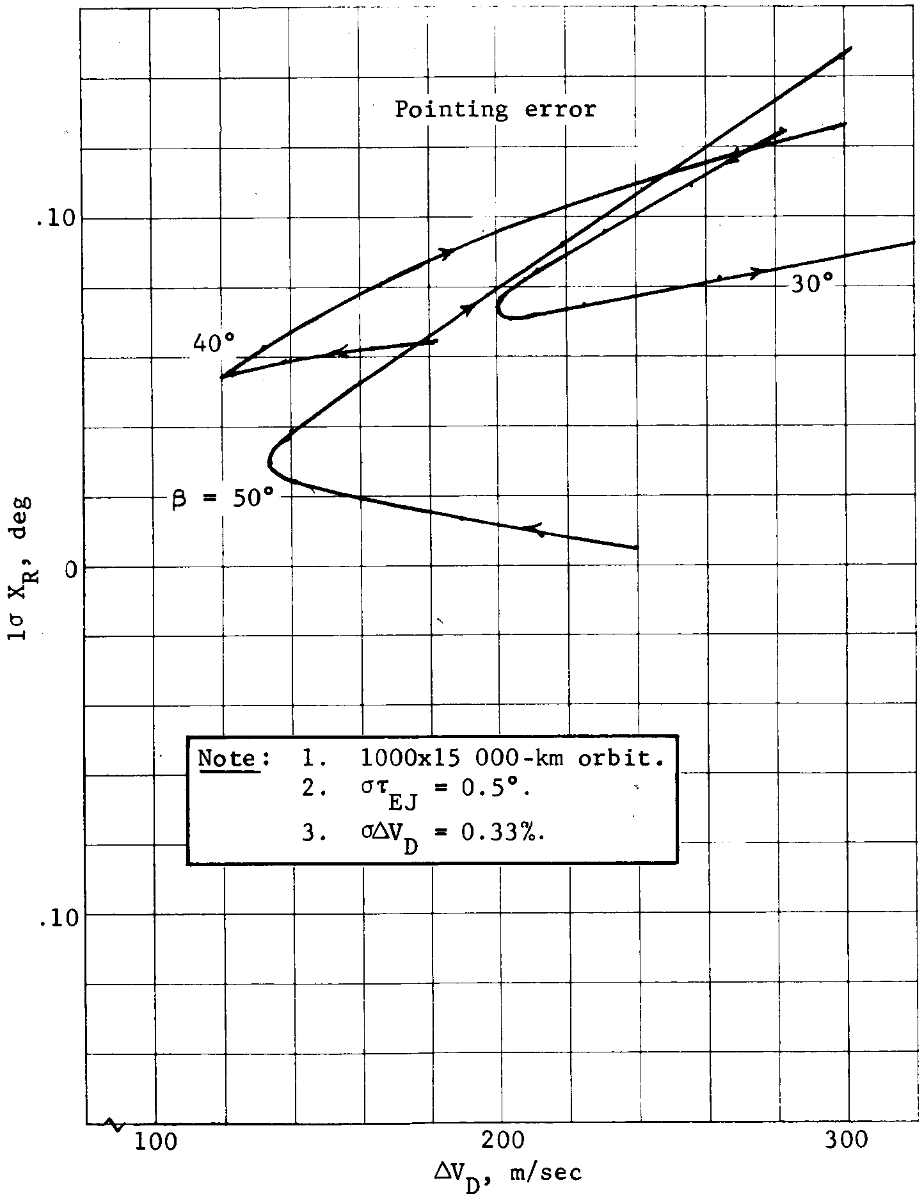

Figure A197.- Dispersion in Crossrange Angle due to Pointing, γ_E = -17.7°

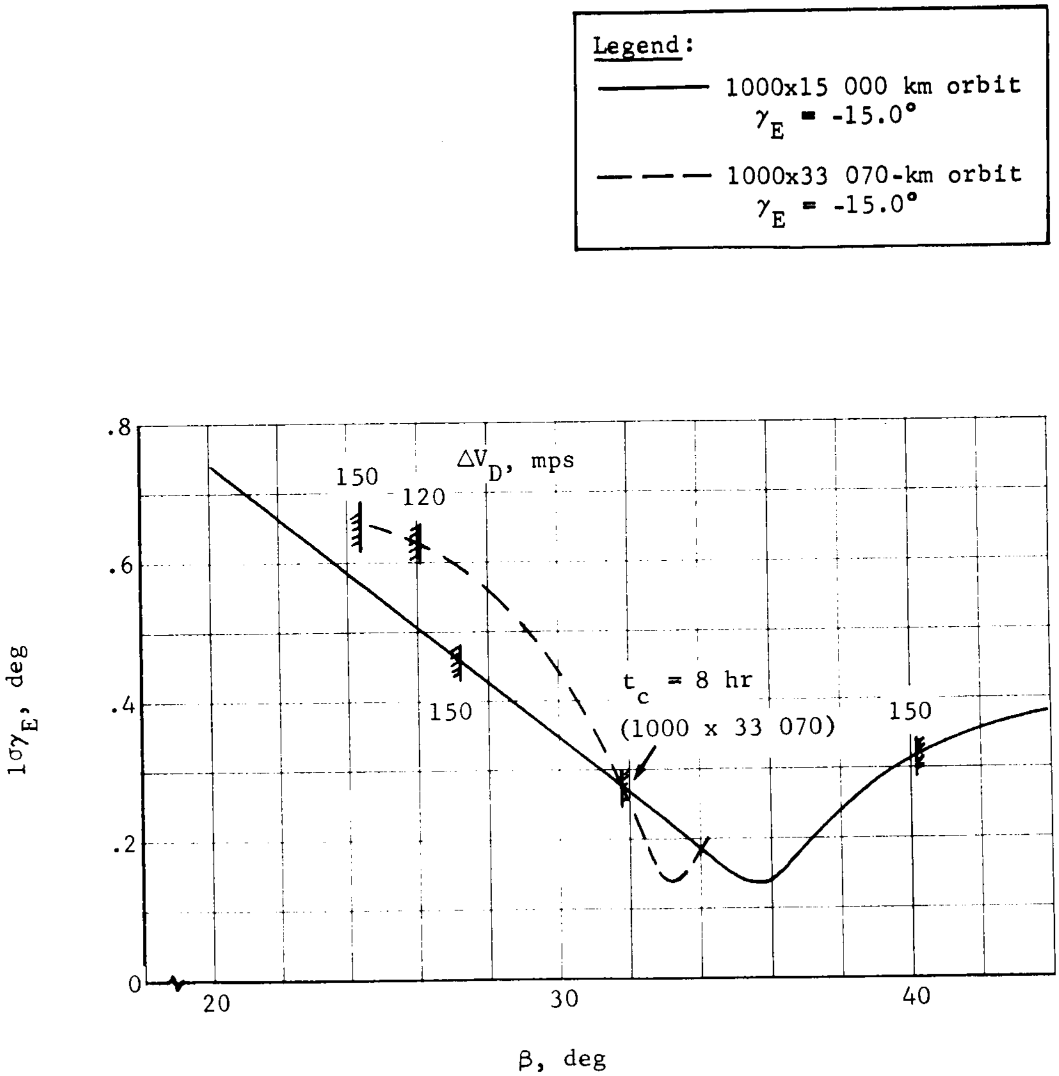

Figure A198.- Total Entry Flightpath Angle Error

APPENDIX A

Entry Corridors and Landing Footprints, Direct and Orbit Modes Compared

The allowable entry corridor for the direct mode is summarized in figure A199 (a) as a function of error in the impact parameter, b. The dashed vertical lines correspond to a capsule ejection distance of 100 000 km and the minimum and maximum navigation errors shown in figure A164. The nominal γ_E curve is 5σ above skipout and varies between -21.2 and -26.7° as a function of error in b. The 1σ touchdown footprint is shown in figure A199(b). The downrange dispersion at touchdown is composed of three parts -- (1) dispersion in φ_E due to navigation uncertainty and ejection maneuver errors, (2) dispersion in downrange angle traversed through the atmosphere due to a dispersion in γ_E, and (3) dispersion in downrange angle traversed through the atmosphere due to atmosphere uncertainty (the difference in downrange angle traversed between the VM-3 and VM-8 atmospheres was taken to be a 6σ dispersion). Parts (1) and (2) are added and RSS'd with (3). The data for downrange angle traversed through the atmosphere are taken from section 1 of Appendix B.

The allowable entry corridor for the orbit mode is shown as a function of β for both orbits in figure A200(a). The touchdown footprints are constructed as for the direct mode and are shown in figure A200(b). The downrange error at touchdown for the orbit mode with the proper choice of β can be as low as 60 km for both orbits. With minimum navigation errors, the downrange error for the direct mode is 115 km and is comparable with the worst-case β for the orbit mode.

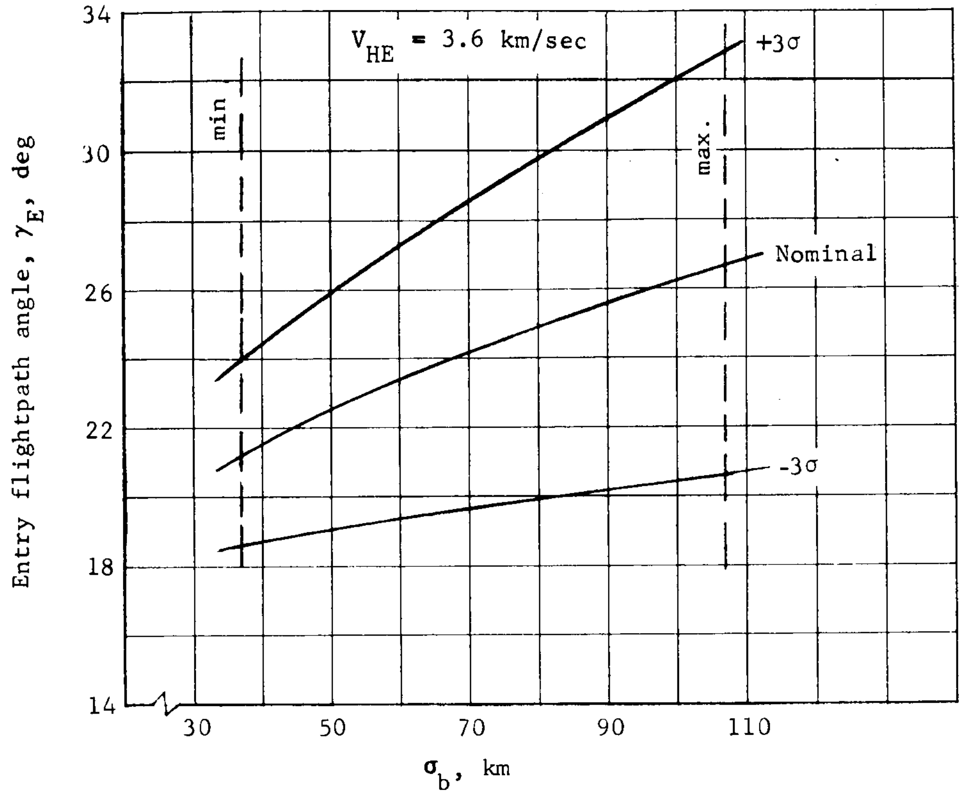

(a) Allowable Entry Corridor

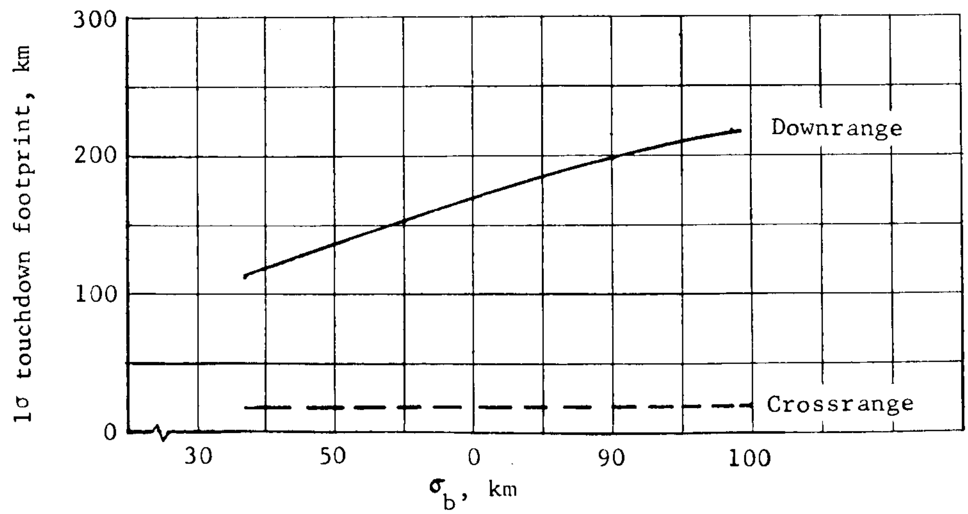

(b) 1σ Touchdown Footprint

Figure A199.- Entry and Touchdown Dispersions, Direct Mode

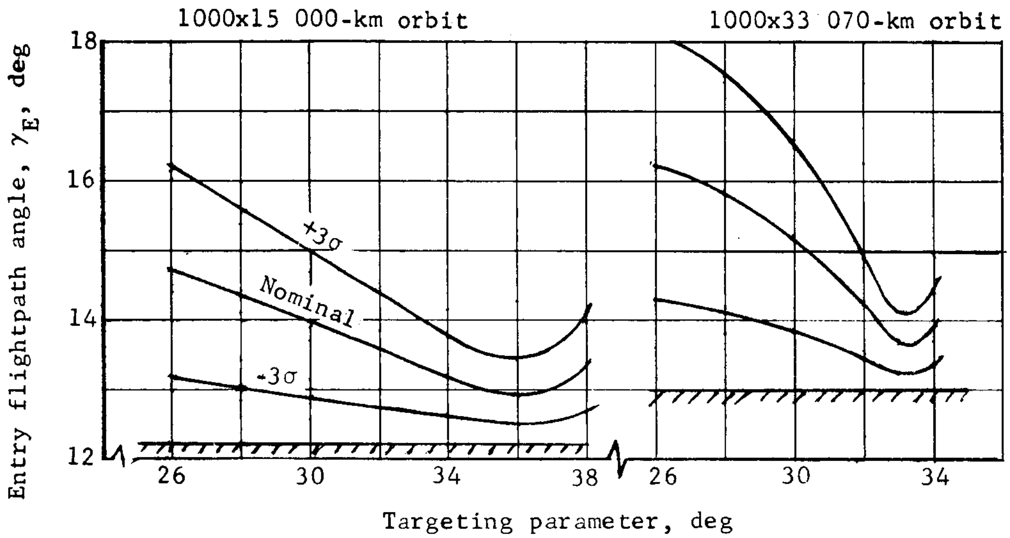

(a) Allowable Entry Corridor

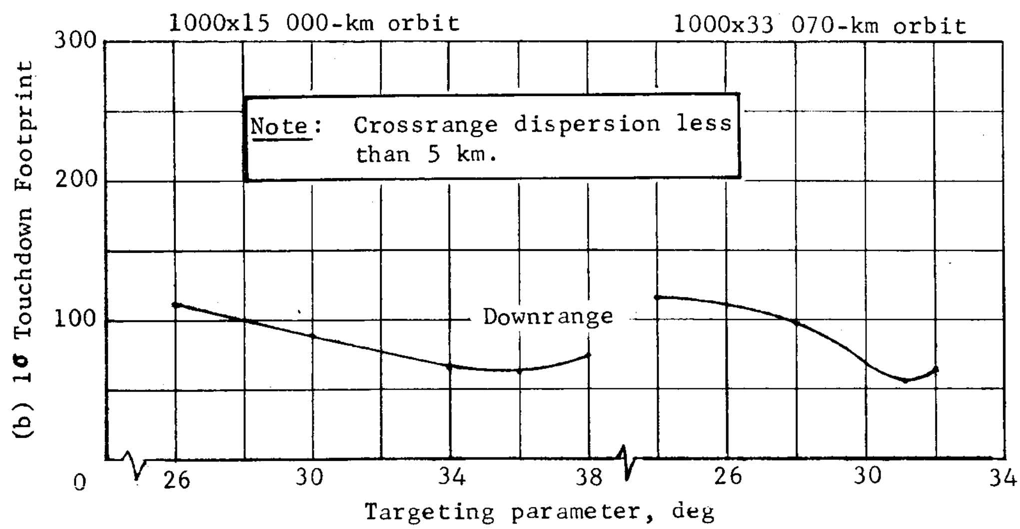

(b) 1σ touchdown footpring, km

Figure A200.- Entry and Toughdown Dispersions, Orbit Mode

APPENDIX A

This page intentionally left blank.

APPENDIX A

4. REFERENCES

A1. Anon.: Launch Vehicle Appendix. PR 22-10-94-2, Martin Marietta Corporation, Denver, Colorado, Sep. 1967.

A2. Anon.: Analysis of Titan IIIF Family Capability for the Mars 1973 Type I Mission. PR 22-10-94-11 (Rev 1), Martin Marietta Corporation, Denver, Colorado, Nov. 15, 1967.

A3. Anon.: Analysis of Titan III Family Capability for the Mars 1975 Type I and Type II Missions. PR 22-10-94-17, Martin Marietta Corporation, Denver, Colorado, Nov. 30, 1967.

A4. Anon.: Trajectory Selection Consideration for Voyager Missions to Mars during the 1971-1977 Time Period. Engineering Planning Document 281, JPL, Sep. 15, 1965.

A5. Anon.: Titan III Family Performance (U). Martin Marietta Corporation, Denver, Colorado, Sep. 1967 (Confidential).